Aramco Journal of Technology

FALL 2020

The *Aramco Journal of Technology* is published quarterly by the Saudi Arabian Oil Company, Dhahran, Saudi Arabia, to provide the company's scientific and engineering communities a forum for the exchange of ideas through the presentation of technical information aimed at advancing knowledge in the hydrocarbon industry.

Editor

William E. Bradshaw
william.bradshaw.1@aramco.com.sa
tel: +966-013-876-0498

Production Coordination

Richard E. Doughty
Corporate Publications, Aramco Americas

Design

Graphic Engine Design Studio
Austin, Texas, U.S.A.

The *Aramco Journal of Technology* gratefully acknowledges the assistance, contribution and cooperation of numerous operating organizations throughout the company.

ISSN 1319-2388

Contents

New Ultra-Strong and Catalyst-Free PDC Cutting Element Technology

Dr. Guodong (David) Zhan, Timothy E. Moellendick, Dr. Bodong Li, Dr. Chinthaka P. Gooneratne, and Dr. Duanwei He

Abstract /

Drilling very hard, abrasive, and interbedded formations requires polycrystalline diamond compact (PDC) cutters, which not only possess higher wear resistance and impact resistance, but also maintains sufficient thermal stability. PDC cutters from conventional high-pressure, high temperature (HPHT) technology have limited thermal stability due to the presence of unavoidable cobalt (Co) catalyst in the cutting structure. Here, we report a new game changing PDC cutter technology via ultrahigh-pressure and high temperature (UHPHT) technology to produce the world's first ultra-strong and catalyst-free PDC cutting elements.

Conventional HPHT technology usually has a synthesis capability of pressures of 5.5 GPa to 7 GPa. In our study, the UHPHT technology has been achieved by an innovative two-stage multi-anvil apparatus with novel high-pressure assembly designs for generating ultrahigh-pressures up to 35 GPa — seven times higher than current PDC cutter technology. Micro-sized fabricated diamond powder was used as a starting material without the use of any catalyst to make ultra-strong and catalyst-free PDC cutting materials using our first proposed high-pressure work hardening approach.

The design principles and experimental study of a centimeter-sized sample chamber for a novel 6-8 type two-stage static ultrahigh-pressure apparatus will be detailed. The conventional PDC cutter manufacturing HPHT technologies will also be reviewed. The hardness and fracture toughness of the new cutting materials were evaluated using a Vickers hardness tester. The new ultra-strong PDC cutting materials — without using any catalyst — were synthesized under applied pressures, nearly three times higher than current PDC cutter manufacturing pressure.

The Vickers hardness of the ultrahigh-pressure synthesized PDC cutting materials reached the top limit of the single crystal diamond, more than 200% higher than current PDC cutters. The PDC cutting elements also possess the metallic fracture toughness, which is also more than 200% higher than that of current PDC cutters. More importantly, the PDC cutting materials exhibit the industry record on wear resistance, which is also more than 200% higher than current PDC cutters.

Materials characterization, including scanning electron microscope (SEM) and transmission electron microscope, indicated that the breakthrough performance is directly related to the unique micro-/nanocomposite microstructure developed under ultrahigh-pressure work hardening conditions. The ultra-strong and catalyst-free PDC cutting elements achieved by innovative UHPHT technology represents a breakthrough for oil and gas drilling technology.

Introduction

Traditional PDC Cutter High-Pressure, High Temperature (HPHT) Technology

Since GE invented its first fabricated diamond in 1954, the technology has spread around the world with the development of more and more high-pressure, high temperature (HPHT) capable tools. One of the most successful tools is the polycrystalline diamond compact (PDC) cutter. PDC cutters are manufactured using the HPHT sintering process. The process fuses a single diamond crystal at HPHT and then combines the diamond material with the tungsten carbide (WC) substrate. Synthetic polycrystalline diamond (PCD) structures create unique ultra-hard engineering tool materials that provide high hardness, high wear resistance, and high impact resistance as well.

The PDC drill bit has been widely welcomed in oil and gas drilling due to its long bit life and ability to maintain a high rate of penetration (ROP). The shear effect of the fixed resistance cutter on the penetrating rock is more effective than the crushing effect of the teeth or inserts on the rolling cones of a roller bit.

There are two main press technologies, including belt press and cubic press, currently used in the production of almost all synthetic diamond powders and sintered PCDs. Other technologies also exist, but because the samples are too small to be large enough to be used in oil and gas drilling applications, their use is limited to research and development. The Belt press was the first concept, developed in the 1950s, when GE successfully

synthesized historical fabricated diamond crystals.

Starting with the initial design in 1954, major improvements included changes in cell size increments and the development of HPHT cell materials with better performance and consistency. Typically, two conical anvils and molds are made of hard metal, such as WC cobalt (WC-Co), while the bonding ring, which is installed with more and more mechanical interference, is made of high strength steel. The load is applied axially to the top and bottom anvils, which are pushed onto the high-pressure cells placed inside the mold. The ceramic material of the cell is squeezed into the gap between the mold and the side of the anvil, thereby providing a seal for the increased pressure in the cell. The current passes through the graphite heater to increase the temperature of the internal part of the cell and begin the sintering process.

Another important HPHT press technology is cubic press technology, which was originally developed as an alternative method for generating diamond synthesis conditions. The shape of the cells is cubic, and six hard metal anvils are pushed down on six cubic faces. In this type of press, the edges of the ceramic material are squeezed into the gap between the anvil surfaces, providing the same sealing effect as the belt press.

Diamond sintering requires extreme heat, extreme high pressure and the use of catalytic solvent metal systems to make the sintering process more economical. Typically, diamonds are sintered at temperatures around 1,400 °C, Fig. 1. The source of catalytic/solvent metals can be enhanced by the direct addition of raw diamond powders, or by in situ processes that place substrate materials in a state where catalytic/solvent metals can flow. The interstitial spacing of the raw diamond material is filled with catalyst or solvent from the substrate, thereby bonding the adjacent diamond crystals together. Co is usually used as a bonding phase for a PDC press.

Fig. 1 *The diamond-graphite equilibrium curve.*

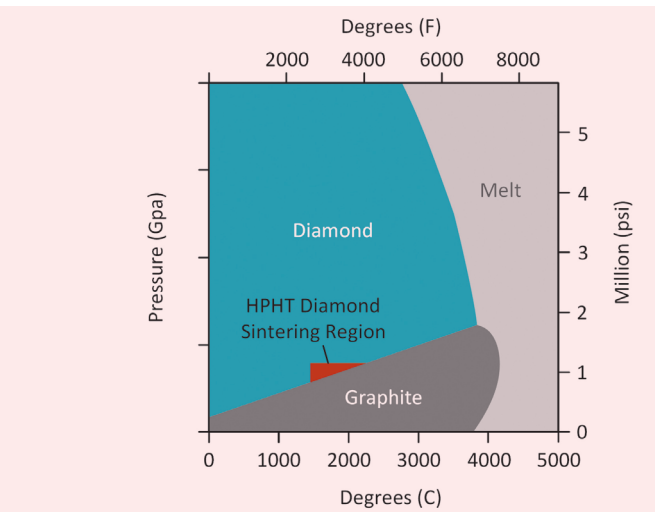

At HPHT, diamond-to-diamond bonding occurs, and metals are infiltrated into diamond abrasive particles, helping to catalyze the bonding process. For the catalytic/solvent metal to be effective, the temperature of carbon dissolution and re-precipitation must be reached. These temperatures usually exceed 1,200 °C[1]. For catalytic solvent systems at active temperatures, in near atmospheric pressure, diamonds are prone to significant degradation to graphite, that is, these extreme temperatures can cause the diamond to return to graphite.

High pressure is also a necessary condition for successful diamond sintering. To maintain the stable phase of the diamond, it is necessary to maintain high pressure during the sintering process. This usually requires a pressure of about 5.5 GPa — nearly 800,000 psi. In this state, the diamond is stable in the sp3 structure and can be sintered without taking into account the significant degradation of the diamond's raw material. In the design and operation of the HPHT system, the system will achieve the required pressure of 800,000 psi and 1,427 °C, while maximizing the life expectancy of expensive hard metal tools, e.g., anvils and molds.

PDC cutters and synthetic diamond manufacturers continue to strive to improve the performance and cost-effectiveness of their HPHT systems, so more extreme sintering conditions can provide the next generation of high-performance drilling products. To achieve these HPHTs at the same time, cubic pressure technology is dominate. The cube press consists of six large pistons, each of which can provide thousands of tons of force.

Each piston pushes a small WC anvil, which in turn compresses a cubic pressure cell that contains the starting material — cemented carbide and diamond powder. Once the cube is pressed, and reaches the required pressure, the current generates the required high temperature through the resistor heater embedded in the pressure unit. These conditions are maintained long enough to ensure the formation of a complete diamond bonded to the diamond. Subsequently, the pressure is limited to a maximum of 10 GPa as the graphite heater will be transferred to the insulated diamond and lose its heater function.

A challenging task for optimizing PDC cutters made from traditional HPHT processes is the removal of Co, which is a key ingredient in the manufacturing process, and is a costly issue thereafter in drilling applications. The PDC relies on a distributed network in which the crystals are strongly combined. The key point is to bond them together with metal catalysts, usually Co. It is also what combines the diamond tables with substrates (WC). Without the Co catalysts, you need to impose extreme pressures and heat that have historically been less commercially viable than they are today. The problem is Co residue. When it heats up due to intense wear friction shear during the drilling process, the metal expands far beyond the diamond and it begins to split. The expansion of Co will lead to the development of cracks, resulting in failure.

Zhan et al. (2014)[2] made the film with a scanning electron microscope (SEM), showing what happened when the PDC sample was heated under reservoir conditions. The result is heat failure, and when irregular cracks appear, the material dims, turning the once even surface into something similar to the cracked mud seen at the bottom of a dry pond. There is a solution to this problem, known as deep leaching technology, by dipping the PDC into acid to leach most of the Co. Consequently, it also has its limitations as some metals are sealed in spaces that the liquid cannot reach, and are left behind.

The industry as a whole is studying (improved) leaching methods or other methods to further reduce the effects of Co. Across the industry, the goal is for PDC cutters to be able to endure longer periods at the resulting high temperatures as they cut through hard, variable formations. The industry's rule of thumb is that high temperatures damages PDC at temperatures higher than 750 °C, and leaching will push that limit to around 1,200 °C. There are many attempts to optimize these limits, but one of the emerging technologies[3-9] identified for breaking through drilling tool technology is ultrahigh-pressure and ultrahigh temperature (UHPHT) technology, without the use of catalysts — that is our present research focus area.

UHPHT Technology

UHPHT technology is cutting-edge. At present, the technology is mainly focused on the study of nanocrystalline diamonds; however, their industrial applications are limited by the size of tiny samples. In this study, we will introduce new UHPHT technologies to create centimeter-sized samples that are sufficient for industrial and scientific applications. Expanding the sample cavity is an important goal in the development of UHPHT devices, and its records are constantly refreshed.

Irifune et al. (2003)[4] made use of the Kawai-type large cavity static pressure device, Fig. 2, to successfully synthesize millimeter-graded nanocrystalline PCD under a high-pressure condition of about 15 GPa. Since then, after nearly 10 years of improvement, the size of synthetic nano-PCD has increased to the centimeter level. Large tonnage high-pressure devices are required to obtain larger sample sizes and to ensure reasonable high-pressure efficiency. The high-pressure occurrence efficiency is mainly affected by the load loss in the transmission process, whether it is the mechanical structure of the assembly or the strength of the final stage of anvil material.

The conveyor process consists of two aspects: (1) the combination of multistage loading, and (2) the final pressure chamber assembly. To improve pressure efficiency, an efficient multistage loading combination and suitable end-level pressure chamber components are required. For the first time in the combination of multistage loading, we have developed a two-stage loading device, Fig. 3. This is directly integrated into the first six-sided cubic pressure chamber[5-7], eliminating the intermediate conversion process loaded by a single axis. Loading into three axes significantly improves the transmission efficiency of the load, compared to the 2-6-8 type loading based on belt press technology.

When the force of the loading system and the strength of the last stage anvil material are high enough, the pressure of the sample cavity can be increased by reducing the pressure contact area, i.e., through shortening the length of the end anvil cutting edge, although this will decrease the sample size. The practicability of a new type of superhard material, such as nanocrystalline PCD and cubic boron nitride, depends to a large extent on the sample size of bulk materials and the pressure required, usually around 14 GPa. Therefore, the challenge to develop a large cavity static pressure device should increase the pressure limit while expanding the cavity.

Ultrahigh-pressure technology based on China's domestic hinge six-sided cubic press, with a centimeter cavity of single cylinder loading capacity, is about 50 MN (5,000 tons). On the other hand, the technology capable of large tonnage six-sided cubic presses is cost-effective that will expand their applications.

Millimeter-scaled samples are still limited to the study of physical properties. The application of centimeter-scaled samples in comprehensive physical

Fig. 2 *A three-stage 2-6-8 type UHPHT press in Japan.*

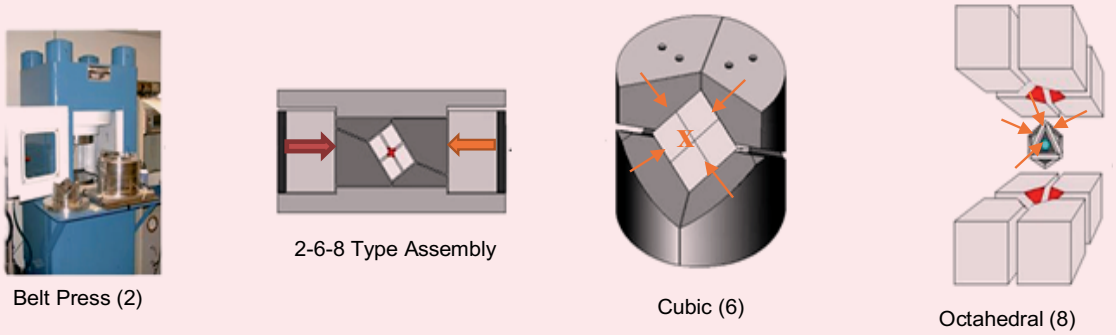

Fig. 3 *Designed two-stage 6-8 type cubic press from the present study.*

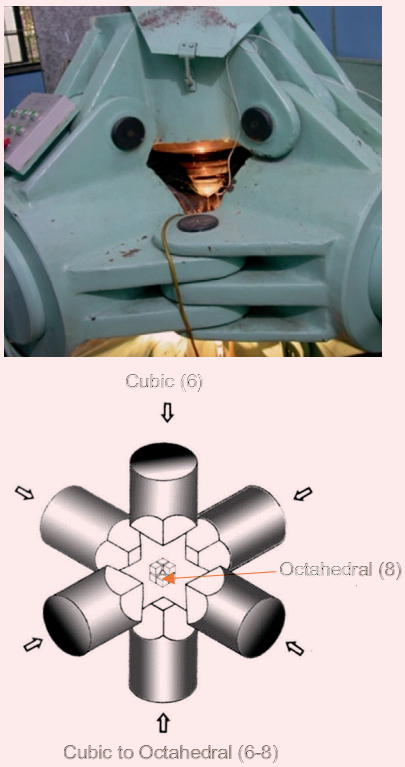

characterization and tool device preparation is more promising. Therefore, the ability to produce centimeter-scaled samples, which are integrated on single-axis (two-sided) presses and the development of a centimeter-scaled high-pressure cavity with more than 14 GPa pressure are of great significance for high-pressure research and the application of new superhard materials.

For the development of pressures greater than 14 GPa of the centimeter-scaled large cavity, the difficulty of a static high-pressure device mainly lies in the lack of mature principle design guidance, and verifies that the experiment cycle is long and expensive. In this study, we developed an advanced two-stage 6-8 type static high-pressure device based on a Chinese domestic DS6 × 800 ton hinged six-face cubic press.

This work focuses on the design principle of a large volume cavity of a two-stage 6-8 type static high-pressure device and experimental research for the first time to synthesize centimeter-scaled samples at a pressure of 14 GPa for oil and gas industry applications.

Results and Discussions

Ultrahigh-Pressure Design Principle, Experimental, and Characterization

Based on the China domestic hinge-type six-face cubic press, the developed two-stage 6-8 type large cavity static high-pressure device consists of two parts, i.e., the primary pressure cubic chamber, and the second stage octahedral pressure booster device. The primary pressure cavity has six anvil-shaped square carbide alloy anvils. The hydraulic cylinders are pushed forward under three axes, together forming a cubic pressure chamber. The second stage pressure booster unit consists of eight angled squares of WC-Co cemented carbide — the end-stage anvil — forming an eight-sided high-pressure cavity where the pressure media is placed inside.

With the end-stage of the anvil propulsion, the eight-faced medium is pressured rheologically and deformed, producing a sealing edge, together with the end anvil faces forming the second stage ultrahigh-pressure chamber. To describe the assembly features of the second stage pressure chamber of a large cavity static high-pressure device, the general method is to give the length, *a*, of the eight-sided pressure media (unit: mm, hereinafter) and the end-stage anvil truncation length, *b*, i.e., *a*/*b*, which is the key to the whole system design. One of the parameters reflects the assembly of important information, such as the basic structure of the two-stage pressure chamber and the approximate size of the sample that can be produced.

The design of this experiment uses a 36/20 assembly, i.e., eight-face body pressure media side length of 36 mm and the end of the anvil front side of the cutting edge length of 20 mm with the use of cemented carbide having a Vickers hardness of about 20 GPa. The loading system is the CS-VII (HD) 6 × 25,000 KN-type six cubic hydraulic machine with a single cylinder with a maximum loading force of 25 MN, and the working cylinder diameter of ⌀560 mm.

The second stage of the eight-sided body cavity is mainly composed of three components: eight cutoff cubic blocks for pressurization, pre-sealing strips between cubic blocks, and octahedron pressure media in the cavity. The loading force acts from six directions of the six outer surfaces of the auxiliary booster unit, Fig. 4, which pushes forward eight cubic blocks, squeezes

Fig. 4 *Newly designed two-stage 36/20 ultrahigh-pressure cell assembly.*

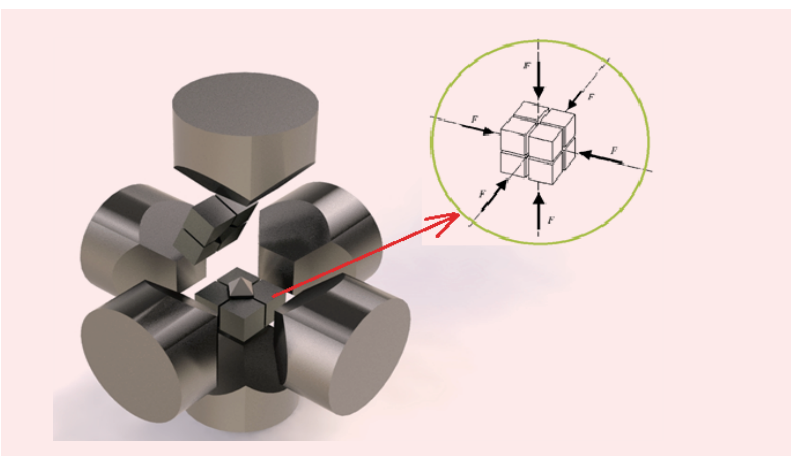

the octahedron pressure transmission media, and establishes ultrahigh-pressure in the cavity. During the loading process, the pre-seal strip and the octahedron transmission medium placed between the cubic blocks are squeezed and flowed to form the sealing edge.

The external force directly acts on the pressurized media, producing the high-pressure of the sample cavity, while the other part acts on the sealing edge, and the sealing of the eight-sided body cavity developed friction between the sealing edge material and the outer surface of the cube booster unit. The pressure occurrence efficiency of the octahedron pressure cavity, i.e., the proportional relationship between the cavity pressure and the system load, depends largely on the load of the force in the system directly acting on the pressure transferring medium — the larger the load consumed by the sealing edge, the lower the pressure occurrence efficiency of the octahedron pressure cavity.

In the large cavity design of the second stage pressure booster unit, the dimensions of *a* and *b* must first be determined. Through the analysis of a pressurized medium and the simplification of mechanical model in the process of compression, some empirical rules can be drawn to guide the design of the whole assembly. To simplify the analysis, it is assumed that the end anvils can move with each other without being destroyed, and that the sealing edges can be infinitely compressed. Figure 5a represents an octahedron in an un-pressured state.

Figure 5b indicates that the eight-sided mass media is compressed under external loading to form a second stage pressure chamber. During the pressure process, the chamfering part of the octahedron is pressed into the gap between the end-stage anvils, together with the sealing edge bearing the high pressure. When the end anvil continues to come into contact with each other, if the seal is omitted, the sealing edge squeezed to the end, the anvil gap will become thinner and thinner.

The original eight-sided body is compressed into the volume limit, Fig. 5c, where the truncation size of the end-stage anvil is the same as the length of the octahedron. The volume ratio can be defined as the assembly limit compression volume ratio, Φ:

$$\Phi = v1/v2 = a^3/b^3 \quad (1)$$

where *v1* represents the initial volume of the eight-face compression media before being compressed, and *v2* represents the volume at which the pressure media is compressed to the ultimate position, i.e., the end volume of the eight-faced body formed by the cutting angle of the anvil.

Figure 6 shows the specific size and the assembly of the ultimate compression volume ratio of the general assembly of the two-stage pressure chamber of the static high-pressure device in the literature and our current 36/20 assembly.

As shown in Fig. 6, the R^2 coefficients of the fitted curves to its octahedral edge length and anvil truncation edge length are 0.88 and 0.93, respectively, which better reflects the trend of the assembly's ultimate compression volume ratio. As can be seen, as the assembly geometry size increases, the assembly's ultimate compression volume ratio is dramatically reduced.

Fig. 5 *Schematic of a pressure medium in the compression process from (a) initial noncompression, (b) during compression, and (c) to the final compression limit.*

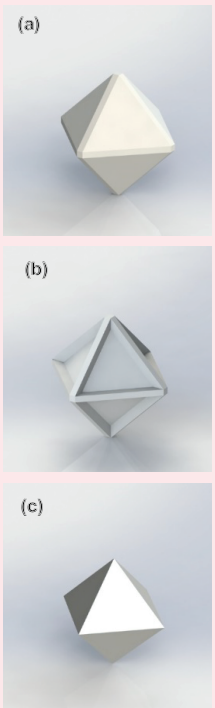

Due to the lack of mature design principles of the high-pressure chamber assembly, we proposed the ultimate *Φ* as an important reference and guidance parameter for assembly design. When designing a new type of assembly, we first need to determine the size of the high-pressure chamber, e.g., the 36/20 assembly used in this study for synthesizing a sample targeting a diameter of 10 mm.

In the HPHT synthesis experiment, the eight-face body pressure media generally includes the following assembly parts: sample wrapping, insulation thermal components, heating components, and conductive components. The sample hole can be calculated by considering the sample size and the size required for each component. In this study, the calculated hole diameter is about 15 mm. Based on the high-pressure cavity pressure, thermal insulation and pressure sealing requirements, the diameter of the polygon triangle of the eight-face body pressure media in the sample hole is estimated at 90% of the diameter of the inner circle.

Therefore, the high-pressure cavity (eight-body pressure media) can be estimated at 29 mm. The high-pressure chamber containing the sample is formed in the compressed eight-face mass pressure media, and its volume (size) is between the eight-face and the eight-body

Fig. 6 *Ultimate compression volume ratio of the assembly with its octahedral edge-length, a, and the anvil truncation edge-length,* b.

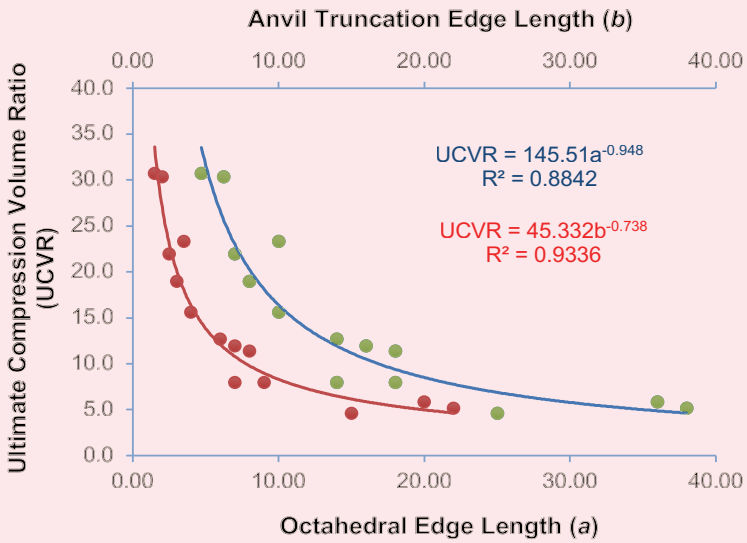

pressure media formed by the cutting angle of the anvil. According to the previous experiment and the number reported in the literature, when the pressure medium from the initial state is compressed to about 14 GPa, the volume collapse rate is about 20%, which can be estimated from the initial eight-face body.

The side length, *a*, of the media is 36 mm. The anvil truncation edge length, *b*, from the combined ultimate compression volume ratio, obtained from Fig. 6, can be reversed to 20 mm. Importantly, after the assembly parameters *a* and *b* are determined, the size of the required sealing edge and the size of the anvil support material can be calculated according to the mechanical structure.

At this point, the assembly required dimensions of each component are designed to be complete. Note that the design of the assembly size should be modified according to the specific circumstances. This includes the need for more high pressure, which can be guaranteed under the premise of the high-pressure seal, to reduce the size of the sealing edge, and the use of the higher strength of the end stage of the anvil material.

Mechanical Properties and Wear Resistance

As the starting material for the experiment, the particle size of the commercially available high purity raw diamond powder is 8 M to 12 M. We use a grundo container to treat the powder in a vacuum furnace. When the vacuum chamber is pumped to 2×10^{-4} Torr, the sample is heated to 1,200 °C at a rate of 15 °C per minute. After maintaining a peak treatment temperature for 90 minutes, the sample is cooled to room temperature at 5 °C per min. Next, the end-processed powder is quickly packed into a cylindrical capsule — made of titanium foil with a diameter of 13 mm and a thickness of 6.3 mm — and placed in a high-pressure unit. High-pressure experiments were carried out using a two-stage multi-anvil device based on a cubic press. Magnesium oxide (MgO) was used as a pressure medium. To produce an ultrahigh-pressure, a high-pressure assembly was developed — 36/20 octahem edge length/truncated edge length. Packaged in titanium foil, the samples were placed in MgO sleeves. The tantalum tube was used as the heater, and a zirconium dioxide sleeve as the thermal insulator. The pressure is calibrated according to the phase change of several reference materials at room temperature (bismuth, zinc telluride, and zinc sulfide).

The treatment temperature of the pressure chamber was measured using a thermocouple. In our experiment, we first increased the pressure to 5 GPa within 2 hours, then heated the sample to 100 °C and increased the speed to 100° per minute. We maintain a constant temperature of 1,000 °C for 1 hour and increased the pressure to 14 GPa, and then increased the desired temperature at a constant pressure of 200 °C per minute at 14 GPa. Following that, at P-T peak conditions, the sample remained for 10 minutes and gradually annealed to a temperature of 100 °C, reducing the pressure to 5 GPa within 4 hours.

Finally, we cooled it to room temperature at a rate of 2 GPa. Then we released the pressure over 30 minutes. Capsules extracted from a multi-hammer combination were opened and processed under acidic conditions to remove the titanium foil. After that, the sample was cleaned in water, and then cleaned with ethanol in an ultrasonic bath.

The powder X-ray diffraction (XRD) in X-ray diffractometer with Cu kα radiation (= 0.15406 nm) on 0.01°/s, for 2 = 10°-100° characterizes the starting material and the treated sample at room temperature.

The morphology and microstructure of the polished sample was studied by SEM. Samples prepared at 14 GPa and 1,900 °C are characterized by transmission electron microscopes with an accelerated voltage of 200,000 volts. The volume density of the prepared sample was measured by the Archimedes method, and the phase reference strength was quantitatively analyzed by XRD to calculate the relative density. In the backscatter geometric backscatter, based on the triple grating monochrome, the micro-Raman scattering spectrum is collected at room temperature and is accompanied by the electron multiplying charge coupled device, which is excited by solid-state lasers 532 nm, and collect 100x, 0.90 NA objective.

A Vickers single diamond indenter on polished samples performs the Vickers hardness (Hv) test. The load force is 29.4 N and the duration is 15 seconds. The SEM measures the Vickers indentation length of the polished sample. In traditional PCD manufacturing, pressure and temperature are two key variables because they are important in determining the final performance of sintered diamond products. Likewise, these same variables also represent the principle technical challenges in designing the HPHT apparatus for optimizing the manufacturing process.

Usually, the diamond powder sintering process consists of two steps. First, the pressure is raised to nominal levels, with little or no heating. At this stage, all crystals are driven into each other and are becoming more and more compressed. Many diamond grains are relatively sliding, most of which are cracked into two or more fragments; the overall effect of which is to increase the apparent density of the powder.

By measuring the particle size distribution before and after full pressure of the cold operation, it is easy to quantify the powder breakage caused by pressure increase. Interestingly, the rougher powder has a higher degree of crushing than the finer powder. In terms of the average number of points of contact, this fact can easily be proven.

Under atmospheric pressure, diamonds are not at a stage of thermal stability, but graphite is at a stage of temperature stability. Diamonds do not spontaneously convert to black carbon at room temperature because the reaction speed is almost zero. Although, if the temperature exceeds 1,200 °C, the reaction speed will accelerate, causing the diamond to form graphite spontaneously. To make a diamond, or to sinter it, this condition is necessary to support the heat stabilization phase of the diamond, not the graphite. In other words, we need to increase the pressure and temperature to speed up the synthesis, or bonding process.

Figure 1 shows the diamond-graphite equilibrium curve, according to which the increase in temperature per 38 °C requires an increased pressure of psi to remain within the stable range of the diamond. It is also clear that the need for rapid response (and therefore high temperatures) contradicts the manufacturing need to work at lower pressures to extend the life of high-pressure tools.

In this study, the microcrystalline diamond (MPD) powder was treated at 14 GPa at very high pressure without any additives at different temperatures. This is 2.5 times higher than traditional HPHT processes. Most importantly, we can produce cylindrical samples with a diameter of 11 mm and a thickness of 6 mm, which is the largest sample in the world. These samples are large enough to manufacture industrial cutting/drilling tools and scientific research samples. It was found that MPD materials have relatively low stress zones, known as Y regions, located in triangular diamond particle boundaries, which may be the cause of the presence of reinforced graphite.

It was also noted that the Y zone consists of diamond nanoparticles embedded in turbine graphite and amorphous carbon. Dense dislocation, dual boundary, and stacked faults were observed, indicating that each particle contained a diamond laminate in nanoscale thickness[5]. These substructures observed in large diamond particles are typical features of cold plastic deformation or post-working hardening materials. This is consistent with recent reports that nanodiamonds made from specially designed onion carbon nanoparticles have similar properties[7].

The results of the Hv test of the MPD samples processed at a temperature of 1,900 °C are measured using a standard square pyramid diamond indenter. The load force is 29.4 N and the residence time is 15 seconds. The MPD material has a hardness of 121 GPa, which is up to the maximum limit for monocrystalline diamonds, and is twice as high as conventional PCD composites. The ultrahigh hardness of MPD materials can be attributed to nanostructure defects caused by high-pressure hardening, such as stacked nanoplate layers, stacked faults, and twin microstructures.

Figure 7 is a schematic of the microstructural change mechanism with increased pressures, forming a superstrong diamond. Typically, MPD material consists of a diamond skeleton consisting of micron-sized particles and isolated Y zones. Each micron-sized particle has a substructure of stacked nanoplates, while the Y zone consists of nanocrystal diamond grains embedded in turbine graphite and amorphous carbon.

This unique micro-nested structure stems from the plastic deformation of diamond particles and the mutual transformation of diamonds produced during the HPHT process. The crystallization defect plays a role in preventing disalignment in the deformation process, which is beneficial to its mechanical properties. In addition, during processing, particles form plastic deformation in substructures by squeezing diamond particles, further increasing hardness due to the Hall repair effect.

The fracture toughness of the MPD sample has been characterized and calculated by:

$$K_{IC} = \xi (E/H_V)^{1/2} (P/c^{3/2}) \text{ (MPa m}^{1/2}\text{)} \quad 2$$

where ξ is the calibration constant of 0.0166 (±0.004), E is the Young's modulus (GPa) (in the experiment we used the aggregate Young's modulus, 1,050 GPa,

for diamond), P is the loading force (N), and c is the length of the crack.

The K_{IC} of the MPD prepared at 14 GPa and 1,900 °C is 18.7 MPa $m^{1/2}$, the highest in the world. This is 3.7 to 5.5 times higher than a monocrystalline diamond. Interestingly, microcracks are mainly produced on diamond microcrystals and terminate at the grain boundary (Y zone). The Y region of the nanostructure, consisting of nanocrystal diamond particles, turbine graphite, and amorphous carbon, can significantly prevent further crack expansion, thereby greatly improving the fracture toughness of the preparation sample.

The turning log testing to assess the wear resistance of the MPD material is carried out at a speed of 1,000 m/min with a feed rate of 0.4 mm and a cutting depth of 0.5 mm. The G ratio is calculated based on the wear flat volume to assess the wear resistance of the material. The best PDC cutters used in the oil industry for performance comparison also prepare the reference baseline diamond table. The results of the new UHPHT diamond cutting material set a new industry record for wear/abrasion resistance, more than 2.3 times higher than the best wear-resistant PDC cutters currently used in the oil industry.

Figure 8a is an image of the new UHPHT synthesized MPD, and Fig. 8b is the reference cutter, generated under the same testing condition, showing industry record wear resistance of the UHPHT MPD diamond cutting material.

Conclusions and Future Direction

In conclusion, we have successfully synthesized and tested a new PDC cutting material using our innovative UHPHT technology. These test results set a new industry record for wear resistance of more than two times higher than the current PDC cutters used in the oil and gas drilling industry. The new material achieves fracture toughness close to the metal, and its hardness is more than two times harder than that of the current PDC technologies.

As seen in Fig. 9, there are also many promising areas to explore, but we are facing new challenges because of the synthetic conditions of industrial high-pressure from the traditional 5 GPa, 1,500 °C region to 20 GPa, 2,000 °C. In these new temperature and pressure zones of 20 GPa and 2,000 °C, the challenges include development of the required large cavity industrial equipment to deliver the combination of the high precision temperature and the pressure control. This is necessary to achieve the required conditions for diamond synthesis, i.e., high efficiency with precise control.

These ultra-strong and catalyst-free PDC cutting elements achieved in this study represent a potential breakthrough in the oil and gas drilling technology. Research continues to produce larger volumes of UHPHT cutting material needed to create full-scale cutters ready for field-testing with the goal of achieving "One Run to Total Depth" game changing drill bit technology.

Fig. 7 *A schematic of the microstructural change mechanism with increased0 pressures, forming a superstrong diamond.*

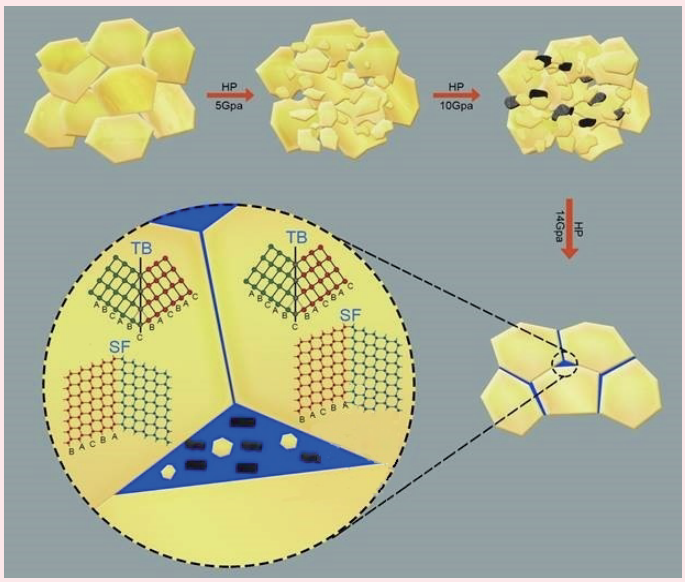

Fig. 8 *An image of the new UHPHT synthesized MPD (a), and the reference cutter (b), generated under the same testing condition, showing industry record wear resistance of the UHPHT MPD diamond cutting material.*

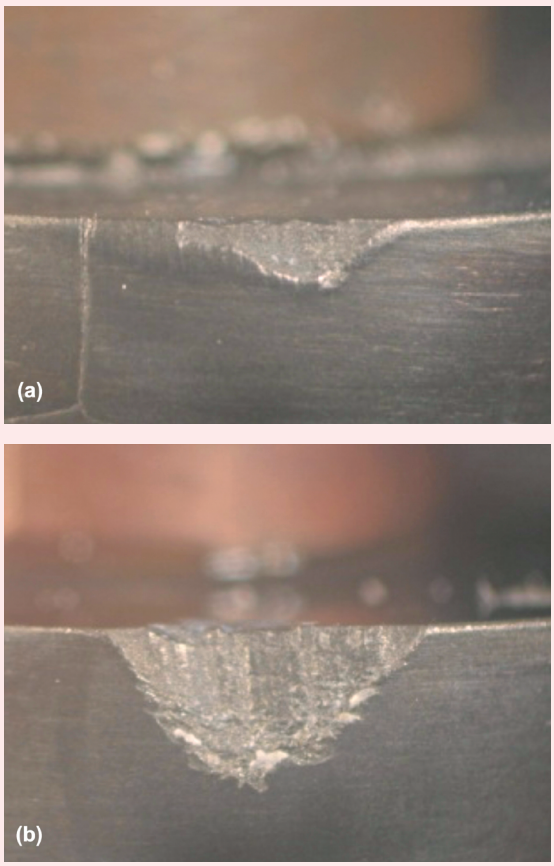

Fig. 9 *Future research directions for UHPHT[10].*

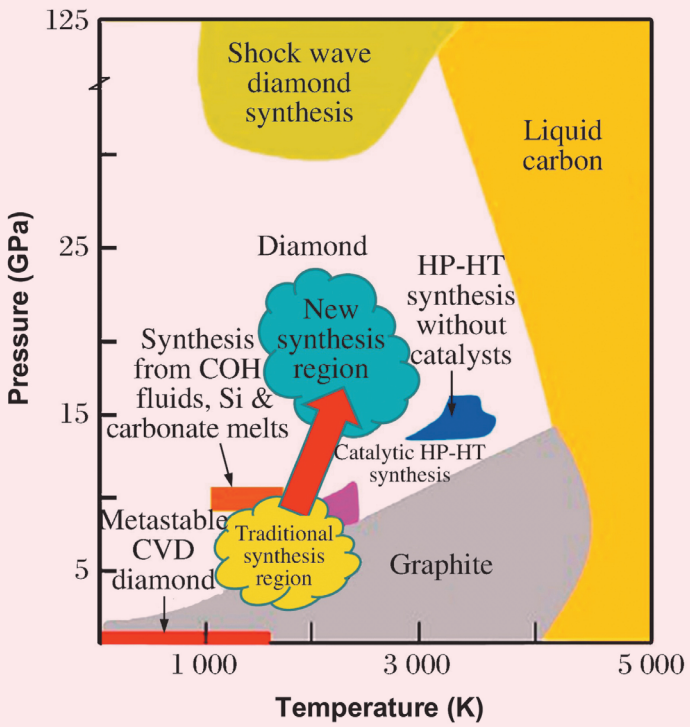

Acknowledgments

This article was previously presented at the International Petroleum Technology Conference, Dhahran, Saudi Arabia, February 13-15, 2020.

References

1. Bellin, F., Dourfaye, A., King, W. and Thigpen, M.: "The Current State of PDC Bit Technology," *World Oil*, September 2010, pp. 41-46.
2. Zhan, G., Patin, A., Pillai, R., Gilleylen, R., et al.: "In Situ Analysis of the Microscopic Thermal Fracture Behavior of PDC Cutters Using Environmental Scanning Electron Microscope," SPE paper 168004, presented at the IADC/SPE Drilling Conference and Exhibition, Ft. Worth, Texas, March 4-6, 2014.
3. Rassenfoss, S.: "Seeking Ways to Make Better Diamonds by Tending to the Tiniest Details," *Journal of Petroleum Technology*, Vol. 66, Issue 6, June 2014, pp. 38-47.
4. Irifune, T., Kurio, A., Sakamoto, S., Inoue, T., et al.: "Ultrahard Polycrystalline Diamond from Graphite," *Nature*, Vol. 421, Issue 6923, 2003, pp. 599-600.
5. Liu, J., Zhan, G., Wang, Q., Yan, X., et al.: "Superstrong Micro-Grained Polycrystalline Diamond Compact through Work Hardening under High Pressure," *Applied Physics Letters*, Vol. 112, Issue 6, February 2018, pp. 061901-061905.
6. Liu, Y., Zhan, G., Wang, Q., He, D., et al.: "Hardness of Polycrystalline Wurtzite Boron Nitride (wBN) Compacts," *Scientific Reports*, Vol. 9, Issue 1, December 2019.
7. Xu, C., He, D., Wang, H., Guan, J., et al.: "Nano-Polycrystalline Diamond Formation under Ultra-High Pressure," *International Journal of Refractory Metals and Hard Materials*, Vol. 36, January 2013, pp. 232-237.
8. Crane, D., Zhang, Y., Douglas, C., Song, H., et al.: "Innovative PDC Cutter with Elongated Ridge Combines Shear and Crush Action to Improve PDC Bit Performance," SPE paper 183984, presented at the SPE Middle East Oil and

About the Authors

Dr. Guodong "David" Zhan

Ph.D. in Metallurgical Engineering, Huazhong University of Science and Technology

Dr. Guodong "David" Zhan is a Science Specialist and the Team Leader of the Advanced Drilling Tools team in the Drilling Technology Division at Saudi Aramco's Exploration and Petroleum Engineering Center – Advanced Research Center (EXPEC ARC). David is a world-renowned materials scientist and expert in advanced drilling tools/technology. He has over 25 years of experience in industrial R&D and managerial positions, including positions as Chief Engineer and R&D Manager at top oil/gas and semiconductor global companies, such as Schlumberger, NOV, and Applied Materials.

Additionally, David has held academic positions at the University of London and the University of Colorado at Boulder, and staff scientist positions at the Japan National Institute for Materials Science.

He is an active member of the Society of Petroleum Engineer (SPE) where he serves on several conferences such as the SPE International Petroleum Technology Conference and the Asia Pacific Drilling Technology Conference/International Association of Drilling Contractors as co-chair and technical committee member. David is also serving as an editorial board member and reviewer for a number of international scientific journals published by The Minerals, Metals and Materials Society and the Material Research Society.

He has published 90 peer-reviewed articles in journals such as *Nature Materials* and *Nature Scientific Reports*, 90 conference proceedings, and has more than 70 filed/published/granted U.S. patents, with an H-index of 35.

In 1994, David received his Ph.D. in Metallurgical Engineering from Huazhong University of Science and Technology, Wuhan, China, and completed a postdoctoral fellowship in Nanomaterials and Nanotechnology at the University of California at Davis.

Gas Show and Conference, Manama, Kingdom of Bahrain, March 6-9, 2017.

9. Giumelli, M., O'Shea, P., Maliardi, A., Sosnowski, P., et al.: "Offshore Exploration Program Benefits from Rolling PDC Cutter Technology, Timor Sea Australia," SPE paper 170532, presented at the IADC/SPE Asia Pacific Drilling Technology Conference, Bangkok, Thailand, August 25-27, 2014.

10. Peng, F. and He, D.: "Development of Domestic Hinge-type Cubic Presses Based on High-Pressure Scientific Research," *Chinese Journal of High Pressure Physics*, Vol. 32, Issue 1, 2018, pp. 51-56.

Timothy E. Moellendick

B.S. in Petroleum Engineering, Marietta College

Timothy E. Moellendick is the Chief Technologist for the Drilling Technology Division at Saudi Aramco's Exploration and Petroleum Engineering Center – Advanced Research Center (EXPEC ARC). Timothy is considered the industry expert in casing and liner drilling applications and engineering.

In his previous role as Director of Technology for Schlumberger, he was responsible for growing the technical and operational knowledge base used to develop, plan, and execute this technology worldwide. Timothy has also held drilling operations and engineering positions, including Senior Drilling Engineer, Drilling Manager for North America, Senior Field Engineer/Directional Driller and Operations Coordinator for the Gulf Coast of Mexico.

With more than 25 years of oil and gas industry experience, he leads a team of world-class researchers in developing the next generation of drilling technology required by Saudi Aramco's Drilling and Workover stakeholders.

In 1996, Timothy received his B.S. degree in Petroleum Engineering from Marietta College, Marietta, OH.

Dr. Bodong Li

Ph.D. in Electrical Engineering, King Abdullah University of Science and Technology

Dr. Bodong Li joined Saudi Aramco in 2015. He is the Technology Leader on Internet-of-Things (IoT) and Robotics at Saudi Aramco's Upstream Advanced Research Center. Bodong is also a member of the Drilling Technology Division focusing on research and development of advanced drilling tools.

He has 12 granted U.S. patents, and has authored and coauthored numerous articles published in scientific journals and conference papers covering the areas of sensing and downhole technologies.

Bodong is an active member of the Society of Petroleum Engineers (SPE) and the Institute of Electrical and Electronics Engineers.

He received the Discovery Scholarship and Fellowship from King Abdullah University of Science and Technology (KAUST).

Bodong received his M.S. degree in Mechanical Engineering and his Ph.D. degree in Electrical Engineering, both from KAUST, Thuwal, Saudi Arabia.

Dr. Chinthaka P. Gooneratne

Ph.D. in Electrical Engineering, Kanazawa University

Dr. Chinthaka P. Gooneratne is the Technical Leader for Sensors and Instrumentation (S&I) and Internet-of-Things (IoT) in the Drilling Technology Division at Saudi Aramco's Exploration and Petroleum Engineering Center – Advanced Research Center (EXPEC ARC). Chinthaka has over 10 years of experience in creating, leading, and managing programs designed to commercialize innovative S&I systems and developing emerging markets, such as micro-electromechanical system actuators and IoT edge platforms, that utilize advanced S&I.

He is the author of 35 filed/published/granted U.S. patents, 36 peer-reviewed journal papers, one book, five book chapters, and 40 conference papers.

In 2006, Chinthaka received the Monbukagakusho Scholarship from the Government of Japan.

He received his Ph.D. degree in Electrical Engineering from Kanazawa University, Kanazawa, Japan, in 2009, where he was the recipient of the President's Award for Outstanding Doctoral Research.

Dr. Duanwei He

Ph.D. in Condensed Matter Physics, Institute of Physics, Chinese Academy of Sciences

Dr. Duanwei He is a Professor at the Institute of Atomic and Molecular Physics, Sichuan University. Duanwei is a world-renowned scientist and expert in hard materials and high-pressure physics. His current research interests include advanced superhard materials and bulk nanostructured ceramics, development of technology for large volume high-pressure systems, and elastic and plastic behavior of strong materials under high pressure.

Duanwei has held several different positions, including Sr. Research Engineer at Schlumberger MegaDiamond, Research Staff at Los Alamos National Institute for Materials Research, and at Princeton University.

He holds 15 granted U.S. patents, and has published 150 journal papers, with an H-index of 32.

Duanwei received his Ph.D. degree in Condensed Matter Physics from the Institute of Physics, Chinese Academy of Sciences, Beijing, China.

A Rigorous Mixed Integer Nonlinear Programming Model to Optimize the Operation of an Integrated Gas-Oil Separation Network

Abdullah H. Al Ghazal, Dr. Yufeng He, Mohammed A. Al-Huraifi, and Ramsey J. White

Abstract /

Producing and processing significant volumes of crude oil requires connecting to wells in different fields that are usually spread across large geographical areas. Gas-oil separation plants (GOSPs) then process the collected crude oil. These facilities are often grouped into clusters that are within approximate distances from each other. GOSPs are often connected laterally via swing lines, which allows for shifting part or all of the production from one GOSP to another. Transfer lines also exist to allow processing intermediate products in neighboring GOSPs, thereby increasing complexity and possible interactions. In return, this provides an opportunity to leverage mathematical optimization to improve network planning and load allocation.

This work addresses optimizing the operation of a complex network of GOSPs. The goal is to operate this network such that oil production targets are met at minimum energy consumption, thereby minimizing operational expenditure and greenhouse gas emissions. This article proposes a novel methodology to formulate and solve this problem. It describes the level of fidelity used to represent physical process units. This varies from use of high-fidelity models to represent certain equipment to a more simplified representation elsewhere. A mixed integer nonlinear programming (MINLP) problem is then formulated and solved to optimize load allocation, swing line flow rates and equipment utilization, with the objective to minimize energy consumption.

The model demonstrates advanced capabilities to systematically prescribe optimal operating points. This was then applied to an existing integrated network of GOSPs and tested at varying crude oil demand levels. The results demonstrate the ability to minimize energy consumption by up to 51% while meeting oil production targets without added capital investment.

Introduction

In regions that are rich with oil deposits, such as the Arabian Peninsula, major oil fields extend over large geographical areas. Hundreds of oil wells can therefore be spread over large zones while producing from the same reservoirs. The crude oil produced from those wells is then sent via complex networks of pipelines to be separated at gas-oil separation plants (GOSPs). The purpose of the GOSPs is to separate the three-phase feed into gas, water, and dried crude oil. Gas is compressed and sent to gas plants for further processing. Oil, on the other hand, is desalted, further dehydrated, and then sent to either refineries or export terminals. Finally, water is re-injected underground to maintain reservoir pressure and improve oil recovery[1].

Due to the size of these oil fields, multiple GOSPs often exist to process feed from the same reservoir. GOSPs, which are located within a close distance from each other, are often interconnected laterally via swing pipelines, which allow shifting part or all of the production from one GOSP to another.

The purpose of those pipelines is to provide an added flexibility to the operation of the overall network. For example, when a bottleneck exists in one GOSP relating to water processing capacity, the production from wells with higher water cut may be diverted to a GOSP that is not similarly bottlenecked. This allows processing higher total crude volumes and leads to improving the utilization of these assets. This also allows the optimal distribution of crude oil to minimize energy consumption for the overall network while meeting production quotas. Similarly, the availability of swing lines can allow shifting production from GOSPs experiencing planned or unplanned outages to others[2].

Additionally, GOSPs are often connected via transfer lines, which allow transferring intermediate products to nearby GOSPs. For example, it may be financially prudent to equip only some GOSPs with gas compressors. Nearby GOSPs can then send their separated gases to be compressed elsewhere. The same may apply to water or oil processing equipment. On the other hand, while devising load allocation plans, it is essential to account for a wide set of constraints relating to equipment capacities and operational limitations.

By optimally leveraging these assets, major oil and gas companies are able to continuously maintain and

improve production agility. The goal is to cut cost while maintaining supply reliability, which is impactful on the world's economy.

On the other hand, given the thousands of variables and constraints involved in operating those networks, the problem lends itself very well to mathematical optimization. Indeed, operating such networks based on heuristics may often lead to suboptimal results. In contrast, and as will be demonstrated in this article, optimal load allocation can lead to significant benefits.

The case study used in this article is inspired by a real-world network, which provides an elaborate example of integrated GOSPs, where the goal is to drive the entire network toward an optimal solution.

Traditionally, tackling the optimization of large systems was mostly done using linear programming (LP) models. Those models are typically large and are used to answer high-level questions relating to the operation of those plants and networks. The use of rigorous or nonlinear models was mostly reserved for subsystems of the supply chain. This is predominately due to the significant added complexity of optimizing larger systems using rigorous approaches[3].

More recently, nonlinear programming (NLP) models have started to gradually replace the LP models. This is mainly attributed to the advancement of efficient optimization algorithms and computing power[3]. NLP models can overcome several problems associated with the LP models. NLPs allow delivering solutions that are more accurate and therefore implementable in the field. This is in contrast with the often-inaccurate solutions provided by the LP models[4].

Where there are significant nonlinearities and a presence of discrete decisions, it is often necessary to formulate and solve mixed integer nonlinear programming (MINLP) problems. Those typically present significant challenges and require specialized solution techniques.

This work shall address constructing an original rigorous model and using an MINLP formulation to optimize the operation of an integrated GOSP network. The objective is to minimize the total energy consumption while meeting preset oil demand targets.

Literature Review

The oil and gas industry receives significant attention from academic researchers and industry practitioners alike. This is partly attributed to the drive within oil and gas majors to continuously improve profit margins and ensure environmental sustainability.

Indeed, given its typically high volumes and slim margins, the oil and gas industry must continuously evaluate, report, and improve on its profitability and sustainability metrics. To achieve this, the industry in part, must improve on its supply chain planning activities[5].

This gave rise to the concept of Enterprise-Wide Optimization (EWO). This is defined as coordinating the optimization of the various operations within a defined supply chain. The goal is often to minimize costs, inventories, and environmental impact, while improving profitability, asset utilization, and agility[6]. Researchers have addressed the optimization of a variety of complex supply chains within the wider process industry. This ranged from pharmaceuticals[7, 8] to refineries[9] and integrated chemical sites[10].

Many EWO problems can be formulated as mixed integer linear programming (MILP) models. Those models are often very large. Their size can also be several times larger when considering multiple periods. As most real-world problems involve nonlinearities, these were often addressed by introducing new variables and equations to perform piecewise linear approximations or exact linearization. Although, this can only be done in limited cases[11].

On the other hand, there remains a class of problems, which necessitates handling nonlinearities in addition to discrete decisions, leading to MINLP formulations. It was also reported that MINLPs combine the difficulties associated with MILPs and NLPs[3]. This includes the combinatorial features of the mixed integer portion and the nonconvexities often associated with nonlinearities. These problem classes are most often solved by the general branch and bound methods. An alternating sequence of solving the master mixed integer and the sub-nonlinear problems is employed. A globally optimal solution can only be guaranteed in convex problems[3, 12].

As EWO problems are usually nonconvex, a local optimal solution is often accepted as a sufficient outcome. Applying rigorous global optimization techniques, — such as the one used in the Baron solver[13] — is often computationally expensive and is not practiced for sizable EWO problems[11].

Papageorgiou (2009)[14] presented an overview of the mathematical models used for the optimization of the process industries' supply chain, focusing on the strategic and tactical level. He addressed the issue of modeling uncertainty using multistage stochastic models, and highlighted the use of multiple objective formulations to address environmental impact as a secondary objective function[14]. Sahebi et al. (2014)[15] who presented a review of the existing work addressing crude oil supply chains also highlighted these aspects. They note the importance of developing efficient algorithms and techniques to address the complexity of these problems.

Researchers have also employed various frameworks to optimize oil and gas planning and scheduling models.

Wassick (2009)[10] employed a resource task network (RTN), initially described by Pantelides (1994)[16] to optimize the scheduling of an integrated chemical site. He showed how an integrated site can be composed of various subsystems, which perform different tasks. The RTN formulation was then used to optimize the scheduling of the site's wastewater treatment[10].

A framework for the optimization of petroleum supply chains was proposed by Neiro and Pinto (2004)[17]. It focused on oil and gas downstream assets, including

refineries, storage tanks, and pipelines. They described a large-scale multiple period MINLP model to optimize the complex topology, which consisted of connecting multiple nodes representing each element of the network. Their manipulated variables included flow rates, operational parameters, and facilities assignment[17].

Several researchers have addressed the optimization of oil and gas midstream operations to various extent.

Wang (2003)[18] reviewed oil and gas upstream optimization problems and categorized them into gas lift and production allocation, processing plants design and operation optimization, and reservoir development and planning optimization. He further divided optimization problems based on timescale into operational, tactical, and strategic problems.

Al-Sobhi and Elkamel (2015)[19] simulated and optimized a natural gas processing network consisting of liquefied natural gas, gas to liquids, and methanol plants. To address a problem of a similar nature, Li and Li (2015)[20] proposed a stochastic model for the design and operation of natural gas networks under uncertainty. A modified nonconvex generalized Benders decomposition method was then applied to solve it[20].

Thijssen et al. (2007)[21] examined building a network planning tool. The presented network consisted of wellhead platforms to oil and gas export facilities.

Liu et al. (2016)[2] proposed a MILP model to optimize a network of GOSPs. The objective was to ultimately minimize the network's operating expenditure. Their model made use of transfer lines to swing production fully or partially from some plants to others. They represented the network using a state task network, which was described[22], and employed piecewise linearization to handle nonlinear power consumption curves.

To the best of the authors' knowledge, there is no proposed framework in the literature, which addresses coupling the use of physics-based simulators and MINLP models to optimize the operation of integrated GOSP networks. The objective of this work is to address these gaps and present results to quantify and demonstrate the benefits of the proposed methodology.

Problem Statement

The configuration of GOSPs can vary significantly, however, they often contain pieces of equipment that are highly energy-intensive. This mainly includes low- and high-pressure gas compressors and water injection pumps. Accordingly, optimizing the operation of such equipment can have a significant impact on improving energy efficiency, and consequently further minimizing processing cost and greenhouse gas emissions.

Figure 1 shows a simplified block flow diagram representing a typical GOSP. Crude oil is received at one or multiple high-pressure production trap(s) (HPPT). This is a three-phase separator, which separates high-pressure gas, crude oil, and oily water. The high-pressure gas either free-flows to a nearby gas plant or is sufficiently compressed through a high-pressure compressor to allow overcoming pipeline pressure drop and reaching gas plants that are remotely located from the GOSP at the desired pressure.

Water from the HPPTs and the desalting train flows to a water-oil separator (WOSEP). The water is separated and then re-injected into the reservoir. This serves two purposes, namely finding a suitable disposition for contaminated water, and maintaining reservoir pressure to improve oil recovery. Separated oil flows to the low-pressure production trap (LPPT).

The LPPT receives feed from the HPPT and the WOSEP. A further pressure drop allows releasing more gases. Those gases are compressed at the low-pressure compressor and then further compressed at the high-pressure compressor, which also receives feed from the HPPT.

Fig. 1 *A simplified block flow diagram of a typical GOSP.*

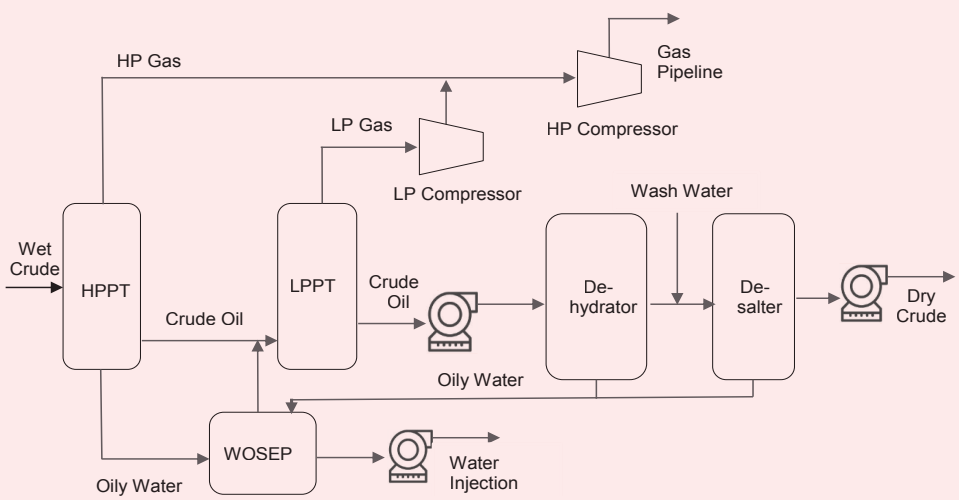

Crude oil from the LPPT is pumped to the dehydrator and then the desalter to remove emulsified water and dilute the salt contained within. Dry desalted crude oil is then pumped out of the GOSP.

The presence of these numerous variables and differing constraints makes operating the network most profitably very difficult due to the thousands of options, which are possible. This very much lends the problem to mathematical optimization. A mathematical solver is often able to highlight solutions, which are not readily visible to the network's planner.

The network optimization of GOSPs can also lead to opportunities, whereby some production from shutdown GOSPs can be recouped by diverting their feed to nearby GOSPs while considering the various limitations such as gas compression and water processing capacities.

Within this work, two GOSP networks will be considered, Areas "B" and "C." Both networks are located within the same reservoir and produce Arabian Light crude oil. As such, they can be lumped in the same problem formulation toward a single objective function.

Figure 2 shows the Area B GOSP network, which is connected by a variety of swing lines. Some groups of wells are considered swingable while others are not. Feed from a group of swingable wells is typically sent to the primary GOSP, but can be diverted to the secondary one. Feed from non-swingable wells can only be diverted to a single GOSP. GOSP B-2 is a compression station. Its purpose is to compress gases from GOSPs B-3 and B-6, both of which do not contain compressors.

Figure 3 shows the Area C GOSP network, where only a single swing line exists from GOSP C-4 to C-3. This provides a more limited swinging capability.

Methodology

The model development process started with building a physics-based model to simulate the individual GOSPs process flow and the network's overall topology. gPROMS ProcessBuilder, an equation oriented (EO) modeling platform, was used since it lends itself for use in process optimization. Unlike sequential modular simulators, EO modeling does not require directionality of computation. Moreover, it allows for efficient handling of multiple recycles, which is essential for optimizing GOSPs, as they contain a variety of recycle streams, such as the aforementioned water being recycled from dehydrators to WOSEPs.

A disadvantage of EO simulators is that their numerical solvers require good initial guesses. Failing to provide those may lead to numerical failures. This is partly overcome through recent advances in initializing techniques, which allow presetting variables using homotopy continuation techniques.

Infochem Multiflash was used as the physical property package. This package is well suited for the given application because of its ability to generate tight convergence of iterations and of partial derivatives with respect to composition, pressure, and temperature. In addition, phase equilibria is determined for a variety of pressure, volume, temperature, enthalpy, entropy, and internal energy combinations.

The package also provides the composition of a given phase at a given pressure or temperature. For this work, the Soave-Redlich-Kwong equation of state was chosen since it is able to sufficiently account for fugacity calculations. It was also compared against other equations of state and demonstrated better capabilities in representing multiphase crude oil separation processes.

Process Simulation Models

Individual GOSPs were modeled to match the topology provided in the latter section. Each GOSP is

Fig. 2 *The Area B GOSP network, which is connected by a variety of swing lines.*

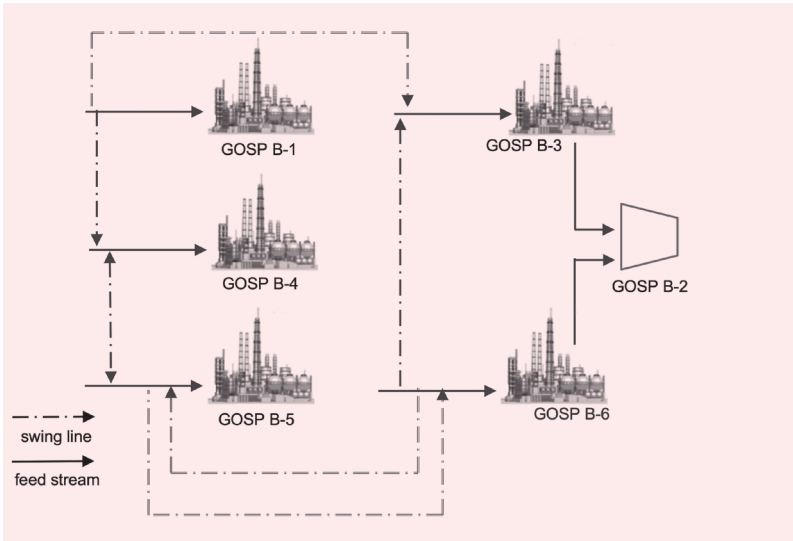

Fig. 3 *The Area C GOSP network, where only a single swing line exists from GOSP C-4 to C-3.*

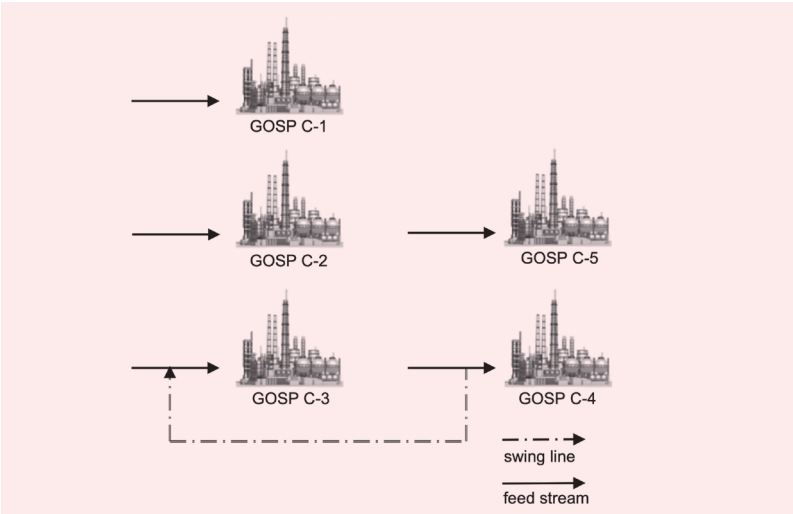

physically connected to a large number of wells through a complicated network of pipelines, trunk lines, and headers. The models did not include a representation of individual wells as this was deemed outside the scope of this work. Instead, wells were grouped and represented as swingable and non-swingable feed sources. A non-swingable group of wells can only feed a single GOSP. In the model, each group is represented by a single feed stream with an averaged producing gas-oil ratio (GOR) and water cut.

High-fidelity separators were used to flash the streams feeding the HPPTs and the LPPTs. Equation 1 provides the mass balance for each component, i, around those separators:

$$\hat{\forall}\frac{d\tilde{m}_i}{dt} = F^{in}w_i^{in} - F_L x_i - F_V y_i \quad , \text{i} = 1, \ldots, \text{NC} \qquad (1)$$

where $\hat{\forall}$ is the characteristic volume, $\tilde{m}_i$ is the volumetric mass holdup, F^{in}, F_L, and F_V are the inlet, outlet liquid, and outlet vapor mass flow rates, respectively. Finally, x_i and y_i are the mass fractions of component i in the liquid and vapor phases, respectively.

The energy balance is then expressed by Eqns. 2 and 3:

$$\hat{\forall}\frac{d\tilde{u}}{dt} = F^{in}h^{in} + Q^{in} - F_L h_l - F_V h_v \qquad (2)$$

$$\tilde{u} = \tilde{m}_T h - 100\,P \qquad (3)$$

where $\tilde{u}$ is the volumetric energy holdup, h^{in} is the inlet mass specific enthalpy, and Q^{in} is the energy rate for the heat supplied to the vessel. In addition, h_L and h_V are the outlet liquid and vapor mass specific enthalpy, respectively.

Since the models have an underlying assumption of a steady-state, all terms involving holdup in Eqns. 1, 2, and 3 are set to zero.

The physical property package is then used to calculate the fugacity coefficients. The phase equilibrium is then obtained using Eqns. 4 through 6:

$$\frac{y_i\emptyset_{i,v}}{\sum_{j\in NC}\frac{y_i}{MW_j}} = \frac{x_i\emptyset_{i,L}}{\sum_{j\in NC}\frac{x_i}{MW_j}} \quad , \text{i} = 1, \ldots, \text{NC} \qquad (4)$$

$$\sum_{i\in C} x_i = 1 \qquad (5)$$

$$\sum_{i\in C} y_i = 1 \qquad (6)$$

where MW_i is the molecular weight of component i. $\emptyset_{i,v}$ and $\emptyset_{i,L}$ are the fugacity coefficients of component i in the vapor and liquid phases.

Performance maps were used to predict the compressor's outlet pressure based on the flow rate. These maps provide relationships between the volumetric flow rate, the compressor's efficiency and the polytropic head. Performance maps can be either 1D or 2D. 1D maps do not include a dimension for varying compressor speeds, while 2D maps allow varying performance at feasible compressor speeds. The minimum flow through compressors for anti-surge control are also taken into consideration through use of recycle streams.

It is then possible to use Eqns. 7 and 8 to determine the head and efficiency from the volumetric flow rate:

$$H_P = M_{head}(F_v) \qquad (7)$$

$$\eta_p = M_{efficiency}(F_v) \qquad (8)$$

where F_v is the inlet design volumetric flow rate. H_P is the design polytropic head. M_{head} is the map head function, $M_{efficiency}$ is the map efficiency function, and η_P is the polytropic efficiency.

Equation 9 can then calculate the power demand for polytropic compression:

$$H_P = 1000\,\frac{W}{F} \qquad (9)$$

where W is the power demand for polytropic compression.

Similarly, the fluid's enthalpy can be determined after calculating the power supply to the fluid and the fluid's flow rate using Eqn. 10.

$$W = F(h_{out} - h_{in}) \qquad (10)$$

where h_{out} is the outlet mass specific enthalpy.

It is then possible to account for the mechanical losses, which lead to the mechanical power demand being larger than the power required to compress the fluid. Assuming steady-state conditions, the mechanical losses can be determined by Eqn. 11:

$$W_{mech}\frac{\eta_{mech}}{100} = W \qquad (11)$$

where W_{mech} is the compressor mechanical power demand and η_{mech} is the mechanical efficiency.

The centrifugal pump model can be used to represent charge, shipping, and saltwater injection pumps. Equation 12 gives the power demand, W_{is}, for an ideal isentropic process.

$$W_{is} = F(h_{is} - h_{in}) \approx F\frac{10^2(P^{out} - P^{in})}{\rho} \qquad (12)$$

where P^{out} and P^{in} are the fluid outlet and inlet pressure; ρ is the fluid density.

Then, the actual power, W_{act}, supplied to the fluid can be determined by Eqn. 13:

$$W_{act}\frac{\eta_{is}}{100} = W_{is} \qquad (13)$$

where η_{is} is the isentropic efficiency.

The fluid's outlet enthalpy, head, efficiency, and the pump's torque requirement can then be determined in a similar fashion to the centrifugal compressors as described by Eqns. 7 through 11.

For simplicity, a number of pieces of process equipment, i.e., WOSEPs, dehydrators, and desalters, were represented as component splitters. Those pieces of equipment do not largely affect routing and loading decisions. Their capacities were, nevertheless, captured and embedded in the optimization problem formulation.

After building individual plant models, those were joined into a network model. The network model was built to match the previously provided description. Feed streams were relocated from individual models to the overall topology. They were connected to the plants'

models through a series of aggregators and routers. Aggregators allow combining multiple streams into a single stream. Routers allow specifying one or more possible outlets. Those are specified discretely, such that only one outlet stream can be selected at any time by the optimizer.

Optimization Problem Formulation

In this section, we describe how the optimization problem was posed, and present details on how constraints and the objective function were formulated.

The total power consumption (*TPC*) of a GOSP is defined as:

$$TPC_g = \sum_{hpc \in HPC} PC_{hpc} + \sum_{lpc \in LPC} PC_{lpc} + \sum_{wip \in WIP} PC_{wip} + \sum_{sp \in SP} PC_{sp} \quad 14$$

where *PC* is the power consumption, *hpc* and *lpc* are the high-pressure and low-pressure compressors, respectively; *wip* and *sp* are the water injection and crude shipping pumps, respectively.

The total feed (*TF*) to a GOSP is described as:

$$CAP_g^{min}.Y_g \leq TF \leq CAP_g^{max}.Y_g \quad 15$$

where CAP_g^{min} and CAP_g^{max} are the minimum and maximum capacities of a GOSP, respectively. Y_g is a binary variable. It equals 0 if the GOSP is off and 1 if the GOSP is on.

The water handling capacity (*WHC*) of a GOSP is then defined as:

$$WHC_g \leq WHC_g^{max}.Y_g \quad 16$$

The capacity of the high-pressure and low-pressure compressors is defined as:

$$0.8\,.CompCAP_{hpc,g}^{max}.Y_g \leq CompCap_{hpc,g} \leq CompCAP_{hpc,g}^{max}.Y_g \;\forall\; hpc \in HPC \quad 17$$

$$0.8\,.CompCAP_{lpc,g}^{max}.Y_g \leq CompCap_{lpc,g} \leq CompCAP_{lpc,g}^{max}.Y_g \;\forall\; lpc \in LPC \quad 18$$

Both the high-pressure and low-pressure compressors are operated to deliver gas at a minimum head pressure. This is defined as:

$$CompHead_{hpc,g} \leq CompHead_{hpc,g}^{max}.Y_g \;\forall\; hpc \in HPC \quad 19$$

$$CompHead_{lpc,g} \leq CompHead_{lpc,g}^{max}.Y_g \;\forall\; lpc \in LPC \quad 20$$

The total oil production, which is one of the main constraints, is described as:

$$TotalOil \geq SPR_g \;\forall\; g \in G \quad 21$$

where SPR_g is the total rate leaving the shipping pump at each GOSP.

The minimum pressure of the water injection pumps was described by polynomials that define the flow/pressure relationships. The polynomial was regressed as a best fit of historical data. The model is constrained to deliver a pressure, which is at least equivalent to the minimum pressure at the water flow rate. This often mandates adding additional parallel pump(s) to meet the required pressure.

Moreover, it was often necessary to add some mathematical expressions that describe the relationship between various GOSPs. For example, if the gas leaving the first GOSP is processed at a second GOSP, it is essential to maintain that the first GOSP cannot be operated while the second is shut down. On the other hand, the second GOSP can still operate if the first is shutdown as long as it is able to meet the compressor's flow rates.

This is described through the following key equation:

$$Y_{g'} \leq Y_g \quad 22$$

The objective function is then simply defined as the minimization of the TPC of all the GOSPs. This is described as:

$$Min \quad TPC_G = \sum TPC_g \;\forall\; g \in G \quad 23$$

After formulating the problem, a steady-state optimization routine was performed, where both continuous and discrete variables were optimized to minimize energy consumption while satisfying the given constraints.

Due to the nature of the described equation system, a nonlinear behavior can be observed in addition to several binary variables. This makes this an MINLP problem, which follows the particularities previously described.

The gPROMS — the modeling platform used — uses the Outer Approximation Equality Relaxation Augmented Penalty OAERAP algorithm to solve MINLP problems. This is a modified version of the Outer Approximation/Equality Relaxation method. When the optimization problem is convex, this algorithm can guarantee global optimality.

The OAERAP algorithm applies decomposition techniques to break the problem into a master MILP problem and a series of NLP sub-problems.

A global optimum cannot be guaranteed because of the linearization being applied to non-convex functions. Due to the high nonlinearity of the GOSP optimization problem — arising from various physical separation and compression equations — the solution may find difficulty arriving at a global optimum. This was often addressed by changing initial guesses. Indeed, a good initial guess substantially improves the solver's chances of arriving at a global optimum.

Results

In this section, we apply the proposed model to a case concerning the same GOSP networks described earlier. The goal is to evaluate the model's performance, the results validity, and the benefits of using the proposed model vs. heuristics.

Table 1 provides a summary of the main capacities for the GOSPs in both areas under consideration.

Table 1 *A summary of the main capacities for the GOSPs in both areas under consideration.*

GOSP	Maximum Crude Oil Capacity (% of Total)	Design WOSEP Capacity (% of Crude Oil Capacity)	Number of Salt Water Injection Pumps	Number of Low-Pressure Compressors	Number of High-Pressure Compressors
B-1	5.52%	86.8%	2	1	0
B-2	N/A	N/A	N/A	1	2
B-3	12.57%	49.5%	4	0	0
B-4	12.57%	49.5%	4	1	2
B-5	12.57%	49.5%	3	0	0
B-6	6.48%	96.1%	2	0	0
C-1	12.57%	75.8%	4	1	2
C-2	12.57%	49.5%	4	1	2
C-3	12.57%	49.5%	3	1	1
C-4	6.29%	99.0%	4	1	1
C-6	6.29%	N/A	N/A	0	0

For the purpose of this case study, the optimizer, while being maintained within the provided available potential (avails), adjusted the feed rates to each GOSP. Avails represent production capabilities as determined by production engineering and reservoir management strategies. Typically, rates are controlled by adjusting the choke valves of the producing wells at the well pads. Operators will strive to ensure that each GOSP receives the required production rates.

It was assumed that the flow rates can be perfectly controlled to produce the required flow rates, the averaged GORs, and water cuts. Flow rates were aggregated previously and the model was provided with an initial guess, a minimum and a maximum rate for each feed stream. As previously described, feed streams comprise aggregates of both swingable and non-swingable wells. The minimum for each feed stream was set to zero. The initial guess was provided as the starting production target, which is between the minimum and the maximum. The maximum is the available potential flow rate.

The total oil production target was set as a percentage of the total avails. The goal is to allow studying the model's response as oil production targets are altered.

The base case in all scenarios assumed that all GOSPs are maintained operational as is the common practice. On the other hand, the optimizer provided the flexibility to recommend shutting down GOSPs if it is deemed optimal. It was also assumed that no swing lines are used during normal operation per common practices, since their use is typically limited to shutdowns.

The 50% case is taken as an example. Table 2 lists the model statistics and computational results for this case.

Figure 4 presents the power consumption comparison

Table 2 *The model statistics for the 50% throughput level scenario.*

Case	50% Throughput
Number of Variables	122
Objective Function (MW)	32.5
CPU(s)	248

for each GOSP between the optimal and base solutions at the 50% production level. It shows that the optimal solution does not guarantee that all GOSPs consume less power than in the base solution. Indeed, it can be observed that four GOSPs consume more power in the optimal case. On the other hand, seven GOSPs consume less power in the optimal case. This is because the optimization model considers the whole network at once and manipulates all controlled variables to achieve a better overall solution rather than optimizing each GOSP individually. This indeed demonstrates the value of optimizing the network as a single entity.

Figure 5 is a schematic showing the utilization of optimal swing lines for the GOSPs of Area B and Area C. It shows that only two swing lines were used. It also shows that the optimizer recommends shutting down a total of six GOSPs. This is an exceptional case due to the very low throughput level being tested. The case was purposely devised to test the algorithm's performance and robustness in handling production levels, which are not normally experienced. This is in addition to normal production levels.

The model's results are largely sensible since it elects to

shutdown GOSPs with the higher power consumption. The optimizer, nevertheless, shuts down GOSPs B-3 and B-6, although their power consumption is relatively low, having no compressors. This is because they are linked with GOSP B-2, a high-energy consumer, which receives their gases for compression.

To evaluate the optimal solutions achieved for all cases under consideration, the results of the optimal cases are compared with those of the base case where GOSPs are not shut down, and swing lines are not utilized.

Figure 6 is a comparison of the base power consumption vs. the optimal power consumption between the two solutions for all cases. It can be seen that the savings progressively declines as the throughput level is increased. As the throughput levels approach the maximum avails, the optimization potential decreases and there is less room for substantial savings. The figure shows that power reductions start at 51% corresponding to a throughput of 50%, and reach 1% at a throughput equaling 100% of avails.

Fig. 4 *The comparison for each GOSP's power consumption between the optimal and base solutions at the 50% production level.*

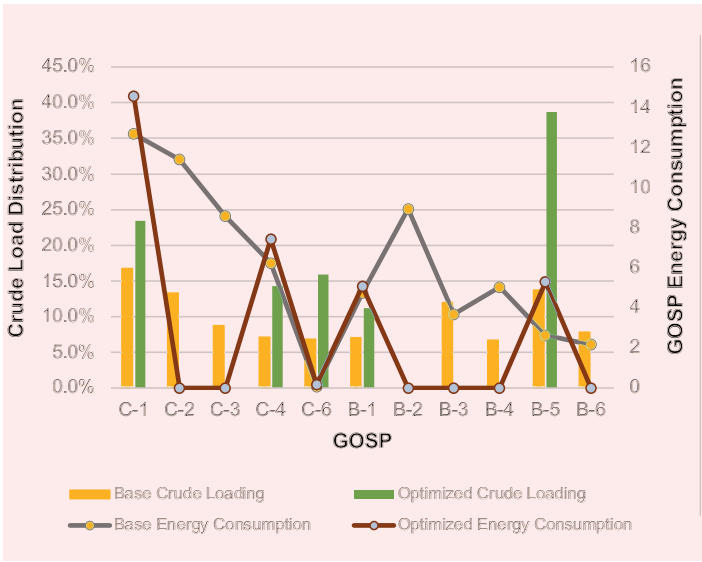

Fig. 5 *A schematic showing the utilization of optimal swing lines for the GOSPs of Area B and Area C.*

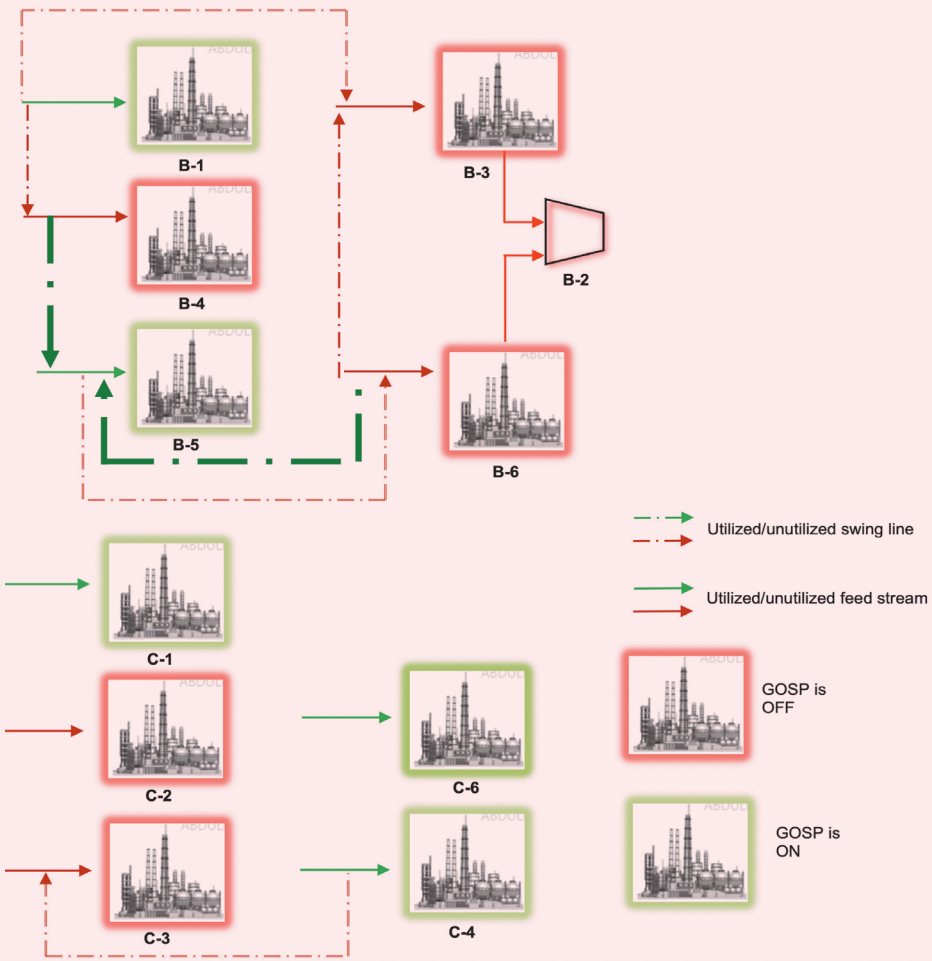

Fig. 6 *A comparison of the base power consumption vs. the optimal power consumption between the two solutions for all cases.*

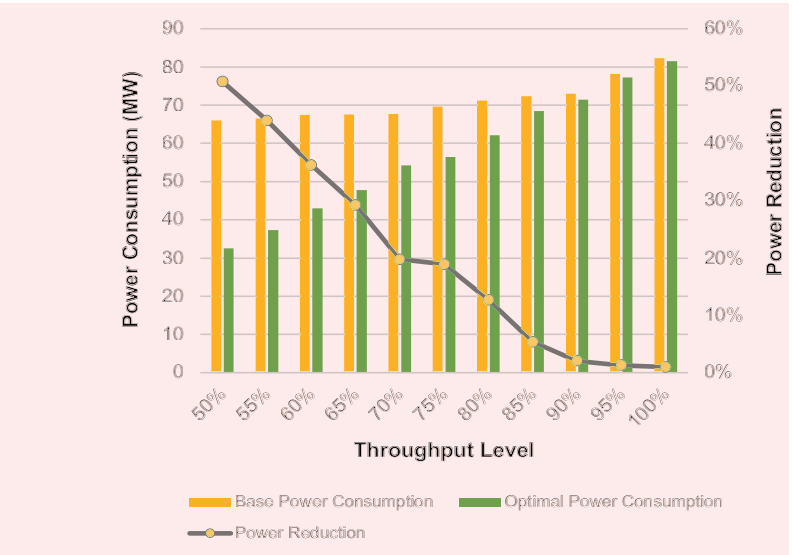

Fig. 7 *The number of pieces of rotating equipment being utilized in the base scenario vs. the optimal scenario.*

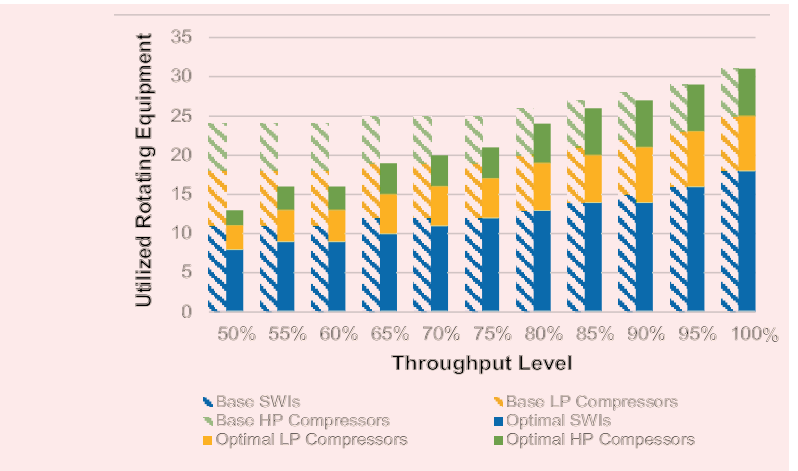

Figure 7 shows the number of pieces of rotating equipment being utilized in the base vs. the optimal scenario. It can be observed that as throughput levels increase, the optimal number of pieces of rotating equipment starts approaching the base solution's scenario. Indeed, at the 100% case, both numbers are equal. This is sensible as increasing the throughput mandates using more rotating equipment, leaving little room for optimization.

Conclusions

In this work, we built a rigorous model that strived to optimize the operation of an integrated network of GOSPs. The rigorous physics-based simulation model was augmented with a MINLP model with an objective function that tried to minimize power consumption. This is key to maintaining sustainability through further reducing greenhouse gas emissions.

We applied the model to production data and demonstrated its capability to propose optimized solutions, which can lead to significant power savings.

Future work can include expanding the model's scope both horizontally and vertically. Horizontal expansion refers to including additional GOSPs, such that the model has a wider optimization scope. Vertical expansion refers to integrating upstream wells' data and downstream gas plants. This is expected to yield significant value.

References

1. Abdel-Aal, H.K., Aggour, M. and Fahim, M.A.: *Petroleum and Gas Field Processing*, Marcel Dekker Inc., New York, 2003, 364 p.

2. Liu, S., Alhasan, I. and Papageorgiou, L.G.: "A Mixed Integer Linear Programming Model for the Optimal Operation of a Network of Gas-Oil Separation Plants," *Chemical Engineering Research and Design*, Vol. 111, July 2016, pp. 147-160.

3. Grossmann, I.E. and Biegler, L.T.: "Optimizing Chemical Processes," *CHEMTECH*, December 1995, pp. 27-35.

4. Alhajri, I., Elkamel, A., Albahri, T. and Douglas, P.L.: "A Nonlinear Programming Model for Refinery Planning and Optimization with Rigorous Process Models and Product Quality Specifications," *International Journal of Oil Gas and Coal Technology*, Vol. 1, Issue 3, January 2008, pp. 283-307.

5. Shah, N.: "Process Industry Supply Chains: Advances and Challenges," *Computers & Chemical Engineering*, Vol. 29, Issue 6, May 2005, pp. 1225-1235.

6. Shapiro, J.F.: *Modeling the Supply Chain*, 2nd edition, Cengage Learning, 2006, 608 p.

7. Shah, N.: "Pharmaceutical Supply Chains: Key Issues and Strategies for Optimization," *Computers & Chemical Engineering*, Vol. 28, Issues 6-7, June 2004, pp. 929-941.

8. Papageorgiou, L.G., Rotstein, G.E. and Shah, N.: "Strategic Supply Chain Optimization for the Pharmaceutical Industries," *Industrial & Engineering Chemistry Research*, Vol. 40, Issue 1, 2001, pp. 275-286.

9. Menezes, B.C., Grossmann, I.E. and Kelly, J.D.: "Enterprise-wide Optimization for Operations of Crude Oil Refineries: Closing the Procurement and Scheduling Gap," *Computer Aided Chemical Engineering*, Vol. 40, 2017, pp. 1249-1254.

10. Wassick, J.M.: "Enterprise-wide Optimization in an Integrated Chemical Complex," *Computers & Chemical Engineering*, Vol. 33, Issue 12, December 2009, pp. 1950-1963.

11. Grossmann, I.E.: "Advances in Mathematical Programming Models for Enterprise-wide Optimization," *Computers & Chemical Engineering*, Vol. 47, December 2012, pp. 2-18.

12. Grossmann, I.E.: "Research Challenges in Planning and Scheduling for Enterprise-wide Optimization of Process Industries," *Computer Aided Chemical Engineering*, Vol. 27, 2009, pp. 15-21.

13. Sahinidis, N.V.: "BARON: A General Purpose Global Optimization Software Package," *Journal of Global Optimization*, Vol. 8, Issue 2, March 1996, pp. 201-205.

14. Papageorgiou, L.G.: "Supply Chain Optimization for the Process Industries: Advances and Opportunities," *Computers & Chemical Engineering*, Vol. 33, Issue 12, December 2009, pp. 1931-1938.

15. Sahebi, H., Nickel, S. and Ashayeri, J.: "Strategic and Tactical Mathematical Programming Models within the Crude Oil Supply Chain Context — A Review," *Computers & Chemical Engineering*, Vol. 68, September 2014, pp. 56-77.

16. Pantelides, C.C.: "Unified Frameworks for the Optimal Process Planning and Scheduling," in *Proceedings of the Second International Conference on Foundations of Computer Aided Operations*, (eds.) Rippin, D.W.T., Hale, J.C., and Davis, J.F., AICHE, 1994, 488 p.

17. Neiro, S.M.S. and Pinto, J.M.: "A General Modeling Framework for the Operational Planning of Petroleum Supply Chains," *Computers & Chemical Engineering*, Vol. 28, Issues 6-7, June 2004, pp. 871-896.

18. Wang, P.: "Development and Applications of Production Optimization Techniques for Petroleum Fields," Ph.D. Thesis, Stanford University, March 2003, 196 p.

19. Al-Sobhi, S.A. and Elkamel, A.: "Simulation and Optimization of Natural Gas Processing and Production Network Consisting of LNG, GTL, and Methanol Facilities," *Journal of Natural Gas Science and Engineering*, Vol. 23, March 2015, pp. 500-508.

20. Li, D. and Li, X.: "Global Optimization of an Industrial Natural Gas Production Network," *IFAC-PapersOnLine*, Vol. 48, Issue 8, 2015, pp. 337-342.

21. Thijssen, N., Li, K-J. and Mittendorff, I.: "Enhancement of Oil and Gas Production via Network Optimization," Chapter 11 in *Process Systems Engineering, Vol. 3, Supply Chain Optimization*, (eds.) Pistikopoulos, E.N., Georgiadis, M.C., Dua, V. and Papageorgiou, L.G., 2007, pp. 325-338.

22. Kondili, E., Pantelides, C.C. and Sargent, R.W.H.: "A General Algorithm for Short-term Scheduling of Batch Operations—I. MILP Formulation," *Computers & Chemical Engineering*, Vol. 17, Issue 2, February 1993, pp. 211-227.

About the Authors

Abdullah H. Al Ghazal

B.Eng. in Chemical Engineering, University of Manchester

Abdullah H. Al Ghazal is a Process Optimization Engineer working in the Process Modeling and Optimization Unit of Saudi Aramco's Process & Control Systems Department. During Abdullah's career, he has led several key projects, which strive to integrate and optimize Saudi Aramco's hydrocarbon value chain.

Abdullah's work has spanned the company's Upstream and Downstream operations, and leverages cutting-edge technologies such as artificial intelligence, rigorous modeling, and mathematical optimization.

Currently, he is leading the development and deployment of a number of technologies in the areas of virtual sensing, hybrid modeling, and network optimization.

Abdullah received his B.S. degree in Chemical Engineering from the University of Manchester, Manchester, U.K., and is currently pursuing an M.S. degree with Imperial College London, London, U.K.

Dr. Yufeng He

Ph.D. in Chemical Engineering, Edinburgh University

Dr. Yufeng He is an Engineering Specialist working in the Process Modeling and Optimization Unit of Saudi Aramco's Process & Control Systems Department, developing process simulation and process optimization solutions.

Previously, Yufeng worked with Honeywell Process Solutions U.K. as an OTS Project Engineer and Consultant developing operator training simulators for refining and petrochemical processes.

He received his B.S. degree in Chemistry from the Peking University, Beijing, China, and his Ph.D. degree in Chemical Engineering from the University of Edinburgh, Edinburgh, U.K.

Mohammed A. Alhuraifi

M.S. in Petroleum Engineering, Imperial College London

Mohammed A. Alhuraifi is a Production Optimization Specialist working in Saudi Aramco's Southern Area Production Engineering Department. Mohammed's work experience is mainly related to production engineering in Abqaiq, Ain Dar, and the Shedgum oil fields. He has also worked with the Production & Facilities Development Department as well as the Process & Control Systems Department.

In 2008, Mohammed received his B.S. degree in Petroleum Engineering from the King Fahd University of Petroleum and Minerals (KFUPM), Dhahran. In 2011, he received an M.S. degree in Petroleum Engineering from Imperial College London, London, U.K.

Ramsey J. White

M.S. in Chemical Engineering, University of Houston

Ramsey J. White is a Chemical Engineer and is the Lead Process Engineer in Saudi Aramco's Southern Area Oil Operations Technical Support Department.

Ramsey has over 20 years of professional experience, including 13 years at Saudi Aramco where he has been involved in process troubleshooting, risk analysis, process and energy optimization for gas-oil separation plant upgrade and technology projects.

Prior to joining Saudi Aramco, Ramsey worked at SNC-Lavalin in Houston, TX, as a Process Engineer on several petrochemical and refinery upgrade projects.

He received his B.S. degree in Chemistry from the American University in Cairo, Egypt, and his M.S. degree in Chemical Engineering from the University of Houston, Houston, TX.

Predicting the Flowing Bottom-Hole Pressure in Gas Condensate Wells Using Artificial Neural Networks

Fahad H. Al Shehri, Muqbil S. Alkhalaf, and Dr. Muhammad Arsalan

Abstract /

Installation of production tubulars is a critical job that has a direct impact on the overall productivity of the well. Therefore, it is equally significant to predict the accurate flowing bottom-hole pressure (FBHP) to garner the utmost benefits from the system by constructing the right vertical lift performance curves. In fact, constructing the accurate vertical lift performance curves helps us identify the liquid loading times of wells, and therefore predict when to install velocity strings or different artificial lift systems. For years, efforts were extended into developing mechanistic models and correlations to predict FBHP.

Consequently, all present correlations are developed under laboratory conditions and each have their own limitations for specific types of flow regimes. Mechanistic models integrate the physics of downhole conditions, yet they do not provide accurate results for the FBHP. Therefore, an artificial neural network (ANN) model was utilized in this article. The designed model has been validated over a diverse range of data sets; therefore, it has been developed for the purpose of providing efficient results.

More than 30,000 data points were collected from various wells with a wide range of inputs. The inputs utilized in the artificial intelligence (AI) model are from daily flow back data, including wellhead pressure, wellhead temperature, true vertical depth, fluid specific gravity, chloride content, water cut, fluid rates, and the water-gas ratio. The data were then split as per the ratio of 4:1 for training and testing to generate accurate results. Then, the model was tested on other new wells to test its accuracy. Eventually, the results from the designed model were compared with the results of existing correlations and it was evident that the AI model outperformed them in terms of average absolute percent error (AAPE), and correlation coefficient.

Introduction

As yet no accurate predictive system exists for predicting the flowing bottom-hole pressure (FBHP), and direct measurements using downhole memory gauges are costly and require maintenance as well as interruption of production. Most of the developed correlations are either empirical or semi-empirical, which are developed in laboratory conditions and have their limitations. The reason behind these correlation models has been the complexity of the system and multiphase flow.

Since the early 1940s, engineers have put their efforts in developing countless correlations to address this problem. The major reason behind the failure of these correlations was the fact that they have been designed in laboratory conditions, which is apparently far different from the downhole conditions, thereby, they turn out to be inaccurate. Until recent days, some of the prominent and acceptable correlations are the ones proposed by Hagedorn and Brown (1965)[1] and Duns and Ros (1963)[2].

In comparison with conventional correlations, artificial intelligence (AI) tends to produce efficient results. The artificial neural network (ANN) is one of the techniques that lie under the domain of AI. ANN models are based on the brain functionality and are capable of performing tasks in a mechanism similar to the human brain. ANN consists of input, hidden, and output layers. The input layer has the input parameters we insert into our model. For the hidden layers, we can have one or more layers and each one has a certain number of neurons. Each neuron is a unit that receives the input and normalizes it, and then puts it in a nonlinear function and passes it on to the next neurons. Finally, the output layer gives the normalized output values of the problem from all of the neurons from the hidden layers.

The core objective of this article is to highlight an ANN model capable of predicting FBHP in a gas condensate field in the Middle East using the technique of ANNs. The designed model has been verified by testing on a wide range of data sets. To develop the ANN model, a field data set of more than 30,000 data points from various wells on the same field were collected. The collected data set was divided in the ratio of 4:1 for

the purpose of training and testing. A subset of the data set was named as the testing subset, and were not used in the training phase of the ANN model. In fact, the testing subset was utilized in predicting the accuracy of the model and was later compared against the results attained from the existing correlations and mechanistic models.

Model Development

The developed ANN model is based on the concepts of feed forward neural networks, which operate on the principles of sensory units that contains an input layer and one or more hidden layers, and then finally an output layer. The developed model contains an input layer, which is represented by the input parameters. The optimum number of neurons was determined via a loop, which was five neurons. This was to get the lowest error for training and testing for the developed single layered model with one node at the output layer, which represents the bottom-hole pressure.

The set of nodes that are represented in the output layer represents the result of the overall network as achieved in response to the activation pattern attained from the hidden layer. Figure 1 shows the multiple layers of the ANN model, which clearly shows the input, hidden, and output layers.

The activation function used here is based on the sum of inputs multiplied with their respective weights. The model functions on the concepts of artificial neurons implemented in the feed forward neural network, which uses the back propagation algorithm, Eqn. 1.

$$(x.w) = \sum_{i=0}^{n} \text{xi wji} \quad (1)$$

As the input function lies on the values of the inputs and weights, consequently, the output function would be the activation function, thereby the neurons would be called linear. Subsequently, this function has certain limitations and the commonly attained output function is the log sigmoid functions, Eqn. 2.

$$\text{Oj(x. w)} = \frac{1}{1+e^{-(x,w)}} \quad (2)$$

For this model, the output results are completely dependent on the activation function. Subsequently, this signifies that input values and their respective weights define the output results, therefore, the objective at this stage is to give certain input values that could help in achieving accurate output values. The error is calculated by finding the difference between the actual output from the downhole memory gauge readings and the desired output. Moreover, it has been observed that the errors mainly lie on the weights, and the errors can be minimized by adjusting the weights. The error function here is defined as:

$$(x.w.d) = (\text{Oj(x. w)} - \text{dj})^2 \quad (3)$$

The total error of the network can therefore be calculated by finding the sum of all of the neurons in the output layer:

$$(x.w.d) = \sum_j (\text{Oj(x. w)} - \text{dj})^2 \quad (4)$$

For minimizing the total error mentioned in Eqn. 4, the gradient descent can be used, and the following adjustment rule for the weights can be obtained.

$$\Delta wji = -\eta \frac{\partial E}{\partial \text{Wji}} \quad (5)$$

By making changes to Eqn. 5, updated weights are obtained as:

$$(k+1) = (k) + \Delta wji \quad (6)$$

Data Acquisition and Pre-Processing

For predicting the FBHP the ANN model was con-

Fig. 1 *The proposed ANN structure, showing the multiple layers of the model, which clearly shows the input, hidden, and output layers.*

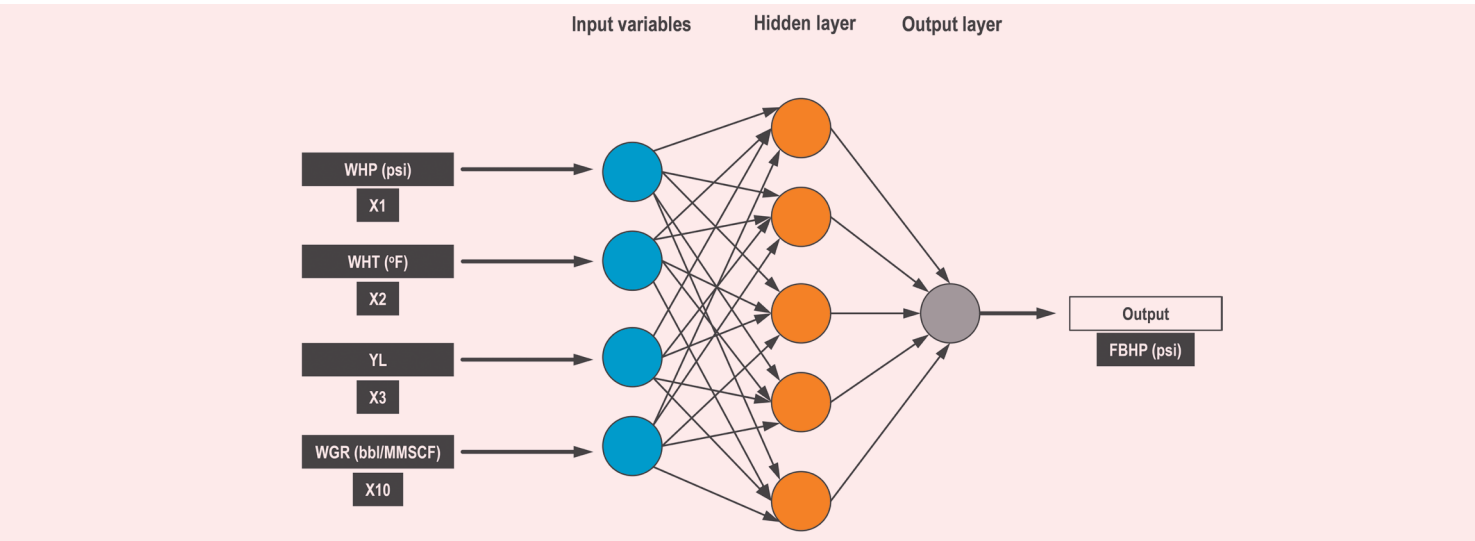

structed using data sets that were attained from different wells with a wide range of inputs on the same field. More than 30,000 data points were collected for the construction of the ANN model. Altogether, there are 10 different input variables and one output variable. The various parameters for input variables are collected from daily flow back data. The measurements were taken every 15 minutes for the input data.

Considering the scope of the project, the values of data that were collected when no fluid was flowing were eliminated from the overall data set. Moreover, any outlier or bad values that were recorded from the meter range were also excluded from the overall data set. Whole data has been collected for a timespan of several months to validate the achieved outcomes of the model. For increasing accuracy, the data is first normalized before training the neural network and later data is de-normalized and reorganized.

Data had to be processed before using the model. Figure 2 is a correlation coefficient matrix heat map, which was constructed to illustrate the significance of each input with respect to the FBHP. Figure 3 shows the feature importance, indicating the significance of each input in affecting the output result.

Basic statistics for training data were obtained to eliminate outliers via the interquartile range method:

$$\text{Lower outliers} < P_{25} - 1.5\ IQR \quad (7)$$

$$\text{Upper outliers} > P_{75} + 1.5\ IQR \quad (8)$$

Fig. 3 *The feature importance, indicating the significance of each input in affecting the output result.*

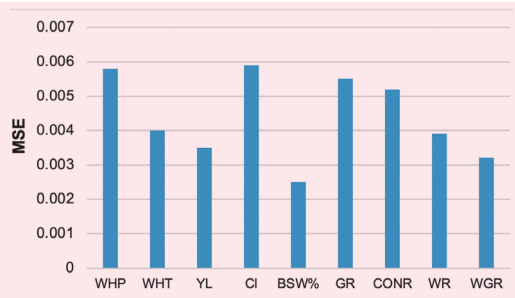

Training and Testing the Model

Taking the basic first step here, the ANN with a single hidden layer is being considered. To achieve the optimum number of neurons, a loop was used to optimize the error when changing the number of neurons. The trained network has an average absolute percent error (AAPE) and correlation coefficient of 0.0924% and 0.999%, respectively. For testing, the AAPE and CC were 0.0942% and 0.999%, respectively.

Figure 4a shows the training ANN model with five neurons for the prediction of the FBHP. Figure 4b shows the testing ANN model with five neurons for the prediction of the FBHP.

The developed ANN model was then tested on the new well's data set, which is hidden from the model.

Fig. 2 *The correlation coefficient matrix.*

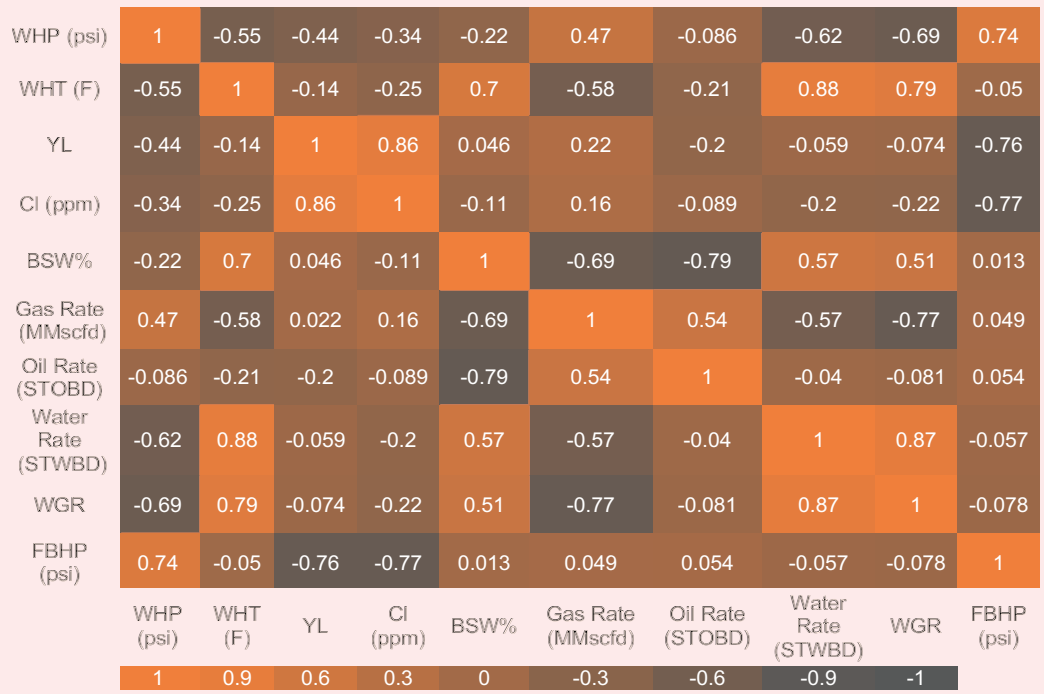

Fig. 4a *Training the ANN model with five neurons.*

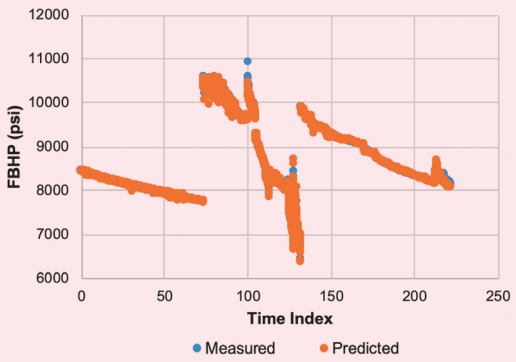

Fig. 4b *Testing the ANN model with five neurons (4:1 ratio).*

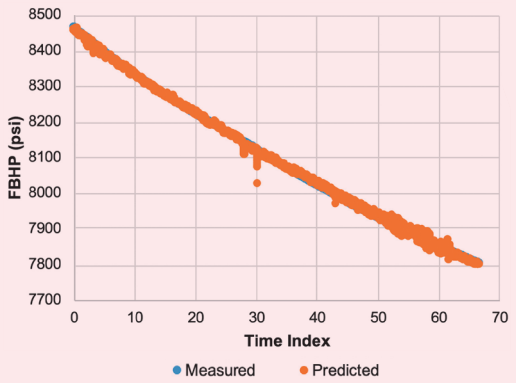

The results were as shown in Fig. 5 for Wells 1, 2, and 3, respectively.

Results and Discussions of the Model

Based on Fig. 5, we can summarize the results from each well in terms of AAPE and CC values, Table 1.

The weights and biases of the ANN model are connected to the input layer, which is further connected with a hidden layer and the hidden layer is then connected with an output layer. From this ANN model, which lies on the principles of weights and biases, a new correlation has been derived. The weights and biases are summarized in Tables 2 and 3.

Where $W_{i,j}$ are the weights of each input (j) in each neuron (i), $W_{i,2}$ are the weights between the hidden layer and output layer for each neuron. b_1 is the bias between the input layer and the hidden layer. b_2 is the bias between the hidden layer and the output layer. Once these inputs are inserted into the hidden layer, neurons will take the inputs and assign each one of them weight and bias terms, and evaluate it in a nonlinear function. In our case, we found out that the log sigmoid function gives the best results for the ANN model. Now, for the purpose of using the model outside of the

Fig. 5 *Applying the trained model on new Wells 1, 2, and 3, respectively.*

MATLAB software, we can extract the correlation from the log sigmoid transfer function:

$$0j(x.w) = \frac{1}{1+e^{-(x,w)}} \quad (9)$$

After we extract the correlation, we have to normalize the inputs between -1 and 1, and then insert them into the obtained correlation and finally de-normalize the output with respect to the training model's FBHP normalized data. The obtained correlation is:

See top of next page for equation 10 (10)

Comparison with Empirical and Mechanistic Models

Figure 6 shows the proposed ANN model, which was plotted against common empirical and mechanical

$$FBHP = \sum_{1}^{5} b_2 + w_2 * \left(\frac{1}{1 + e^{-(wi,1*WHP+wi,2*WHT+wi,3*TVD+wi,4*Yl+wi,5*Cl+wi,6*BSW\%+wi,7*gas\ rate+wi,8*oil\ rate+wi,9*water\ rate+wi,10*WGR+bi,1)}}\right) \quad (10)$$

Table 1 *Testing wells results.*

Parameter	Well 1	Well 2	Well 3
AAPE_Train%	0.2105	0.2105	0.2105
AAPE_Test%	1.6025	1.5663	2.6317
Corrcoeff_Train%	0.9993	0.9993	0.9993
Corrcoeff_Test%	0.9640	0.9808	0.9167

Table 2 *Weights and biases between the hidden and output layers.*

Neuron	1	2	3	4	5
$W_{i,2}$	-1.4579	4.164	0.0483	0.0118	0.0555
$b_{i,1}$	-3.9403	0.3117	-23.1643	-23.4394	46.226
b_2			-1.6265		

Table 3 *Weights and biases between the input and hidden layers.*

Neuron (1)	$W_{i,j}$									
1	0.6168	0.0665	0.0267	2.3394	0.0131	0.2258	-1.4975	2.4139	1.1084	-3.8252
2	1.4875	0.013	0.0263	0.4389	-.0114	0.1121	-0.5478	0.7222	0.6156	0.2659
3	-23.963	-63.9676	48.808	47.7479	19.5879	40.0019	-90.0887	-24.0065	-64.502	32.7538
4	145.4	-103.86	9.4841	-85.346	-85.885	120.761	40.7866	32.8917	-42.9817	64.2688
5	37.265	-5.6391	-50.8461	-116.232	-116.232	31.8959	75.7677	-25.571	-21.7203	-36.7612

models utilized by Prosper, post-shutdown for Wells 1, 2, and 3.

Based on our results, we can see that the ANN model provides consistent results with minimum error. Some other Prosper correlations provides more accurate results in one well, but very far results when applied to other wells.

Conclusions

In this study, an ANN model developed on the principles of a back propagation learning algorithm was developed, which is capable of predicting the FBHP. As discussed in the article and proven from the results, that new model is capable of providing accurate results based on the precise values of empirical correlations and mechanistic models. The best correlation coefficient achieved by the developed model was 0.999, and the lowest AAPE for training and testing were 0.0924% and 0.0942%, respectively.

Results of the developed model indicate that the model supports the actual physical downhole process. The article clearly signifies the role of an ANN in solving complex engineering problems where by training more and more data, better results could be achieved. The developed model can only perform with the specific data range and it must not proceed the range of input variables.

Fig. 6 *Comparing the ANN model (red) with Prosper correlations with respect to DHMG data (black) for Wells 1, 2, and 3, respectively.*

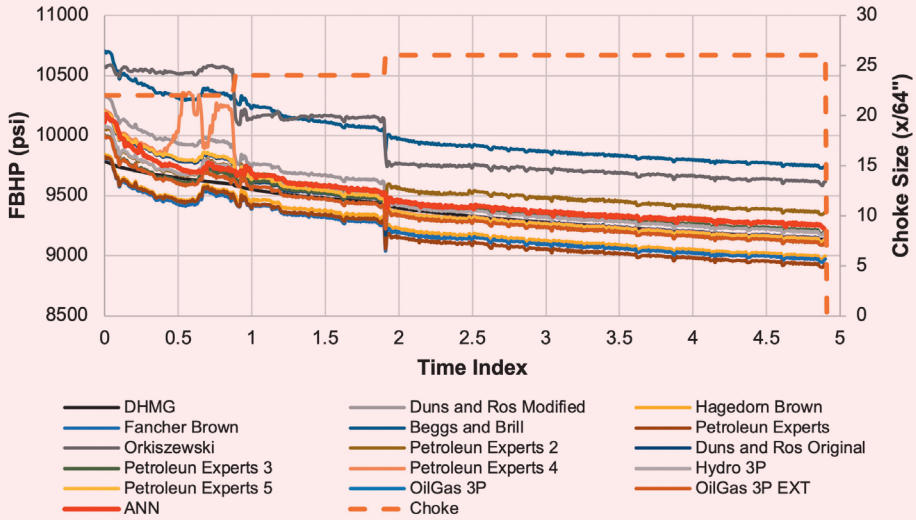

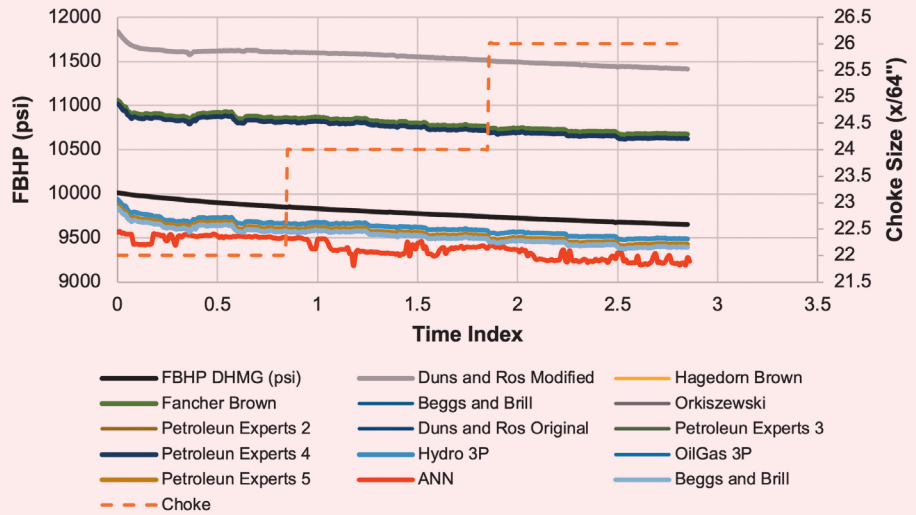

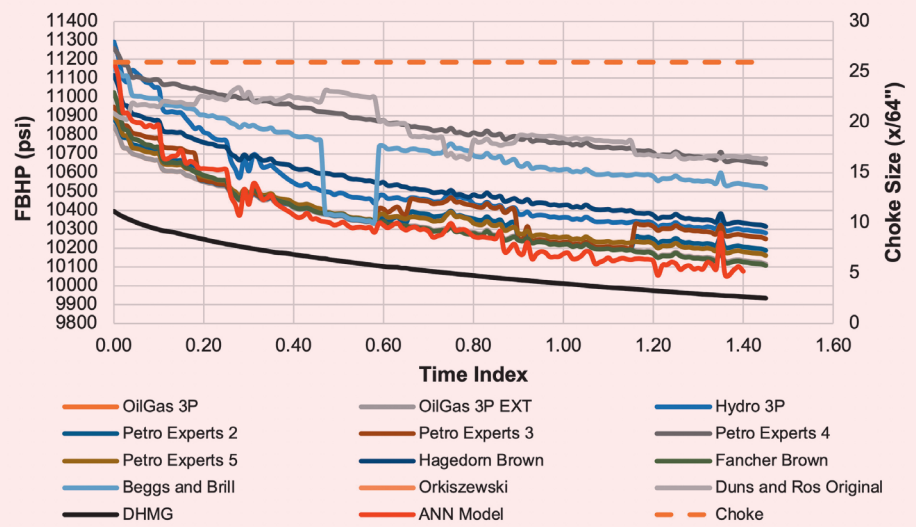

References

1. Hagedorn, A.R. and Brown, K.E.: "Experimental Study of Pressure Gradients Occurring during Continuous Two-Phase Flow in Small Diameter Vertical Conduits," *Journal of Petroleum Technology*, Vol. 17, Issue 4, April 1965, pp. 475-484.

2. Duns, H. and Ros, N.C.J.: *Vertical Flow of Gas and Liquid Mixtures from Boreholes*, The Hague, Bataafse Internationale Petroleum Maatschappij, N.V., 1963.

About the Authors

Fahad H. Al Shehri

B.S. in Petroleum Engineering, King Fahd University of Petroleum and Minerals

Fahad H. Al Shehri is a Production Engineer working in the Production Technology Division of Saudi Aramco's Exploration and Petroleum Engineering Center – Advanced Research Center (EXPEC ARC) where he is focused on multiphase flow metering systems.

Prior to his current position, Fahad was working with the south Jafurah unit in the Well Completion Operations and Production Engineering Department.

He has been an active member of the Society of Petroleum Engineers (SPE) since 2017.

Fahad received his B.S. degree (first honor) in Petroleum Engineering from King Fahd University of Petroleum and Minerals (KFUPM), Dhahran, Saudi Arabia.

Muqbil S. Alkhalaf

B.S. in Chemical Engineering, University of Colorado

Muqbil S. Alkhalaf is a Chemical Engineer working in the Production Technology Division of Saudi Aramco's Exploration and Petroleum Engineering Center – Advanced Research Center (EXPEC ARC), where he works on providing Fourth Industrial Revolution (IR 4.0) based solutions and technologies, gaining extensive knowledge over the past two years. During this period, Muqbil has published and presented several technical papers.

He received his B.S. degree in Chemical Engineering with a minor in Computer Science from the University of Colorado at Boulder, Boulder, CO.

Dr. Muhammad Arsalan

Ph.D. in Electronics Engineering, Carleton University

Dr. Muhammad Arsalan joined Saudi Aramco in 2013 as a Senior Research Scientist. He is leading a team of experts in multiphase metering, sensing, intervention, and robotics focus area within the Production Technology Division of Saudi Aramco's Exploration and Petroleum Engineering Center – Advanced Research Center (EXPEC ARC). Muhammad is also leading the global digital transformation team of EXPEC ARC in advanced sensing domain. His team is working on innovative surface and subsurface production monitoring, control, and optimization technologies.

Muhammad is a seasoned professional with over 20 years of experience in academia and various industries, including biomedical, space, chemicals, and oil and gas. He has over 100 international granted patents and publications related to integrated sensors, systems, and tools.

Muhammad is the recipient of several major national and international awards and distinctions for his entrepreneurial skills and his groundbreaking contributions to the innovation, research and technology development.

Muhammad is the co-founder of two North American technology startups.

In 2004, he was an Invited Researcher and Natural Sciences and Engineering Research Council–Japan Society for the Promotion of Science (NSERC–JSPS) Fellow with the Tokyo Institute of Technology. From 2005 to 2008, Muhammad was an NSERC Alexander Graham Bell Graduate Scholar with the Carleton University.

From 2009 to 2010, he was a National Aeronautics and Space Administration (NASA) postdoctoral Fellow. In 2010, Muhammad joined King Abdullah University of Science and Technology (KAUST) in Thuwal, Saudi Arabia, as an NSERC postdoctoral Research Fellow.

From 2011 to 2016 he was an Adjunct Research Professor with Carleton University, Ottawa, Canada.

Muhammad received his B.Eng. degree from the Institute of Industrial Electronic Engineering, NED University of Engineering and Technology, Karachi, Pakistan in 1999, and his M.S. and Ph.D. degrees, both in Electronic Engineering, from Carleton University, Ottawa, Ontario, Canada, in 2004 and 2009, respectively.

Novel Approach for Lost Circulation Treatment while Drilling with an MPD System by Using a Combined High Strength, Pressure Activated and Thixotropic Swelling Polymer

Ebikebena M. Ombe, Odai A. Elyas, Darrell Cox, and James A. Barry

Abstract /

This article is a study on a novel approach for a specialized lost circulation treatment while drilling with a managed pressure drilling (MPD) system through weak and over-pressurized zones were high-density water-based drilling fluids are required. These weak zones are characterized by natural and induced fractures. This study includes a review of different lost circulation scenarios encountered while drilling, a root cause analysis of these losses and the successful applications of this novel high strength, pressure activated, high solids lost circulation material (LCM) pill combined with a unique thixotropic swelling polymer pill. The combination pill was applied in a high-pressure, high temperature (HPHT) environment where conventional LCM could not stop or minimize the losses.

This new technique uses two pills pumped in tandem, a swelling polymer pill followed by a high strength pressure-activated pill. The technique involves mixing, pumping, spotting, and squeezing procedures while the wellbore was pressurized via the annulus. It resulted in the total treatment of the losses as well as strengthening of the formation to being able to withstand 2 pcf of additional equivalent mud weight (MW) to its in situ fracture pressure limit. Previously, other conventional lost circulation treatment techniques and products only resulted in a temporary fix of the lost circulation, and the wellbore eventually broke down again after drilling resumed. This occurred because the LCM did not remain in the fractures and was eventually removed from the wellbore.

This new technique is safe, reliable, and reduces the frequency and likelihood of formation influx and losses. It also improves cross-flow management and minimizes nonproductive time associated with lost circulation.

This article will discuss different lost circulation scenarios, and the successful application of the high strength, pressure activated, high solid squeeze and thixotropic swelling polymer solutions. It will also highlight the formation lithology and characteristics of the lost circulation zone as well as illustrate the operational sequence for spotting this specialized lost circulation treatment.

Introduction

Lost circulation is a common problem in oil and gas drilling operations, and the losses can often be stopped by pumping conventional lost circulation material (LCM) pills down the drillstring to seal off the loss zone. These LCM pills are composed of fibrous (cedar bark, shredded cane stalks, mineral fiber, and hair), flaky (mica flakes and pieces of plastic or cellophane sheeting) or granular materials (ground and sized limestone or marble, wood, nut hulls, Formica, corncobs, and cotton hulls), which are suspended in a liquid medium, usually the drilling fluid[1]. The other alternative is to set a cement plug(s) across the lost circulation zone, either via the drillstring or via an open-ended work string. These lost circulation treatments, however, have the following limitations:

1. For conventional LCM pills, when applied, the LCM plugs off the loss zone close to or at the face of the wellbore. Unfortunately, this LCM is easily eroded by the flow of drilling fluid and the drillstring movement when drilling resumes, thereby causing the reopening of the loss zone and the reoccurrence of lost circulation.
2. For cement plugs, their application requires time for the cement to set and plug-off the loss zone. Unfortunately, the cement usually flows deep into the loss zone before it has the chance to set. This is the case, especially with losses into highly fractured or cavernous formations. In addition, the cement slurry can be easily contaminated by the turbulent flow of the wellbore fluid into the loss zone, which will interrupt the cement setting process and further jeopardize the lost circulation treatment[2].

The concept of using a high strength, pressure activated, high solids squeeze to combat lost circulation has

been in existence in the oil and gas drilling industry for more than 50 years. Its first application dates back to 1956 while the first commercial product was introduced in 1964[3]. Today, many variants of this treatment are available in the industry, and have been applied as lost circulation treatments with great success. Subsequently, the introduction of a thixotropic swelling polymer as a pre-treatment is relatively new, but it has also been successfully applied in lost circulation treatments.

Principle of the Pressure-Activated LCM and Swelling Polymer Treatment

The high strength, pressure-activated LCM is unique from the conventional lost circulation treatments previously mentioned, in that the LCM treatment is activated when the liquid phase is separated from the solids phase by squeeze pressure. This squeeze action leaves behind a solid plug, with a compressive strength close to that of a cement plug, which plugs off the loss zone.

Figure 1 is an image of the resulting high strength plug from a laboratory test where the pressure-activated LCM was subjected to squeeze pressures. Figure 2 is a chart showing the progressing compressive strength of the plug as more squeeze pressure was applied. As the squeezing pressure is applied to the pill, it forces the crystalline structure of the solids in the pill to become smaller and more compact, thereby expelling the liquid within the pill and building up the strength of the resulting plug, Fig. 3.

Fig. 1 *High strength plug from a laboratory test on the pressure-activated LCM pill.*

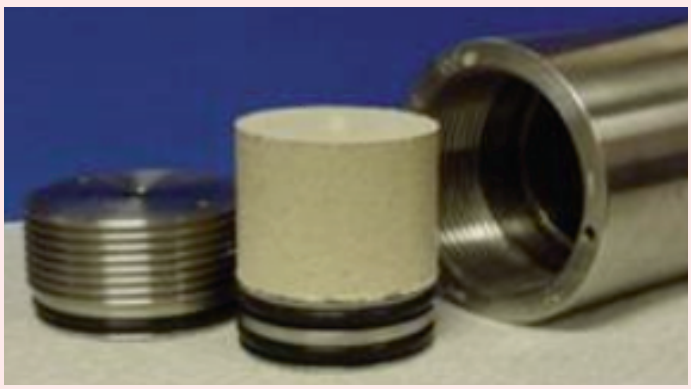

The thixotropic swelling polymer pill is composed of a polymer, which swells when it is exposed to water. Figure 4 shows a sample the thixotropic swelling polymer prior to activation and 30 minutes after activation. This pill is pumped ahead of the pressure-activated pill to provide a filler or base for the squeeze process. By placing this swelling pill ahead of the pressure-activated pill, it creates a temporary barrier to retain the pressure-activated pill within the loss zone, and provides a support for the squeeze pressure to be applied. The swelling pill is very sensitive to water and begins to swell as soon as it is exposed to water when mixing is initiated on the surface.

The swelling action can, however, be inhibited by a reduction of the pH of the fluid until the pill is ready to be pumped into the wellbore. Once inside the wellbore, it begins to react with the water from the drilling fluid and the formation, causing it to swell up to 30 times its original volume. The resulting jelly-like pill forms a base support within the loss zone for the following pressure-activated pill to rest on and receive the required squeeze pressure.

Note that the resulting plug from the combined pressure-activated LCM and swelling polymer treatment is usually formed within the loss zone rather than close to or on the face of the wellbore, which minimizes the possibility of the pill being eroded when drilling resumes, unlike the conventional LCM pill.

Pressure-Activated LCM and Swelling Polymer Application Procedure

The application process of the combined pressure-activated LCM and thixotropic swelling polymer has several stages. They are as follows:

1. Preparing of mixing pits: Two separate mixing pits

Fig. 2 *Applied squeeze pressure vs. resulting plug compressive strength.*

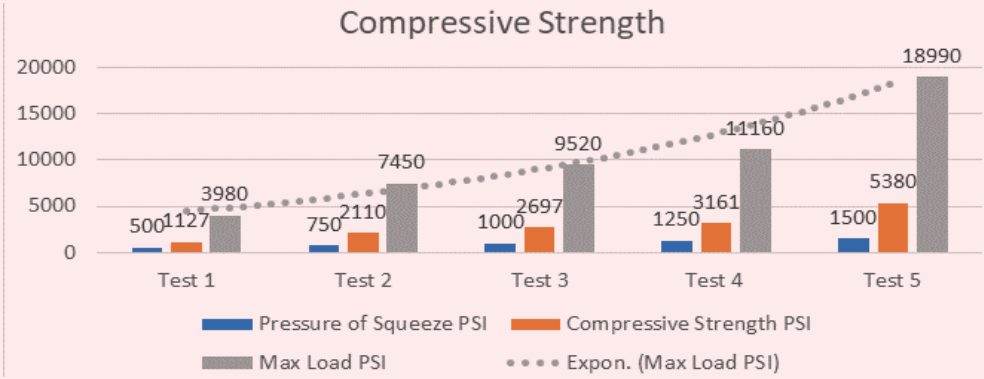

Fig. 3 *(a) Crystalline structure of a pressure-activated LCM before squeeze pressure, and (b) after applying the squeeze pressure.*

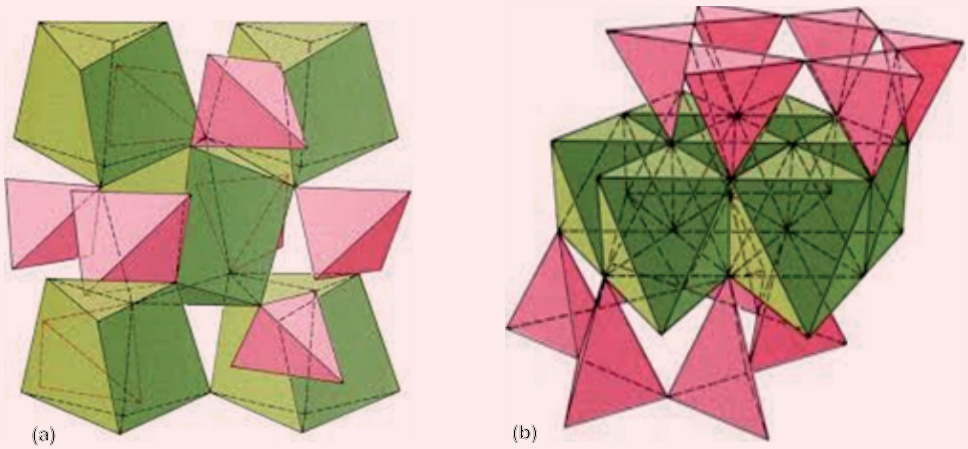

Fig. 4 *(a) A thixotropic swelling polymer sample before water is added, and (b) 30 minutes after water is added.*

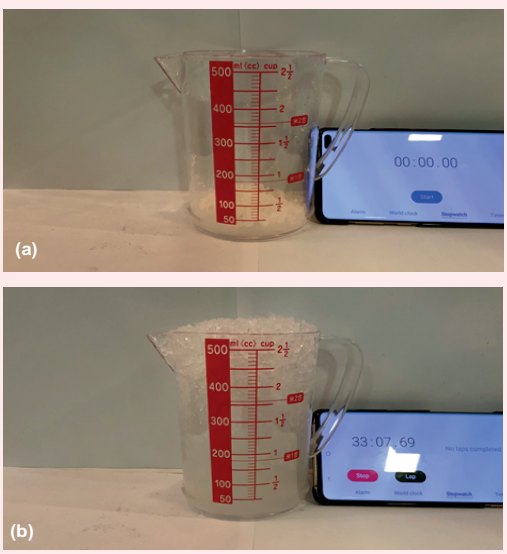

with agitators are required within the rig mud system, one for the swelling polymer pill and the other for the squeeze pill. Ideally, these pits should be as close as possible to the mud pump suction line and should have minimized dead volumes. The filter screens in the mixing pump suction lines and the mud pump suction line should also be removed. These pits and their mixing lines must be cleaned thoroughly to remove any potential contaminants.

2. Mixing each pill: The pressure-activated pill must be pre-mixed first, before the swelling polymer pill, and without any weighing material. As mixing progresses, the slurry will start to foam and become thicker. At this point, it may require some de-foaming and thinning agents. This pill can also be pre-mixed and stored for up to a month before application, as it is chemically inert and will only activate if it is pressurized. Subsequently, a sample of the pill must be tested before application to confirm its potency.

   The weighing material should be added to bring the pill to its required density not more than an hour before pumping into the well. The thixotropic swelling polymer pill must be mixed last, due to its sensitive nature. The mixture should not be completed before the drillstring is at the required depth of application and not more than 1 hour before it is pumped. Since the polymer immediately begins to react when in contact with water, it may be necessary to keep its pH within the range of 2.5 to 3.0 by treating it with citric acid. This will prevent premature swelling, which may plug the drillstring while pumping.

3. Pumping pills down to the loss zone: The depth of application for the pills is dependent on the severity of the losses. For total losses, it is advisable to position the drillstring bit well above the loss zone, usually at the previous casing shoe if it is not too shallow from the loss zone. This will allow the pills to drop down with the fluid flow into the loss zone. For partial losses, it is recommended to position the bit as close to the loss zone as possible, since there is a chance the pills may follow the partial fluid flow upwards in the annulus, and therefore not be placed in the loss zone where it is required.

   The swelling polymer pill is pumped first, followed by 2 to 3 bbl of the original drilling fluid as a spacer, and then by the pressure-activated pill. The pill train is then displaced down the drillstring with the original drilling fluid to the loss zone. For treating partial losses, the pills should be pumped with the well shut-in, i.e., with a closed blowout preventer. This will effectively bullhead the pills into the loss zone to initiate the squeeze process.

For total losses, i.e., with no mud returns, the well does not need to be shut-in. In this case, the well may start having returns, especially as the swelling polymer pill starts to react after it has exited the drillstring into the open hole. Consequently, care must be taken to closely monitor the rates of return, since a sharp and persistent increase may also be an indication of a well influx.

After displacing all the pills out of the drillstring, the drillstring is pulled up above the theoretical top of the pills (assuming no losses) and then flushed with mud to ensure that no traces of the pills are left inside.

4. Squeezing the pills: If returns are observed, the blowout preventer is then closed (if it is still open) and the squeeze pressure is applied in stages, until a predetermined maximum allowable pressure is reached. This maximum allowable pressure is driven by the last formation integrity test (FIT) done on the last casing shoe above the open hole. If this maximum squeeze pressure is achieved, it will be held for at least 1 hour to allow for full activation and strengthening of the pill.
5. Evaluating the losses after application: After holding the squeeze pressure for a minimum of 1 hour, the pressure is then bled off in stages while monitoring the volume of mud returns. As stated before, an increase in mud returns may be an indication of a well influx and this should be controlled accordingly. After bleeding off all the pressure, a flow check is performed to confirm the well stability. Normal drilling operations can then proceed. If, however, the losses are still not cured, or returns are not observed, a second pill train may be required.

Case Study of Application of Combined Pressure-Activated Pill and Swelling Polymer Pill

This case study discusses the application of the combined loss treatment on one well, Well-A, in a field of interest, where total losses were encountered while drilling the 12" hole section with a managed pressure drilling (MPD) system. The formation being drilled is a fractured, high-pressure, high temperature (HPHT) reservoir charged with saltwater. It is about 1,500 ft thick and mainly consists of Middle to Upper Triassic dolomitic mudstone with anhydrite streaks. It was deposited in a low-angle lagoon to supratidal depositional environment, Fig. 5. The high-pressure zones are believed to be within the anhydrite streaks, formed as a result of tectonic, hydrocarbon generation processes, formation uplifting, and hydrothermal expansion. These geological processes are also believed to be the reason for the fractured nature of the formation[4].

Due to its fractured nature and high pore pressure, the drilling mud weight (MW) window in this formation is very narrow, usually between 0.5 pcf and 1.0 pcf, and sometimes there was no MW window at all. With such a narrow MW window, the formation is prone to lost circulation and subsequent well control situations. To mitigate this challenge, a fully automated MPD system was deployed to drill through it. With the MPD system, the equivalent circulating density (ECD) and bottom-hole pressure were easily controlled, thereby enabling drilling within the narrow MW window.

Well-A 12" Hole Section Summary

Figure 6 is the well profile of Well-A, showing the 13⅜" casing and 12" hole section with a drillstring. The 12" hole section was drilled across the high-pressure formation to the 9⅝" casing point, utilizing the MPD system. The system was used to apply an ECD of 152 pcf to the well, while drilling with a 145 pcf water-based drilling fluid densified with a manganese tetroxide (Mn_3O_4) and barite. This drilling fluid was used, as it was less susceptible to weighing material sagging, formation saltwater contamination, high rheology, dehydration, and thermal instability.

The MPD system was also used to adjust the bottom-hole ECD to keep it within the drilling mud window, thereby reducing the likelihood of losses/formation breakdown while applying enough overbalance to prevent any influx from the formation. In

Fig. 5 *The HPHT formation lagoon to supratidal depositional environment[5].*

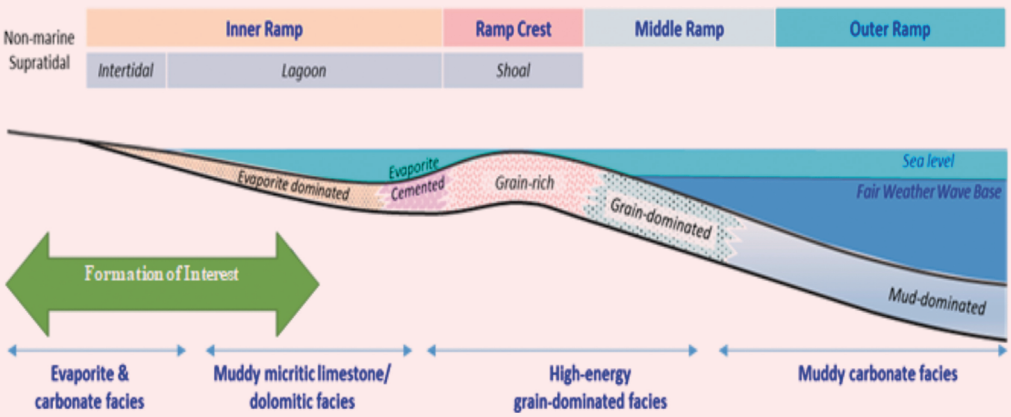

Fig. 6 *The well profile of Well-A showing the 13⅜" casing and 12" hole section with a drillstring.*

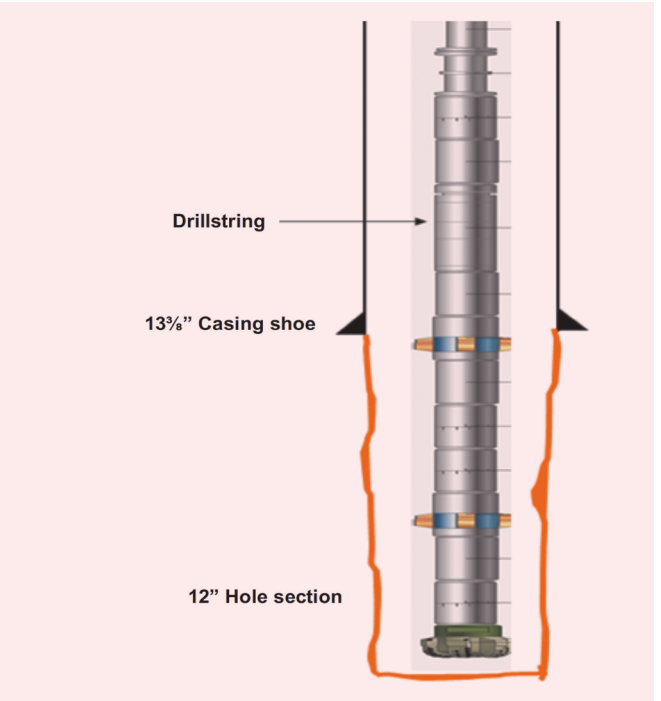

the event where a MW window was nonexistent, i.e., where the formation fracture pressure was less or equal to the formation pore pressure, the mitigation plan was to adjust the ECD to the minimum level required to keep the formation overbalanced while treating the resulting losses with LCM pills, pumped down the drillsting to the lost circulation zone.

Figure 7 shows the drillstring configuration for drilling this hole section. Note that the 12" bit was fitted with 6 × 20 nozzles with a total flow area of 1.841 in^2. This nozzle size was selected to produce sufficient bit hydraulic horsepower per square inch for optimal drilling while providing sufficient total flow area for pumping a high concentration of LCM (up to 200 ppb) through the drillstring without plugging it.

Well-A 12" Hole Section Drilling Summary

Drilling the 12" hole section commenced with 145 pcf mud while maintaining an ECD of 152 pcf on the bottom with the MPD system. After drilling 186 ft into the high-pressure formation, a 100 bbl/hr partial lost circulation occurred. These partial losses were controlled by first reducing the bottom-hole ECD to 149 pcf and spotting some LCM on the bottom via the drillstring. The ECD was then increased back to the original value of 152 pcf and drilling resumed. After drilling 438 ft into the high-pressure formation, the MPD system detected a 1 bbl gain in the active mud system — the well had taken in an influx. Drilling was halted and the influx was circulated out, after which the ECD was increased to 153 pcf to maintain the required overbalance.

After the influx was circulated out, partial losses occurred again, this time at 120 bbl/hr. Again, the losses were controlled by spotting an LCM pill via the drillstring, after which drilling resumed. Unfortunately, total lost circulation occurred after drilling 556 ft into the formation. At this point, the losses could not be controlled with conventional LCM pills. Furthermore, the MPD system could not maintain the required 153 pcf ECD on the bottom, due to the losses. This led to the well taking in an influx, and therefore had to be shut-in. Drilling could not continue until the influx was circulated out. The influx, in turn could not be circulated out until the losses were cured.

Figure 8 shows the drilling mud window and ECD profile for Well-A's 12" hole section, with notes of all the lost circulation and well control events.

The challenge here, as mentioned, was that after stopping the losses, the LCM was washed out and eroded from the wellbore around the loss zone when drilling resumed. This caused the loss zone to be reopened and the lost circulation to reoccur. At this point, the combined high strength, pressure-activated pill and thixotropic swelling polymer pill were deployed to stop the losses, and strengthen the wellbore.

Application of Combined Pills in Well-A

The pits were prepared as per the procedures discussed earlier in the article. The required pill volumes were also determined by considering the length of the open hole and the depths of the loss zones. It was finally decided to pump a volume equal to 1.5 to 2.0 times the open hole volume for each pill. This would allow the pill treatment to cover all the potential loss zones encountered while drilling.

The drillstring bit was placed at the 13⅜" casing shoe and pills were mixed, also as per the procedure discussed earlier. There were challenges with weighing up the swelling polymer pill to the required 145 pcf. The density could only be built up to 138 pcf without jeopardizing the effectiveness of the pill, and at this point, it was decided to pump the 138 pcf swelling polymer as it was while compensating it with back pressure from the MPD system.

The combined pill train was pumped and displaced out of the drillstring, after which it was dropped down the open hole to the loss zone. Initially, there were no returns, and back pressure was still being applied via the MPD system. The swelling polymer pill was allowed to swell for a period of about 2 hours after which the squeeze pressure was applied in stages via the MPD system. A total of 26 bbl of fluid were squeezed into the well after which the squeezed pressure built up to an equivalent MW of 157 pcf at the 13⅜" casing shoe, which was 2 pcf higher than the FIT carried out on the casing shoe.

The pressure was bled down to the previous equivalent MW required for overbalance (153 pcf) and the well was monitored for 1 hour via the MPD system. No losses or gains were observed. The drillstring was washed down to the bottom of the well where the

well was again monitored for another hour. Again, no losses or flow was detected. Drilling resumed and continued to the 9⅝" casing point without any further lost circulation issues.

The application of the combination pills in Well-A was a total success. The pills not only stopped the losses, but also strengthened the formation so it could support an equivalent MW higher than the initial FIT value.

Fig. 7 *The 12" hole drillstring configuration.*

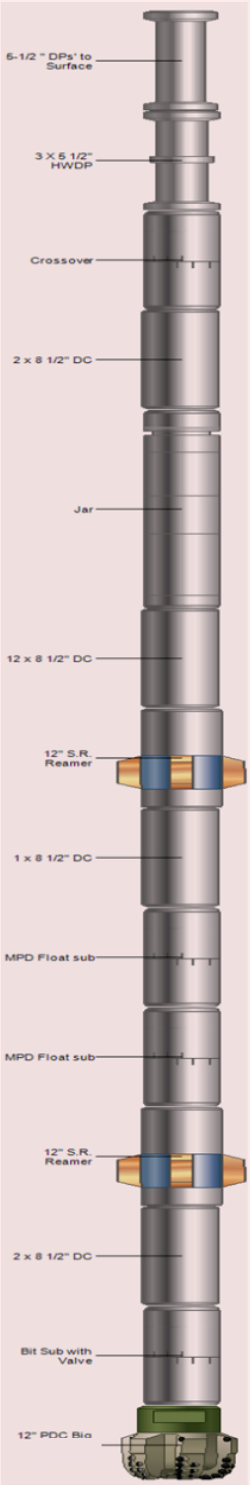

	Description	OD (in) / ID (in)	Max OD (in)	Bottom Size / Top Size (in)	Botom Connection / Top Connection	Length (ft)	Cum. Length (ft)	Cum. Weight (1000 lbm)
1	12" PDC BIT (6 x 20 nozzles)		12.000	6.625	REG	1.12	1.12	0.3
2	Bit Sub with Valve	8.500 / 2.813	8.500	6.625 / 6.625	Regular / Regular	5.00	6.12	1.1
3	2 x 8 1/2" DC (2 joints)	8.500 / 2.875	8.500	6.625 / 6.625	REG / REG	60.51	66.63	11.4
4	12" S.R. Reamer	8.600 / 3.000	12.000	6.625 / 6.625	REG / REG	7.59	74.22	13.2
5	MPD Float sub	8.375 / 3.000	9.750	6.625 / 6.625	REG / REG	3.82	78.04	13.8
6	MPD Float sub	8.375 / 3.000	9.750	6.625 / 6.625	REG / REG	3.82	81.86	14.4
7	1 x 8 1/2" DC	8.500 / 2.875	8.500	6.625 / 6.625	REG / REG	30.25	112.11	19.6
8	12" S.R. Reamer	8.500 / 3.000	12.000	6.625 / 6.625	REG / REG	7.63	119.74	21.3
9	12 x 8 1/2" DC (12 joints)	8.500 / 2.875	8.500	6.625 / 6.625	REG / REG	363.05	482.79	83.1
10	Jar	8.000 / 3.000	8.875	6.625 / 6.625	REG / REG	30.10	512.89	86.6
11	2 x 8 1/2" DC (2 joints)	8.500 / 2.875	8.500	6.625 / 6.625	REG / REG	58.69	571.58	96.6
12	Crossover	8.250 / 3.125	8.250	6.625 / 5.500	REG / XT54	3.25	574.83	97.1
13	3 X 5 1/2" HWDP (3 joints)	5.500 / 3.250	7.250	5.500 / 5.500	XT54 / XT54	91.36	666.20	102.7
14	5-1/2 " DPs' to Surface	5.428 / 4.778	7.000	5.500 / 5.500	XT54 / XT54			

Fig. 8 *A chart showing the 12" hole section drilling mud window and the ECD profile of Well-A.*

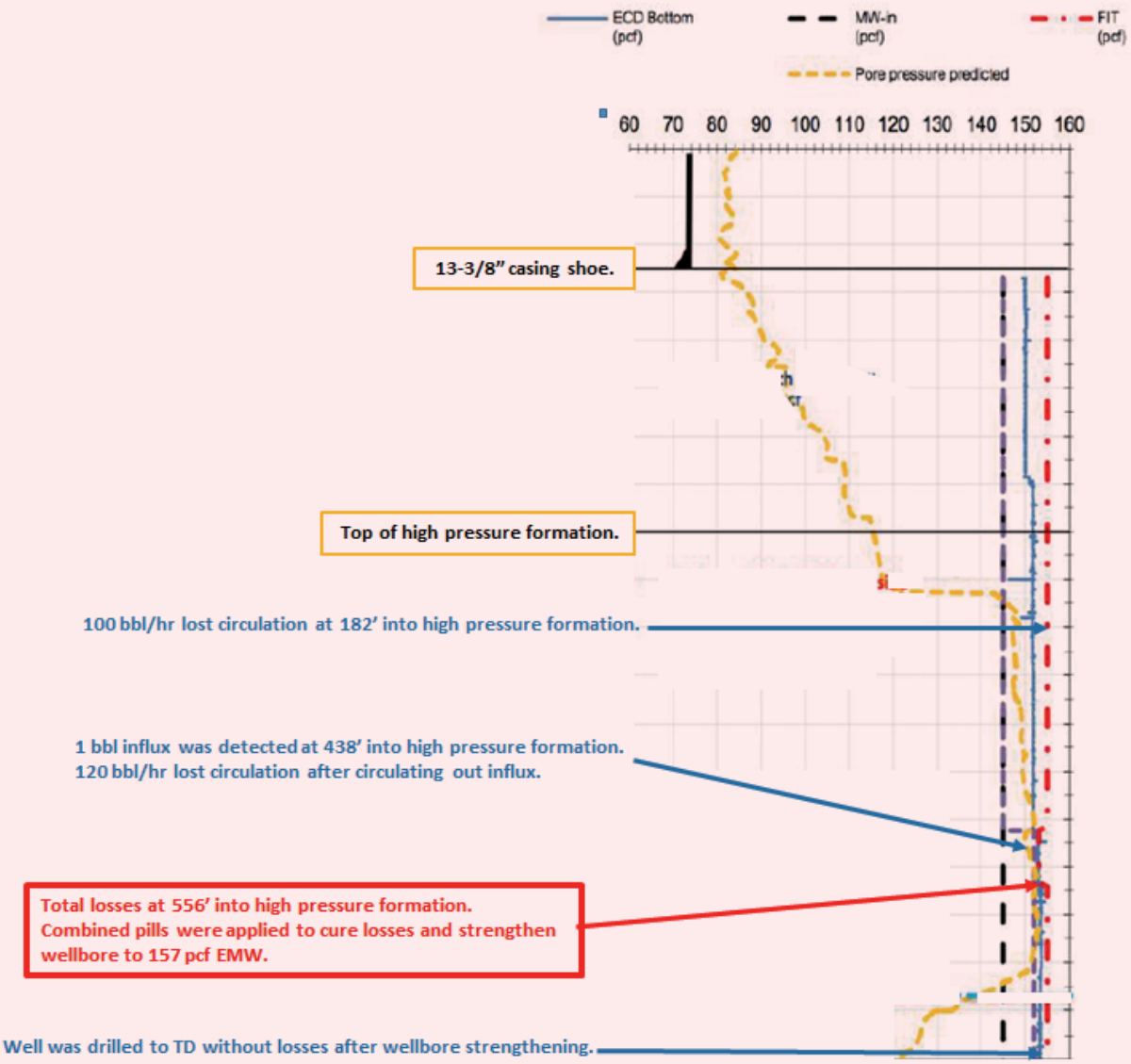

Applications in Other Wells in the Field of Interest

This technique has been used in other wells in this field across the same fractured HPHT formation. In one particular well, severe partial losses were encountered. Here, the combination pill was applied and it reduced the losses to a minimum level, which allowed drilling to continue to the casing point.

In another well in the same field, which also encountered total losses across the formation, the combination pill was applied but was not able to stop the losses, and two cement plugs were applied without success. Subsequently, the losses were finally stopped by pumping the thixotropic swelling polymer pill in combination with a third cement plug. Drilling then resumed and continued to the casing point without any subsequent losses.

Other Variants of the Application

The combined pill technique has been used in a number of wells since the application discussed in this article, with varying levels of success. Consequently, some of these treatments have been done with some modifications to the original technique — one of which is mentioned in the previous paragraph — where the swelling polymer pill was pumped ahead of a cement plug instead of the pressure-activated pill. These new techniques are as follows:

1. The thixotropic swelling polymer pill is first applied as a single pill, and then displaced into the loss zone. After allowing time for swelling, the pressure-activated pill is then pumped into the loss zone. This variant allows the pill more time to swell before pumping the pressure-activated pill, thereby increasing its

effectiveness.

2. The pressure-activated pill is applied as a stand-alone pill. This is more suited for treating partial losses.
3. Conventional LCM is added to the pressure-activated pill to enhance its performance. This resulting pill has both the characteristics of the pressure-activated pill and the conventional LCM pill.

Conclusions

The application of the combined high strength, pressure-activated pill and thixotropic swelling polymer pill in the field of interest has proven to be a successful treatment for lost circulation where other conventional lost circulation treatments had failed. It has enhanced the MPD operations across the HPHT fractured formations in this field by strengthening the formation beyond its initial tested strength, thereby increasing the MW window. It has also proven to be a very versatile lost circulation treatment technique, which can be adapted to a wide variety of lost circulation challenges.

Acknowledgments

This article was previously presented at the International Petroleum Technology Conference, Dhahran, Saudi Arabia, January 13-15, 2020.

References

1. Schlumberger: Lost Circulation Material description, *Schlumberger Oilfield Glossary*, (https://www.glossary.oilfield.slb.com/en/Terms/l/lost-circulation_material.aspx), viewed October 5, 2019.
2. Canson, B.E.: "Lost Circulation Treatments for Naturally Fractured, Vugular, or Cavernous Formations," SPE paper 13440, presented at the SPE/IADC Drilling Conference, New Orleans, Louisiana, March 5-8, 1985.
3. Al-Sabagh, A.M., El-Awamri, A.A., Abdou, M.I., Hussein, H.A., et al.: "Egyptian Diatomite as High Fluid Loss Squeeze Slurry in Sealing Fractures and High Permeable Formation," *Egyptian Journal of Petroleum*, Vol. 25, Issue 3, September 2016, pp. 409-421.
4. Alrasheed, A.A., Oqaili, A.H., Aljubran, M.J. and Ezi, P.C.: "Deployment of Fully Automated MPD and Manganese Tetroxide Mud System to Drill Ultra-Narrow Mud Window in HPHT Gas Wells," SPE paper 190000, presented at the SPE/IADC Managed Pressure Drilling and Underbalanced Operations Conference and Exhibition, New Orleans, Louisiana, April 17-18, 2018.
5. Aljubran, M.J., Ombe, E.M., Alluhaydan, A.S. and Thomas, S.: "Innovative Mechanical Tapered Scab Liner Design and Deployment to Restore Well Integrity," SPE paper 192407, presented at the SPE Kingdom of Saudi Arabia Annual Technical Symposium and Exhibition, Dammam, Saudi Arabia, April 23-26, 2018.

About the Authors

Ebikebena M. Ombe

M.S. in Offshore and Ocean Technology (Subsea Engineering Option), Cranfield University

Ebikebena M. Ombe is a Drilling Engineer with 15 years of oil and gas drilling industry experience. He works with Saudi Aramco's Gas Drilling Engineering Department, where he is responsible for the design, drilling and completion of gas development wells for Saudi Aramco.

Before joining Saudi Aramco in 2014, Ebikebena worked as a Well Engineer for Shell. While at Shell, he worked with both the front end well design group and the well delivery department, and was involved with the design and construction phases of numerous oil and gas drilling and workover projects. Ebikebena also worked as the regional wells directional survey focal point for Shell's Sub-Saharan Africa drilling operations.

He received his B.S. degree in Metallurgical and Materials Engineering from the Obafemi Awolowo University, Ile-Ife, Nigeria, and his M.S. degree in Offshore and Ocean Technology (Subsea Engineering Option) from Cranfield University, Bedford, U.K.

Odai A. Elyas

B.S. in Petroleum and Natural Gas Engineering, Pennsylvania State University

Odai A. Elyas is a Petroleum Engineer working with the Drilling Technology Team of Saudi Aramco's Exploration and Petroleum Engineering Center – Advanced Research Center (EXPEC ARC). He has worked on several projects in the fields of drilling automation and localization, where he was involved in studying various chemicals used for drilling operations, and analyzing local chemical producers to find suitable products to be deployed in drilling operations.

Odai has also been on several assignments with the Gas Drilling Engineering Department, the Gas Drilling Department and the EXPEC ARC Cementing Services Unit. While on these assignments, he gained extensive experience in drilling high-pressure, high temperature extended reach gas wells, and providing technical support for cementing operations.

Odai received two B.S. degrees, one in Petroleum and Natural Gas Engineering, and the other in Energy Business and Finance, both from Pennsylvania State University, State College, PA. He is looking forward to pursuing his M.S. degree in Petroleum Engineering at the University of Texas at Austin, Austin, TX.

Darrell Cox

B.S. in Petroleum Resource Engineering, The Northern Alberta Institute of Technology

Darrell Cox is a highly experienced Drilling Fluid Engineer with over 40 years of experience in the oil and gas drilling industry. Darrell is currently the Operations Manager for Turbochem International Eastern Hemisphere operations based in the Kingdom of Saudi Arabia. He is involved with providing lost circulation solutions and technical support for oil and gas drilling operations in the Middle East.

During Darrell's extensive career, he has worked in many roles, from Rig Floorman to Drilling Fluids Engineer. Darrell has also held Drilling Fluids Coordinator and managerial positions in major oil and gas service companies around the world. Most recently, he has been involved with providing lost circulation solutions with an emphasis on improving zonal isolation in cementing operations for oil and gas wells in the Middle East.

Darrell received his B.S. degree in Petroleum Resource Engineering from The Northern Alberta Institute of Technology (NAIT), Edmonton, Alberta, Canada.

James A. Barry

B.S. in Business Administration, University of St. Thomas

James A. Barry is a Drilling Fluids Specialist with over 15 years of experience in the oil and gas industry. James is the Global Corporate Sales and Technical Support representative for TurboChem International based in Houston, TX. Prior to this position, he was the Managing Director of TurboChem International Eastern Hemisphere, supporting oil and gas operations in the Middle East, North Africa, as well as Southeast and Subcontinental Asia.

James has had a dynamic career and has worked in many specialties, including QHSE (quality, health, safety and environment management), drilling fluids engineering, and solids control and drilling waste management. Most recently, he has primarily worked on lost circulation solutions and novel pre-cement and casing applications to ensure zonal isolation and wellbore integrity for oil and gas wells.

James has received numerous industry awards/recognitions, including the Society of Petroleum Engineers (SPE) Outstanding Service Awards in 2013 and 2017. He has served as the past Chairperson of the SPE/UAE Northern Emirates Section forum.

James received his Bachelor of Business Administration degree from the University of St. Thomas, Houston, TX.

Simultaneous Injection and Fracturing Interference Testing SIFIT — A Novel Technique

Mohamed Larbi Zeghlache, Mustapha Berkane, and Wael Soleiman

Abstract /

Wireline formation testers (WFTs) are a major component of providing quantitative geomechanical information obtained through induced hydraulic fractures, commonly called a microfracture. This type of information is used to infer critical data such as borehole stability studies, field stress mapping, stimulation planning, seal integrity tests, and other applications. Likewise, vertical interference tests (VIT) conducted with WFTs provides valuable information about flow barriers, zone connectivity, and quantitatively determines localized horizontal and vertical permeabilities. Both techniques are used over separate stations and different depths as it may involve various hardware in different trips in the wellbore. In this article, a novel technique to combine both tests simultaneously using an optimized hardware configuration and interpretation will be demonstrated.

Pressure test data in low permeability reservoirs is commonly affected by "supercharging" fluid that leaks into the invaded zone from hydrostatic pressure and cannot quickly dissipate, thereby making it difficult to accurately obtain true formation pressure measurements. This, in turn, affects the VITs where the pressure response at the observation point is influenced by the supercharged pressure, resulting in the erroneous calculation of vertical permeability. By initiating a microfracture while monitoring its response, this provides a better estimate to reservoir pressure and improves VIT success in a low permeability formation.

The combination of a microfracture and VIT at the same depth provides unique information about the reservoir and may enhance the data quality on these stations. The safety and cost are positively impacted in improving the operational efficiency. New methods and techniques can emerge from the utilization of this methodology and improve reservoir understanding and characterization. In fact, a feasibility test using this unique approach was conducted and validated in a carbonate reservoir. The results indicate that the created microfractures provide a means of dissipating the "supercharging" effect, masking the true formation pressure, thereby reducing the uncertainty in the calculated reservoir properties using the VIT data.

This technique may be further developed to include — for future implementation — other sensors at different places and positions in the downhole modular tools to acquire more information that will bring novel insight on the tested reservoir zones.

Introduction

A diagnostic fracture test, also known as a pre-fracture test, injection falloff test, a data-fracture, and mini-fracture or microfracture, are tests that can be used to determine mechanical properties of a geologic formation. In this article, the microfracture test is referred to as any of these listed fracturing techniques.

A vertical interference test (VIT) can be used to determine permeability anisotropy and/or barriers, while a mini-fracture can be used to determine a minimum fracture initiation pressure. Traditionally, these tests are performed with different wellbore testing tools and must be performed in separate operations in the wellbore. If a situation arises where both tests need to be performed, the need for two complex operations, and potentially two trips, can lead to excessive time and cost.

This article describes a method for testing geomechanical properties of the reservoir rock. The tested properties include vertical permeability and "fracture-ability." The method involves the acquisition of VIT data followed by microfracture on the same station to determine both anisotropy and the fracture pressure at the same depth in a given reservoir formation. For this purpose, any type of formation testing tools might be considered for the above mentioned objectives. This may include, but not limited to, a wireline formation tester (WFT), logging while drilling (LWD) formation testing, surface testing, etc[1].

The main benefit of this technique is that testing tools or equipment are not moved, pulled out or replaced between tests. The tests can also be started at the same time, or certain aspects of each test can be performed at the same time. Details on overlapping aspects of the tests are discussed in this article. Such systems save a

considerable time and cost over traditional techniques. Additionally, extra sensors can be added to the wellbore tool to determine more geomechanical properties within a single trip. The geomechanical properties that can be determined include, but are not limited to Young's modulus, Poisson's ratio, in situ stresses, electrical properties (conductivity and dielectric) and the direction or spatial variability of these properties when multiple sensors are used.

These properties can also be used with other logging measurements to determine additional interpreted properties such as water, oil, and gas saturations in the rock pore space. The results of simultaneous injection and fracturing interference testing (SIFIT[1]) are validated in a carbonate reservoir demonstrating all the features and actual benefits.

VIT

Both vertical and horizontal permeabilities are critical parameters in the understanding of the fluid flow through petroleum reservoirs and the implementation of the production and injection strategies; the VIT can also be used to test potential flow barriers[2]. The horizontal permeability is relatively simple to obtain using a single source in the likes of WFTs, LWD, or well testing. The vertical permeability/anisotropy is obtained through VIT, which requires a specific setup composed of a source for the drawdown known as "sink" and an observation point that must be vertically separated from the sink.

There are several configurations available with WFTs that can obtain VIT data, but the most common configuration is made up of the straddle packer and a single probe, Fig. 1.

The process is to initiate a pulse by pumping out fluid from the formation through the sink probe while monitoring the pressure changes in the observation probe. A variety of fluid identification sensors are also used during the pump out to ensure that a homogeneous native fluid is flowing across the sensors prior to starting the buildup phase. This procedure is to ensure that the in situ conditions are honored during the test and the fluid viscosity is measured in real time. If the spherical and/or the radial flow response of the sink and the observation probe overlay on a log-log plot, then a unique Kv/kh can be matched for that model.

The absence of a signal in the observation probe can be interpreted as a flow barrier as long as there is sufficient drawdown in the sink and/or an appropriate distance between the sink and the observation probe. Therefore, great care needs to be taken for both job planning and the interpretation work so that the appropriate design and formation parameters are well understood before inferring such a conclusion.

Microfracture Test

Microfracture is a cost-effective method, which saves rig time associated with conventional fracture methods that require surface pumping equipment. This technique

Fig. 1 *A standard configuration of the VIT, made up of the straddle packer and a single probe.*

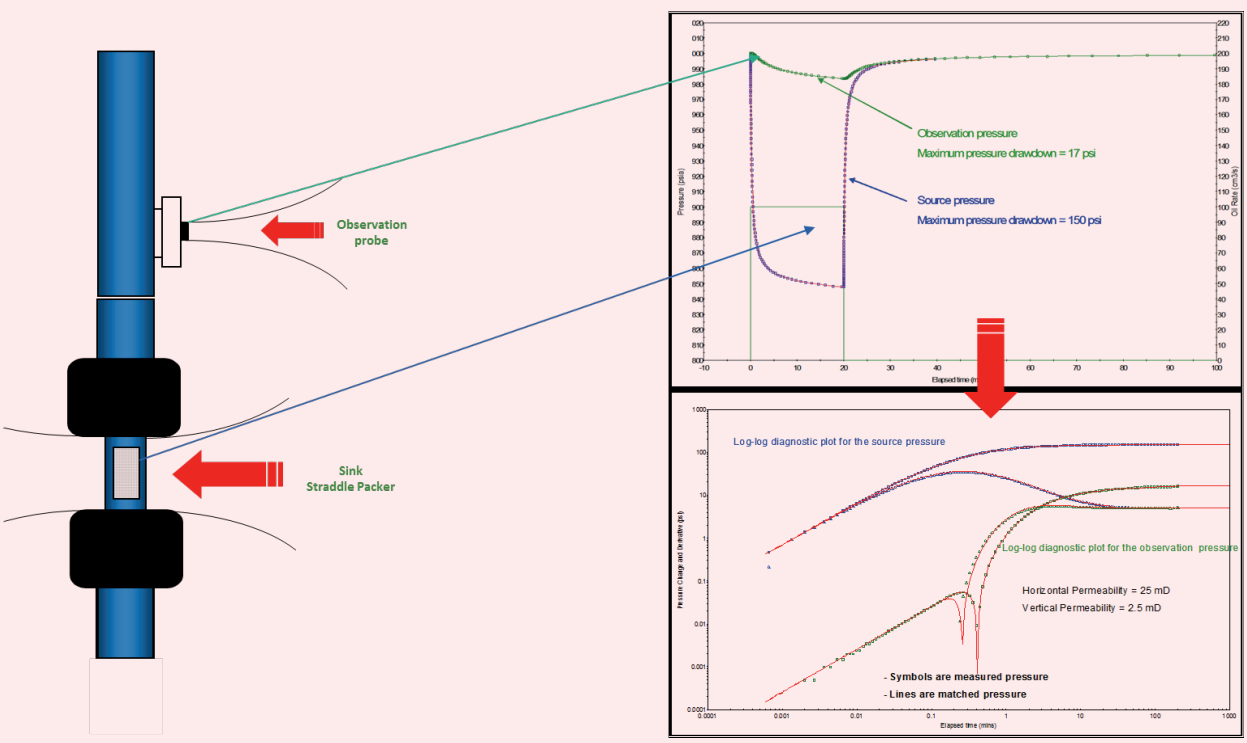

is performed at a 1-m isolated discrete interval, Fig. 2, to determine quantitatively: formation breakdown pressure, closure pressure (minimum horizontal stress), and formation pressure and fracture reopening (formation tensile strength)[3]. Also, it allows stress contrast determination along the reservoir (fracture vertical migration).

Fig. 2 *Microfracture standard configuration.*

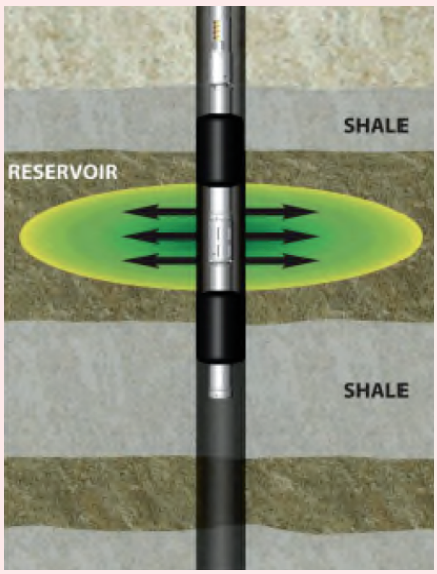

Microfracture Prejob Assessment

The pre-job assessment consists of estimating rock strength and the fracture gradient to compare them to the maximum pressure capability allowed by the straddle packer module at downhole conditions.

The rock strength and fracture gradient are estimated from preexisting field information or open hole logs — acoustic and density — acquired in previous runs (usually in the same well where the microfracture is planned). Interval selection is recommended along with the likelihood of formation breakdown. The microfracture test selection consists of identifying a 1-m interval with natural barriers to fracture propagation above and below the straddle packer positions.

Microfracture General Procedures

The maximum differential pressure across the inflatable packers (absolute bottom-hole pressure (BHP) of the isolated interval minus hydrostatic pressure) depends on borehole size, Fig. 3.

The injection pressure capability of the straddle packer for a microfracture operation on a 6½" open hole is limited to the maximum differential pressure inside the packers. This pressure limit will decrease in larger boreholes. The maximum differential pressure allowed by the straddle packer is 3,500 psi (241 bar) above the hydrostatic pressure in 8½" holes; whereas it

Fig. 3 *Maximum differential pressure across the inflatable packers.*

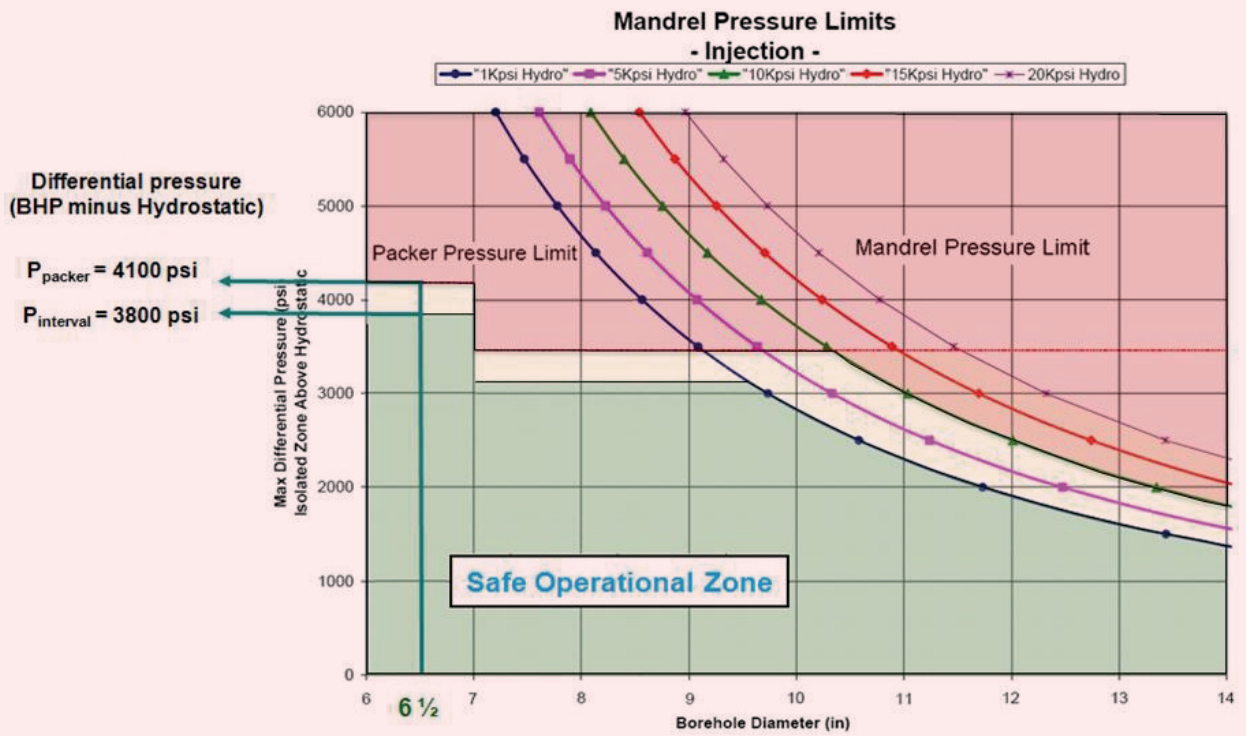

can go higher in 6½" holes — the microfracture with the slim straddle packer kit can safely reach 4,000 psi of differential pressure.

Since the pressure between the packers should be lower than the pressure inside the packers by 150 psi (10.3 bar) to maintain a good seal in the testing interval, the maximum differential pressure allowed between the packers in the isolated interval should be around 3,300 psi (in a 8½" in open hole). In some cases, 50 psi is sufficient to maintain a seal, but it depends on borehole quality. The pressure inside the packer elements will increase as the pressure of the isolated zone increases while injecting into the formation. The absolute pressure inside the elements will be higher than the isolated interval pressure.

WFT Tool Description

Some modifications are necessary to the straddle packer for microfracture operations. First, the strain gauge for the straddle packer element pressure reading is replaced with a 7.5 K strain gauge. Second, the borehole fluid pressure relief valve had the washers installed to increase the pressure relief to 3,500 psi. Finally, filters were installed in the six tank carrier. Solid particles in the mud tend to plug these filters while pumping into the testing interval or inflating the elements.

Usually, a large 885 cc pump is used to reduce the time for the packer inflation and deflation to save rig time; however, it does not necessarily produce higher power to generate enough pressure for a microfracture test. Therefore, a 500 cc pump was used.

An additional 56.7 cc small volume pump was installed next to the straddle packer for accurate drawdown testing. Figure 4 illustrates the WFT tool configuration.

SIFIT — A Novel Technique

Because of the heterogeneity in reservoir layers and fluids filling the pore space, there is no single configuration of the modular formation testing tools available to perform advanced tests, e.g., VIT. Multiple configurations are possible and each have different applications, limitations, and advantages. For example, a single probe above a dual packer may not be applicable for high permeability or high mobility formations, this is mostly due to low drawdown pressure created by the dual packer as a result of high mobility. In this case, not enough interference pressure disturbance is created at the packer's interval that can be observed at the monitoring probe. An azimuthal multi-probe configuration uses directional probes at the same depth, which can give additional information to reduce uncertainties related to vertical permeability interpretation.

In extreme cases, i.e., very tight or highly permeable formations, it is very challenging to produce a pressure wave that can cause interference due to either very high or very low drawdown at the source. This is the case of several carbonate fields in the Middle East where traditional VIT is challenging.

Formation testing and sampling have always been the most complicated, costly and time-consuming open hole logging operation. Borehole conditions and risks are often associated with conveyance, whereas tool operations and stationary time are challenges that define the success of formation testing and sampling. Therefore, it is important to improve the safety, quality, and efficiency for such logging operations. For all these challenges, an opportunity was identified to optimize such complex operations by simultaneously addressing multiple challenges in a safe and cost-effective way. Consequently, SIFIT was implemented and validated[1].

A SIFIT technique was deployed for the first time in a carbonate reservoir. A sidetrack well was drilled with 6⅛" bit size across the target reservoir. A comprehensive logging program was successfully executed comprising the following suits:

- Run 1: LWD triple combo
- Run 2: Image/X-Dipole sonic
- Run 3: Pressures/samples/microfracture/VIT

The objective of the microfracture testing on the studied well is to measure the fracture initiation, propagation, closure, reopening, and final fracture closure pressures. The well targeted an area of the reservoir that did not have fractures so that the far field stresses — not affected by borehole stresses — of the matrix could be measured to validate and calibrate the horizontal stress profile. The microfracture testing procedure included formation breakdown, fracture propagation, fracture reopening cycle, and pressure falloff for fracture closure identification. The fracture closure is observed by natural leakoff pressure decline behavior.

Fig. 4 *The WFT tool configuration.*

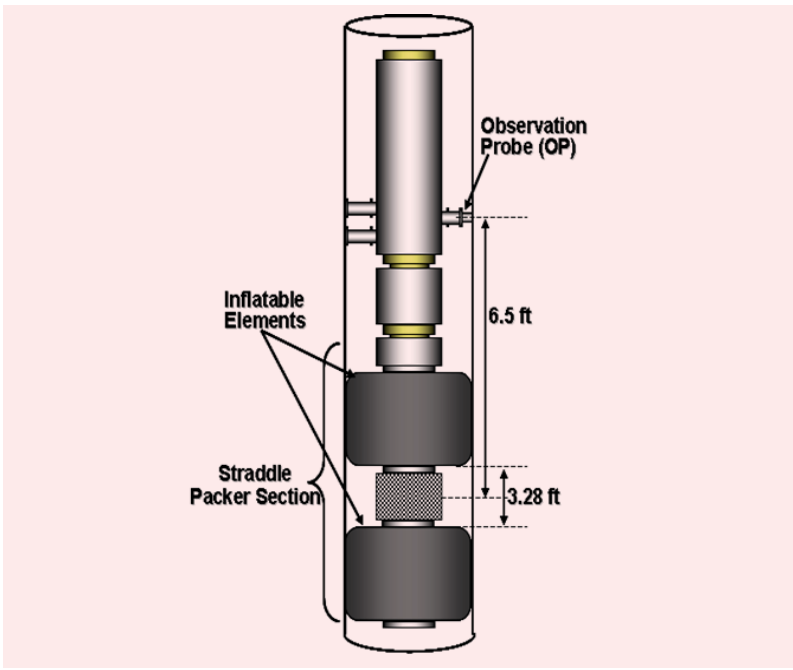

Two microfracture intervals were selected for testing this formation. The first microfracture was conducted at Depth 1, a midpoint of the isolated interval. The second microfracture was conducted at Depth 2. Both tests achieved formation breakdown, propagation, reopening, and closure. The analysis of the pressure data from each test is presented in the following sections. This includes pressure decline curves that were analyzed to establish the fracture closure pressure. The decline curves were analyzed using the square root of time method, log-log derivative method, and the Nolte-G function method.

SIFIT was applied while conducting the microfracture by using the single probe on the testing tool, positioned at 6.5 ft above the midpoint of the straddle packer, to observe the pressure response during the injection cycles. This provided an interference test and the data from the observation probe was recorded for further analysis and interpretation.

Selected Testing Intervals

The open hole logs from this well were used to assist in selecting suitable depth intervals for the attempted SIFIT. The selection of the points is based on borehole quality, borehole image data, formation stress contrast, formation mechanical properties, and in situ stress conditions. Extensive breakouts compromise the sealing capacity of the inflatable elements against the formation, and highly rugose borehole walls can deteriorate the rubber during inflation and deform the elements.

It is crucial for optimum fracture containment and proper fracture propagation that the inflatable elements are positioned on layers with stress contrast compared to the isolated formation interval to avoid sleeve fracturing and early hydraulic communication between the fracture and the hydrostatic pressure.

Figure 5 shows the image log over the selected intervals with an indication of how the straddle packer is positioned. The injection area is enclosed between the packer elements.

The formation breakdown pressure and reopening pressures are observed on the gauge in the isolated volume at the point where the pressure stops increasing while pumping continues. The propagation time is then measured as the additional pumping time after breakdown/reopening occurs until the pump is stopped and pressure decline starts due to leakoff.

The fracture closure was identified by three different methods:

1. SQRT pressure decline analysis using the BHP vs.

Fig. 5 *Selected stations with an image log and open hole logs.*

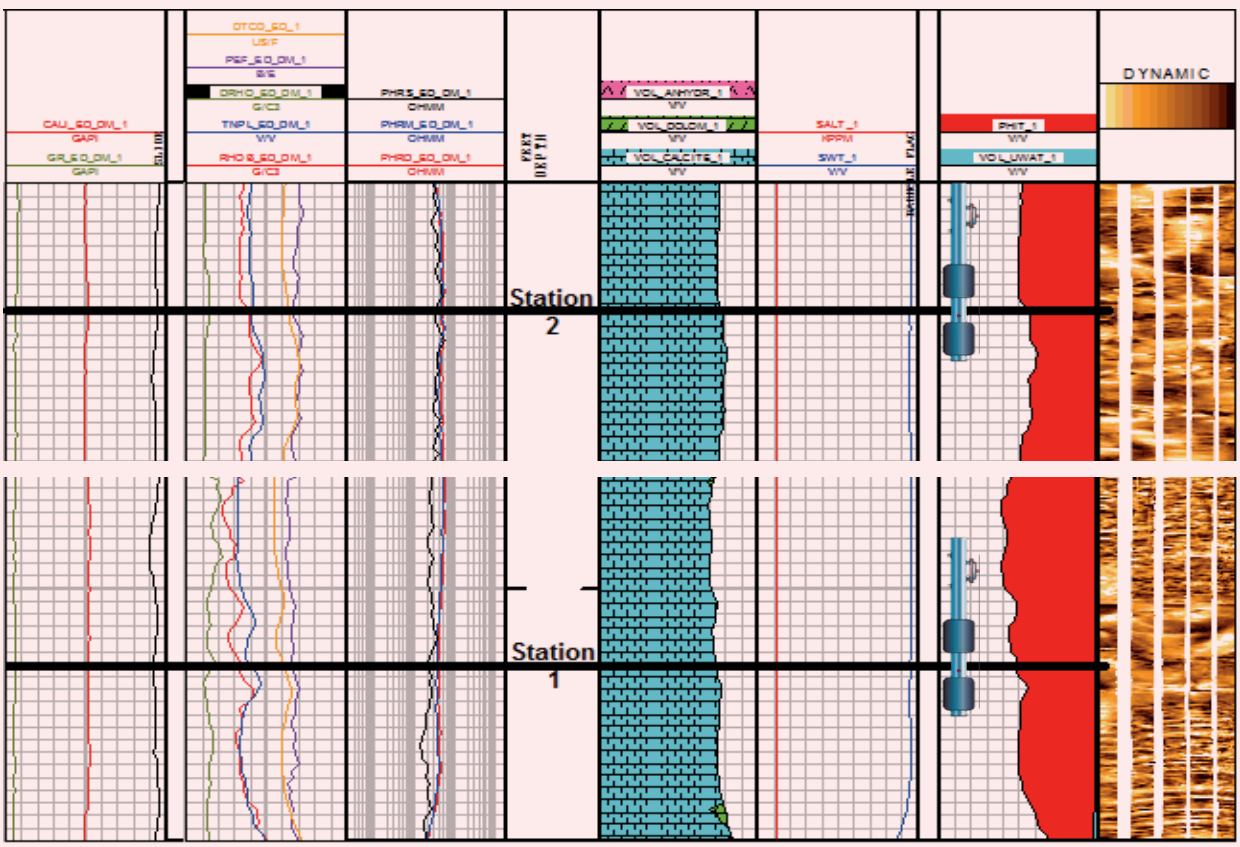

the square root of the shut-in time.

2. Log-Log pressure decline analysis using the pressure derivative of the delta pressure and delta time in the log-log plot.
3. G-function analysis by plotting the GdP/dG on a pressure vs. the G-time plot.

The first method consists of plotting the BHP vs. the square root of time and finding the change of the linear decreasing trend as the fracture closure. The second method looks for a change of slope of the pressure derivative d(logΔP)/d(logΔt) from a constant linear behavior around 0.5 into a decreasing trend (this change is associated to fracture closure). The final method looks for the change of behavior in the GdP/dG curve, from a linear increasing to a decreasing trend.

The analysis for each microfracture station is described in more detail in the following sections.

First Station Analysis

Figure 6 shows the entire microfracture sequence, where the BHP of the isolated interval and the absolute pressure inside the packers are denoted in blue and pink, respectively. The flow rate is presented with brown line (cc/s) while the accumulative displaced volume is in green (liters).

The straddle packers are inflated in approximately 20 minutes. The elements are recharged until they squared off and pressure is stabilized. After this, the observation probe (OP) is extended and a drawdown is performed to set the OP at formation pressure. The hydrostatic pressure is then recorded. Two packer integrity tests are done to confirm the seal prior to attempting formation breakdown. This is done by injecting with the pump up to 900 psi to 1,000 psi above hydrostatic pressure.

The formation breakdown is observed at P_frac on the gauge, which represents the absolute pressure in the interval. This is done by applying ~1,500 psi of differential pressure across the packers. The fracture is propagated for approximately 10 minutes after formation breakdown. After this, the pump is stopped to allow fracture closure via natural leakoff.

When closure pressure is detected via one of the three methods mentioned earlier, another pumping injection cycle is started to reopen the fracture. The fracture reopened at P_reop and the fracture is propagated for 12 minutes. The higher reopening pressure indicates a "ductile" reopening, which is not common, but possible, especially in carbonate. The build up of fracture propagation pressure indicates an increased stiffness as a function of ductility during propagation. At the end of this cycle, the pump is stopped to allow pressure bleed off and fracture closure via natural leakoff.

Last, the fracture is reopened one more time with relatively lower pressure and propagation of 10 minutes. During this third reopening/propagation cycle, the pressure increased indicating higher stiffness. Throughout all three cycles (breakdown + 2 reopening cycles) the cumulative displaced volume is recorded (green curve).

The main purpose of repeating stress leakoff cycles is to ensure proper induced fracture propagation to reach far field stress with minimum near wellbore stresses (hoop stresses) similar to what was noticed in the Pc difference between the first cycle and the consecutive two cycles. This shows in the pressure history match

Fig. 6 *The SIFIT sequence at Station 1.*

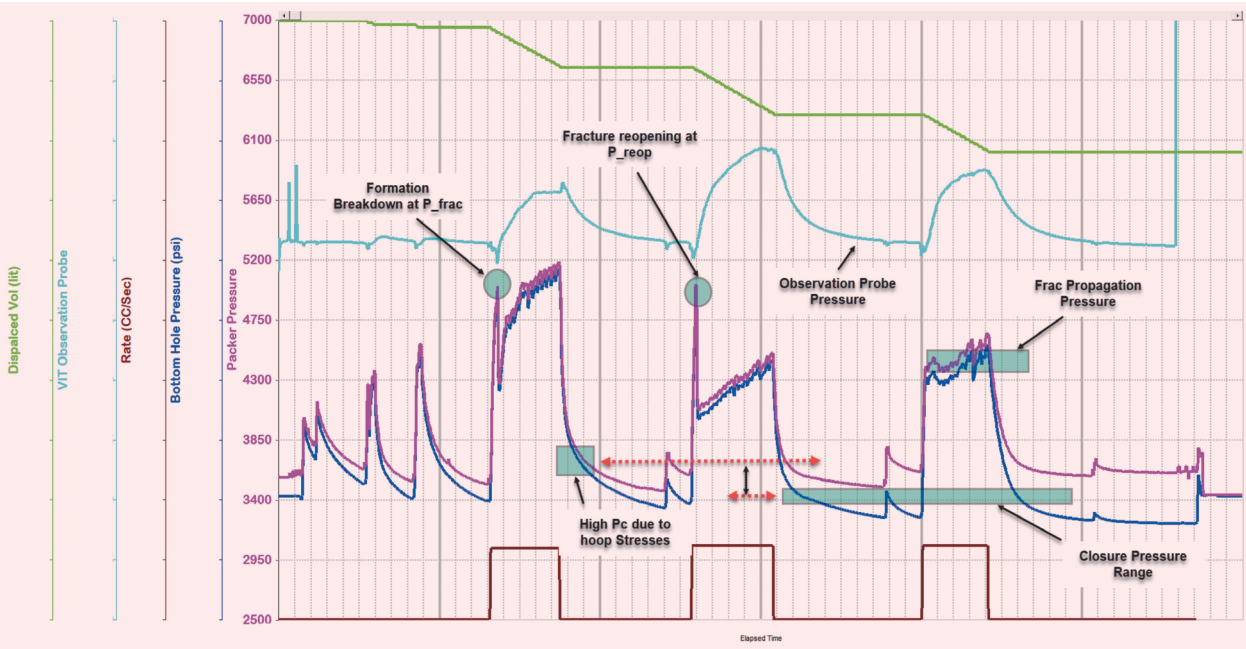

plot deviating from the model fit.

The vertical interference, due to the injection cycles, is recorded in the OP, Fig. 6, and the modeled pressure history match is illustrated in Fig. 7. At this station the test was concluded after the final microfracture reopening cycle. The data from the OP was mainly used to provide confirmation of the vertical communication through the formation.

An image log is run pre- and post-SIFIT to capture the aperture and orientation of the fracture. Figure 8 shows the pre-image on the left and the post-image on the right. Despite the evidence of fracture initiation and reopening, the image showed lower resolution across the zone of interest due to borehole condition deterioration and multiple wiper trips post-fracture and prior to the image log.

Each of the natural leakoff pressure decline curves was analyzed for closure pressure as will be described later. Figures 9 and 10 shows the charts of the final analyzed decline curve.

Second Station Analysis

The entire SIFIT sequence is illustrated in Fig. 11, where the BHP of the isolated interval and the absolute pressure inside the packers are denoted in blue and pink, respectively. The flow rate is presented with a brown line (cc/s) while the cumulative displaced volume is in green (liters).

Almost the same sequence of events is followed as in the first SIFIT station. On the third and fourth cycles, there is a slight nonlinear response on the pressure curve as it increases to reopen the fracture. This might be due to one of two effects or mix of both: elasticity in the packer elements or naturally high ductility of carbonate causing ovalization to the packer elements as pressure increases to reopen the fracture and propagate afterwards; however, this does not affect the microfracture closure analysis.

Similar to the first test, the modeled pressure history, Fig. 12, was utilized for each of the natural leakoff pressure decline curves analyzed for closure pressure, Figs. 13 and 14.

An image log was run pre- and post-SIFIT to analyze the aperture and orientation of the fracture. Figure 15 shows the pre-image on the left and the post-image on the right.

The interference of the injection pressure was also recorded at the observation probe, as indicated in Fig. 16.

There are three concepts to compare for validation of the SIFIT technique:

1. Traditional VIT in adjacent well across the same formation (field data).
2. VIT performed by pump out post-microfracture.
3. Analysis of the OP data during fracture cycles (SIFIT).

Analysis of SIFIT is conducted using data of Station 2 to determine horizontal and vertical permeability (k_{xy} and k_z) post-microfracture and investigate the effect of the induced microfracture on a standard pump out and interference test.

Fig. 7 *The pressure history plot and model match at Station 1.*

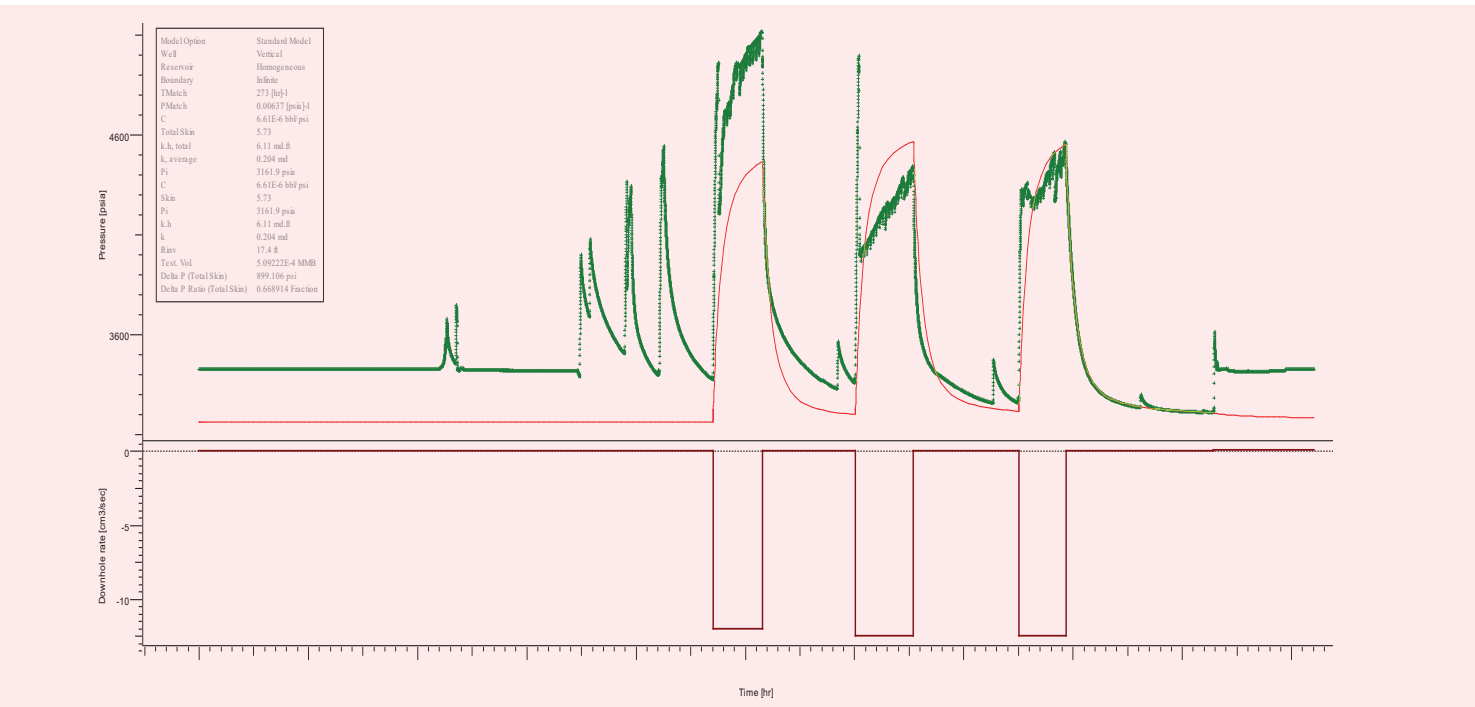

Fig. 8 *The image data pre- and post-SIFIT across Station 1.*

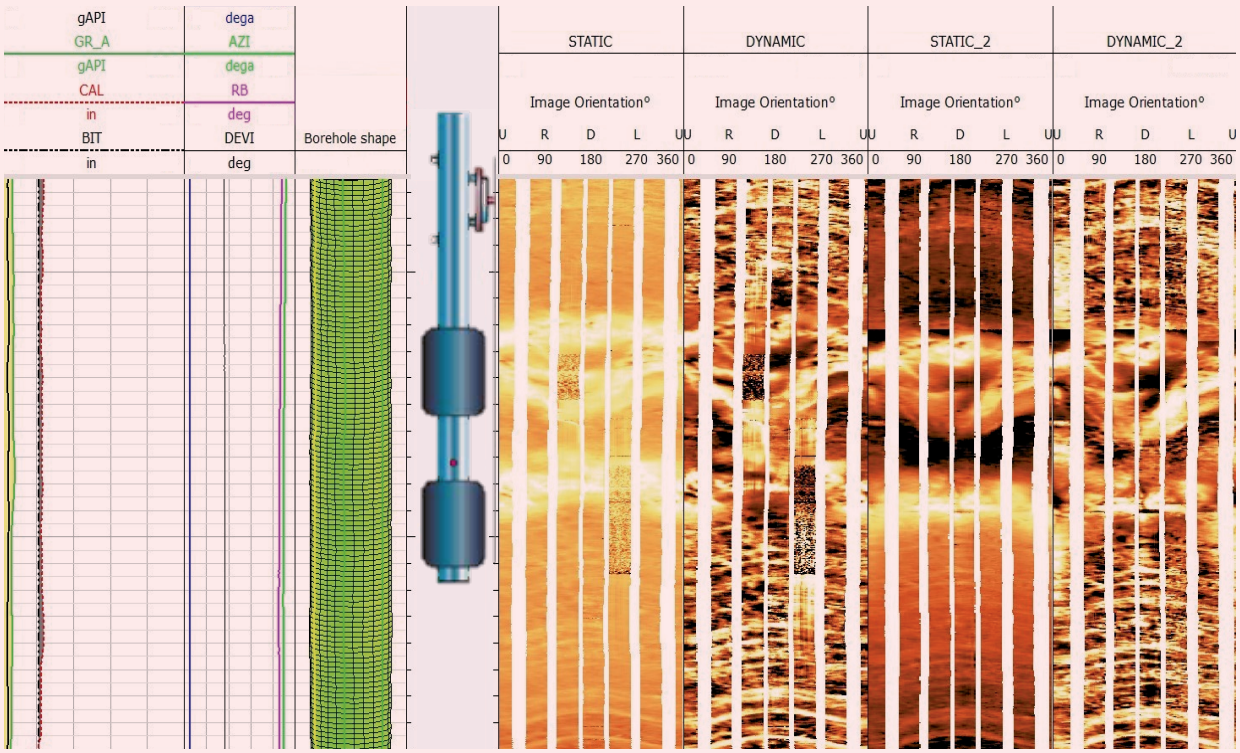

Fig. 9 *The log-log pressure derivative plot.*

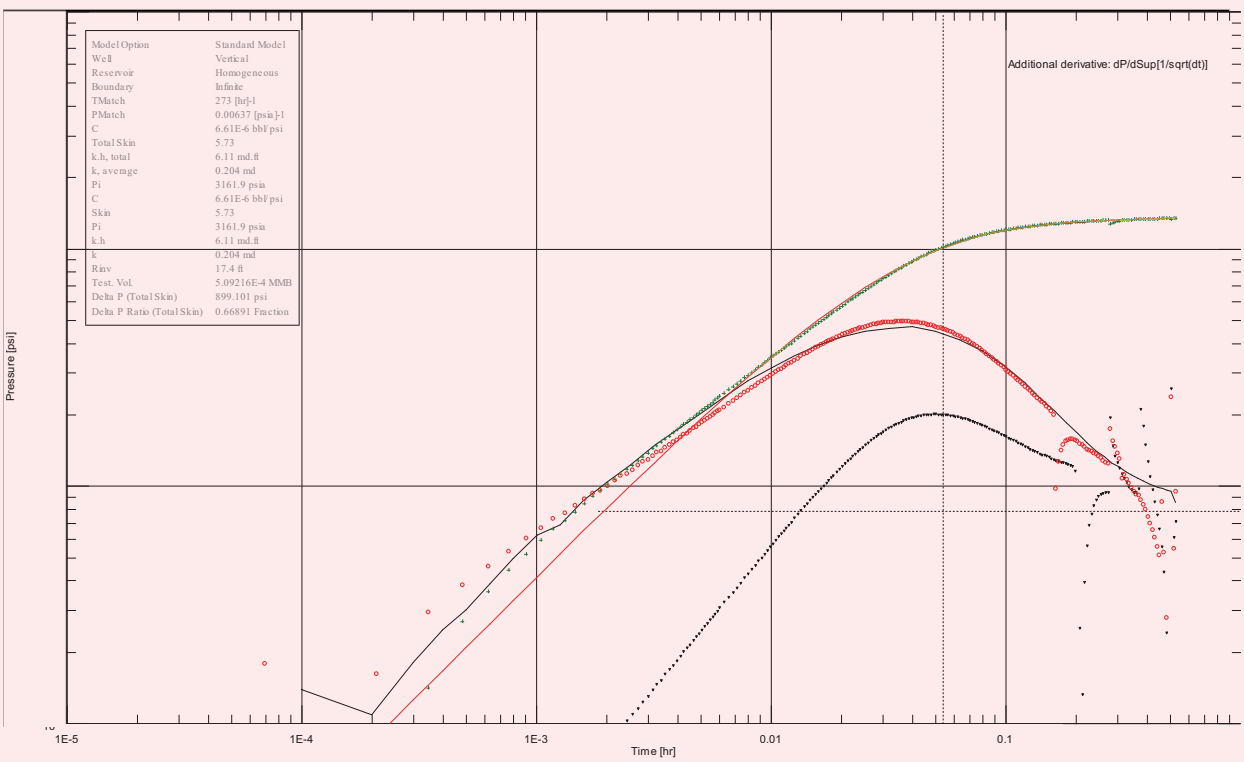

Fig. 10 *The square root function.*

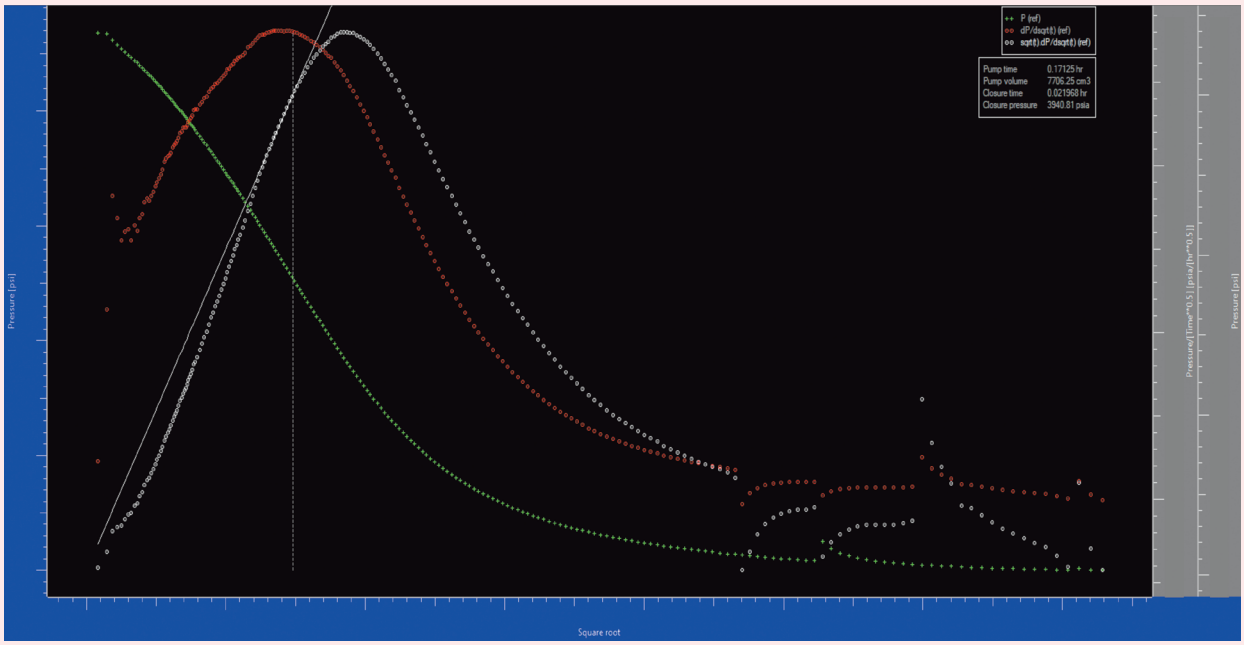

Fig. 11 *The SIFIT sequence at Station 2.*

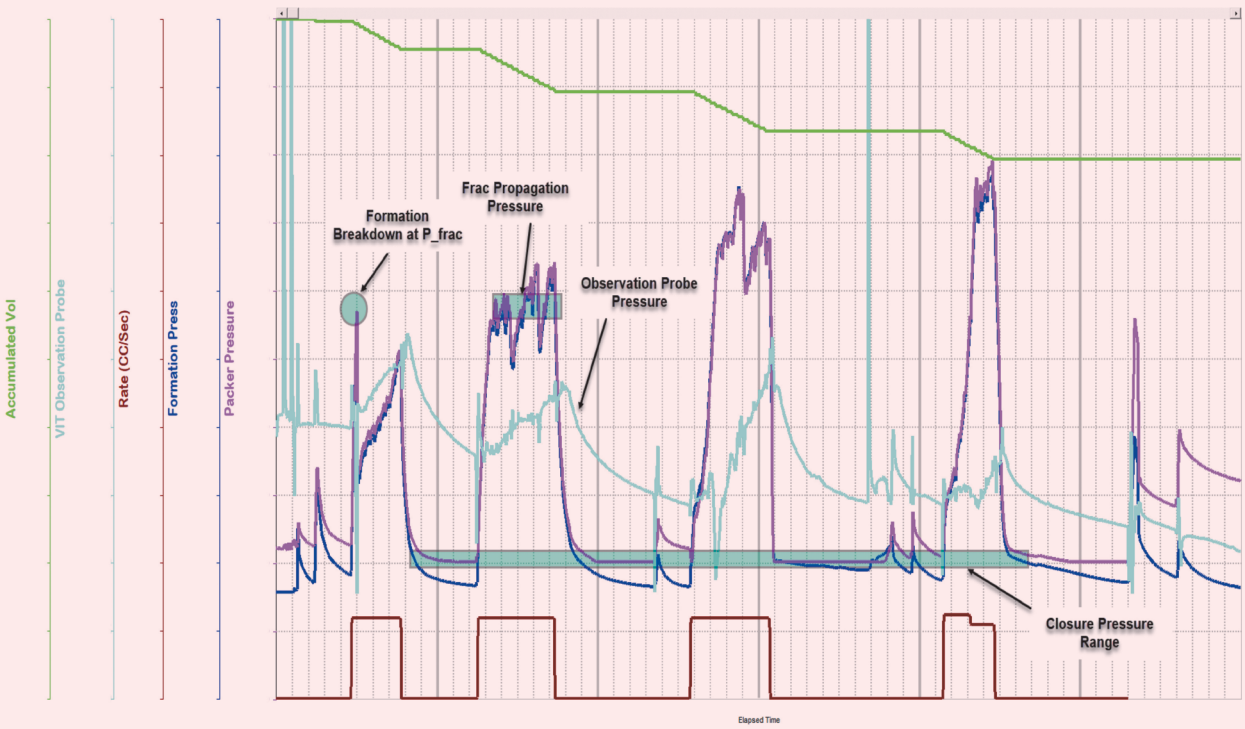

Fig. 12 *The modeled pressure history plot and the model match at Station 2.*

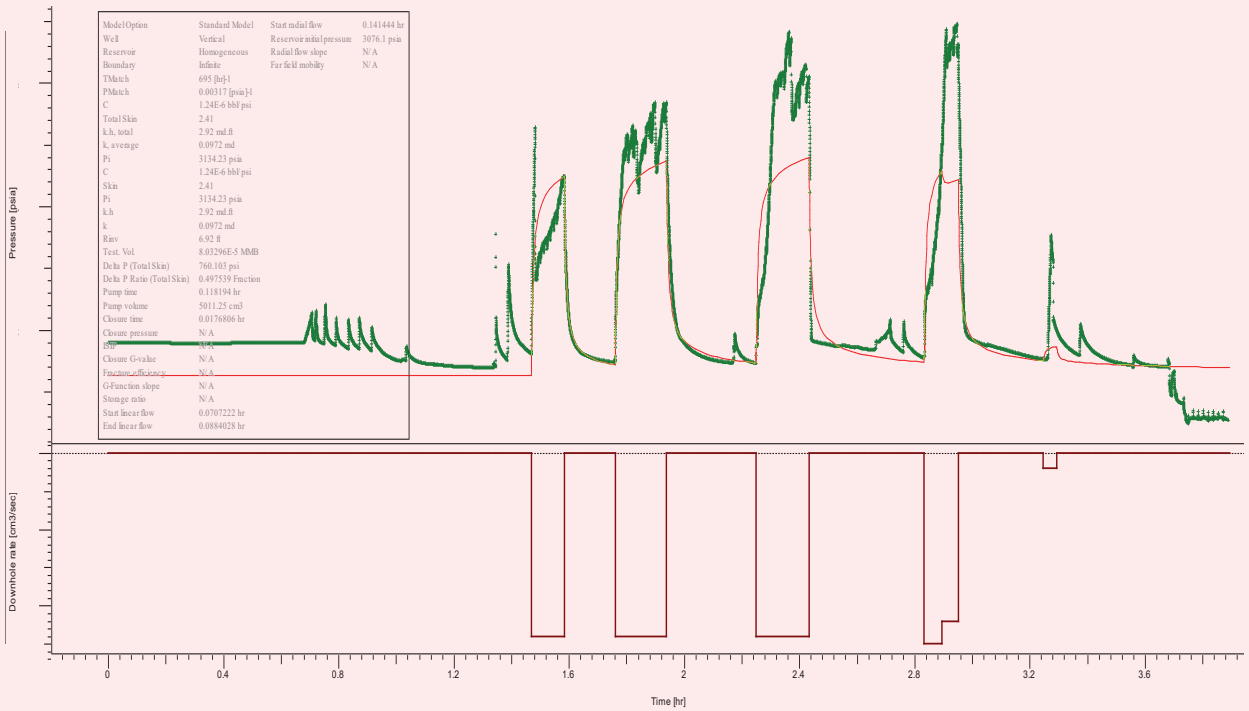

Fig. 13 *The square root function at Station 2.*

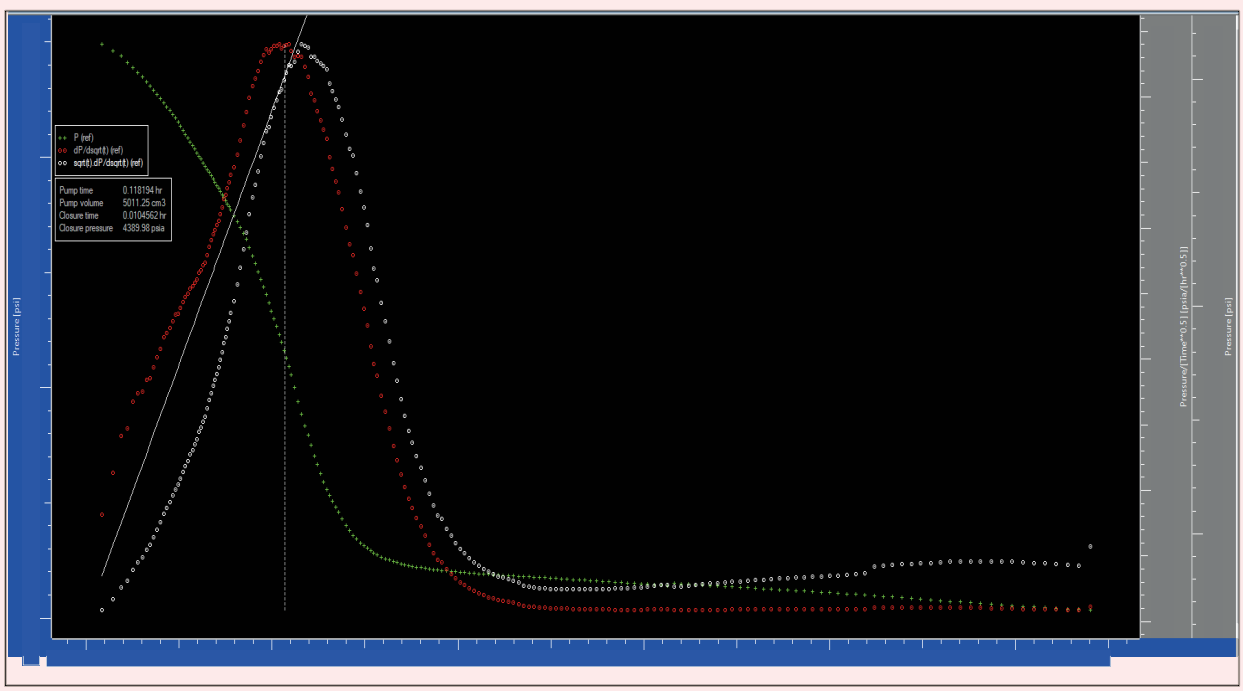

Fig. 14 *The G-Function at Station 2.*

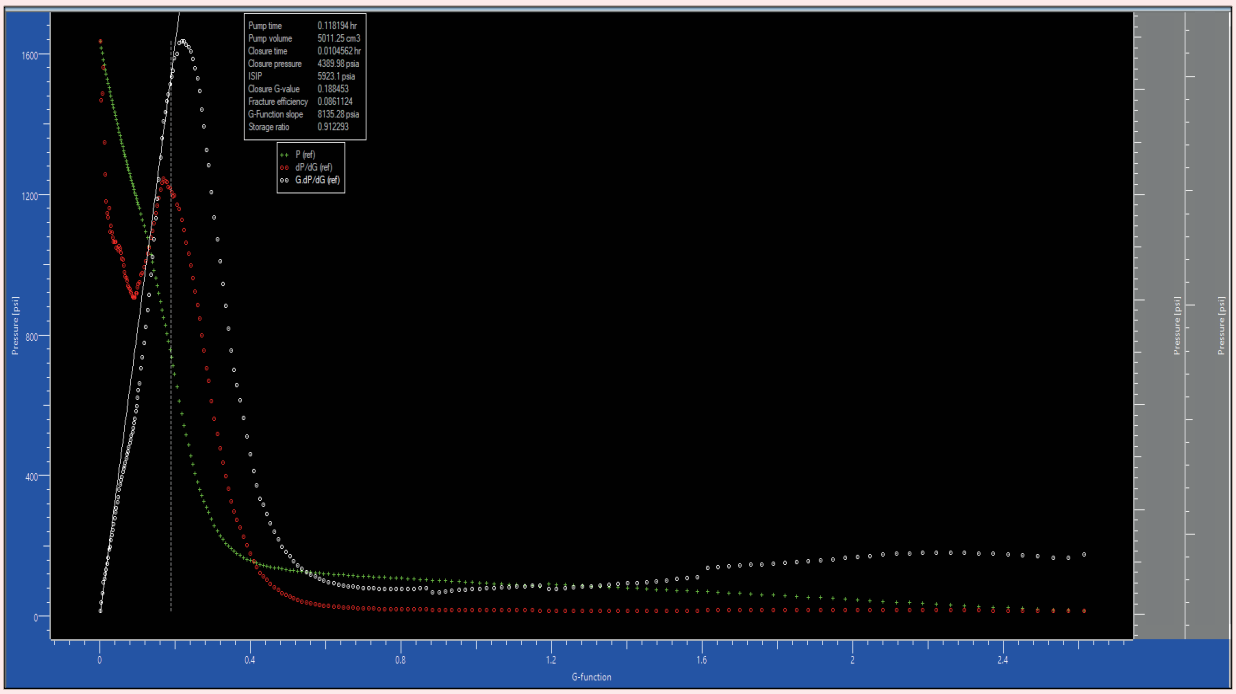

Fig. 15 *The image data pre- and post-SIFIT across Station 2.*

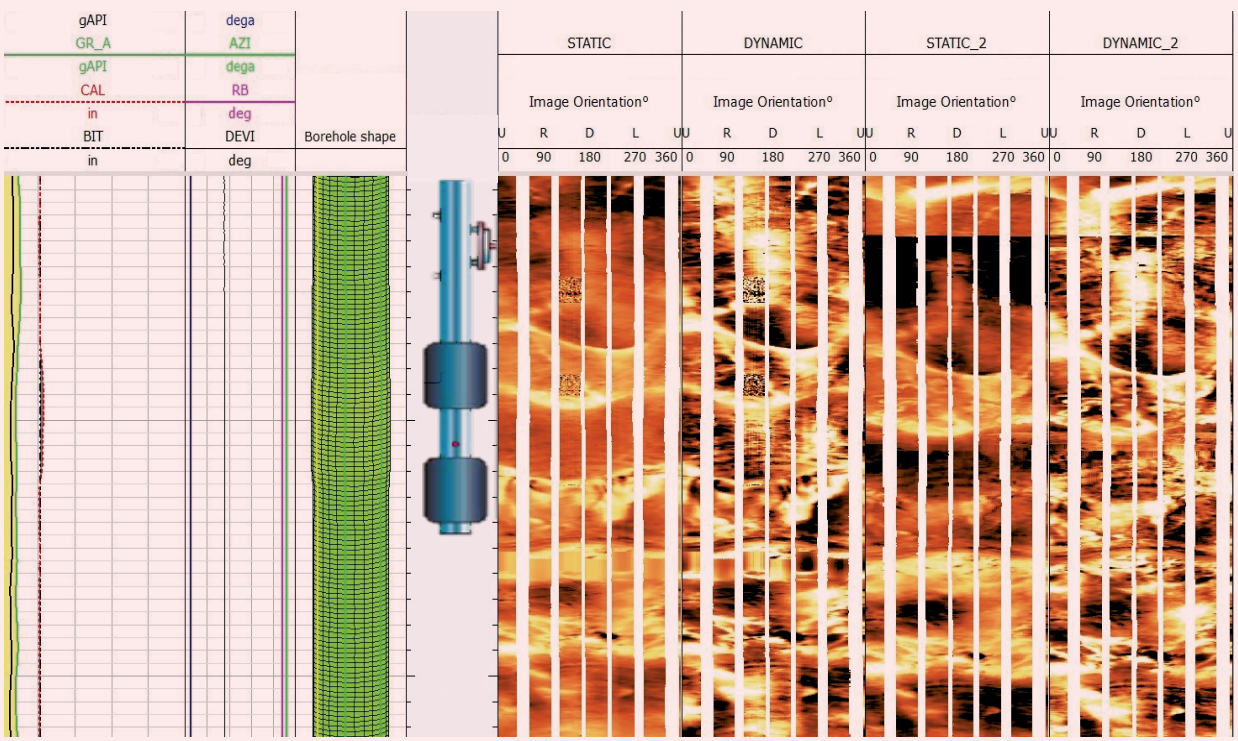

Fig. 16 *The observation probe data at Station 2.*

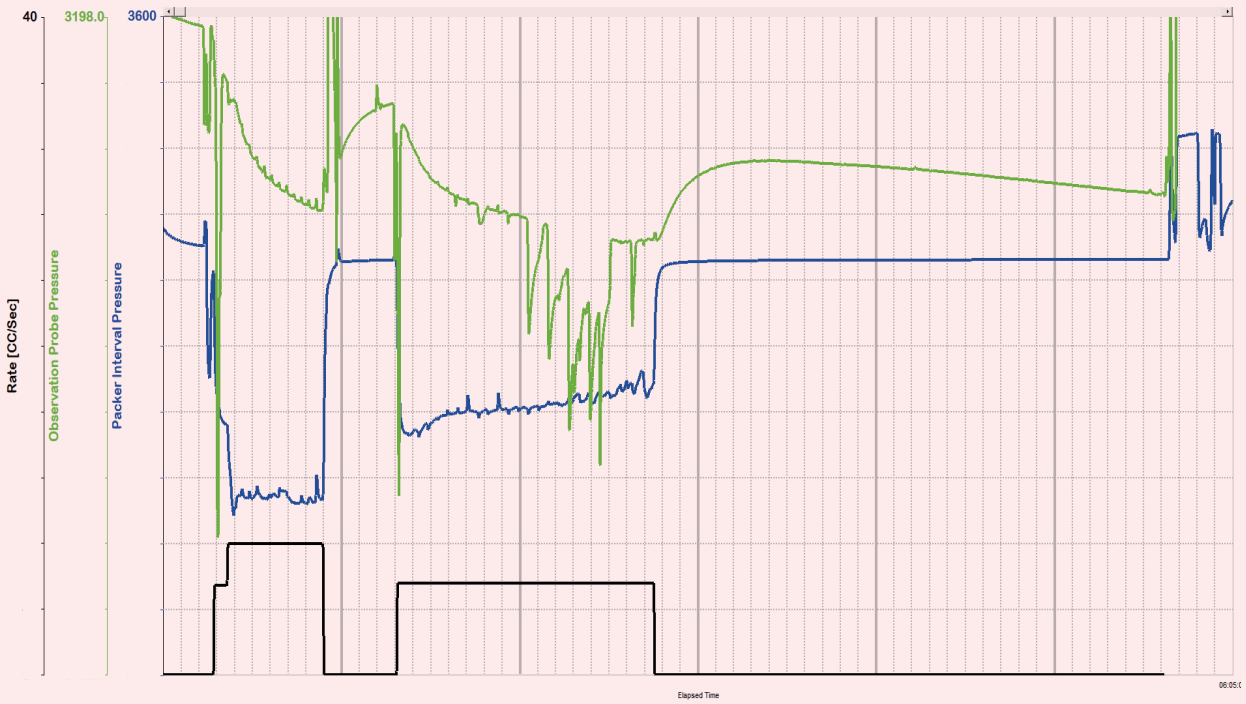

The pressure of the OP is high — ~10 psia to 12 psia — above formation pressure indicating supercharging prior to the microfracture test. The OP pressure starts to decrease during the microfracture injection period since more fractures are connected and more reservoir volume is connected to the wellbore. As a result, the high pressure at the OP starts to decrease slowly. The OP pressure responds exactly during the injection and falloff periods, indicating that it is in communication with the injection pressure via the formation layers.

Interpretation Results

A homogeneous model was used for the interpretation with no significant layering within the 60 ft vertical boundaries of the reservoir zone.

Figure 17 shows the final match on the log-log derivative plot, while Fig. 18 shows the pressure history match. The straddle packer pressure and derivative raw data are shown in blue (triangle and square points) and the matched curve data is in red. The OP pressure and derivative raw data are shown in green (triangle and square points) and the matched curve data is in green.

The match on the source pressure data is excellent. The OP data cannot be matched as well, due to the supercharging as explained earlier. The early time OP pressure data is matched to calculate the vertical permeability correctly.

This solution does not assume radial flow but rather a shift in the spherical flow due to the test being closer to the upper boundary. The radial flow would be reached after seven hours of buildup based on the calculated k_z from the OP pressure data[4].

The model matches properly the OP data, especially toward the end of the SIFIT cycles (post-fracture). This provides a high fidelity on the analysis results of the VIT pre- and post-fracture for further interpretation

Fig. 17 *The final log-log derivative match plot of the VIT data.*

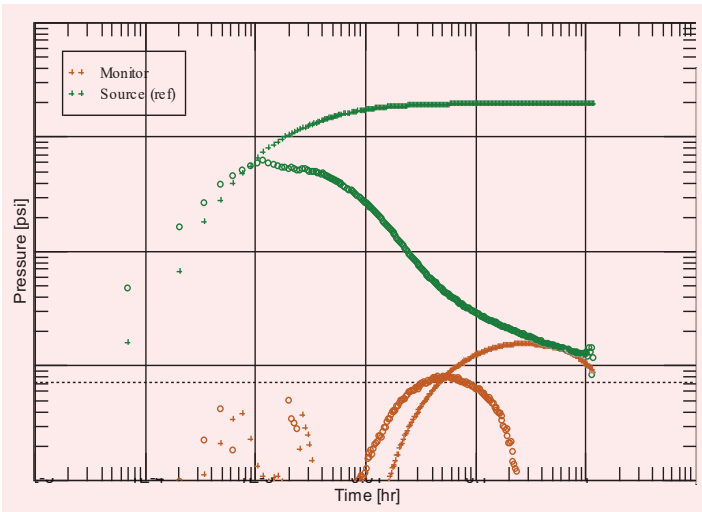

Fig. 18 *The history match for the OP pressure at Station 2.*

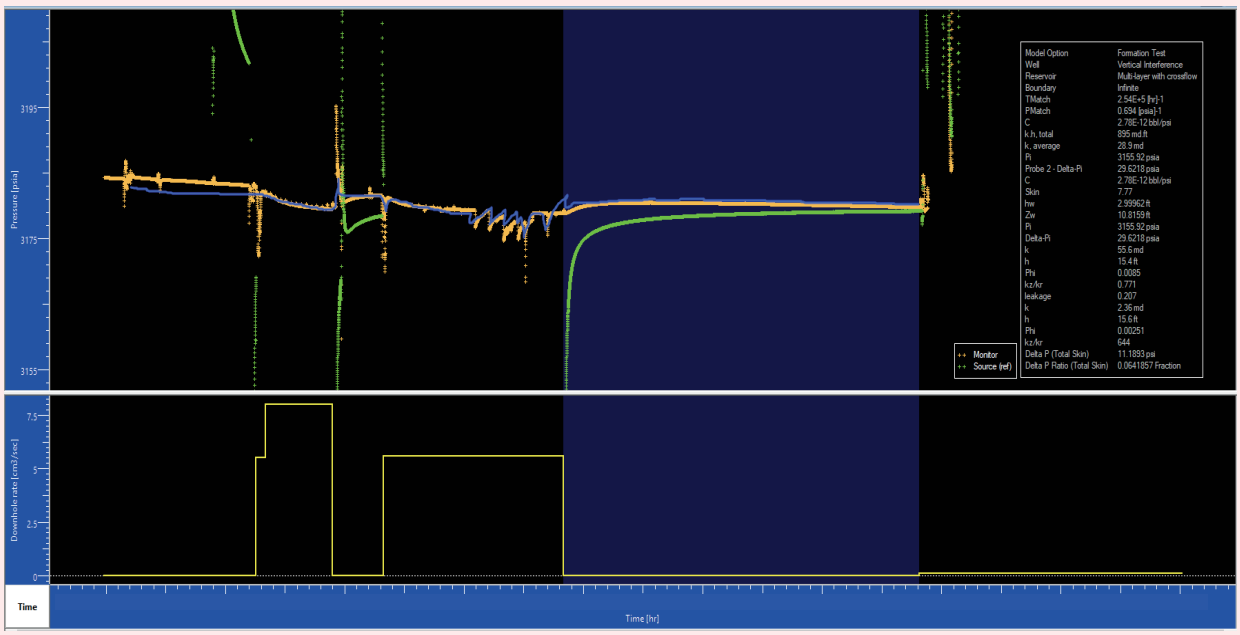

and future work using this technique. The objective then would be to build a model that uses OP data during the SIFIT injection/falloff cycles to derive more realistic reservoir properties that mimic actual reservoir fluid dynamics throughout the life cycle of the studied field — enhanced recovery stages.

Conclusions

When producing fluids from a reservoir, it can be helpful to know certain properties of the geologic formation. Several tests to determine geomechanical properties can be performed after drilling the target reservoirs. Such tests can include a VIT and an injection falloff test.

The VIT normally involves pumping fluid out of the geologic formation and into the wellbore while monitoring a pressure signal with a pressure sensor. An injection falloff test involves pumping a small volume of fluid into the geologic formation until a fracture is initiated, followed by natural pressure falloff due to fracture closure. Combining both techniques in one go improves safety, quality, and efficiency of this complex operation. The results show improvement over standard application, especially in tight reservoirs with supercharging effect.

Acknowledgments

This article was previously presented at the International Petroleum Technology Conference, Dhahran, Saudi Arabia, February 13-15, 2020.

References

1. Larbi Zeghlache, M. and Proett, M.: "Simultaneous Interference Testing and Fracturing Testing," U.S. Patent No. 10,704,369, July 2020.
2. Al-Harthi, M.A., Pardo, C., Kilany, K., Al Otaibi, M., et al.: "Comprehensive Reservoir Vertical Interference Testing to Optimize Horizontal Well Placement Strategy in a Giant Carbonate Field," SPE paper 178013, presented at the SPE Saudi Arabia Section Annual Technical Symposium and Exhibition, al-Khobar, Saudi Arabia, April 21-23, 2015.
3. Kuhlman, R.D.: "Microfrac Tests Optimize Frac Jobs," *Oil & Gas Journal*, January 1990.
4. Sheng, J.J.: "A New Technique to Determine Horizontal and Vertical Permeabilities from the Time-Delayed Response of a Vertical Interference Test," *Transport in Porous Media*, Vol. 77, April 2009, pp. 507-527.

About the Authors

Mohamed Larbi Zeghlache

M.S. in Reservoir Engineering and Field Development, French Petroleum Institute

Mohamed Larbi Zeghlache is a Senior Petrophysicist and the inventor of SIFIT technique. Mohamed is the well integrity subject matter expert working with the Production Technology Team of Saudi Aramco's Exploration and Petroleum Engineering Center – Advanced Research Center (EXPEC ARC). He previously led the well integrity logging team in the Reservoir Description and Simulation Department.

Since joining Saudi Aramco, Mohamed has been responsible for formation evaluation and well placement in Ghawar carbonates and Central Arabia clastics.

He has 18 years of experience in the oil and gas industry, and previously worked with both Schlumberger and Halliburton where he held various positions, including Wireline Field Engineer, Log Analyst, Business Development, and Technical Advisor.

Mohamed is the author of several Society of Petroleum Engineers (SPE) publications, and patents.

He received his M.S. degree in Reservoir Engineering and Field Development from the French Petroleum Institute (IFP), Paris, France.

Mustapha Berkane

B.S. in Geophysics, Algerian Petroleum Institute

Mustapha Berkane is the formation testing and sampling subject matter expert with Saudi Aramco's Reservoir Description and Simulation Department, focusing on wireline and logging while drilling operations. Mustapha has more than 25 years of experience in oil and gas explorations as a Geophysicist. He started his working carrier in January 1995 as a Wireline Engineer in North Africa with a focus on remote location followed by several assignments in North Sea installations in the U.K., Norway, and then the Middle East.

Following that, Mustapha worked in several management and technical support assignments before joining Saudi Aramco as a Petrophysicist in 2014.

In 1994, he received his B.S. degree in Geophysics from the Algerian Petroleum Institute, Boumerdes, Algeria.

Wael Soliman

B.S. in Mechanical Engineering and Mechatronics, Helwan University

Wael Soliman is Halliburton's Formation Evaluation and Reservoir Solutions Advisor in the Middle East and North Africa (MENA), and Asia Pacific regions. Wael joined Halliburton in 2000 and has held various operational and technical positions, including Open Hole and Cased Hole Wireline Operations Technical Advisor, Formation Testing and Sampling Champion in the MENA region, and Europe and Sub-Saharan Africa (ESSA) Senior Regional Wireline Technical Advisor handling deep-water ESSA projects.

For more than 15 years, he has been deeply involved in both wireline and logging while drilling formation testing and sampling technology innovation, advanced applications development, and their introduction on a global level.

Wael received his B.S. in Mechanical Engineering and Mechatronics from Helwan University, Cairo, Egypt.

Oil Field Chemicals Delivery and Slow-Release Using Nanoencapsulation

Dr. Nouf M. AlJabri and Dr. Yun Chang

Abstract /

A reservoir's condition is considered as a harsh environment for most oil field chemicals to remain stable and functional. The nanoencapsulation and slow-release technology may offer a possibility to deliver a chemical of interest to a selective target using smart nanocapsules despite the environmental conditions. Therefore, the encapsulation of the oil field chemicals, such as surfactants and acids, can be utilized to deliver these chemicals to deeper layers of a formation effectively, compared to the conventional production operations.

Therefore, these work objectives are: (1) developing cost-effective nanocarriers to deliver chemicals to deeper layers of formations compared to current production practices, and (2) synthesizing nanocarriers with improved stability and slow-release of enhanced oil recovery/improved oil recovery (EOR/IOR) chemicals over time at the reservoir's temperature. We have synthesized several slow-release templates: (1) surfactant nano-salt complex for EOR, (2) surfactant nanocapsules (liposome) for EOR, and (3) acid nanocapsules for IOR. Different synthesis approaches were explored to synthesize these nanoencapsulation platforms, such as chemical precipitation and polymerization.

Scanning electron microscopy, optical microscopy, dynamic light scattering, pH, and surfactant electrodes were used to characterize the nanocapsules, and surfactant nanoscale dispersion. Furthermore, the stability and slow-release of capsules and dispersions under reservoir conditions were evaluated by incubating and monitoring the samples in an oven at 95 °C to 120 °C for several days.

The findings showed that the liposomes contained 11 wt% of petroleum sulfonates while the average particle size was 80 nm. Notably, liposomes and acid nanocapsules exhibited a gradual release for over 60 hours and 144 hours, respectively. The results demonstrate the possibility of synthesizing acid and surfactant nanocapsules with a slow-release property for EOR/IOR operations. Subsequently, the slow-release technology may bring new potentials to conventional oil production jobs.

Introduction

Microencapsulation and nanoencapsulation technologies have become popular in many fields, such as food engineering[1, 2], cosmetics[3], and pharmaceuticals[4] because of their efficiency in designing smart carriers. Both encapsulation techniques, despite the capsules' size, allow one to encapsulate the material of interest, protect it from the environment and deliver it to the targeted sites. The encapsulated material can vary from gases to liquids to solids based on the desired application. Figure 1 shows three different structures of nanocarriers.

The oil and gas industry also can benefit from this technology, as a reservoir's environment is relatively harsh for most oil field chemicals to remain stable and functional. The encapsulation of the oil field chemicals in stable shells can offer many advantages, such as: (1) protecting the chemicals from the reservoir environment as well as maintaining their functionality, (2) deliver these chemicals to deep layers in the formations, and (3) utilize the reservoir atmosphere to trigger the slow-release of the capsules.

Indeed, some criteria must be fulfilled to synthesize smart carriers for reservoir applications, such as the size, responsiveness, and stability of the capsules. The carrier's size must be ≤ 200 nm — ideally ≤ 80 nm — to allow the carrier's free transportation through the reservoir's rocks. Moreover, these carriers have to exhibit improved stability in the reservoir environment.

We believe that the implementation of the targeted and slow-release technology using nanocapsules and microcapsules to deliver the oil field chemicals can substantially reduce the cost of the enhanced/improved oil recovery (EOR/IOR) conventional methods via reducing the amount of chemicals. For example, surfactant encapsulation for EOR and acid encapsulation for well stimulation are two potential areas where chemical encapsulation may offer several advantages over the conventional methods.

The reason for choosing surfactant encapsulation is that they are mostly used in oil fields to boost oil recovery beyond the waterflood baseline. Over a decade, they showed a substantial impact to improve the residual oil

Fig. 1 *Different types of nanocarriers: (a) single-core nanocapsule, (b) multiple core nanocapsule, and (c) liposomes/lipid-based nanocapsules.*

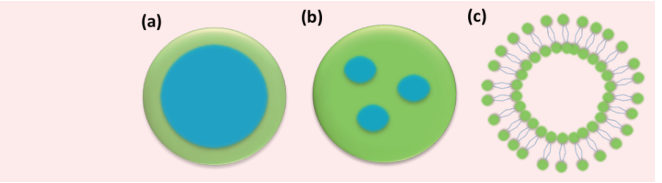

recovery either by reducing the interfacial tension (IFT) between oil and water, or by altering the reservoir's rock wettability[5, 6]. Some surfactants have succeeded in reducing the IFT values down to the ultra-low region of 0.001 dyne/cm at low concentrations, 1 ppm to 10 ppm[7]. Moreover, many parameters can limit the surfactant flood effectiveness, such as: (a) high viscosity, (b) high retention/adsorption near the wellbore area, and (c) low stability at high temperatures of ≥ 80 °C, as well as high salinity of ≥ 25,000 ppm.

Specifically, the petroleum sulfonate surfactants are the most abundant and inexpensive surfactants that can enhance oil recovery. Nevertheless, this class of surfactant is unstable in reservoir conditions and tends to react with the naturally existing cations in the reservoir to form a stable complex. As a result, the surfactant flood performance will be jeopardized.

This complex concept has inspired us to mimic the complex formation process to make a surfactant delivery system. This can occur by reacting petroleum sulfonate surfactants with metal cations at controlled flow rates to form the surfactant nano-salt complex. This type of engineered complex has limited solubility in water and showed excellent stability in the reservoir conditions. Notably, these surfactant nano-salt complexes have the ability to release the surfactant in the presence of the residual oil. The immobilized oil in the reservoir would serve as a trigger to gradually release the surfactant from the complex. Subsequently, surfactants can be delivered selectively to where they are most needed in the reservoirs via an effecient and economical process. Therefore, the performance of the surfactant flooding can be improved.

The acids' encapsulation and slow-release is another potential area to explore the encapsulation technology's impact on improving the productivity of the long laterals to maximize the recovery. This is because the acid uniform distribution, especially in the long laterals, is considered an area of improvement due to the reservoir's heterogeneity and the wells' complex geometries[8]. In conventional operations, the rates of acid injection and acid-rock reaction are important factors to control the wormhole dimensions.

Therefore, the inappropriate controlling of these factors either may increase the formation of permeability or cause formation damage[9]. We envision that the acid encapsulation and its slow-release will allow controlling wormhole dimensions and improving the current practices of filter cake removal. The real value of acid encapsulation is to produce and release the encapsulated acid in situ on demand. Both the reservoir's temperature and the formation water will trigger the release in the formation to control wormhole dimensions and successfully stimulate the well.

In this work, we explored the slow-release technology techniques for EOR/IOR. We have synthesized two surfactant encapsulations and slow-release systems: (1) liposomes, and (2) surfactant nano-salt complex. Furthermore, we encapsulated an acid precursor, which can be converted into acid in situ using the reservoir conditions. The synthesis, characterization, and slow-release phenomena of the synthesized nanocapsules were analyzed and reported.

Experimental Details

Both sulfonated surfactants, EOR 2095 and MLA 3071, were obtained from Chemtura and used without further treatment. The HPT-1 polymer was obtained from Halliburton. The aluminum nitrate nonahydrate ($Al(NO_3)_3.9H_2O$) was purchased from Aldrich Chemicals. The surfactant nano-salt complex was prepared by mixing 100 mL of 1.0 wt% surfactant solution and various amounts of HPT-1 in a reactor. An $Al(NO_3)_3.9H_2O$ solution (1.0 to 10.0 mL) was pumped at a fixed flow rate into the reactor with vigorous stirring.

Some variables, such as an excess addition of anions, temperature, and reactants addition rates were used to control the particle size[10]. Moreover, the dispersion's stability was controlled by the HPT-1 amount[11]. The metal's salt solubility in water was analyzed by measuring the free metal ions and surfactant concentrations in the dispersions using a titrator installed with ions and surfactant electrodes, respectively.

Liposomes (Lipid-based nanocapsules) were synthesized to encapsulate and slow-release of the petroleum sulfonate surfactants. This can be approached by dissolving a known lipid formula in 20.0 mL of chloroform, which was evaporated after dissolving the lipid using rotavapor to form a dried lipid film. Next, the film was rehydrated with a mixture of alkylbenzene sulfonate and olefin sulfonate. As the last step, the produced liposome sizes were homogenized to form uniform nanosized capsules[12, 13].

Both interfacial and in situ polymerization techniques were used to produce acid nanocapsules[5]. The triacetin that represents the oil phase was encapsulated inside a polymeric shell. The shell's monomer (A) was dissolved in triacetin, while the shell's monomer (B) was dispersed in water. Later, the oil phase that contained monomer (A) was added to the aqueous phase that contained that second monomer in the presence of an inert polymer to control the capsule's dispersions, to start the polymerization.

In this technique, both oil and water-soluble monomers reacted at the oil-water interface to form a polymeric shell that encapsulated the acid. The capsule's content was measured using the formula:

- Encapsulation efficiency% =

$$\left(\frac{Total\ amount\ of\ surfactant\ (or\ acid) - total\ amount\ of\ surfactant\ detcted}{Total\ amount\ of\ surfactant}\right) * 100$$

The stability of the surfactant loaded capsules in reservoir conditions was tested by incubating the samples in an oven at 120 °C. The slow-release profile of the nanocapsules was produced by using an automatic titrator (Metrohm Inc.) using a surfactant electrode to monitor the concentration of the surfactant's release. The acid nanocapsules' release was monitored by a pH meter over an extended time at 95 °C. The pH value, in this case, is a reflection of triacetin hydrolysis and acetic acid dissociation.

Results and Discussion

Surfactant Nano-Salt Complex

The surfactant nano-salt complex (Al-EOR2095) was synthesized using the surfactant salt precipitation method to produce a water insoluble surfactant encapsulating system. Figures 2a and 2b show the transmission electron microscope (TEM) and the particle's distribution results of the synthesized Al-EOR2095 nano-salt complex. Notably, the Al-EOR2095 nano-salt complex's average size was in the acceptable range of 87 nm.

As we emphasized earlier, the size of the nanocapsules are crucial to maximizing the efficiency of using them as carriers for EOR applications. The nanocapsules' size can be controlled via adjusting some synthesis parameters such as reactant flow rate, HPT-1 concentration, Al substrate's volume, and EOR2095 concentrations. The optimization of these variables is essential to control the dispersion's diameter.

The Al-EOR2095 complex solubility (pKsp) is found to be in the order of 10. The Ksp of the Al-EOR2095 salt was measured to be 1.9 x 10^{-14}. The amount of $Al(NO_3)_3.9H_2O$, which was added to the EOR2095 solution, was used to modify and estimate the free EOR2095 surfactant concentrations. The results showed that free EOR2095 concentrations were reduced significantly after the formation of the Al-EOR2095 nano-salt complex, indicating that the complex formation is ongoing.

Figure 2c shows the presence of the free EOR2095 surfactant concentration vs. the Al cations' volumes. Notably, the data indicated that the free EOR2095 concentration could be maintained if Al surfactant salt particles remained fixed.

Liposomes

A mixture of alkylbenzene sulfonate and olefin sulfonate were encapsulated in liposomes as described in the experimental section. The liposome capsules' average size was 80 nm, while the capsule's encapsulation efficiency was 11%. The liposome's homogenization was conducted using a rotator stator and microfluidizer, and both samples were imaged by optical microscopy after homogenization, Figs. 3a and 3b.

The results indicated that the use of a microfluidizer had generated nanosized capsules, which were not the case when the rotor stator was used. The stability of the formulated liposomes was evaluated by placing the liposome samples in an oven at 120 °C to test the nanocapsule's thermal stability in the reservoir's condition. Furthermore, the released surfactant concentration over time was monitored using a surfactant electrode to assess the liposomes' slow-release capability. Figure 3c

Fig. 2 *(a) Al-EOR2095 nano-salt complex TEM image, (b) size distribution, and (c) the aluminum cation solution impact on the complex formation.*

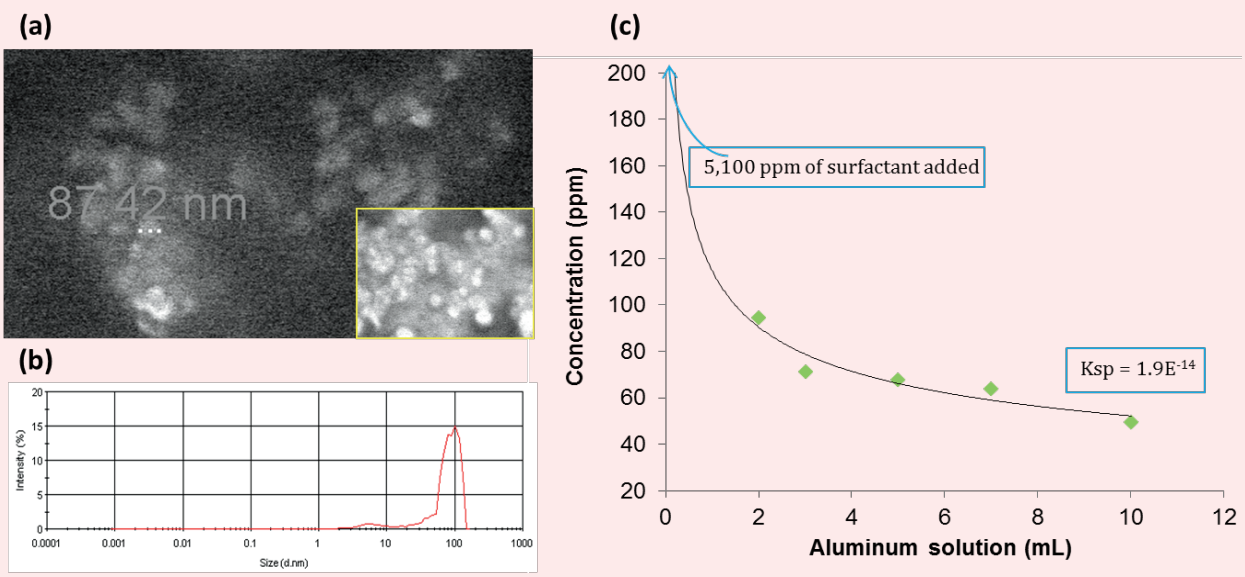

Fig. 3 *An optical microscope image of the liposomes: (a) post-homogenization using a rotator stator, (b) post-homogenization using a micro-fluidizer, and (c) the liposome's gradual release phenomena at 120 °C.*

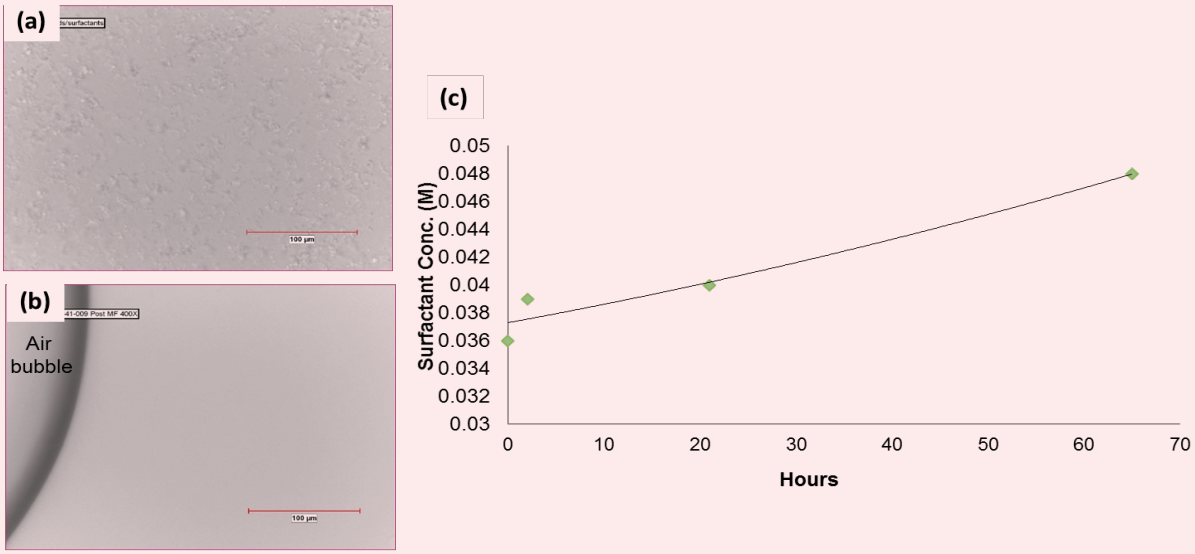

shows the liposome's gradual release profile over time.

The free surfactant concentration measurement was 0.036 M and gradually increased to 0.048 M over 60 hours. It should be noted that the initial free surfactant concentration measurements suggest that the encapsulation efficiency needs to be further improved. Moreover, the capsule's nanosizes can be homogenized using a low-energy microfluidizer to avoid the capsules breaking, and early release of the encapsulated surfactants.

Acid Nanocapsules

The triacetin was used as an acid precursor and was encapsulated using both interfacial and in situ polymerization methods for comparison purposes. The nanocapsules that were prepared using interfacial polymerization has a mean particle size of 200 nm while the acid encapsulation efficiency was 15 wt%, Fig. 4a. This capsule's size is relatively suitable for reservoir application, but the synthesis route has to be further modified to enhance the encapsulation

Fig. 4 *(a) SEM image of the acid loaded nanocapsules synthesized by the interfacial polymerization method, (b) SEM image of the acid nanocapsules synthesized by the in situ polymerization method, and (c) the acid nanocapsule's slow-release profile.*

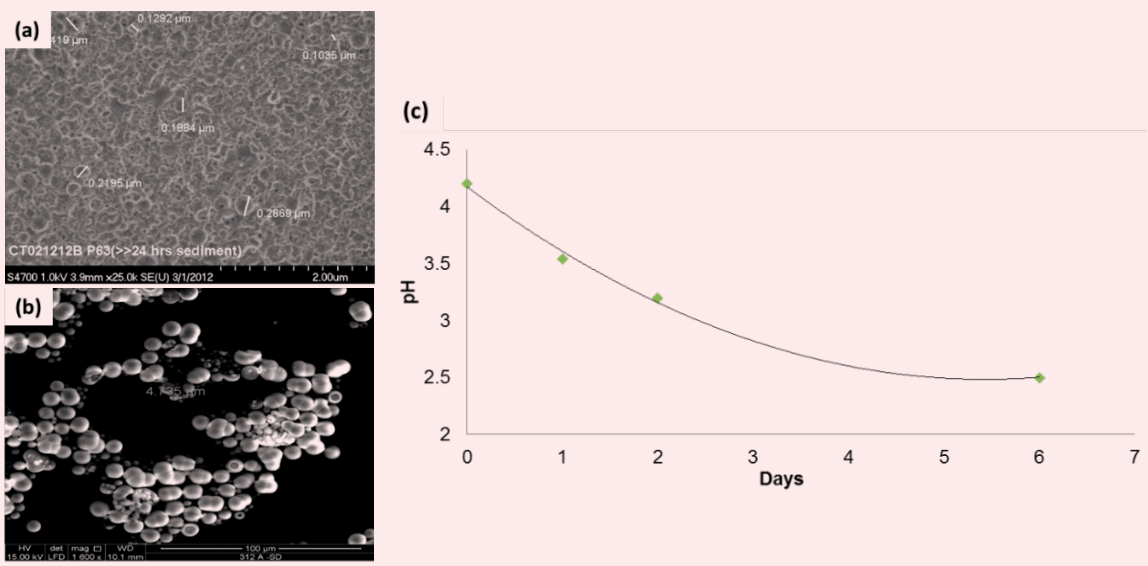

efficiency. On the other hand, the in situ polymerization produced larger particle sizes, with improved encapsulation efficiency.

The capsule's average particle size is 200 nm, while the encapsulation efficiency approached 400 wt%. Figure 4b shows the scanning electron microscope images of the acid nanocapsules. The acid nanocapsule samples were placed in an oven at 95 °C to monitor the capsule's gradual release over time. The hydrolysis of the triacetin in the reservoir conditions — to gradually release the acid in situ — is illustrated in these steps:

- Triacetin + H_2O → 3 C-C (=O)-OH
- CC (=O)-OH → CC (=O)-O^- + H^+ $K_a = 10^{-4.75}$
- $[H^+] = [CC (=O)-O^-] = (K_a * [CC (=O)-OH])^{\wedge 0.5}$
- $pH = -\log [H^+] = -0.5*(\log K_a + \log [CC (=O)-OH])$

The acid precursor has a first-order hydrolysis rate with a rate constant of 7.05×10^{-5}/sec. Therefore, more than 99% of the triacetin was converted to acetic acid in situ in 24 hours. Moreover, the release rate indicates that the capsules degrade slowly by the formed acid. The decrease in pH was monitored and indicated a gradual decrease in pH values from 4.3 to 2.6 over six days, Fig. 4c.

Conclusions

In summary, we demonstrated nanoencapsulation methodologies and slow-release technology for EOR/IOR reservoir applications. We showed the synthesis and characterization of two types of nanocapsules to deliver and slow-release commonly used oil field chemicals.

Surfactant responsive nanocapsules were prepared to serve as a surfactant carrier for EOR operations using the surfactant salt precipitation method, and the liposomes method. The PETRONATE® EOR2095 encapsulation efficiency in the liposome capsules was 11 wt% with the mean capsule size of 80 nm. Note that the size of the lipid-based nanocapsules is easier to control than the polymeric-based nanocapsules because of the shell flexibility. The liposomes' release was characterized by titration using a surfactant electrode.

The surfactant loaded liposomes were incubated in an oven at 120 °C, and the free surfactant's concentration was monitored to evaluate the release. The data indicates that the gradual release was triggered when the temperature approached 120 °C, indicating that the liposome's release is triggered by the temperature increment. Interestingly, the liposomes' gradual release was continued for more than 60 hours.

Acid nanocapsules were prepared using in situ and interfacial polymerizations. Notably, the in situ polymerization is easier to formulate spherical nanocapsules with higher encapsulation efficiency compared to the interfacial polymerization. The in situ encapsulation resulted in capsules with an encapsulation efficiency of 80 wt% and a mean diameter of 400 nm.

The acid nanocapsules showed high stability at 95 °C for several days. The acid precursor hydrolysis was triggered in the presence of water at 95 °C to produce the acid in situ. The capsules were remarkably stable under the reservoir conditions, and the pH was monitored and showed a gradual reduction in pH values from 4.3 to 2.6 over six days.

Acknowledgments

The authors would like to thank the technical support provided by Fouad A. Sadis, from the Reservoir Engineering Technology Division (EXPEC ARC). The samples were provided by Curt Thies of Thies Technology, and Andrew Loxley with Particle Sciences.

References

1. Esmaeili, A. and Gholami, M.: "Optimization and Preparation of Nanocapsules for Food Applications Using Two Methodologies," *Food Chemistry*, Vol. 179, July 2015, pp. 26-34.
2. Paredes, A.J., Asencio, C.M., Manuel, L.J., Allemandi, D.A., et al.: "Nanoencapsulation in the Food Industry: Manufacture, Applications and Characterization," *Journal of Food Bioengineering and Nanoprocessing*, Vol. 1, Issue 1, 2016, pp. 56-79.
3. Rafiee, Z., Nejatian, M., Daeihamed, M. and Jafari, S.M.: "Application of Curcumin Loaded Nanocarriers for Food, Drug and Cosmetic Purposes," *Trends in Food Science & Technology*, Vol. 88, June 2019, pp. 445-458.
4. Yin, C., Zhao, Q., Li, W., Zhao, Z., et al.: "Biomimetic Anti-Inflammatory Nanocapsule Serves as a Cytokine Blocker and M2 Polarization Inducer for Bone Tissue Repair," *Acta Biomaterialia*, Vol. 102, January 2020, pp. 416-426.
5. Sirdesai, M. and Khilar, K.C.: "A Model for Microencapsulation in Polyurea Shell by Means of Interfacial Polycodensation," *The Canadian Journal of Chemical Engineering*, Vol. 66, Issue 3, June 1988, pp. 509-513.
6. Hirasaki, G.J., Miller, C.A. and Puerto, M.: "Recent Advances in Surfactant EOR," *SPE Journal*, Vol. 16, Issue 4, December 2011, pp. 889-907.
7. Wellington, S. L. and Richardson, E.A.: "Low Surfactant Concentration Enhanced Waterflooding," *SPE Journal*, Vol. 2, Issue 4, December 1997, pp. 389-405.
8. Rostami, A. and Nasr-El-Din, H.A.: "New Technology for Filter Cake Removal," SPE paper 136400, presented at the SPE Russian Oil and Gas Conference and Exhibition, Moscow, Russia, October 26-28, 2010.
9. Zain, Z.M., Suri, A. and Sharma, M.M.: "Mechanisms of Mud Cake Removal during Flow Back," SPE paper 58797, presented at the SPE International Symposium on Formation Damage Control, Lafayette, Louisiana, February 23-24, 2000.
10. Stavek, J., Sipek, M., Hirasawa, I. and Toyokura, K.: "Controlled Double-Jet Precipitation of Sparingly Soluble Salts. A Method for the Preparation of High Added Value Materials," *Chemistry of Materials*, Vol. 4, Issue 3, May 1992, pp. 545-555.
11. Derjaguin, B. and Landau, L.: "Theory of the Stability of Strongly Charged Lyophobic Sols and of the Adhesion of Strongly Charged Particles in Solutions of Electrolytes," *Progress in Surface Science*, Vol. 43, Issues 1-4, May-August 1993, pp. 30-59.

12. Akbarzadeh, A., Rezaei-Sadabady, R., Davaran, S., Joo, W.S., et al.: "Liposome: Classification, Preparation, and Applications," *Nanoscale Research Letters*, Vol. 8, Issue 1, February 2013.

13. Wagner, A. and Vorauer-Uhl, K.: "Liposome Technology for Industrial Purposes," *Journal of Drug Delivery*, Vol. 2011, December 2010.

About the Authors

Dr. Nouf M. AlJabri

Ph.D. in Chemical Engineering, King Abdullah University of Science and Technology

Dr. Nouf M. AlJabri is a Petroleum Engineer with the Reservoir Engineering Technology Division at Saudi Aramco's Exploration and Petroleum Engineering Center – Advanced Research Center (EXPEC ARC). Nouf is spearheading research efforts on novel functionalization of nanomaterials for targeted delivery of enhanced oil recovery chemicals.

Her research is focused on developing new disruptive concepts for upstream nanotechnologies and nanomaterials.

Previously, Nouf was a visiting scientist with Professor Timothy M. Swager at MIT to design and synthesize novel advanced materials to resolve key upstream challenges.

She received her M.S. degree and Ph.D. degree in Chemical Engineering from King Abdullah University of Science and Technology (KAUST), Thuwal, Saudi Arabia.

Dr. Yu Chang

Ph.D. in Chemical Engineering, Georgia Institute of Technology

Dr. Yun Chang has worked for Eastman Kodak, Sasol Ltd., and Saudi Aramco during his 30-year career. Yun's areas of expertise include nanoparticles synthesis, particles functionalization for colloidal stability, nanoencapsulation, and controlled release technologies.

He is author of 35 journal publications and several U.S. patents.

Even in retirement, Yu has been working on supercritical CO_2 purification of medicinal natural products.

In 1985, he received his Ph.D. degree in Chemical Engineering from Georgia Institute of Technology. Atlanta, GA.

Novel Robust Polymer Gels for Water Shut-off Application in Sandstone Reservoir

Dr. Ayman M. Al-Mohsin, Dr. Jin Huang, Dr. Mohammed A. Bataweel, and Abdullah K. Abadi

Abstract /

Use of polymer gels are effective methods for water shut-off (WSO) applications in sandstone oil reservoirs having high water cuts. The WSO application can extend the economic life of the field once the undesired water production is minimized. A novel polymer gel was developed for WSO applications that extend the limitations of the current available materials for a sandstone formation.

The new developed system offers chemical bonding of an organically cross-linked polymer (OCP) gel to the sandstone rock surface, enabling the WSO system having enhanced stability with superior performance. The fluid system is low toxic and environmentally acceptable. It is comprised of a polymer gel and adsorption components for sandstone formations. To enhance the blocking efficiency of the WSO polymer gel, a specific adsorption component for sandstone formations was introduced into the OCP gel. The gelant can be placed as a single-phase, low-viscosity solution into the targeted formation zones. The new system can be widely applied for oil fields with excess water production.

A lab rheology study of the newly developed polymer gel reveals that both the gelation time and the formed gel strength were greatly affected by the addition of the sandstone adsorption component. By using the appropriate retarder, the gelation time can be controlled without compromising gel strength. The new polymer gel was placed in a high permeability sandstone core plug, and chase water was subsequently injected to measure the blocking capacity. The core flow test indicates substantial drops in water production. The new polymer system was able to withstand 3,500 psi of differential pressure at 200 °F, and did not allow the flow of water inside the core sample.

The new polymer gel system is expected to control water production through high permeability streaks and large pore openings. The system can be injected in porous media without injectivity reduction due to their low initial viscosity. This work provides significant insight using a polymer gel system as an effective chemical treatment intended for carbonate substrate as a WSO material.

Introduction

When water production from the oil field surpasses a certain limit, oil production becomes inefficient. Therefore, an improved oil recovery technique is necessary to decrease the water cut to economically satisfactory levels. In addition, water production can lead to several oil field related issues; such as costs related to water handling, scale, corrosion, and water/oil separation. These costs climb as water production increases.

There are several water production mechanisms, which can be identified using different tools. Water production has a different level of complexity. Starting with simple cases related to wellbore component leaks, which can be solved using mechanical means, are simple fixes around the wellbore area. All the way to more challenging problems that need innovative chemical solutions deeper in the reservoir. There are different water production mechanisms that can be identified such as a source of unproductive water.

The reasons of undesired water production can be classified into two significant groups. Some are induced through wellbore completion, such as casing leaks, tubing and packer leaks, barrier breakdown, completion in a near water zone, and channels behind pipes. Other forms of unwanted water production are related to reservoir related problems; e.g., high permeability streak, water coning, moving oil-water contact, and fracture features[1].

The theory of shutting/reducing water from an oil producer has been implemented since the early decades of the oil industry. Several innovative solutions have been developed and applied for either conformance control (injectors) or water shutoff (WSO) (producers). This requires a deep understanding of water production mechanisms, reservoir conditions, and well completions for selecting the proper technology to solve a specific problem and to increase the success rate.

Polymer gel as a chemical treatment is being implemented due to its cost-effectiveness for operations and handling, ease of use and efficiency, and for handling reservoir related problems. This technology is comprised of a polymer and a crosslinker (gelant) mixed before pumping into the targeted zone. Then, the mixture is injected into a water-bearing zone of the reservoir. At certain reservoir conditions, gel will form plug pores

and pore throats, Fig. 1.

Wide-ranging collections of polymer gels are commonly based on the type of the crosslinker to be used[2]. The choice of gel treatment involves several factors to be considered, including conformance problems, the point of application, the state of the gelant for injection, the polymer gel stability in the downhole environment, and the economic costs. Based on the polymer composition used, polymer gels are classified into organic cross-linked polymer (OCP) gel or inorganic cross-linked polymer[3] gels. Based on the gelation times, inorganic crosslinkers such as chromium(III)[4] and aluminum(III)[5] ions have been used for polymer gels in low temperature reservoirs, while organic crosslinkers such as polyethylenimine have often been used for polymer gelation in high temperature reservoirs.

Some of the major challenges faced by the polymer gel technology for WSO include high performance and stability under reservoir conditions and minimization of potential environmental effects. Besides stability, the success of polymer gel for treatment of a reservoir also depends on its compatibility with the rock surface. The polymer gels face instability and degradation issues in the high-pressure reservoirs demanding WSO treatments. Although there have been successful cases of polymer gel WSO treatments as given in reviews, there is still a need to address the issue of gel stability and strength for a wide range of operating conditions such as high-pressure reservoirs.

In the field of WSO, an adsorption component integrated with organic polymer gels offers a solution to the current issues faced. Polymer-graphene hydrogels are other potential candidates for robust WSO treatment. In this article, a polymer gel system that is composed of low toxic OCP gel and an adsorption component are discussed. This novel reboost of the well-defined and flexible adsorption components enables the new system to chemically bond to the rock surfaces of the sandstone reservoir.

This represents a significant breakthrough as it can overcome one of the key obstacles of water control in sandstone formations. In this article, a newly developed WSO material designed from combining OCP gel and adsorption components, which can provide sufficient gel time at temperatures up to 250 °F, is presented.

This article describes the lab work for fluid formulation optimization of gelation time at a given temperature, and the core flow tests for investigating the thermal stability and blocking efficiency of the new system.

Experimental

Materials

The smart polymer gel system comprised of an OCP gel and the adsorption components.

OCP gel: The OCP gel comprises a base polymer and an organic crosslinker. The OCP gel system is well investigated and has been applied in the oil fields for WSO applications, showing good stability over a wide temperature range. For the OCP gel fluid, potassium chloride was used in the concentration of 2 wt% (or 167 lb/1,000 gal) in deionized (DI) water to prepare all the gelling solution — except for one case when synthetic field mixing water was used. Ammonium chloride (NH_4Cl) was used as a retarder in the tests in the concentration of 1.2 wt% to 3.6 wt% (100 to 300 lb/1,000 gal) in DI water.

Adsorption Component: To enhance the blocking efficiency of the WSO polymer gel, we introduce the adsorption components into the OCP gel. The adsorption components can be used alone or be combined to add to the existing OCP gel in flexible ways, depending on the reservoir rock mineral type (sandstone) and its permeability nature.

Figure 2 illustrates the possible mechanisms for how the OCP gel interacts with the sandstone rock surface through the adsorption components. In the case of sandstone rock, the presence of X component "bridges" the OCP gel and surface silanols of the sandstone, thereby making the OCP gel "adsorbed" onto the sandstone surface.

Gelation Time Determination

The gelation time in this is defined as the initial gelation time in which the gel fluid viscosity significantly increases, meaning the onset of gel formation. It refers to the time needed to reach the inflection point on the

Fig. 1 *The gelation process in porous media.*

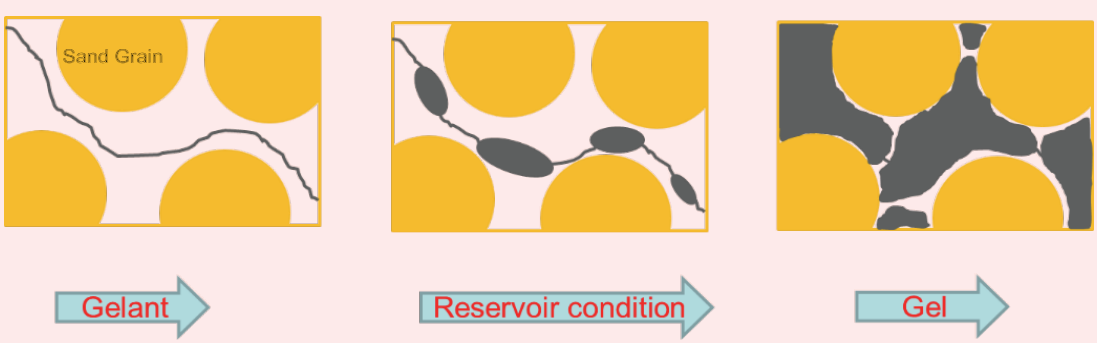

Fig. 2 *Proposed mechanism of smart polymer gel adsorbed on sandstone.*

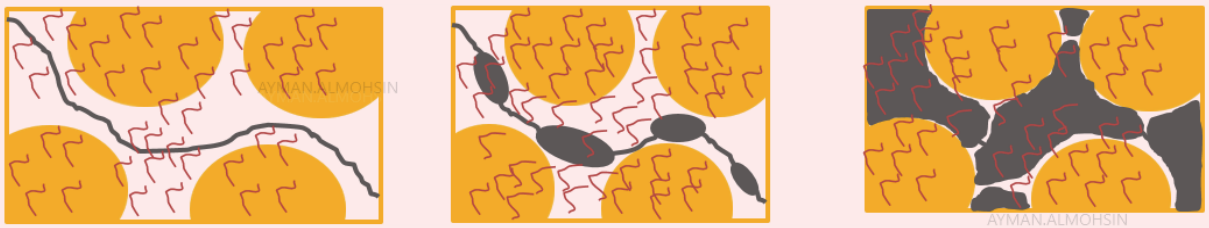

viscosity-time curve.

A reasonable "gelation time" must be realized to allow safe pumping operation of the fluid through the tubular and into the target zone. Two methods were used to determine the gelation time in this study: (1) a visual inspection method using test tubes for quick initial screening, and (2) a technique that used the HPHT viscometer by observing the drastic change in solution viscosity during the measurement. The second method was the main method adapted in this study because it is more accurate and reliable.

Figure 3 shows the viscosity-time curve used for determining the gelation time of the fluid and the picture of a completely gelled composite polymer gel. The sample viscosity changes were monitored as a function of time at a given constant shear rate.

All fluid rheology measurements in the lab studies were performed using a Chandler Model 5550 HPHT rheometer. A freshly prepared gel fluid (~52 mL) prepared according to the previously mentioned procedure was placed in the cup and affixed to the rotor fixture on the rheometer. The sample was set at a constant shear rate of 10 s^{-1} on the smooth bob-sleeve (R1-B5) with ~500 psi of nitrogen applied pressure at a preset testing temperature.

Gel Strength Measurement

Gel strength required for achieving higher success mainly depends on the problem type, and is related to treatment volume[6]. Polymer gel strength has to be high enough to resist water flow[7]. The gel strength of the new developed polymer gel was evaluated by rheological measurements. Oscillatory gel moduli measurements were performed using an Anton Paar MCR 502® rheometer with a 4 cm diameter and 1.0 mm gap parallel plates. Gelling solutions were prepared and heated at a designed temperature of 180 °F for 24 hours to ensure formation of rigid gels.

Formed gels were cooled to room temperature and kept for two months. All gel moduli measurements were conducted at a room temperature of ~25 °C. To determine the linear viscoelastic range of the new gel material, an oscillatory amplitude sweep test was first performed scanning from strain = 0.1% to 100% at a constant shear frequency = 1 Hz. After that, all the oscillatory frequency sweep tests were conducted in the shear frequency range ω = 0.1 to 100 rad/s at strain = 2%.

The formed polymer gels are viscoelastic material. The storage moduli (G') and loss moduli (G") are parameters reflecting viscous and elastic components of material behavior. In this study, the value of the G' was used as a quantitative indicator to compare the gel strength of new developed polymer gel and the OCP gel. A gel will be considered as "strong" with a G' value more than 10 Pa[8].

Fig. 3 *A representation to determine the gelation time by viscosity-time measurement.*

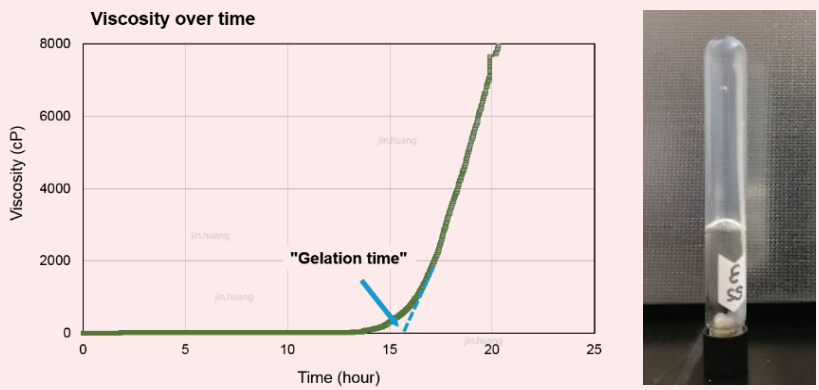

Coreflooding Test

Figure 4 is a schematic diagram of the coreflood setup. The core holder is accommodated in a constant temperature oven, which can hold the core at a mimicked reservoir temperature of 180 °F, and a confining pressure of 2,500 psi. The pressure drop across the core plug was monitored using a set of pressure transducers. The fluid was delivered using a high-pressure, high volume Quizix pump. The pore pressure was maintained at 500 psi using a back pressure regulator. A Berea sandstone core plug was used in this work having around 21% porosity and 1,700-mD brine permeability.

Coreflood experiments were conducted to evaluate the tendency and stability of chemical material to shut off water production in the sandstone formation. The coreflooding setup was modified to bypass the WSO chemical from the face of the core plug to ensure all the lines are clean during shut-in. A cylinder was installed on the downstream side of the core holder to accumulate particles coming out from the core plug, and to avoid plugging the lines.

Coreflood test procedure: Coreflood experiments were performed by initial saturating of the core with Cla-Web — a clay stabilizer. Several pore volumes (PVs) were injected into the sandstone core plug. Then the core permeability was obtained by using Darcy's law for a linear flow. Then, approximately 10 PV of the gelant were injected at a flow rate of 0.5 ml/min.

Note that the test was conducted under a back pressure of 524 psi and temperature of 180 °F (82 °C). Finally, a post-flush Cla-Web was injected to determine the plugging efficiency of the newly developed composite gel at a constant rate of 1 ml/min.

Results and Discussion

Gelation Time Study

Formulation and screening tests of the polymer gel fluid were conducted by either static tube tests or rheometer tests at a wide range of temperatures to study the gelation behavior and performance of the system for WSO application. During the studies, the gel fluid formulation was chosen for the sandstone formation with bottom-hole static temperatures of 180 °F.

Gelation Time Comparison between OCP Gel and New Polymer Gel (OCP Gel + Adsorption Component)

As the planned field trial is for sandstone, an "injectivity" issue (or "compatibility" problem) associated with the OCP gel has been identified in the previous coreflood tests. We modified the gel fluid formulation by adding NH_4Cl as a retarder to prevent early stage gelation or precipitation by high pH additive. After modification, a smart polymer gel fluid containing adsorption component aminosilane was prepared. Figure 5 is the rheometer test results.

It was clear that the addition of 300 lb/Mgal of NH_4Cl delayed the gelation time of the pure OCP gel from ~2 hours to ~15 hours. Further adding of the adsorption component aminosilane shorted the gelation time to ~10 hours. As a bridging/adsorption component, aminosilane can react with the OCP base polymer via H-bonding and amidation reaction; therefore, it might

Fig. 4 *A schematic of the coreflooding setup.*

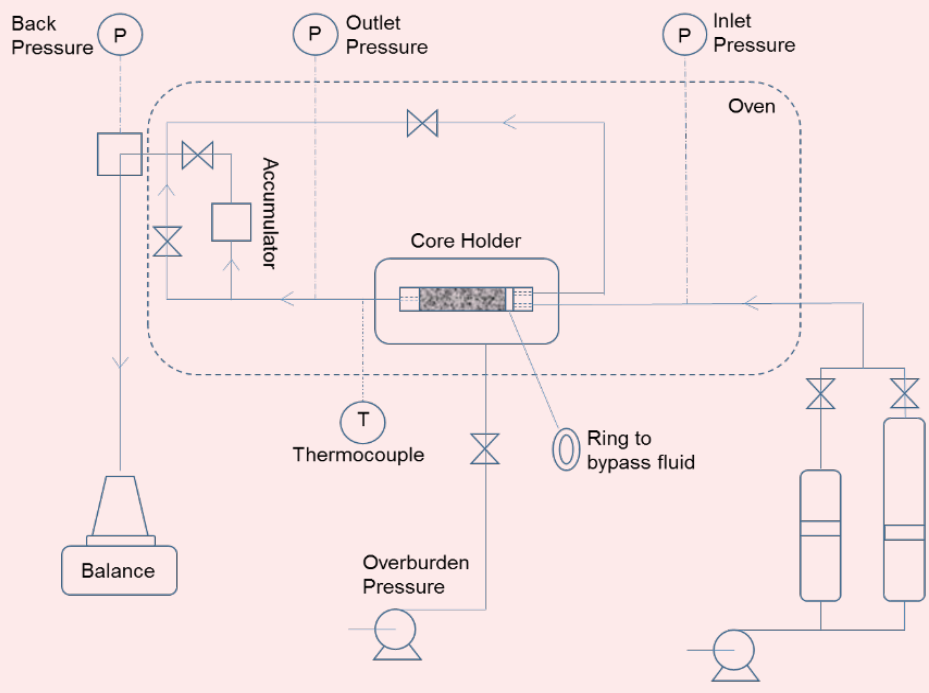

Fig. 5 *The gelation time of the smart polymer gel designed for a sandstone formation at a temperature of 180 °F.*

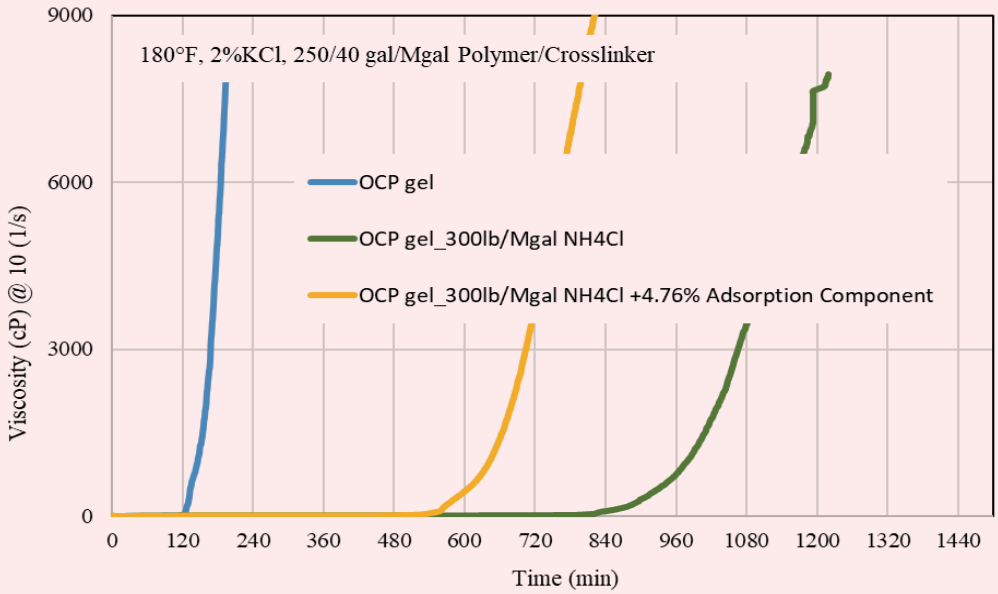

function as a synergy agent for organic crosslinker to promote the crosslinking process, thereby accelerating the gelation. This gel fluid formulation shows good performance in the coreflooding test. Required gelation time can be achieved by fine-tuning of the recipe such as to increase/decrease the concentration of the crosslinker or aminosilane, the ratio of base polymer over crosslinker, etc.

To improve the injectivity of the main stage of the treatment, a gel fluid prepared by using synthetic field mixing water was tested on the viscosity and gelation time. Figure 6 shows the rheometer test results of a developed smart gel with synthetic mixing water and with lab DI water. It is clear that the addition of the field mixing water did not significantly change the gelation time.

Fig. 6 *Gelation time of the smart polymer gel designed for sandstone formation at a temperature of 180 °F.*

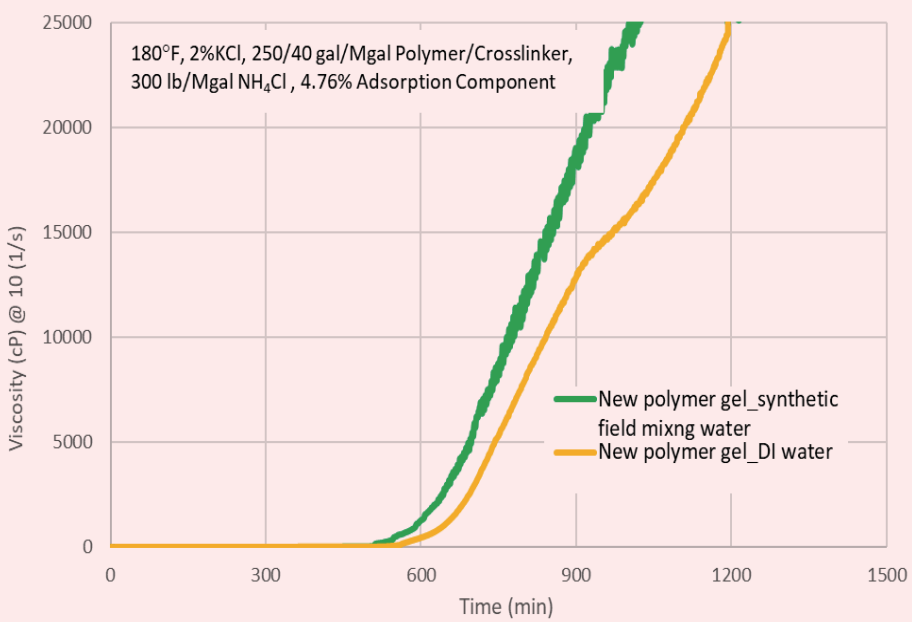

No gelation time measurements were taken into consideration for the extra pumping time that can result from the cooling effect around the wellbore area due to preflush and treatment injection. This effect should work as an extra safety measure for proper pumping operation.

The gel strength required for achieving a higher success rate mainly depends on the problem type, and is related to treatment volume[6]. Generally, for a thick matrix having water production issues, this compares the results of the storage modulus for the new polymer gel and OCP gel prepared at 180 °F, Fig. 7. The results suggest that both the OCP gel and the new polymer gel are very strong. Consequently, the storage modulus of the new polymer gel is almost three times that of the OPC gel, indicating the gel strength increases with the addition of the adsorption component. Some reservoirs exhibit high pressure, which requires a strong gel.

Coreflooding Test

Initially, Cla-Web was injected at different flow rates of 1 ml/min, 2 ml/min, and 4 ml/min to determine the pressure drop for each flow rate to calculate the permeability of the core, Fig. 8. The average water permeability was determined using Darcy's equation and found to be around 1,710.7 mD.

Fig. 7 *Storage moduli vs. frequency for the new polymer gel and OCP gel.*

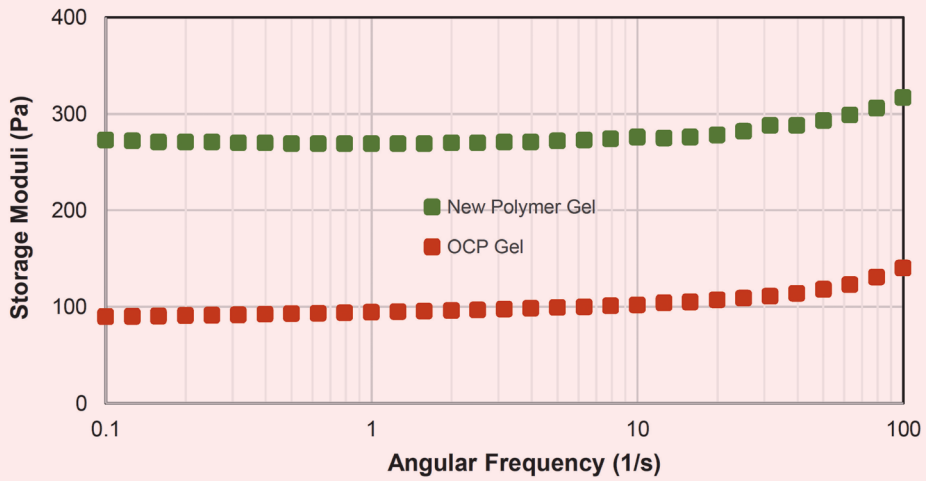

Fig. 8 *Pressure drop of the Cla-Web preflush at different flow rates: 1 ml/min, 2 ml/min, 4 ml/min, 2 ml/min, and 1 ml/min.*

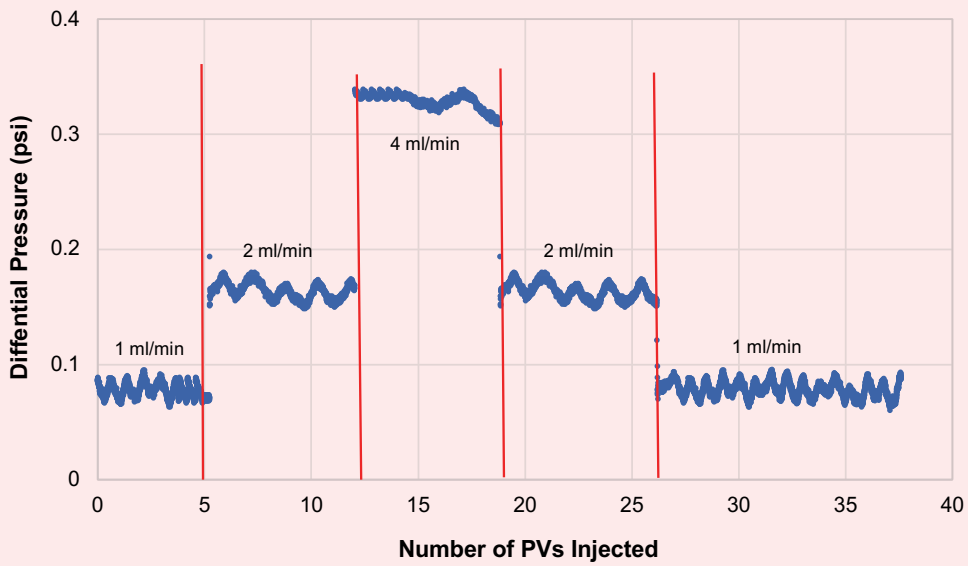

Fig. 9 *Pressure drop of the Cla-Web preflush and the gelant fluid.*

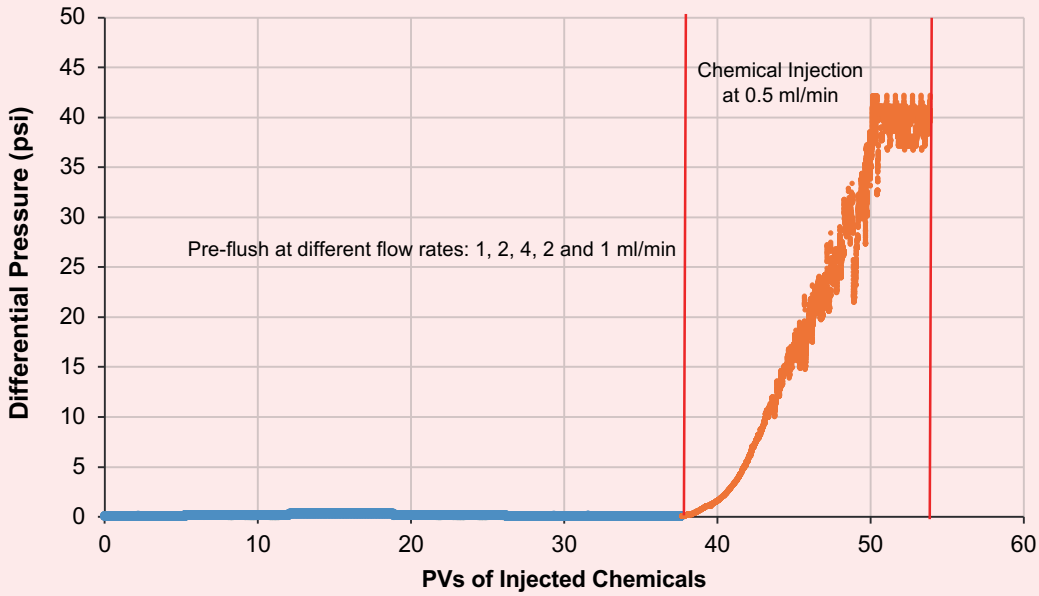

Injectivity Test

Despite the complexity of the phenomena governing injectivity, some simple considerations suggest an experimental method that can be used to explain these phenomena. One method is to inject multiple PVs into the formation core at a constant flow rate. It is very important to measure the injectivity of gelant material before the field trial. Therefore, a coreflood test was conducted to evaluate the injectivity of this chemical treatment.

Figure 9 shows the pressure drop data collected during this work. The pressure drop across the core kept increasing during the chemical placement and flattened at 40 psi after 10 PVs at 180 °F (83 °C).

Endurance Test (Long Constant Pressure Experiment)

Once the curing time — 42 hours — is completed, the Cla-Web was injected (post-injection) to determine the plugging efficiency of the chemical treatment. Figure 10 depicts the pressure drop during all stages with respect to time. As can be seen, there is a sharp increase in injection pressure at a constant rate (1 ml/

Fig. 10 *Durability test to evaluate the stability of WSO material at 180 °F.*

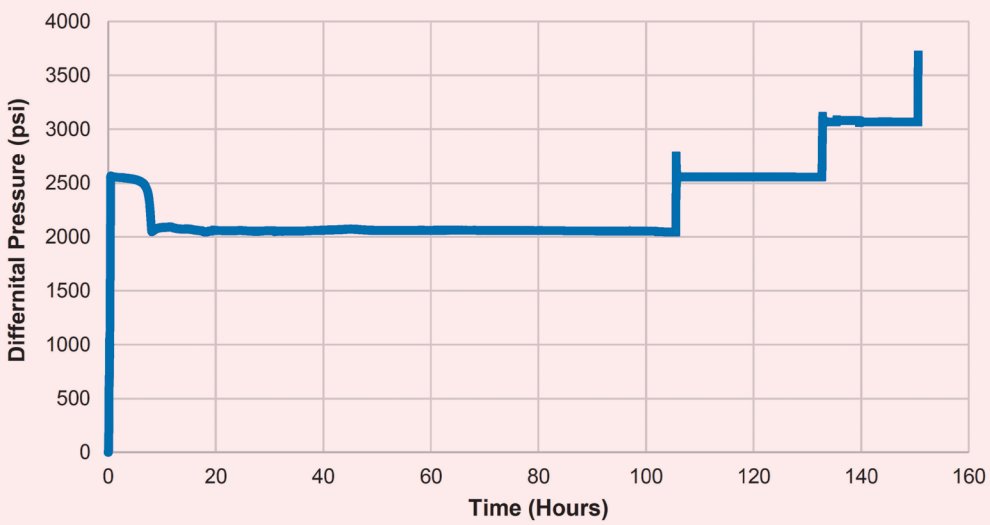

min) with total differential pressure of approximately 2,540 psi at the initial injectivity test after chemical curing. After that, the pump was switched to a constant pressure mode to determine how much pressure the gel can withstand. As can be seen the pressure held for almost 6 hours.

Afterwards, the pressure was reduced to 2,060 psi to avoid a pressure gradient that can fracture the core. The measured differential pressure is equivalent to 8,240 psi/ft holding pressure for the treated matrix by this WSO material. After that, an endurance test was started and the differential pressure was held at 2,060 psi for 100 hours. This was followed with an extended period of 132 hours at a differential pressure of 3,000 psid, with minimal leakoff through the treated core plug.

The averaged measured leakoff rate during this period were 0.01 cm^3/min. The equivalent drawdown pressure that the core was able to withstand is 12,500 psi/ft — 3,000 psid for 2.88" core plug. After 6.25 days at 183 °F, a second, high-pressure stability test was conducted to assess the holding pressure of the chemical plug. The pressure drop increased to 2,559 psid with no evidence of flow through the plug sample. In addition, a third test with higher pressure was conducted to evaluate the stability of the WSO material at 3,071 psid for 16 hours with no sign of flow. The outcome from this work provided needed information showing that this is a complete shut-off material.

Conclusions

A smart polymer gel system has been developed for sandstone WSO application. The fluid system shows a number of advantages, including:

- The newly developed system can chemically bond to carbonate/sandstone reservoir rock surfaces.
- The gelation time can be controlled by fine-tuning the fluid formulation, which allows a predictable pumping time at a temperature up to 250 °F. The gelation time decreases with an increase in temperature and polymer concentration.
- The developed fluid is a low toxic, environmentally acceptable, single-phase solution, which can be injected easily with no modifications to the current pumping practices.
- The developed gel system showed a significant pressure increase after the treatment with good durability and effective WSO during the extended coreflooding experiment with great stability at high temperature.

Acknowledgments

This article has been prepared for presentation at the SPE Conference at Oman Petroleum and Energy Show, Muscat, Oman, September 14-16, 2020.

References

1. Smith, D. and Ott, B.: "Winning the Battle against Unwanted Production: A Comprehensive Review of Conformance Engineering. Part 1: Understanding the Problem," *World Oil*, May 2006, pp. 63-68.
2. Al-Muntasheri, G.A. and Zitha, P.L.J.: "Gel under Dynamic Stress in Porous Media: New Insights Using Computed Tomography," SPE paper 126068, presented at the SPE Saudi Arabia Section Technical Symposium, al-Khobar, Saudi Arabia, May 9-11, 2009.
3. Al-Muntasheri, G.A., Sierra, L., Garzon, F.O., Lynn, J.D., et al.: "Water Shut-off with Polymer Gels in a High Temperature Horizontal Gas Well: A Success Story," SPE paper 129848, presented at the SPE Improved Oil Recovery Symposium, Tulsa, Oklahoma, April 24-28, 2010.
4. Sydansk, R.D.: "A Newly Developed Chromium(III) Gel Technology," *SPE Reservoir Engineering*, Vol. 5, Issue 3, August 1990, pp. 346-352.
5. Al-Assi, A.A., Willhite, G.P., Green, D.W. and McCool, C.S.: "Formation and Propagation of Gel Aggregates Using Partially Hydrolyzed Polyacrylamide and Aluminum Citrate," *SPE Journal*, Vol. 14, Issue 3, September 2009, pp. 450-461.
6. Smith, J.E.: "The Transition Pressure: A Quick Method for Quantifying Polyacrylamide Gel Strength," SPE paper 18739, presented at the SPE International Symposium on Oil Field Chemistry, Houston, Texas, February 8-10, 1989.
7. El-Karsani, K.S.M., Al-Muntasheri, G.A., Sultan, A.S. and Hussein, I.A.: "Gelation of a Water Shutoff Gel at High Pressure and High Temperature: Rheological Investigation," *SPE Journal*, Vol. 20, Issue 5, October 2015, pp. 1103-1112.
8. Moradi-Araghi, A., Beardmore, D.H. and Stahl, G.A.: "The Application of Gels in Enhanced Oil Recovery; Theory, Polymers and Crosslinker Systems," in Stahl, G.A. and Schulz, D.N. (eds.), *Water-Soluble Polymers for Petroleum Recovery*, Springer: Boston, MA, pp. 299-312, 1988.

About the Authors

Dr. Ayman M. Al-Mohsin

Ph.D. in Petroleum Engineering, Missouri University of Science and Technology

Dr. Ayman M. Al-Mohsin has worked with Saudi Aramco since 2014 as a Research Engineer. His research focuses on developing materials to prevent/reduce excess water and gas production during oil recovery.

Ayman received his B.S. degree in Mechanical Engineering from the University of New Haven, West Haven, CT; his M.S. degree in Petroleum Engineering from New Mexico Tech, Socorro, NM; and his Ph.D. degree in Petroleum Engineering from Missouri University of Science and Technology, Rolla, MO.

Dr. Jin Huang

Ph.D. in Inorganic Chemistry, University of Houston

Dr. Jin Huang is a Petroleum Scientist working with the Production Technology Division of Saudi Aramco's Exploration and Petroleum Engineering Center – Advanced Research Center (EXPEC ARC). Her current research interests are water management related oil field chemistry.

Prior to joining Saudi Aramco in 2015, Jin worked as with Weatherford Laboratories Inc. and Intertek Westport Technology Center in Houston, Texas. She was intensively involved in reservoir fluids analysis, drilling fluid analysis and water chemistry. Jin also worked at GTC Technology Inc. in Houston as a Process Chemist, and worked as a postdoctoral researcher at Texas A&M University, College Station, Texas.

In 1994, Jin received her B.S. degree in Polymer Chemistry from Tianjin University, Tianjin, China; and in 2004, she received her Ph.D. degree in Inorganic Chemistry from the University of Houston, Houston, TX.

Dr. Mohammed A. Bataweel

Ph.D. in Petroleum Engineering, Texas A&M University

Dr. Mohammed A. Bataweel is a Champion for the Smart Fluid focus area in the Production Technology Division of Saudi Aramco's Exploration and Petroleum Engineering Center – Advanced Research Center (EXPEC ARC). Mohammed has led his team in the development and deployment of several in-house technologies in Saudi Aramco fields. Throughout his career, he has represented his department on several field development, asset, and multidisciplinary teams.

Mohammed's research interests include formation damage due to drilling and completion fluids, investigation and mitigation of injectivity decline, conformance control, sand production prediction, special core analysis, chemical enhanced oil recovery, productivity enhancement technologies, visualization of fluid flow in porous media, and oil field chemicals.

He is an active member of the Society of Petroleum Engineers (SPE) where he has served on several conferences. Mohammed initiated and co-chaired several SPE advanced technical workshop series in the region. He has published more than 40 SPE papers in local and international conferences and refereed journals.

Mohammed received his B.S. degree in Mechanical Engineering from King Fahd University of Petroleum and Minerals (KFUPM), Dhahran, Saudi Arabia, and his M.S. degree in Petroleum Engineering from Harriot-Watt University, Edinburgh, U.K. Mohammed received his Ph.D. degree in Petroleum Engineering from Texas A&M University, College Station, TX.

Abdullah K. Abadi

Diploma in Industrial Chemistry Technology, Jubail Industrial College

Abdullah K. Abadi is a Rheology and Coreflooding Technician working with the Production Technology Division of Saudi Aramco's Exploration and Petroleum Engineering Center – Advanced Research Center (EXPEC ARC).

In 2009, he received his Diploma in Industrial Chemistry Technology, from Jubail Industrial College, Jubail, Saudi Arabia.

Quantifying Displacement and Strain Deformation of Multi-Material Rocks around Growing Hydraulic Fractures

Dr. Murtadha J. AlTammar and Dr. Mukul M. Sharma

Abstract /

Synthetic materials are used to cast sheet-like, porous test specimens that have strongly bonded layers with contrasting mechanical properties. The layered specimen is placed between two thick, transparent plates, and constant anisotropic far-field stresses are applied to the specimen. Fracturing fluid is injected in the center of the specimen, and the induced hydraulic fracture propagation is captured with high-resolution digital images, and then subject to subsequent image processing. Displacement of the specimen body around the growing fracture is resolved using Digital Image Correlation (DIC) analyses. Discrete Fourier transform is applied to smooth displacement data. The smoothed displacement data is subsequently used to quantify the hydraulic fracture width in various spatial positions along the fracture length and to quantify strain deformations around the fracture.

First, we show the deformation profiles around a hydraulic fracture induced in a homogeneous test specimen. Then, we demonstrate displacement and strain profiles around a fracture induced across three-layer specimens. The displacement and strain are shown to be highest at the center of the specimen where fluid is injected and the hydraulic fracture is initiated. The displacement and strain decrease gradually along the length of the fracture away from the middle of the fracture.

For specimens that have a soft middle layer bounded by hard layers, the rate of change in displacement along the fracture length becomes markedly lower in the bounding hard layers. By contrast, the rate of change in displacement is rather uniform across the layers for specimens that have a hard middle layer bounded by soft layers. In some instances, there is a clear asymmetry in measured strain on opposite sides of the fracture where one side of the fracture is strained and the other side has zero strain.

This research presents novel experimental methods that for the first time, enabled visualizing and quantifying the deformation of multiple material rocks as hydraulic fractures propagate through them. Fundamental insights are presented on how individual layers in the layered test specimens with contrasting mechanical properties deform for the different combinations of layer properties.

Introduction

In AlTammar et al. (2019)[1], we developed a fracture cell and experimental methods to investigate hydraulic fracture propagation across multiple materials with contrasting mechanical properties. A series of hydraulic fracturing experiments were performed in porous, layered test specimens.

Figure 1 shows a schematic of the fracture cell used to perform the experiments. The test specimen is a thin sheet of cast materials placed between two transparent plates. The test specimens are made of mixtures of plaster, talc, and hydrostone in varying proportions to control the strength of the material. The mechanical properties for a wide range of mixtures were measured to establish a specified contrast in Young's modulus (E) and fracture toughness (K_{IC}), when preparing the layered test specimens. The specimen is 6" × 6" and the monitored field of view during the tests is about 4" × 2". A random speckle pattern was painted on the specimen using white and black spray paint. A far-field stress is applied on two parallel sides of the specimen in the x-direction, Fig. 1c, and glycerin is injected at the center of the specimen to induce a fracture.

The fracturing process is recorded using a high-resolution digital camera at 30 frames per second. At the end, key frames of the fracture propagation were obtained from the recorded video and the frames were analyzed using a digital image correlation (DIC) software to resolve full-field displacement and strain as the fracture grows through the specimen. Figure 1d shows a cast three-layer specimen made in the laboratory. Details of the experimental methods are given in AlTammar et al. (2019)[1].

In this study, we performed further analysis on data sets generated from Tests 1 through 3 that were reported[1]. In these tests, we previously utilized displacement and strain data resolved by DIC analysis as a method to track fracture propagation through the test specimen. Specifically, we used the measured normal strain ϵ_{yy} in

Fig. 1 *A schematic of a fracture cell (a) and (b), specimen configuration (c), and a photograph of a cast three-layer specimen (d) used in this study.*

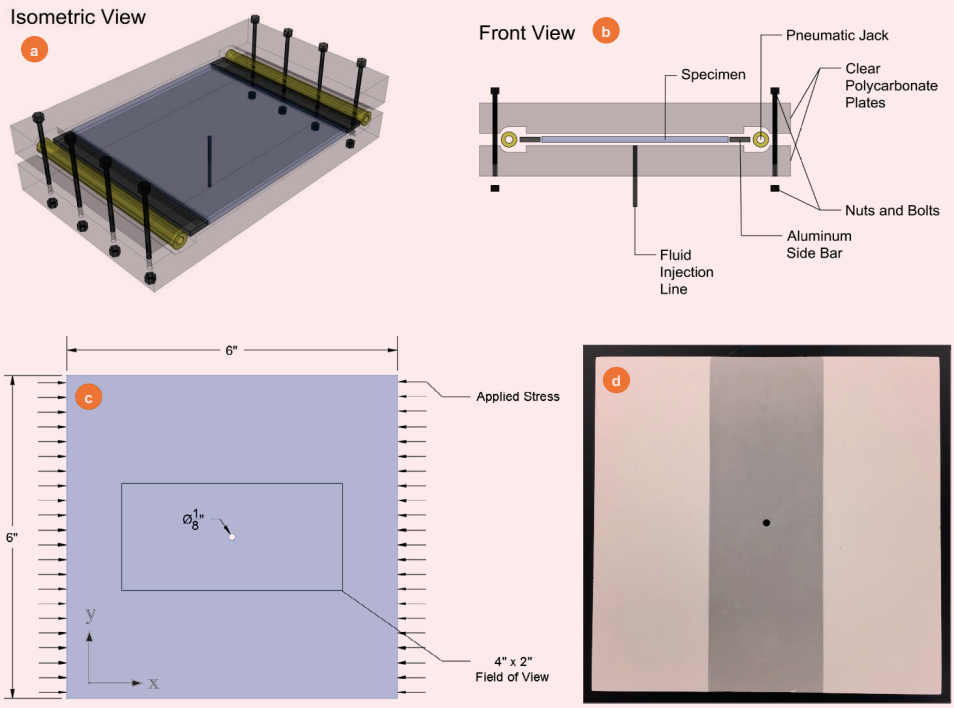

the y-direction to track fracture propagation since the fracture opening is mainly in the y-direction. Figures 2a and 2b shows an example of the displacement and strain fields around a propagating hydraulic fracture. When performing DIC analysis of such fracture propagation experiments, the fracture opening is highlighted as a local, tensile ϵ_{yy} because the two faces of the fracture are separating. In reality, the matrix of the specimen is straining around the propagating fracture. This discrepancy between the resolved ϵ_{yy} and the actual strain is because the separation between the fracture faces is much larger than the strain deformation within the matrix of the specimen around the fracture.

Rather than using the ϵ_{yy} field resolved by DIC analysis, this study estimates the ϵ_{yy} directly from the displacement data. This is accomplished by first smoothing the displacement data using discrete Fourier transform with a low pass filter, then estimating the ϵ_{yy} from the slope of the smoothed displacement data.

The objective of this article is to investigate the deformation characteristics of homogeneous and multiple material test specimens around a growing hydraulic fracture.

Results

Test 1: Homogeneous Specimen

Figure 3 shows the displacement field in the y-direction around a growing hydraulic fracture in a homogeneous specimen as resolved by DIC analysis in Test 1. The specimen material has a measured E of 165,000 psi (165 ksi) and a K_{IC} of 151 psi-in$^{0.5}$. The displacement profiles of the vertical and horizontal cross-sections marked on Fig. 3 are plotted in Figs. 4 through 8. In these figures, the raw displacement data are shown by the thin blue curves and the smoothed displacement data are shown by the thick orange curves.

Looking at the vertical cross-sections that are perpendicular to the fracture trajectory, we see that the fracture opening (fracture width) increases from 0.022 mm at cross-section A to 0.046 mm in cross-section C, and down to 0.021 mm in cross-section E, Figs. 4 to 6. The rate of change of the y-displacement along the y-coordinate provides an estimate for the ϵ_{yy} in the y-direction, shown in by the slopes of the black line segments superimposed on the smoothed displacement data.

For example, in cross-section A, in Fig. 4, the upper part of the specimen above the fracture has an ϵ_{yy} of −0.036% and the lower part below the fracture has an ϵ_{yy} of −0.023%. The negative signs indicate that the propagating fracture induces a compressional ϵ_{yy} in the body of the specimen as expected. Larger ϵ_{yy} are observed at the center of the fracture in cross-section C in Fig. 5, where the upper part of the specimen has an ϵ_{yy} of −0.048% and the lower part of the specimen has an ϵ_{yy} of −0.064%. Similar to cross-section A, the upper part of the specimen has an ϵ_{yy} of −0.027% and the lower part below the fracture has an ϵ_{yy} of −0.02% in cross-section E in Fig. 6.

For the horizontal cross-sections that are parallel to the fracture trajectory, the slopes of the black line

Fig. 2 *An example of a displacement field in the y-direction (a), and its corresponding normal strain field in the y-direction (b) around a growing hydraulic fracture as resolved by DIC analysis.*

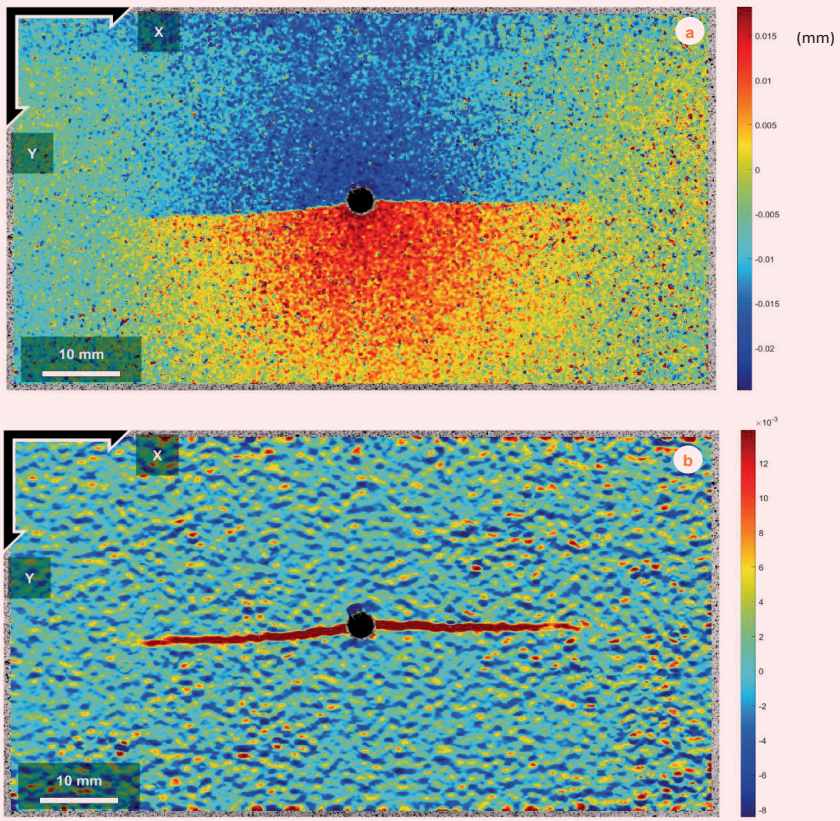

Fig. 3 *The displacement field in the y-direction around a growing hydraulic fracture in a homogeneous specimen as resolved by DIC analysis in Test 1.*

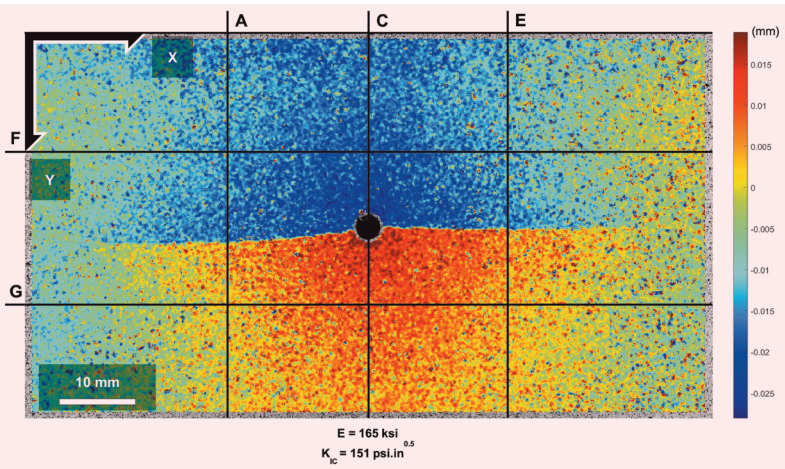

segments give the rate of change of the y-displacement along the x-coordinate, Figs. 7 and 8. In cross-section F in Fig. 7, the y-displacement decreases at a rate of −0.037% in the upper left part of the specimen, whereas the y-displacement increases at a rate of 0.052% in the upper right part of the specimen. Similarly, in cross-section G in Fig. 8, the y-displacement increases at a rate of 0.051% in the lower left part of the specimen, whereas the y-displacement decreases at a rate of −0.045% in the lower right part of the specimen.

Fig. 4 *The y-displacement along cross-section A in Test 1.*

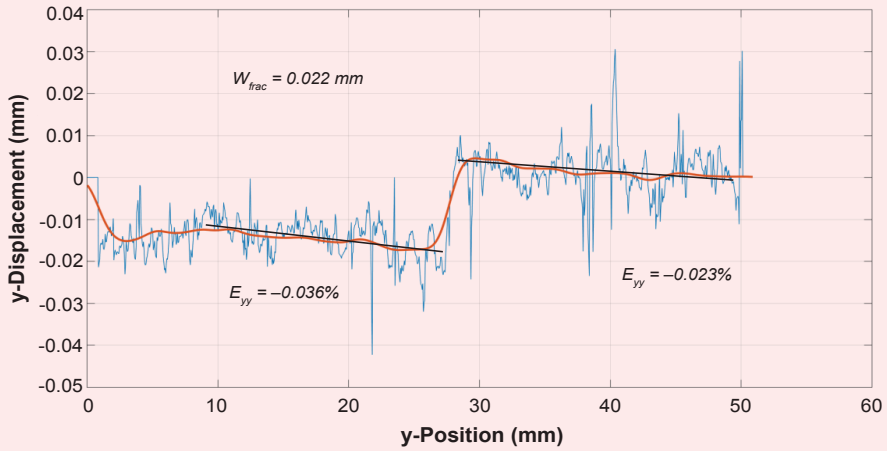

Fig. 5 *The y-displacement along cross-section C in Test 1.*

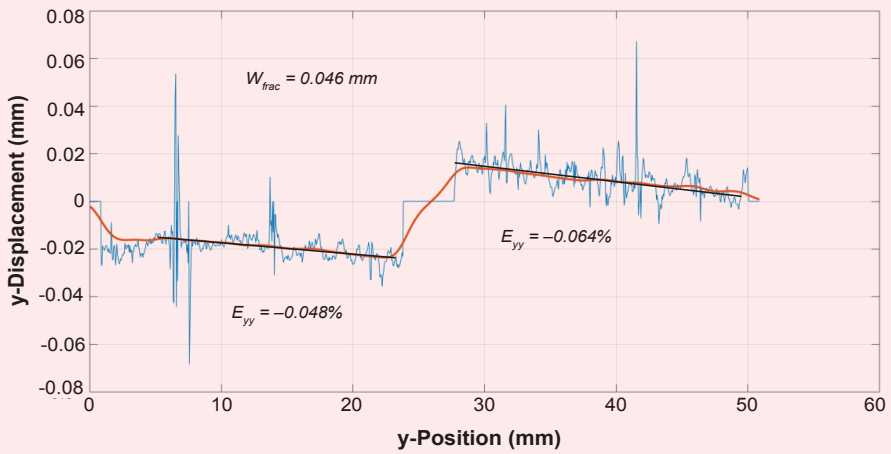

Fig. 6 *The y-displacement along cross-section E in Test 1.*

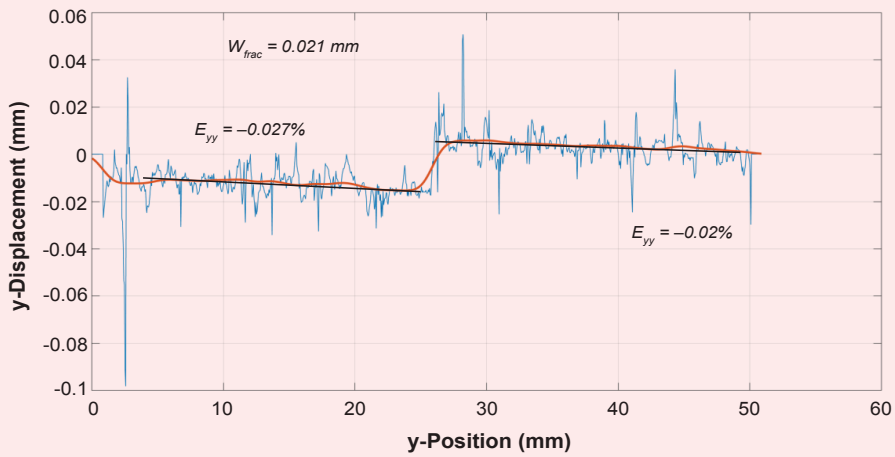

Fig. 7 *The y-displacement along cross-section F in Test 1.*

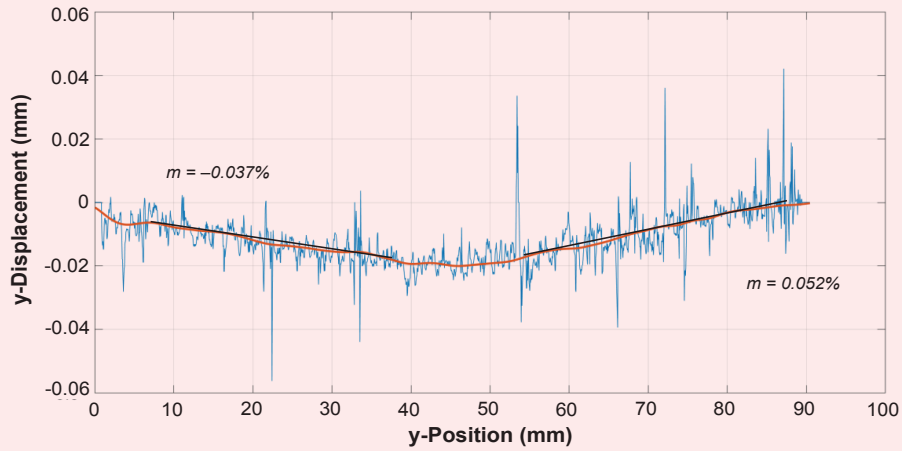

Fig. 8 *The y-displacement along cross-section G in Test 1.*

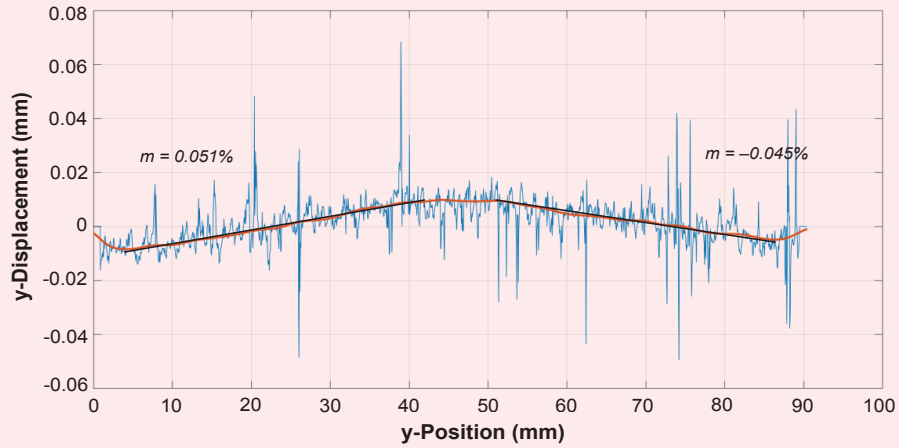

Test 2: Hard Layer Bounded by Soft Layers

Figure 9 shows the displacement field in the y-direction around a growing hydraulic fracture in a three-layer specimen as resolved by DIC analysis in Test 2. The specimen has a hard middle layer bounded by soft outer layers. The middle layer has an E of 84 ksi and a K_{IC} of 103 psi-in$^{0.5}$ while the outer layers have an E of 39 ksi and a K_{IC} of 68 psi-in$^{0.5}$. The displacement profiles of the vertical and horizontal cross-sections marked on Fig. 9 are plotted in Figs. 10 through 16.

From the vertical cross-sections that are perpendicular to the fracture trajectory, the fracture opening is 0.024 mm at cross-section A to the left of the left layer interface, 0.035 mm in cross-section B to the right of the left layer interface, 0.06 mm in cross-section C at the center, 0.035 mm in cross-section D to the left of the right layer interface, and 0.023 mm to the right of the right layer interface, Figs. 10 to 14.

In cross-sections A and B, the upper part of the specimen above the fracture has an ϵ_{yy} of −0.015% and −0.019%, respectively. The lower part below the fracture has an ϵ_{yy} of approximately zero for both cross-sections, Figs. 10 and 11. Larger ϵ_{yy} are observed at the center of the fracture in cross-section C in Fig. 12, where the upper and lower parts of the specimen have an ϵ_{yy} of approximately −0.06%. The ϵ_{yy} in cross-sections D and E in Figs. 13 and 14 are similar to the ϵ_{yy} in cross-sections A and B. For the horizontal cross-sections that are parallel to the fracture trajectory, the rate of change of the y-displacement along the x-coordinate is shown in Figs. 15 and 16.

In cross-section F in Fig. 15, the y-displacement decreases at a rate of -0.049% in the upper left part of the specimen, whereas the y-displacement increases at a rate of 0.053% in the upper right part of the specimen. Similarly, in cross-section G in Fig. 16, the

Fig. 9 *Displacement field in the y-direction around a growing hydraulic fracture in a three-layer specimen in Test 2.*

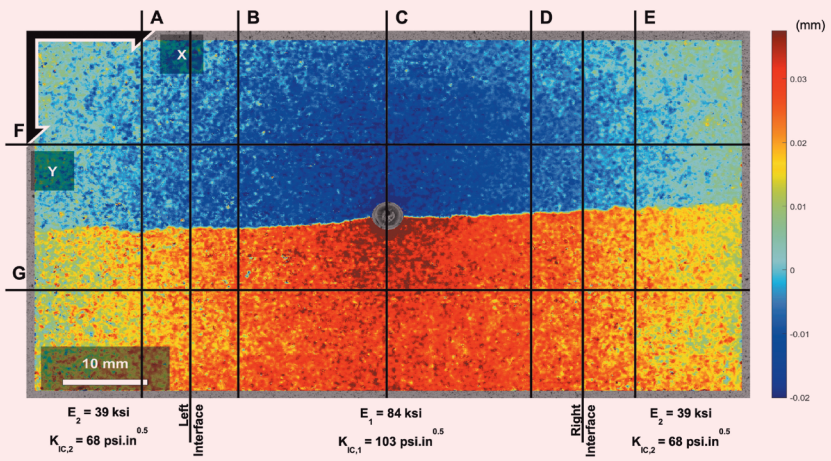

Fig. 10 *The y-displacement along cross-section A in Test 2.*

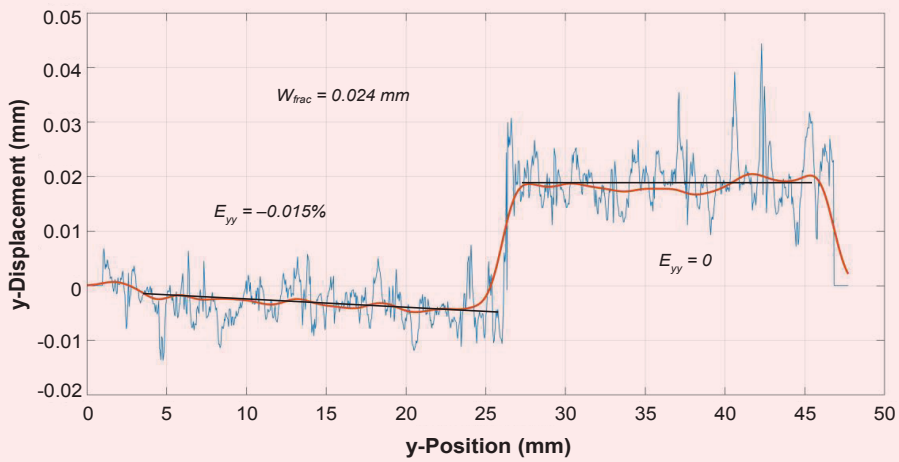

Fig. 11 *The y-displacement along cross-section B in Test 2.*

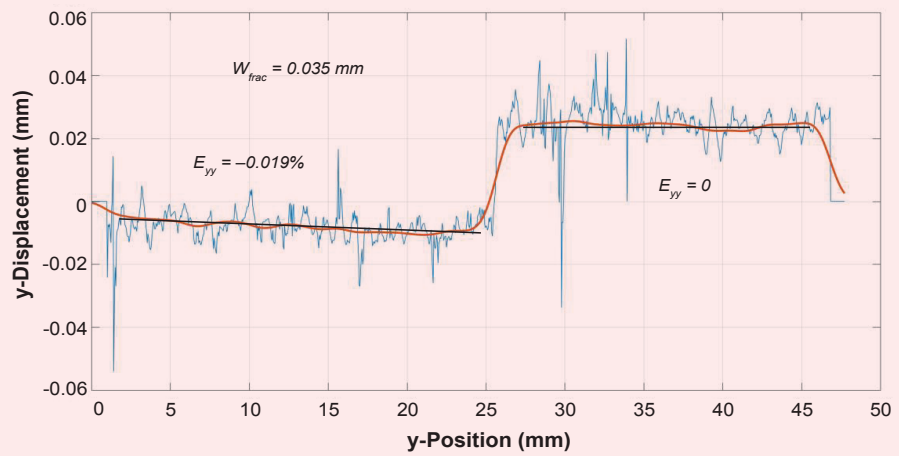

Fig. 12 *The y-displacement along cross-section C in Test 2.*

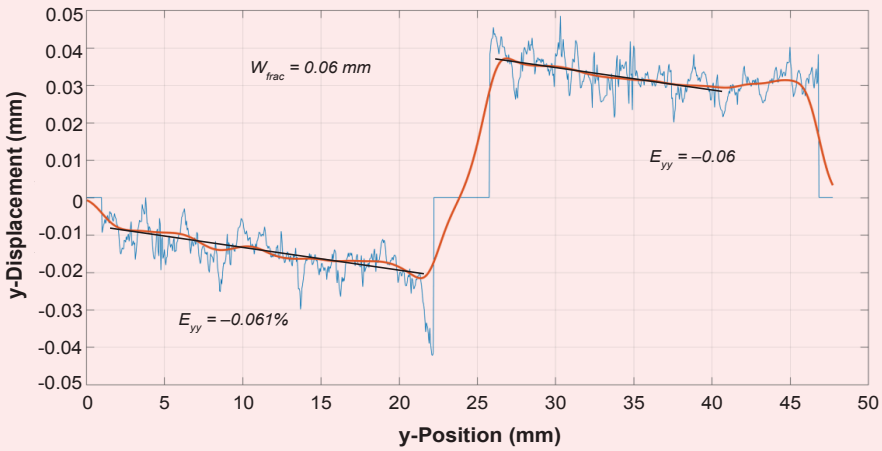

Fig. 13 *The y-displacement along cross-section D in Test 2.*

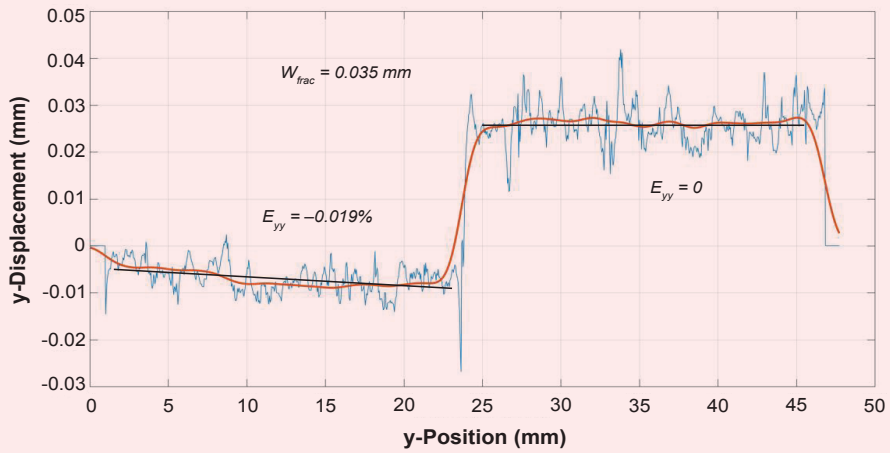

Fig. 14 *The y-displacement along cross-section E in Test 2.*

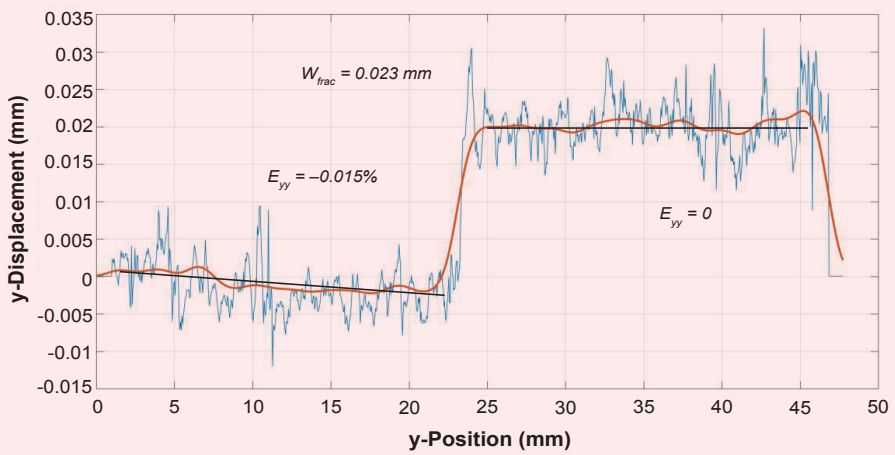

Fig. 15 *The y-displacement along cross-section F in Test 2.*

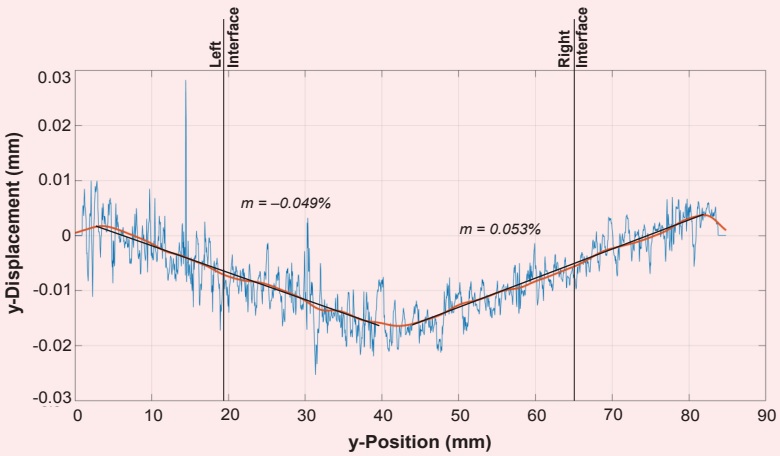

Fig. 16 *The y-displacement along cross-section G in Test 2.*

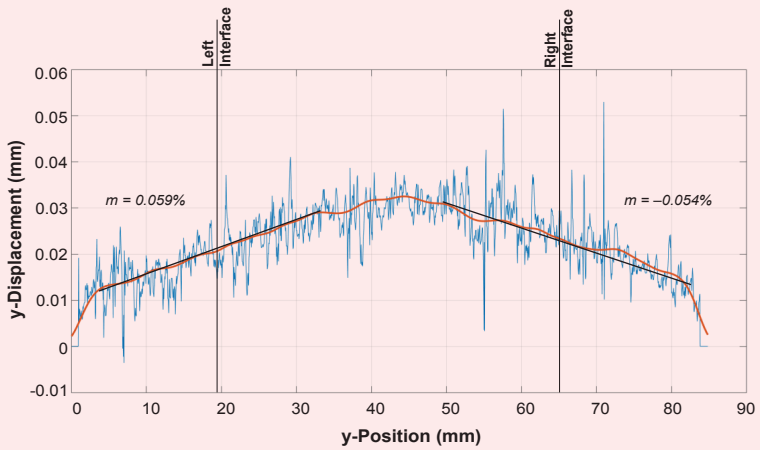

y-displacement increases at a rate of 0.059% in the lower left part of the specimen, whereas the y-displacement decreases at a rate of −0.054% in the lower right part of the specimen. Note that the rate of change of the y-displacement along the x-coordinate does not change across the layer interfaces for both the F and G cross-sections.

Test 3: Soft Layer Bounded by Hard Layers

Figure 17 shows the displacement field in the y-direction around a growing hydraulic fracture in a three-layer specimen as resolved by DIC analysis in Test 3. The specimen has a soft middle layer bounded by hard outer layers. The middle layer has an E of 84 ksi and a K_{IC} of 103 psi-in$^{0.5}$ — same middle layer as in Test 2 — but the outer layers have an E of 396 ksi and a K_{IC} of 233 psi-in$^{0.5}$. The displacement profiles of the vertical and horizontal cross-sections marked in Fig. 17 are plotted in Figs. 18 through 24.

From the vertical cross-sections that are perpendicular to the fracture trajectory, the fracture opening is 0.026 mm at cross-section A to the left of the left layer interface, 0.034 mm in cross-section B to the right of the left layer interface, 0.077 mm in cross-section C at the center, 0.05 mm in cross-section D to the left of the right layer interface, and 0.033 mm to the right of the right layer interface, Figs. 18 to 22.

In cross-sections A and B, the upper part of the specimen above the fracture has an ϵ_{yy} of approximately −0.035% while the lower part below the fracture has an ϵ_{yy} of approximately zero, Figs. 18 and 19. Larger ϵ_{yy} are observed at the center of the fracture in cross-section C in Fig. 20, where the upper part of the specimen has an ϵ_{yy} of −0.095% and the lower part of the specimen has an ϵ_{yy} of −0.055%. In cross-sections D and E, the upper part of the specimen has an ϵ_{yy} of −0.057% and −0.038%, respectively, and the lower part below the

Fig. 17 *The displacement field in the y-direction around a growing hydraulic fracture in a three-layer specimen in Test 3.*

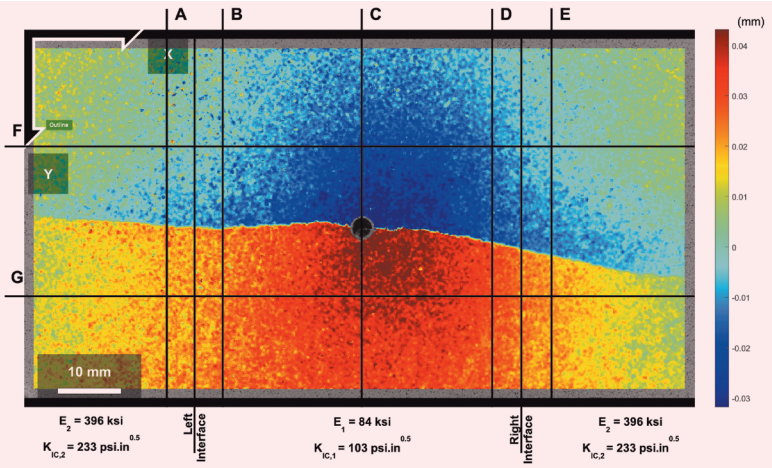

Fig. 18 *The y-displacement along cross-section A in Test 3.*

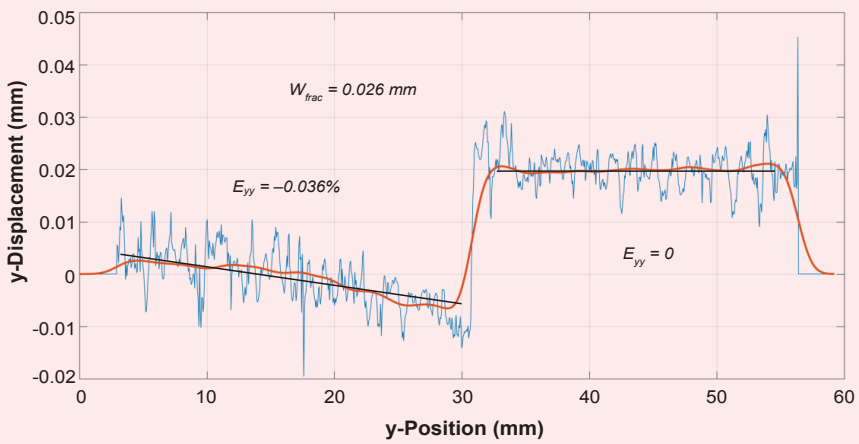

fracture has an ϵ_{yy} of −0.032% and zero, respectively, Figs. 21 and 22. For the horizontal cross-sections that are parallel to the fracture trajectory, the rate of change of the y-displacement along the x-coordinate is shown in Figs. 23 and 24.

In the upper left part of the specimen, the y-displacement decreases at a rate of −0.044% in the left hard layer and decreases at a higher rate of −0.08% in the middle soft layer — left segment of cross-section F in Fig. 23. In the upper right part of the specimen, the y-displacement increases at a rate of 0.092% in the middle soft layer and increases at a lower rate of 0.056% in the right hard layer — right segment of cross-section F in Fig. 23. Similarly, in the lower left part of the specimen, the y-displacement increases at a rate of 0.039% in the left hard layer and increases at a higher rate of 0.077% in the middle soft layer — left segment of cross-section G in Fig. 24.

In the lower right part of the specimen, the y-displacement decreases at a rate of −0.092% in the middle soft layer and decreases at a lower rate of −0.065% in the right hard layer — right segment of cross-section G in Fig. 24. Note that the rate of change of the y-displacement along the x-coordinate changes noticeably across the layer interfaces for both cross-sections F and G in this particular test.

Conclusions

This study presents unique insights into the deformation of multilayer rock specimens in hydraulic fracturing laboratory experiments. Such detailed investigation was made possible through utilizing: (1) cast, synthetic test specimens with controlled layer properties and layer configurations, (2) sheet-like, 2D test specimens, and (3) DIC and discrete Fourier transform.

The deformation characteristics of a homogeneous

Fig. 19 *The y-displacement along cross-section B in Test 3.*

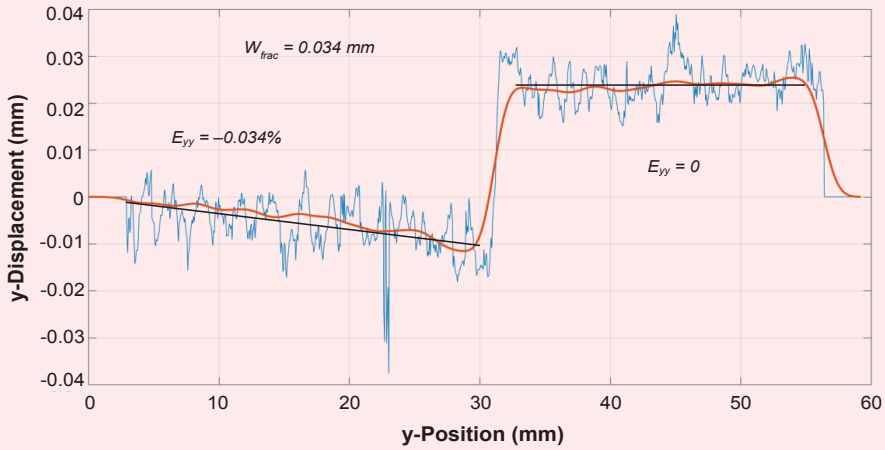

Fig. 20 *The y-displacement along cross-section C in Test 3.*

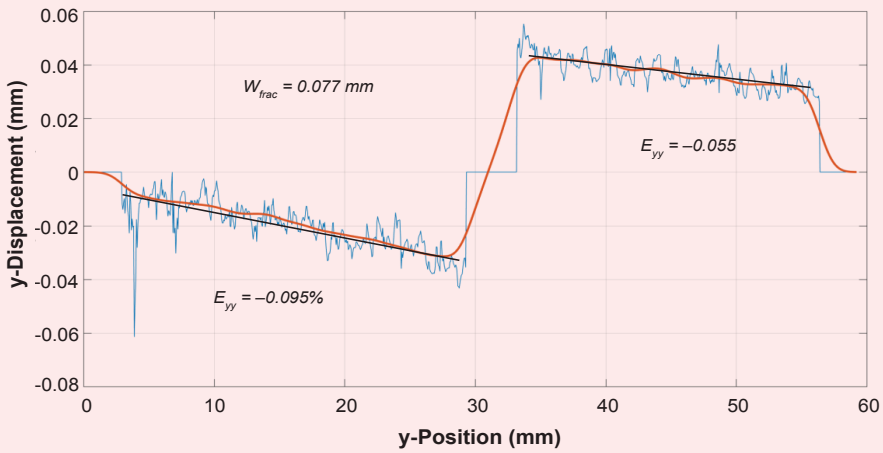

Fig. 21 *The y-displacement along cross-section D in Test 3.*

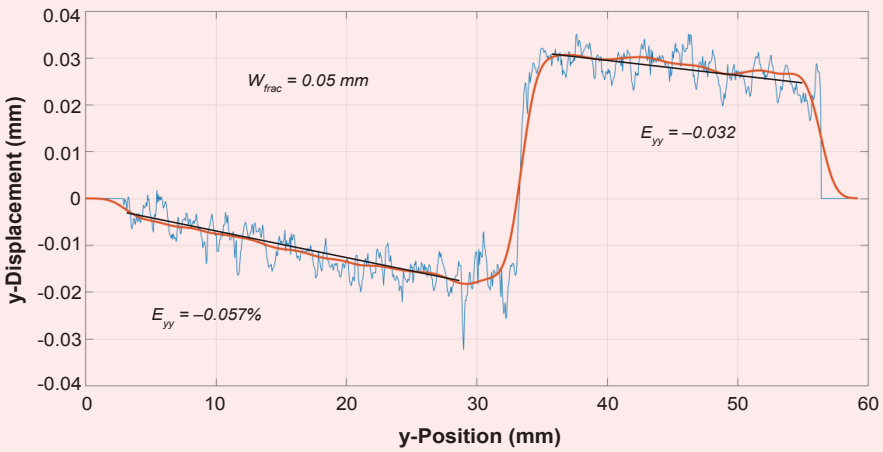

Fig. 22 *The y-displacement along cross-section E in Test 3.*

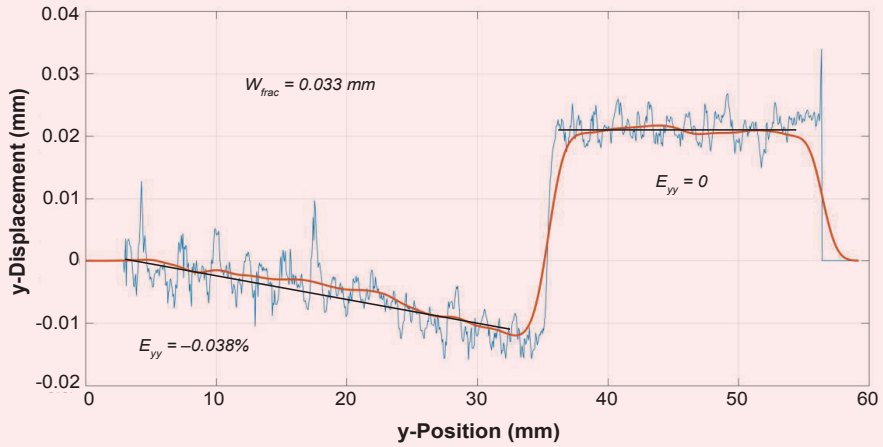

Fig. 23 *The y-displacement along cross-section F in Test 3.*

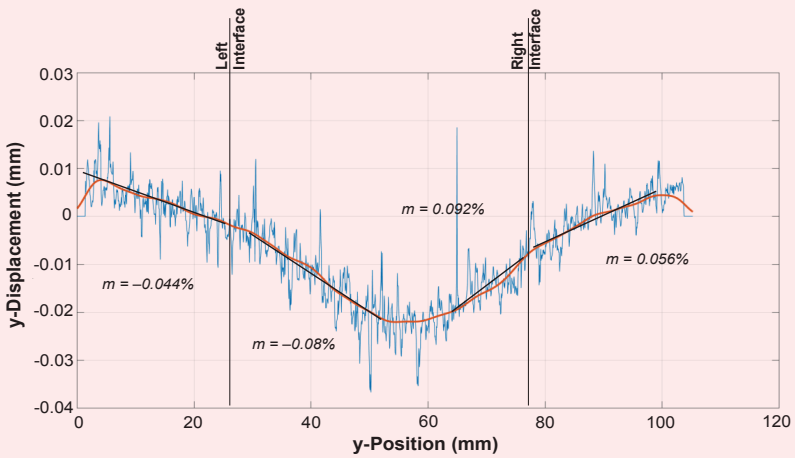

Fig. 24 *The y-displacement along cross-section G in Test 3.*

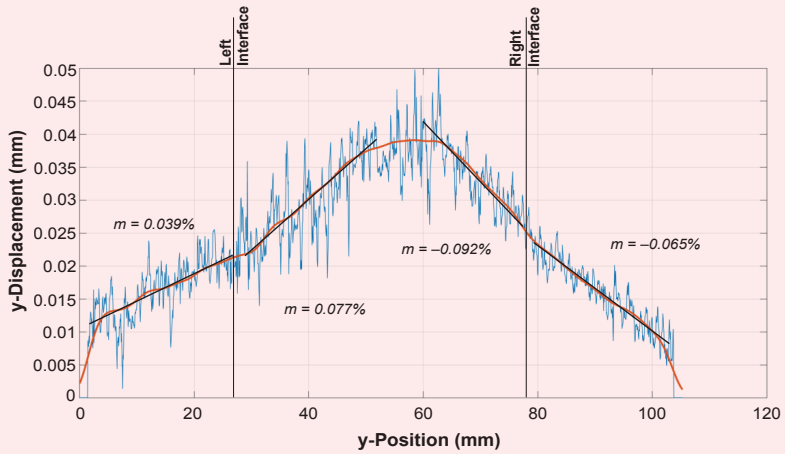

test specimen are demonstrated and compared with the deformation characteristics for two types of mechanically layered specimens: (1) one specimen has a hard middle layer that is bonded to soft outer layers, and (2) the other specimen has a soft middle layer that is bonded to hard outer layers.

Using well-controlled laboratory experiments, this article focused on the observed displacement profiles and ϵ_{yy} magnitudes when a hydraulic fracture propagates through porous test specimens that are mechanically homogeneous as well as test specimens that have contrasting mechanical properties.

Reference

1. AlTammar, M.J., Agrawal, S. and Sharma, M.M.: "Effect of Geological Layer Properties on Hydraulic Fracture Initiation and Propagation: An Experimental Study," *SPE Journal*, Vol. 24, Issue 2, April 2019, pp. 757-794.

About the Authors

Dr. Murtadha J. AlTammar

Ph.D. in Petroleum Engineering, University of Texas

Dr. Murtadha J. AlTammar is a Petroleum Engineer working with the Production Technology Team of Saudi Aramco's Exploration and Petroleum Engineering Center – Advanced Research Center (EXPEC ARC).

Previously, Murtadha worked in the field for 18 months as a Completion and Production Engineer with the Southern Area Gas Production Engineering Division.

He received the 2011 SAPED Significant Achievement Award for leading a well intervention campaign, and also the 2017 EXPEC ARC Best-in-Class Young Researcher Award. Murtadha was an invited speaker at the 2017 American Rock Mechanics Association (ARMA) Hydraulic Fracturing Workshop in San Francisco, CA.

He has been a technical reviewer for many journals. Murtadha has also been a member of organizing several technical committees for the Society of Petroleum Engineers (SPE) and ARMA conferences.

He received his B.S. degree in Petroleum Engineering from the Colorado School of Mines, Golden, CO. Murtadha received his M.S. degree and Ph.D. degree in Petroleum Engineering, specializing in hydraulic fracturing mechanics, from the University of Texas at Austin, Austin, TX.

Dr. Mukul M. Sharma

Ph.D. in Petroleum Engineering, University of Southern California

Dr. Mukul M. Sharma is a Professor and holds the "Tex" Moncrief Chair in the Hildebrand Department of Petroleum and Geosystems Engineering at the University of Texas at Austin, where he has been for the past 34 years. Mukul served as Chair of the department from 2001 to 2005.

During his extensive career, Mukul has made significant contributions in the areas of hydraulic fracturing, injection water management, formation damage, improved oil recovery, and petrophysics.

Among his many awards, he is the recipient of the 2017 John Franklin Carll Award, the 2009 Anthony F. Lucas Gold Medal, and the 2002 Lester C. Uren Award — all prestigious technical awards from the Society of Petoleum Engineers (SPE). In addition, Mukul received the 2004 SPE Faculty Distinguished Achievement Award and the 1998 SPE Formation Evaluation Award.

In 2002, he has served as a SPE Distinguished Lecturer. Mukul has also served on the editorial boards of many journals, and has taught and consulted for more than 50 companies worldwide.

He has published more than 400 journal articles and papers in conference proceedings, and holds 23 U.S. patents.

Mukul has also co-founded two private exploration and production companies, an oil and gas software company, and a consulting company.

He received his B.Tech. degree in Chemical Engineering from the Indian Institute of Technology, Kanpur, India. Mukul received his M.S. degree in Chemical Engineering and his Ph.D. degree in Petroleum Engineering, both from the University of Southern California, Los Angeles, CA.

Have an article you would like to publish? Here are our guidelines.

These guidelines are designed to simplify and help standardize submissions. They need not be followed rigorously. If you have any questions, please call us.

Length

Average of 2,500-4,000 words, plus illustrations/photos and captions. Maximum length should be 5,000 words. Articles in excess will be shortened.

What to send

Send text in Microsoft Word format via email. Illustrations/photos should be clear and sharp. Editable files are requested for graphs, i.e., editable in Excel.

Procedure

Notification of acceptance is usually within three weeks after the submission deadline. The article will be edited for style and clarity and returned to the author for review. All articles are subject to the company's normal review. No paper can be published without a signature at the manager level or above.

Format

No single article need include all of the following parts. The type of article and subject covered will determine which parts to include.

Working Title
Lorem Ipsum here.

Abstract
Usually 150-300 words to summarize the main points.

Introduction
Different from the abstract in that it sets the stage for the content of the article, rather than telling the reader what it is about.

Main body
May incorporate subtitles, artwork, photos, etc.

Conclusion/Summary
Assessment of results or restatement of points in introduction.

Endnotes/References/Bibliography
Use only when essential. Use author/date citation method in the main body. Numbered footnotes or endnotes will be converted. Include complete publication information. Standard is *The Associated Press Stylebook*, 52nd ed. and *Wesbter's New World College Dictionary*, 5th ed.

Acknowledgments
Use to thank those who helped make the article possible.

Illustration/Tables/Photos and explanatory text

If the files are large, these can be submitted separately, due to email size limits. Initial submission may include copies of originals; however, publication will require the originals. When possible, submit original images. Color is preferable.

File Format

Illustration files with .EPS extensions work best. Other acceptable extensions are .TIFF/.JPEG/.PICT.

Permission(s) to reprint, if appropriate

Previously published articles are acceptable but can be published only with written permission from the copyright holder.

Author(s)/Contibutor(s)

Please include a brief biographical statement.

Submission/Acceptance Procedures

Papers are submitted on a competitive basis and are evaluated by an editorial review board comprised of various department managers and subject matter experts. Following initial selection, authors whose papers have been accepted for publication will be notified by email.

Papers submitted for a particular issue but not accepted for that issue may be carried forward as submissions for subsequent issues, unless the author specifically requests in writing that there be no further consideration.

Submit articles to:

Editor
The Saudi Aramco Journal of Technology
C-3D, Room AN-1080
North Admin Building #175
Dhahran 31311, Saudi Arabia
Tel: +966-013-876-0498
Email: *william.bradshaw.1@aramco.com.sa*

Submission deadlines

Issue	Paper submission deadline	Release date
Spring 2021	November 16, 2020	March 31, 2021
Summer 2021	February 9, 2021	June 30, 2021
Fall 2021	May 11, 2021	September 30, 2021
Winter 2021	August 12, 2021	December 31, 2021

There is more.

Applications of Computational Geometry for Automatic Transformation to Unstructured Reservoir Gridding

Firas H. Melaih, Dr. Ali A. Al-Turki, Razen M. Al-Harbi, and Majdi A. Baddourah

Abstract / Reservoir simulation is becoming a standard practice for oil and gas companies, helping with decision making, reducing reservoir characterization uncertainties, and better managing hydrocarbon resources. The reservoir model sizes can reach multibillion grid cells, which led Saudi Aramco to develop an in-house massively parallel reservoir simulator, as well as a pre- and post-reservoir simulation environment[1]. Compared to structured grid modeling, unstructured grid modeling and billon cell pre- and post-simulation processing of reservoir simulation provides engineers with advanced modeling capabilities to represent complex well geometries and near wellbore modeling. Mapping between structured and unstructured (2.5D) domains is not a straightforward task. The indexing in unstructured grids makes creating property modifiers, conducting near wellbore modeling, and local grid refinement difficult.

A Novel Polymer to Create a New Approach of Hole Cleaning

Meshari M. Alshalan, Dr. Abeer M. Al-Olayan, Mohammed M. Al-Rubaii, and Timothy E. Moellendick

Abstract / A new type of drilling fluid, based on a crosslinker, was developed using polymer chemistry to create a superior hole cleaning product that moves drill cuttings, metal, shavings, and other debris out of the wellbore. In addition, the new polymer is capable of transporting cuttings when drilling metallic junk or partial loss of the formation. The gel is generated by adding a crosslinker (borax) to the drilling fluid, and then spotting the second component (polyvinyl alcohol (PVA)) diluted with water at designed percentages. The gel is spotted in the wellbore and then washed out.

Systems and Procedure for Obtaining Relative Permeability Ratio from Data Acquired during Drilling Operation

Babatope O. Kayode and Dr. Bander N. Al-Ghamdi

Abstract / Relative permeability (k_r) is a concept introduced into Darcy's flow equation to account for multiphase flow. k_r is measured through steady-state or unsteady-state laboratory experiments, each with its peculiar advantages and disadvantages. This article discusses the basis for a new, faster, more reliable, and cost-effective methodology for acquiring relative permeability ratio (k_{rr}) data while drilling, and presents the modifications required to current flow equations to replace the use of k_r with the use of k_{rr}.

أرامكو السعودية
saudi aramco

Aramco
Journal
of Technology

Liked this issue? Sign up. It's free.

To begin receiving the *Aramco Journal of Technology* please complete this form, scan and send by email to ***william.bradshaw.1@aramco.com.***

Got questions?

Just give us a call at +966-013-876-0498 and we'll be happy to help!

Scan the QR code to go straight to your email and attach the form!

Subscription Form

Name
Title
Organization
Address
City
State/Province
Postal code
Country
Email address
Phone number
Number of copies

Applications of Computational Geometry for Automatic Transformation to Unstructured Reservoir Gridding

Firas H. Melaih, Dr. Ali A. Al-Turki, Razen M. Al-Harbi, and Majdi A. Baddourah

Abstract /

Reservoir simulation is becoming a standard practice for oil and gas companies, helping with decision making, reducing reservoir characterization uncertainties, and better managing hydrocarbon resources. The reservoir model sizes can reach multibillion grid cells, which led Saudi Aramco to develop an in-house massively parallel reservoir simulator, as well as a pre- and post-reservoir simulation environment[1]. Compared to structured grid modeling, unstructured grid modeling and billon cell pre- and post-simulation processing of reservoir simulation provides engineers with advanced modeling capabilities to represent complex well geometries and near wellbore modeling. Mapping between structured and unstructured (2.5D) domains is not a straightforward task. The indexing in unstructured grids makes creating property modifiers, conducting near wellbore modeling, and local grid refinement difficult.

We present a developed workflow to automatically transform the modeling of property modifiers, near wellbore modeling and local grid refinement between the structured and unstructured domains. Several computational geometry algorithms were developed for efficiency and accuracy, which will preprocess the corners of the top layer cells into data structures. To map regions of interest between domains, the algorithms find all corner points inside them. The regions are translated using the algorithms and the results are exported in the unstructured format.

The two challenges are that the number of corner points is massive, therefore, a brute-force search — even for a simple region of interest is expensive — and irregular regions of interests result in very costly search complexity. We address these by preprocessing the input data in the form of range trees. We also propose a free-shape polygonal search strategy to find all corner points in the regions of interest.

The range tree algorithm provided a fast and robust workflow to perform the transformation from structured to unstructured gridding domains, while providing ease of use with a visual component, to aid with property transformation, near wellbore modeling, and local grid refinement. The algorithm's performance was measured using the time complexity of the preprocessing time, query time, and the space complexity.

The range tree approach is first compared to the other approaches, requiring only O(log(n)+k) operations, compared to the O(n) of linear search. It takes a costly O(nlog(n)) time to preprocess the data into the range tree, however, that is a one-time cost, as well as requiring O(nlog(n)) space in memory.

This work is a major milestone to promote and support the unstructured grid modeling approach for large- and small-scale reservoir simulation models. The algorithm will provide engineers with a simplified workflow and smooth transitioning, allowing advanced capabilities to model complex well geometries and near wellbore modeling, while preserving complex geological features. In addition, this algorithm provides the building blocks in facilitating the migration and conversion of existing structured simulation models.

Introduction

Reservoir simulation is one of the commonly used tools in the oil and gas industry to estimate recovery and conduct studies to support strategic decisions. It is effectively used for the development, production optimization, and management of oil fields. This simulation also gives the reservoir engineers the ability to assess multiple production scenarios to maximize oil recovery and minimize operational cost.

To solve for finite-difference fluid flow (oil, gas, and water) equations for hydrocarbon-bearing formations, a geological model is built from different sources of data sources characterizing the formations. A dynamic model is then built by integrating the static geological model with field dynamic data — pressure, fluid rates, and properties, and development strategies.

The reservoir model needs to be discretized into smaller units to solve fluid flow equations to calibrate and history

match historical field data, and perform predictions. The process of discretization is called "gridding," and the resulting discretized model is referred to as a "numerical grid." The complexity of the reservoir model grid discretization is governed by the complexity of the geology, i.e., fractures, faults, pitchouts, lateral, and vertical heterogeneity, etc. Therefore, different gridding schemes were used, such as structured and unstructured gridding.

Structured grids are three-dimensional (3D) Cartesian grids, which can be defined using the number of cells in each dimension (x, y, and z directions). Accordingly, structured grids inherit the ease of cell indexing from its Cartesian nature. For example, a triplet of three integers (i, j, and k) can reference cells. Furthermore, a region can also be defined using two triplets of the form (i_{start}, j_{start}, and k_{start}) and (i_{end}, j_{end}, and k_{end}). The region in this case is nothing but a rectangular cuboid; however, structured grids have a few caveats when it comes to modeling complex reservoir features such as fractures, faults, and near wellbore regions. This is due to cells being limited in their shapes, i.e., Cartesian nature of the grid. They cannot take more complicated and detailed shapes to represent and preserve complex geological features. For these reasons, unstructured grids were introduced, and found to be more suitable.

Unstructured grids are grids where cells are allowed to take any polyhedral shape. This gridding scheme allows the modeling of complex geological features and near wellbore modeling. Compared to structured gridding, unstructured gridding offers computational efficiency and accuracy when local grid refinement/coarsening is used. One of the flavors of unstructured gridding schemes is the 2.5D unstructured gridding approach. It is a special case, where the grid is divided into identical layers in terms of geometry and number of layers.

The cells within a layer take prism-like shapes, having tops and bottoms that can be of any polygon shape. Subsequently, we will be referring to them simply as "unstructured grids." The 2.5D unstructured grids provide a compromise between structured and fully unstructured grids, having the freedom in the geometrical shapes in lateral directions, with retention of structure in the vertical direction.

These features overcome the aforementioned limitations of structured grids and avoid the unnecessary complexity of the fully unstructured gridding scheme; however, with the flexibility of cell shapes comes different challenges. In particular, unstructured grids lose the ease of indexing in the x and y directions, and cells within a layer can only be indexed using an irregular numbering scheme. Instead, each cell has a unique ID that may not necessarily be in sequence or following a certain order. In addition, these IDs do not encode any spatial reference of the whereabouts of the cells within the grid. Consequently, to specify a single region in an unstructured grid, one must list contiguous cell IDs, which is an arduous task to do manually.

In this article, we leverage algorithms from computational geometry to alleviate the cell's indexing problem in unstructured grids by:

- Efficiently converting regions from the structured domain to the unstructured domain.
- Providing the ability to select arbitrary prism-like regions in unstructured grids.
- Developing a graphical interface to interactively make region selections.

The algorithm could also be used with the structured format to select arbitrary regions rather than only cuboid ones. As the basis for the proposed solution, 2D range trees were used. These 2D range trees are data structures to hold d-dimensional Euclidean points, where the points are dictionary sorted by their coordinates. They are used to answer orthogonal range reporting queries; that is, each query is the Cartesian product of intervals of real numbers. They were developed independently by a handful of authors[2-5].

This article will describe how the algorithms are used, as well as describe how to implement fractional cascading[4,6] to improve their query time complexity, while not increasing the space complexities, nor the preprocessing time complexity.

Problem Definition

Let us start by properly defining the problem: A 2.5D unstructured grid is given — where the 2.5D grid means all the layers are identical in the x and y directions — and a prism-like region, *R*, specified with a triplet of (x, y, and z) coordinates. The top and bottom sides of *R* are the same polygon, *P*, and the height of the top and bottom is specified by the layer number, Fig. 1. The goal is to find the IDs of all the cells of the grid that intersect *R*.

Usually, the grid will be queried many times with different regions. From the computational efficiency viewpoint, the algorithm efficiency heavily depends on the reservoir model size — number of cells — and the irregularity of the selected regions. In simple cases, a handful of queries will not take more than a few seconds when it is solved,

Fig. 1 *A region of a 2.5D unstructured grid.*

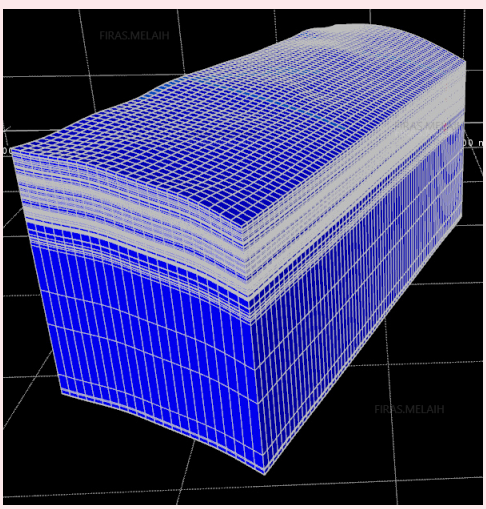

by simply checking *R* against every cell. This problem becomes time-consuming, less efficient, and computationally expensive with the increasing complexity of the region and model's number of cells. A viable solution was devised and is described later.

Simplification

The first step toward computational efficiency is simplifying the problem to a 2D problem. *R* is simply considered a prism. Therefore, its layers can be specified in the usual way, and we can focus on the problem in the lateral directions. Subsequently, we effectively reduced this problem from a 3D problem to a 2D problem.

We can further simplify the problem by observing that a cell intersects *P* if one of its corners is inside *P*, Fig. 2. This turns it into the simpler problem of finding the points that lie inside *P*. This type of problem is called polygonal range searching. Therefore, *n* will denote the number of points in a single layer of our grid.

There are exceptions to this simplification such as edge cases, Fig. 3. These cases occur when a cell does not have any corners inside *P*, but the edges of both the cell and *P* intersect, e.g., if a corner of *P* is inside the cell. This can be remedied by checking nearby neighbors if they intersect *P*, and then adding them to the solution if they do. We can precompute which cells in a layer are neighboring each other to save time.

Fig. 2 *A sample image showing that a cell intersects P if one of its corners is inside P.*

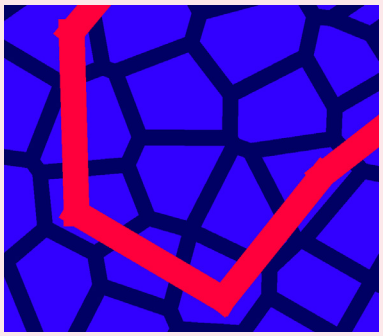

Fig. 3 *None of the corners of the bottom left cell are inside, yet it still intersects.*

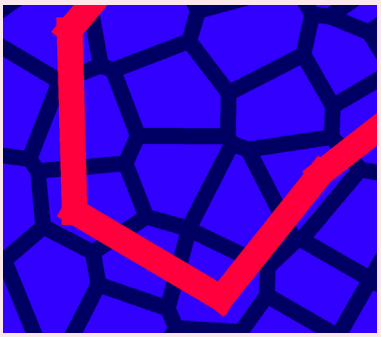

Approaches

Solving the problem in the naïve way, where every point is checked whether it lies in *P* or not, is efficient memory-wise, as it uses no memory overhead, and also is efficient time-wise if a query is made once, or only a handful of times. The complexity of the query time of this solution is O(n), while the space complexity is O(k) for a query (and O(n) for storing the points), where *k* is the number of points inside *P*. (This is in fact the optimal solution, and we cannot do any better.) Consequently, if the model size is large, say 5 million points per layer, and with 200 regions to query, then 1 billion checks are required, going over all the points.

This is why there is a need for preprocessing the points to satisfy all these queries. There is no algorithm tailored for polygonal range searching, specifically in the literature. It can be reduced to other problems via triangulation or other means. We opted to reduce the problem in a different way: To find the bounding box (*B*) of *P*, apply a 2D orthogonal range searching algorithm, and then filter the results with the winding number algorithm. Figure 4 shows an example of a *P* and it's *B*.

For efficiency, the winding number algorithm should be embedded within the orthogonal range searching during appending to the results list. This is to decrease the amount of extra memory to be used. It is counterproductive to include the points inside *B* but outside *P*.

There are two main approaches to solving the orthogonal range searching: k-d trees and 2D range trees. We will be using the 2D range tree algorithm in this article. The 2D range trees have a preprocessing time cost of O(nlog(n)), which we only have to do once, and a query time complexity of O(log(n)+k), which is extremely fast in comparison to the O(n) of the naïve method.

Fig. 4 *The P shown in red, with its B in white.*

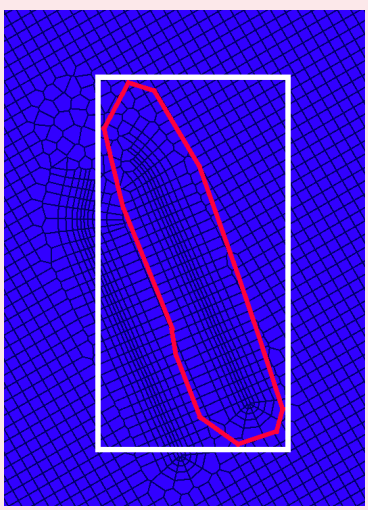

The trade-off is in the space cost, where the naïve method has a space complexity of O(n), while the 2D range tree has a space complexity of O(nlog(n)). This is a point that needs to be emphasized: The tree must be saved as a file after construction, to be used again for later queries. Otherwise, it would have to be constructed every time there is a need to query a set of regions.

2D Range Tree

The idea of a 2D range tree, T, is to have a binary tree ordered by the x coordinates of the points, and then each node, N of T, contains a binary tree called the associated tree A(N), Fig. 5. It consists of only the points in N's subtree, and it is ordered by the y coordinate. This is the reason the space complexity of T is O(nlog(n)); every one of the O(log(n)) levels contains a duplicate of the original n points, where the points are divided among the nodes of the level in the associated trees.

The query is computed by traversing T until reaching the split node, S, a node where there are points with x coordinates between the x coordinates of B in both branches of S. Once there, two traversals occur, one to the left branch, and one to the right branch. Each traversal goes to its respective leaf with the x coordinate of B — or the closest coordinate inside B — while collecting points within P on the way there. Fractional cascading is also used in the algorithm to ensure that the time complexity of the query is O(log(n)+k) rather than $O(\log(n)^2+k)$.

Range Tree Preprocessing

The first step of preprocessing is to make a copy of the layer's points and replace the coordinates with ranks. Ranks are the indices of the points when they are dictionary sorted, i.e., the x rank of a point, p, denoted as $r_x(p)$, is the index of p when the points are dictionary sorted by x first and y second, and the y rank, $r_y(p)$, is the index of p when the points are dictionary sorted by y first and x second. The replacement is to remove (x, y) and use $(r_x(p), r_y(p))$ instead. The reason ranks are used instead of the coordinates directly is that ranks ensure that each pair of numbers is distinct in both entries.

Then, the rank pairs are dictionary sorted by the y ranks, and passed to the root of the tree. This is the beginning of the recursive construction process: At each node, N, N will be passed at the A(N), which it will keep, as well as assigning itself the x rank in the middle of A(N). Then, it will make a copy of A(N) to be split into two halves based on whether the x rank is higher or lower than the N's x rank. Next, these two halves will be passed to the respective child nodes. N_L and N_R will denote the left and right children, respectively.

After the children are done, the cascading will be added to N. In this step, for each of the two child nodes, an array will be created with the same size as A(N), denoted by $C_L(N)$ and $C_R(N)$ for the left and right children, respectively. $C_L(N)[i]$ will store an index j, where $A(N)[i] \le A(N_L)[j]$, but $A(N)[i] > A(N_L)[j-1]$. In other words, $C_L(N)[i]$ will point to the earliest entry in $A(N_L)$, which is greater than A(N)[i], and similarly for the right side. If no such j exists, then it will store the size of $A(N_L)$. Figure 6 shows the cascading.

Fig. 5 *A 2D range tree, where each node has an associated tree[7].*

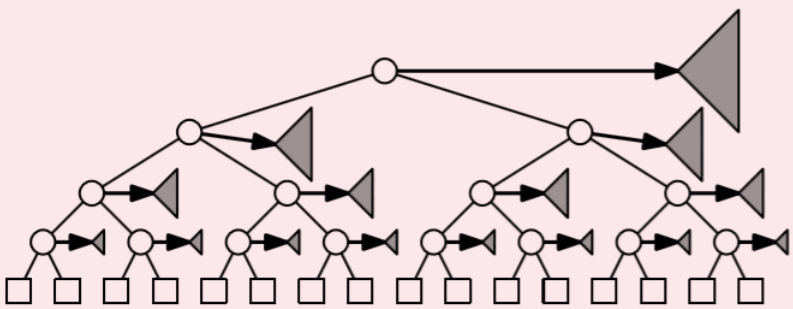

Fig. 6 *Example of fractional cascading (some omitted)[8].*

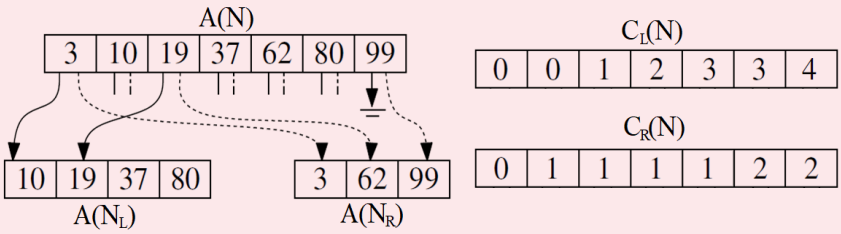

For example, in Fig. 6, A(N)[2] = 19 (using 0-based indexing), and the earliest entry in $A(N_R)$ that is greater than or equal to 19 is 62 at index 1. Therefore, in $C_R(N)$ [2], the value is 1, which is the index of 62 in $A(N_R)$. For A(N)[6] = 99, there is no entry in $A(N_L)$ that is greater than or equal to 99, and so it simply contains 4, which is the length of $A(N_L)$, so that it acts as a sentry.

Without fractional cascading, at each stage of the query, a binary search must be done to find the smallest y rank in A(N) that is inside *B*, and all these binary searches will add up to an $O(\log(n)^2)$ time complexity. Instead, we can eliminate them almost entirely with fractional cascading, having only to do one binary search at the *S*, and then traversing the fractional cascades, as they will land on the first such y rank inside *B*.

Range Tree Query Algorithm

For the query, the first step is to find the *B* of *P* via the minimum and maximum of the x and y coordinates of the vertices of *P*. Then, *B's* x coordinates are translated into ranks by binary searching for the minimum and maximum ranks of points that lie within *B's* x coordinates. Using these two extreme ranks, we traverse *T* to find the *S* — this is achieved by choosing the child nodes that contain both ranks at every level until they are not contained in the same child.

Once *S* is found, two binary searches are done to find the extreme y ranks, similar to the step done earlier for x. This is done now and not with x because it is more efficient to search the smaller array, A(S), rather than the large *A* of the root. Two traversals are done at this part of the algorithm: One to the left branch, and one to the right branch, both going down to the leaves to reach the extreme x ranks.

In the sequel, the "outer node" will refer to the node in the same direction of the traversal, and the "inner node" will refer to the node opposite the direction of the traversal, i.e., if traversing the left branch, the left children are the outer nodes, and the right children are inner nodes, and the opposite holds for the right branch. Whenever the inner node is taken, nothing is to be done, and the traversal continues. Whenever the outer node is taken, all the rank pairs in the inner nodes will have x ranks contained in the x bounds of *B*.

These pairs will be checked against the query *P* for containment using the winding number algorithm. Following the cascade, pointers will guarantee that the checking starts at the earliest pair with a y rank contained in *B*, and the checking can stop once the y rank lies outside *B*.

Results

In Fig. 7, we compare the naïve linear approach against the range tree approach. The x-axis denotes the number of points tested (where it is for a single layer), and the y-axis denotes the amount of time taken in microseconds. Along the x-axis, the number of points starts from eight, and doubles with every iteration. The query is simply a 10 × 10 square near the center of the layer. The reason behind choosing a small region is the time complexity (cost) of the range tree query, which is O(log(n)+k). This means that having a larger region will result in the *k* dominating the term, and therefore, both algorithms will have similar times, and the difference will not be noticeable.

Fig. 7 *The input size (number of layer points) plotted against the amount of time taken by each algorithm in microseconds; naïve in blue, range tree in red.*

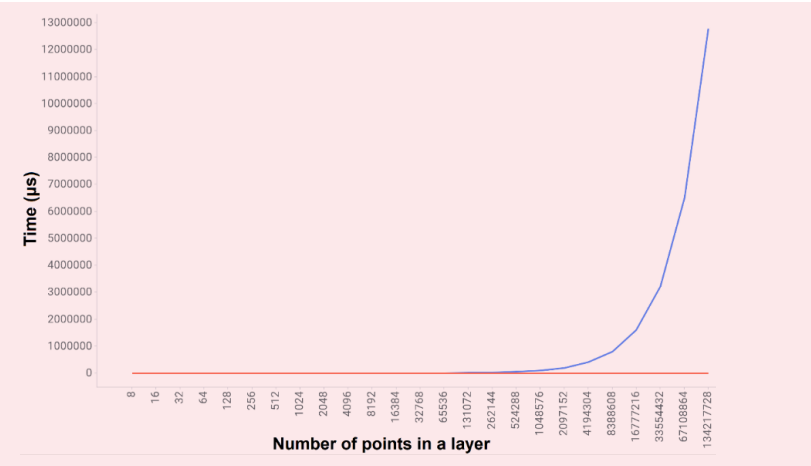

As the number of points grow, the amount of time taken by the naïve algorithm is proportional to it. This is clear as seen in the log-scale graph in Fig. 8, where a line almost perfectly fits on the log base 2 of the input size and the log base 2 of the algorithm time.

On the other hand, the range tree approach only takes a logarithmic amount of time. Given a layer with 134 million points (2^{27}), the query time for the naïve algorithm was 12.7 seconds. Therefore, if we were to suppose that we needed to do this for 1,000 regions, this would take over 3.5 hours. Conversely, the range tree algorithm took only 232 microseconds, and 1,000 queries would take it 0.23 seconds. Table 1 lists the input size vs. time taken in microseconds.

Figure 9 shows a graphical interface, which was implemented to simplify the region's selection. This allows for inspecting, adding/deleting, and editing the regions.

Fig. 8 *The naïve algorithm takes a linear amount of time.*

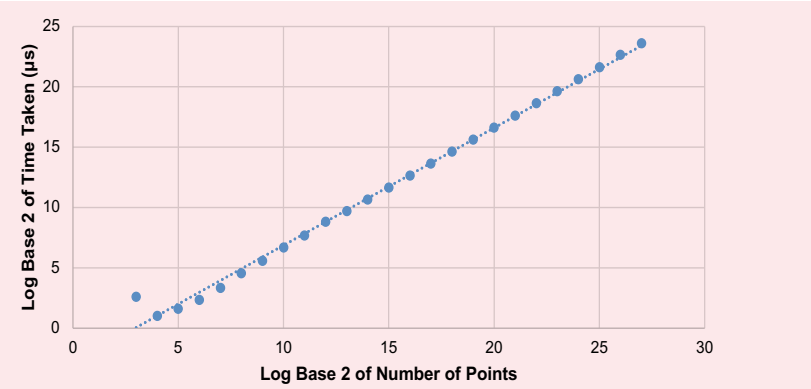

Table 1 *Input size vs. time taken in microseconds by both algorithms.*

Number of Points	Naïve Time (µs)	Range Tree Time (µs)
8	6	19
16	2	4
32	3	8
64	5	9
128	10	13
256	23	18
512	48	19
1,024	101	20
2,048	201	21
4,096	442	21
8,192	827	22
16,384	1,588	23
32,768	3,180	34
65,536	6,297	57
131,072	12,558	76
262,144	25,279	133
524,288	50,505	301
1,048,576	100,392	95
2,097,152	200,640	150
4,194,304	402,064	146
8,388,608	801,379	140
16,777,216	1,602,892	137
33,554,432	3,216,354	143
67,108,864	6,520,000	264
134,217,728	1,278,7232	232

It also facilitates the translation between what is envisioned by the engineers to the simulation model input data and vice versa.

Conclusions

To address mapping between structured and unstructured (2.5D) domains, an efficient workflow was developed to automatically transform the modeling of property modifiers for near wellbore modeling and local grid refinement/coarsening between the structured and unstructured domains. Several computational geometry algorithms were developed and assessed for efficiency and accuracy. The regions are then translated into an unstructured format of the targeted reservoir simulator.

Fig. 9 *An image of the graphical interface to the range tree algorithm.*

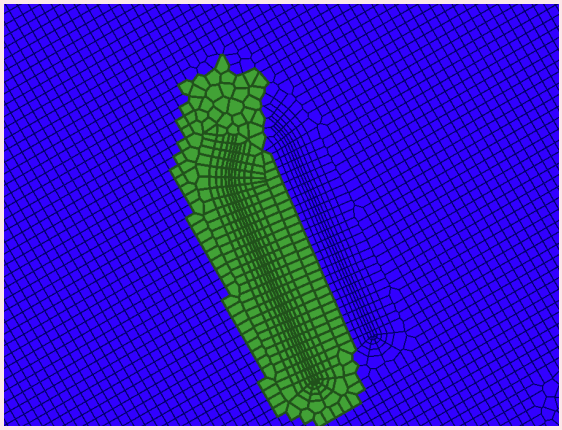

It has been shown that range trees are a viable option to efficiently select regions in grids, whether structured or unstructured, as long as there is a large number of such regions that needs to be created and/or converted. The difference between the range tree approach and the naïve approach in terms of time is huge; the range tree approach takes only fractions of a second to accomplish what the naïve approach can do in hours. This is in agreement with the theory. Its trade-off in the memory footprint is justifiable if there is a large number of regions, where the strength and computational efficiency is demonstrated.

Acknowledgments

This article was prepared for presentation at the European Association of Geoscientists and Engineers Conference and Exhibition, Amsterdam, the Netherlands, December 8-11, 2020.

References

1. Dogru, A.H., Fung, L.S.K., Al-Shaalan, T.M. and Pita, J.A.: "From Mega Cell to Giga Cell Reservoir Simulation," SPE paper 116675, presented at the SPE Annual Technical Conference and Exhibition, Denver, Colorado, September 21-24, 2008.
2. Bentley, J.L.: "Decomposable Searching Problems," *Information Processing Letters*, Vol. 8, Issue 5, June 1979, pp. 244-251.
3. Lee, D.T. and Wong, C.K.: "Quintary Trees: A File Structure for Multidimensional Database Systems," *ACM Transactions on Database Systems*, Vol. 5, Issue 3, September 1980, pp. 339-353.
4. Lueker, G.S.: "A Data Structure for Orthogonal Range Queries," paper presented at the 19th Annual Symposium on Foundations of Computer Science, Ann Arbor, Michigan, October 16-18, 1978.
5. Willard, D.E.: "The Super-B-Tree Algorithm," Technical Report, Harvard University, Cambridge, MA: Aiken Computer Lab, 1979, 39 p.
6. Willard, D.E.: *Predicate-Oriented Database Search Algorithms*, New York: Garland Publication Company, 1979, 384 p.

7. van Kreveld, M.: "Lecture 8: Range Trees," presentation, 61 p. http://www.cs.uu.nl/docs/vakken/ga/2019/slides/slides5b.pdf.

8. de Berg, M., Cheong, O., van Kreveld, M. and Overmars, M.: *Computational Geometry: Algorithms and Applications*, 2nd edition, Springer-Verlag, 2008, 379 p.

About the Authors

Firas H. Melaih

B.S. in Computer Science, King Fahd University of Petroleum and Minerals

Firas H. Melaih is a Petroleum Engineering Systems Analyst working in the Simulation Systems Division of Saudi Aramco's Petroleum Engineering Application Services Department. His primary interests include algorithms and mathematics.

In 2018, Firas received his B.S. degree in Computer Science from King Fahd University of Petroleum and Minerals (KFUPM), Dhahran, Saudi Arabia.

Dr. Ali A. Al-Turki

Ph.D. in Petroleum Engineering, University of Calgary

Dr. Ali A. Al-Turki is a Petroleum Engineering Systems Specialist working in the Simulation Systems Division of Saudi Aramco's Petroleum Engineering Applications Services Department. Ali has been with Saudi Aramco for the past 21 years.

His research interests include multiphase flow in fractures, thermal (SAGD) and thermal solvent (ES-SAGD) recovery processes, assisted history matching methodologies, uncertainty quantification and management, and high performance computing.

Ali is a Society of Petroleum Engineers (SPE) Certified Petroleum Engineer.

He is the author and coauthor many technical papers, along with a number of patents.

Ali received his B.S. degree in Computer Science from King Fahd University of Petroleum and Minerals (KFUPM) Dhahran, Saudi Arabia. He received both his M.S. and Ph.D. degrees in Petroleum Engineering from the University of Calgary, Alberta, Canada.

Dr. Razen M. Al-Harbi

Ph.D. in Computer Science, King Abdullah University of Science and Technology

Dr. Razen M. Al-Harbi is a Petroleum Engineering System Analyst working in the Simulation Systems Division of Saudi Aramco's Petroleum Engineering Applications Services Department. Razen is leading the Fourth Industrial Revolution team in his Division to enable artificial intelligence and machine learning technologies in simulation systems.

His primary research interest includes optimizing massively parallel applications running on large installations of high performance computing (HPC) systems and data analytics on HPC infrastructure.

Razen received his B.S. degree in Information and Computer Science from King Fahd University of Petroleum and Minerals (KFUPM), Dhahran, Saudi Arabia, in 2006. Then, he received his M.Eng. degree in 2006 from Cornell University, and his Ph.D. degree in Computer Science from King Abdullah University of Science and Technology in 2016.

Dr. Majdi A. Baddourah

Ph.D. in Civil Engineering, Old Dominion University

Dr. Majdi A. Baddourah is a Simulation and High Performance Computing Specialist working in the Simulation Systems Division of Saudi Aramco's Petroleum Engineering Application Services Department.

Prior to joining Saudi Aramco in 2003, Majdi worked for Lawrence Berkeley National Laboratory, CA conducting research and development for the U.S. Department of Energy, utilizing high performance computers. He also worked at the NASA Langley Research Center, VA as a High Performance Specialist. Majdi is a key supporter for POWERS and GigaPOWERS, providing support for Saudi Aramco's strategic studies.

He also works with the EXPEC Computing Planning and Technology Division and the EXPEC Computer Operations Department as an active technologist in evaluating the deployment of state-of-the-art high performance computing solutions at minimal cost.

Majdi is the author and coauthor of numerous technical papers. He also holds many U.S. patents. Throughout Majdi's extensive career, he has mentored many young professionals.

Majdi received both his B.S. degree and M.S. degree in Civil Engineering from the University of South Carolina, Columbia, SC. He received his Ph.D. degree in Civil Engineering from Old Dominion University, Norfolk, VA.

A Novel Polymer to Create a New Approach of Hole Cleaning

Meshari M. Alshalan, Dr. Abeer M. Al-Olayan, Mohammed M. Al-Rubaii, and Timothy E. Moellendick

Abstract /

A new type of drilling fluid, based on a crosslinker, was developed using polymer chemistry to create a superior hole cleaning product that moves drill cuttings, metal, shavings, and other debris out of the wellbore. In addition, the new polymer is capable of transporting cuttings when drilling metallic junk or partial loss of the formation. The gel is generated by adding a crosslinker (borax) to the drilling fluid, and then spotting the second component (polyvinyl alcohol (PVA)) diluted with water at designed percentages. The gel is spotted in the wellbore and then washed out.

The strong carrying capacity of the gel is expected to remove all cuttings and debris from the wellbore. The other conventional hole cleaning pills contain large solids and/or are expensive. The other method to clean excessive junk from the wellbore is mechanically, by running many hole cleaning trips, which consumes a lot of rig time.

This practice has saved time by reducing the clean out trips. Moreover, the new product, coined "polysweep" can provide a potential solution to hole cleaning when milling metallic junk or drilling at partial circulation. Polysweep has been successfully trial tested in a deviated well — with partial losses. During the field trial, it was observed that polysweep was effective in carrying all the shaving debris and cuttings out from the wellbore throughout the drilling operation with no trouble. Also, polysweep has shown good compatibility for use in water-based drilling fluids.

Polysweep brings value through both its cost-effective, simple formulation, as well as its ability to reduce the number of wiper trips. Besides that, it is environmentally friendly as all the components of the fluid are nontoxic. The new composition has the potential of producing modified fluids for several different applications, including hole cleaning sweeps, loss circulating materials, and fracturing fluids.

Introduction

Optimization of hole cleaning during a drilling operation is very important to enhance the drilling rate, however, optimum hole cleaning in drilled hole sections remains a major challenge. Hole cleaning must be engineered. The penetration rate is highly dependent on hole cleaning. Insufficient hole cleaning can cause numerous issues, including stuck pipes, decreased drilling rates, significant drag and torque, lost circulation, wellbore instability, erratic trends in equivalent circulating density, more wiper trips, back reaming, bad quality of cement jobs, bit balling, and obviously increases in the cumulative cost of drilling operations and the extension of the overall operational time[1].

If inadequate attention is paid to hole cleaning, such problems can be a root cause of losing the well. To overcome these problems, drilled cuttings should be efficiently transferred from the hole section by drilling fluid to the surface. Hole cleaning is a key element of all successful well design strategies and the issue cannot be over emphasized in horizontal or maximum reservoir contact wells in particular[2].

Hole cleaning is often the deciding factor between the success and failure during drilling. Historically, most stuck pipe incidents can be attributed to poor hole cleaning[3]. It is very important to identify any wellbore stability problems that are affecting the hole cleaning before making changes to the initial planned hole cleaning strategy. Hole cleaning is more difficult with oil-based mud (OBM) due to the following reasons: (1) the cuttings will not easily disperse into the OBM as with water-based mud (WBM), (2) OBM is more Newtonian than WBM, and (3) OBM has lower thixotropic properties than WBM[4].

To achieve optimum hole cleaning it is necessary to increase the flow rate to achieve annular velocity to more than the slip velocity, while simultaneously optimizing mud rheology to increase the transport ratio. Theoretically, if the annular velocity is more than the slip velocity, the mud will lift the drilling cuttings and ultimately the drilling cuttings will be transported out of the wellbore. A low annular velocity can cause an unwanted volume of cuttings in the annulus. Several drilling case studies have proven that if the cutting's concentration or cutting's volume in the annulus is more than 5%[5], it can lead to a tight hole, stuck pipe, or induced loss circulation events.

Inadequate hole cleaning can make drilling cuttings accumulate in the annulus of the open hole section, and as a result, cause the drilling rate to decrease. Drilling in complicated geological zones, such as faults, joints,

fractures, layered formations, weak bedding planes, etc., normally cause instability problems for the hole section, therefore, a better understanding of the geomechanics of the fracturing of the formation will act as an important solution to cure the problems of hole sections[6]. The instability problems of the hole section can be caused by the effect of mechanical influences, chemical influences, or a combination of them.

The density of the mud — too high or too low — as well as the drilling mud parameters and bad operational practices often causes mechanical wellbore damage. This damage may include excessive vibration, high torque and drag, and not performing wiper trips if the hole section dictates[7]. On the other hand, chemical wellbore damage is caused by use of improper drilling fluids or improper concentrations of inhibitors added while drilling reactive shale formations[8]. If the hole starts to have sloughing or caving problems, the quantity of shale transferred to shakers may appear normal, masking the large quantity that may accumulate in the annulus.

Hole cleaning is a common problem encountered while drilling. The consequences of inadequate hole cleaning vary depending on several factors, such as the rate of penetration, the loss severity, and the criticality of the drilled zone[9]. Several materials and methods for optimizing hole cleaning are used globally. Consequently, most of them have shown weakness dealing with the breadth of the required applications, particularly in deviated sections. The main object of any hole cleaning optimization product is to enhance the ability of the mud system to carry out the cuttings all the way to the surface, effectively and economically[10]. Polysweep is a combination of two fluids that will generate a gel phase in seconds after mixing. The created gel is strong enough to remove the drilling cuttings to the surface, even in the most difficult operational environments.

In addition, the same cross-linked synthetic technology (polysweep) can also provide a potential solution to mud losses in high permeable and fractured loss zones. The components used in the formulation react quickly to form a gel with flexible and ductile characteristics, and therefore can provide an effective solution for stopping lost circulation in fractures and high permeable zones. Due to flexible, ductile and deformable characteristics, it can easily mold into the fractures and high permeable zones to produce superior sealing and blocking.

The reaction to form the gel is very fast and does not require special conditions to trigger the reaction. Due to very quick reaction time, the components have to be placed in the loss zone separately to create the gel in situ. One of the components can be added to bentonite mud, and the other component can be pumped to introduce it into the bentonite mud in the vicinity of the loss zone to convert the combined products into a stiff gel. All lab tests were conducted successfully prior to the request of a field trial.

Laboratory Development and Assessment

Compressive Strength

In this test, the compressive strength of the final polysweep material was tested using a stable micro-system, Fig. 1. The test was conducted with different ratios of the crosslinker (borax) and polyvinyl alcohol (PVA) to reach to the optimum ratio that makes the polymer rigid, and at the same time pourable and flexible to allow it to move through the pores. The results show that the strength of the polymer was increased with the increase of the borax concentration ratio, Figs. 2a, 2b, and 2c.

Sealing and Blocking Efficiency Evaluation

Simulating High Permeable loss zone ($CaCO_3$ bed). To evaluate the sealing and blocking efficiency of the polysweep, we used a low-pressure, low temperature (LPLT) test apparatus designed by a Saudi Aramco scientist and high permeable carbonate bed material to simulate a high permeable loss zone, Fig. 3. The LPLT cylinder has a diameter of 7.5 cm and a length of 26.5 cm. The carbonate bed has a measured porosity of 50%.

In this test, the sealing efficiency of the polymer was evaluated by simulating a very high permeable bed made of 4 mm to 6 mm sized carbonate particles. To measure the blocking and sealing efficiency of the polysweep, we conducted tests using drilling mud to simulate a loss circulation event, and then we mixed one component of the polysweep with the drilling fluid, and let it soak

Fig. 1 *An image showing the stable micro-system model.*

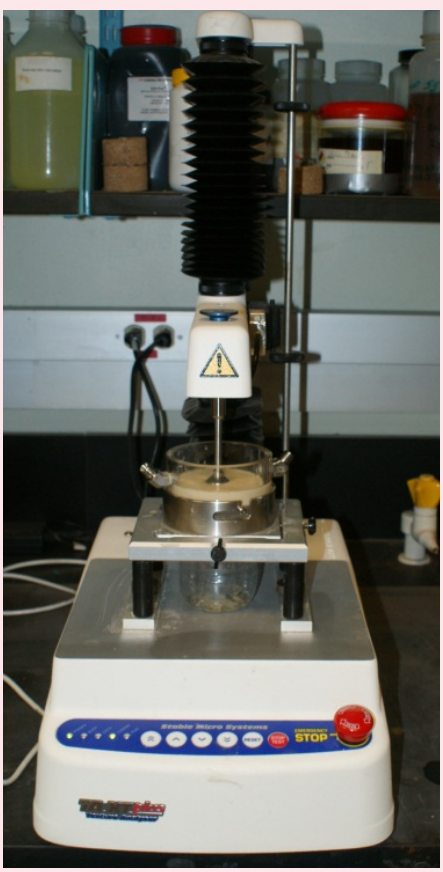

Fig. 2 *The strength of the polymer was increased with the increase of the borax concentration ratio.*

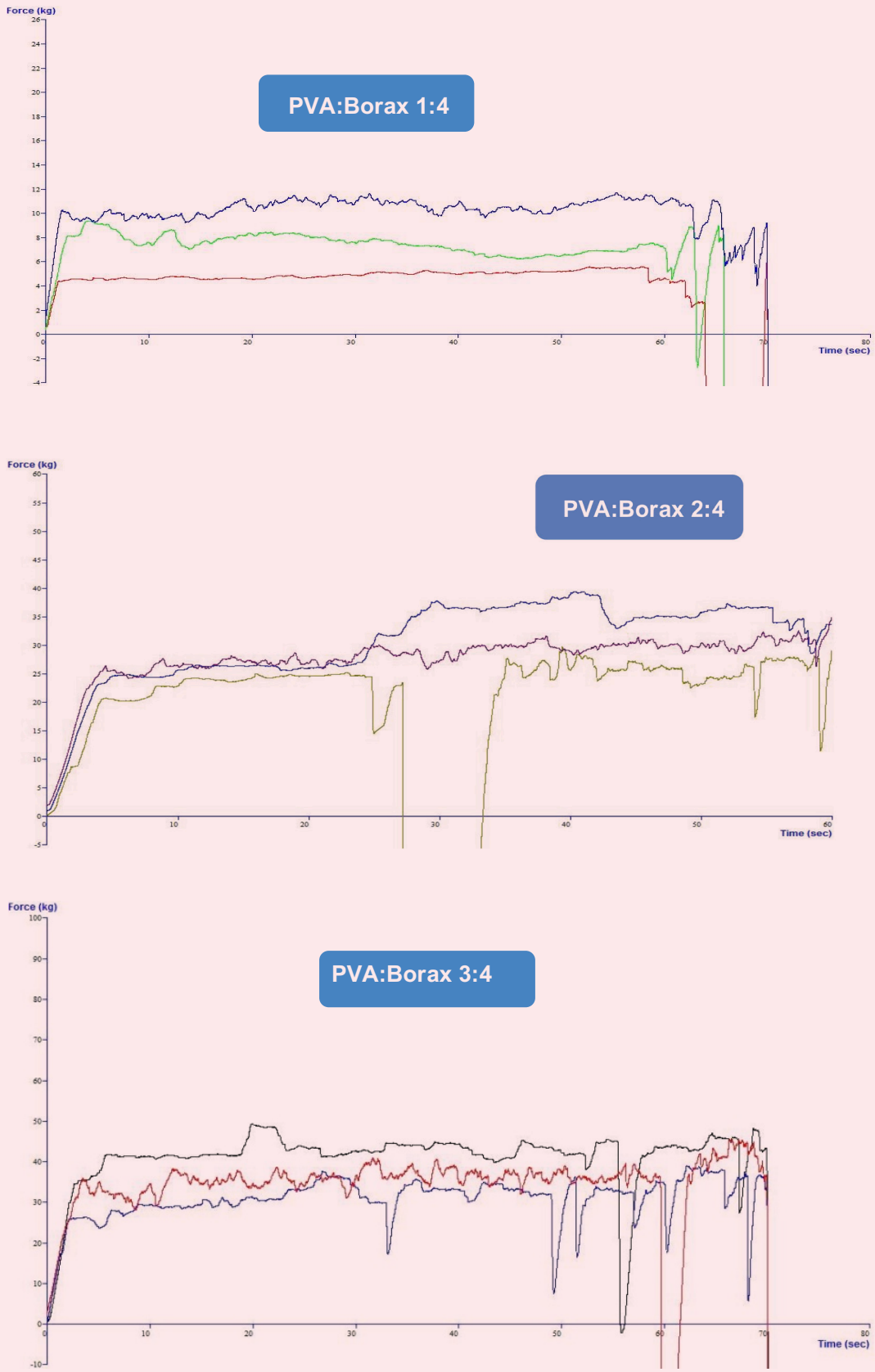

Fig. 3 *The LPLT test apparatus filled with high permeable carbonate bed material.*

for 10 minutes. After that, the other component of the polysweep was added to the mud to measure the sealing and blocking efficiency of the polysweep. We applied a pressure of 100 psi to simulate the overbalance pressure of the borehole at room temperature.

The polysweep was tested and compared to two commercial products used by Saudi Aramco: Stoploss and Soluseal. All tests were conducted three times.

The result shows that both polysweep, Fig. 4a, and Soluseal, Fig. 4b, have a high capacity to plug the pores and prevent the drilling fluid to pass through. On the contrary, stoploss, Fig. 4c, has no ability to plug the pores, and all the liquid passed through.

Simulating Super-K loss zone (Pebble bed). To evaluate the sealing and blocking efficiency of the polysweep for a supper permeable zone, the pebble bed was used to simulate it, Fig. 5a. The result shows that polysweep alone could not plug the pores and all the fluid passed through, Fig. 5b. The test was run again, but this time polysweep was added. The process was conducted in two steps: (1) polysweep was added first and left to soak for 10 minutes, and (2) then date tree roach root fibers was added. This time, the sealing was excellent, plugging the pores completely, not allowing any fluids to pass through, Fig. 5c.

Thermal Stability

The polymer was tested for different temperatures and pressures to evaluate its stability under well conditions. Figure 6a shows the test sample conducted at 80 °F with no pressure. Figure 6b shows the test sample conducted at 150 °F and 500 psi, using static pressure. Figure 6c

Fig. 4 *The LPLT test conducted using carbonate bed material for (a) polysweep, (b) Soluseal, and (c) stoploss.*

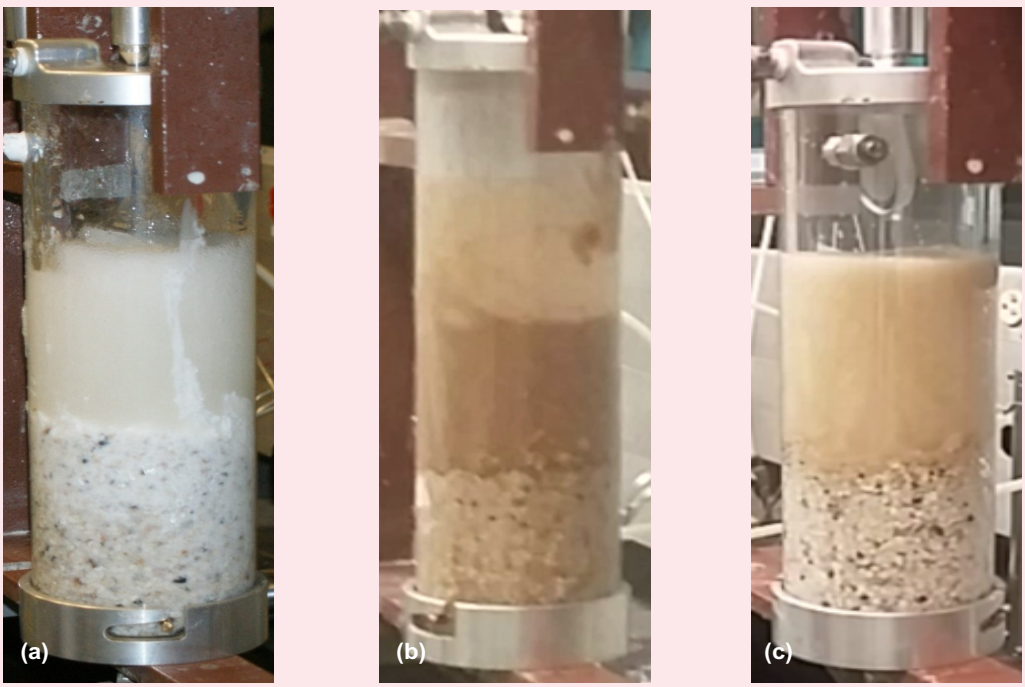

Fig. 5 *The LPLT test using pebble bed for (a) polysweep, (b) polysweep system, and (c) polysweep plus date tree roach root fibers.*

Fig. 6 *Images of the polymer after testing to evaluate its stability under well conditions: (a) at 80 °F with no pressure, (b) at 150 °F and 500 psi, using static pressure, and (c) at 150 °F and 500 psi, after hot rolling.*

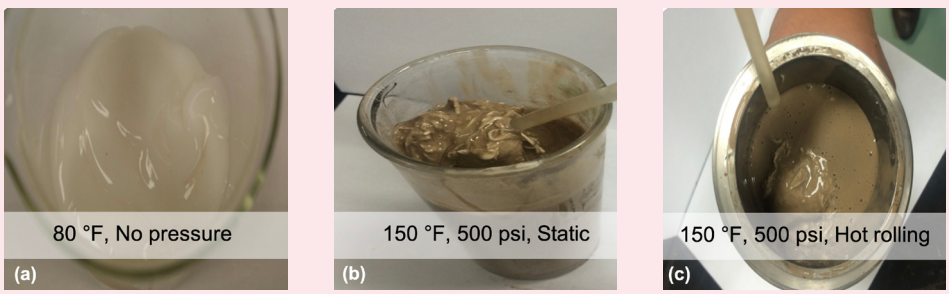

shows the test sample conducted at 150 °F and 500 psi, after hot rolling.

These tests were to observe the attitude of the polymer when increasing the temperature and pressure. The results showed that the polymer is formed direct and the solidification is increased with temperature and pressure. Importantly, the polymer does not show any degradation at these conditions.

Field Trial Test

The developer completed trial tests for polysweep observing the results, and conducted comprehensive lab tests that showed promising results in regard to hole cleaning efficiency. The polysweep is produced when two fluids, one containing PVA and one containing borax, react together. The generated mixture is a strong polymer gel that can remove the cuttings and seal any loss circulation zones.

The field trial was conducted recently. The well encountered partial losses during drilling the 16" hole section at 1,594 ft. The rig laid down the drilling assembly and ran open-ended drillpipe to the top of the loss zone. The rig spotted 140 bbl of the polysweep (15 bbl of hi-vis spacer, 90 bbl of polysweep, 15 bbl hi-vis spacer, and 20 bbl caustic pill) across the loss zone. Static losses dropped to zero. The rig laid down open-ended drillpipe, ran the drilling assembly to the bottom, and resumed drilling with 100% circulation, and all the cuttings that were in the hole were transported to the surface successfully.

Conclusions

The developed crosslinker (polysweep) is a superior hole cleaning product that transports drill cuttings, metal shavings, and other debris out of the wellbore.

- Two fluids when mixed downhole generate gel that has a high carrying capacity.
- The polymer is compatible for use in water-based drilling fluids.
- The gel lifts and carries metal shaving debris during milling operations and provides a reliable solution in partial circulation conditions.
- The polymer helps minimize the number of wiper trips.
- The gel is nontoxic and chemically inert.

Acknowledgments

This article was previously presented at the International Petroleum Technology Conference, Dhahran, Saudi Arabia, February 13-15, 2020.

References

1. Al Rubaii, M.M.: "A New Robust Approach for Hole Cleaning to Improve Rate of Penetration," SPE paper 192223, presented at the SPE Kingdom of Saudi Arabia Annual Technical Symposium and Exhibition, Dammam, Saudi Arabia, April 23-26, 2018.
2. Al Rubaii, M.M., Sehsah, O.R. and Omini, E.: "Approach to Improve Well Drilling Performance," SPE paper 194223, presented at the SPE Kingdom of Saudi Arabia Annual Technical Symposium and Exhibition, Dammam, Saudi Arabia, April 23-26, 2018.
3. Pigott, R.J.S.: "Mud Flow in Drilling," API paper 14-091, presented at the Drilling and Production Practice Conference, New York, New York, 1941.
4. Hossain, M.E. and Al-Majed, A.A.: *Fundamentals of Sustainable Drilling Engineering*, Wiley, March 2015, 786 p.
5. Moore, P.L.: "Five Factors That Affect Drilling Rate," *Oil and Gas Journal*, Vol. 56, No. 40, 1968, pp. 141-170.
6. Al Rubaii, M.M., Al Yami, A.S. and Omini, E.: "A Robust Correlation Improves Well Drilling Performance," SPE paper 195062, presented at the SPE Middle East Oil and Gas Show and Conference, Manama, Kingdom of Bahrain, March 18-21, 2019.
7. Nwagu, C., Awobadejo, T. and Gaskin, K.: "Application of Mechanical Cleaning Device: Hole Cleaning Tubulars, to Improve Hole Cleaning," SPE paper 172403, presented at the SPE Nigeria Annual International Conference and Exhibition, Lagos, Nigeria, August 5-7, 2014.
8. Caenn, R., Darley, H.C.H. and Gray, G.R.: *Composition and Properties of Drilling and Completion Fluids*, 7th edition, Elsevier Inc., 2017, 748 p.
9. Adari, R.B., Miska, S., Kuru, E., Bern, P., et al.: "Selecting Drilling Fluid Properties and Flow Rates for Effective Hole Cleaning in High-Angle and Horizontal Wells," SPE paper 63050, presented at the SPE Annual Technical Conference and Exhibition, Dallas, Texas, October 1-4, 2000.
10. Larsen, T.I., Pilehvari, A.A. and Azar, J.J.: "Development of a New Cuttings Transport Model for High-Angle Wellbores including Horizontal Wells," *SPE Drilling & Completion*, Vol. 12, Issue 2, June 1997, pp. 129-136.

About the Authors

Meshari M. Alshalan

B.S. in Petroleum Engineering, University of Leeds

Meshari M. Alshalan is a Petroleum Engineer working with the Drilling Technology Team of Saudi Aramco's Exploration and Petroleum Engineering Center – Advanced Research Center (EXPEC ARC). Meshari works on number of projects that are focused on advanced drilling and workover methods, as well as developing cost-effective methods for reducing drilling expenses.

In 2016, he received his B.S. degree in Petroleum Engineering from the University of Leeds, Leeds, U.K. Meshari is currently pursuing an M.S. degree in Petroleum Engineering as a part-time student at King Fahd University of Petroleum and Minerals (KFUPM), Dhahran, Saudi Arabia.

Dr. Abeer M. Al-Olayan

Ph.D. in Analytical Chemistry, King Faisal University

Dr. Abeer M. Al-Olayan is a Senior Research Scientist and the Head of Upstream Commercialization at Saudi Aramco's Exploration and Petroleum Engineering Center – Advanced Research Center (EXPEC ARC). Abeer is also Project Leader at the Saudi Aramco Global Research Centers in the U.S. and at MIT.

She was an Assistant Professor with the Chemistry Department of Dammam University before joining Saudi Aramco in 2011.

Abeer has an academic and industrial background with more than 19 years of experience in chemistry and related applications.

She is the recipient of the Woman of the Year Award for Oil and Gas and Petrochemicals in the Middle East for 2017-2018, as well as other local, regional, and international awards. Abeer was selected as one of the top 100 elite figures in Global Energy by the British *Petroleum Economist* magazine.

She is a Visiting Scientist at the Department of Material Science and Engineering at MIT. Abeer also teaches a course related to empowering science in the oil and gas industry at MIT.

She holds an executive certificate on Innovation and Strategy from the MIT Sloan School of Management. Abeer also served on the Board of Directors at the American Chemical Society-Saudi Arabia section as the first female member in 2010.

She is the author of a number of publications, and has several filed patents.

In 1996, Abeer received her B.S. degree in Chemistry from King Faisal University (KFU), Dammam, Saudi Arabia. She received both her M.S. and Ph.D. degrees in Analytical Chemistry from KFU, in 2004 and 2008, respectively.

Mohammed M. Al-Rubaii

M.S. in Petroleum Engineering, King Fahd University of Petroleum and Minerals

Mohammed M. Al-Rubaii is a Drilling Engineer with the Drilling Technology Division of Saudi Aramco's Exploration and Petroleum Engineering Center – Advanced Research Center (EXPEC ARC). He joined Saudi Aramco in 2012. Since that time, Mohammed has worked on several projects regarding hole cleaning automation, formation pressures automation, rheological properties of drilling fluid automation, bit hydraulics automation, and well drilling and operations performance automation.

He has developed several automated models and methods for drilling, which has contributed to increased optimization, time, and cost-effectiveness.

Mohammed is an active member of the Society of Petroleum Engineers (SPE) where he has served on several conferences. Mohammed has published 15 SPE papers, and initiated and co-chaired several SPE advanced technical workshop series in the region.

He is also an active member of the Dhahran Geoscience Society. Mohammed has filed 10 patent applications.

He is currently working on writing a chapter for a book entitled "Data Analytics for Drilling Process Improvement."

Mohammed received both his B.S. degree and M.S. degree in Petroleum Engineering from King Fahd University of Petroleum and Minerals (KFUPM), Dhahran, Saudi Arabia. He is currently studying for his Ph.D. degree in Petroleum Engineering at KFUPM.

Timothy E. Moellendick

B.S. in Petroleum Engineering, Marietta College

Timothy E. Moellendick is the Chief Technologist for the Drilling Technology Division at Saudi Aramco's Exploration and Petroleum Engineering Center – Advanced Research Center (EXPEC ARC). Timothy is considered the industry expert in casing and liner drilling applications and engineering.

In his previous role as Director of Technology for Schlumberger, he was responsible for growing the technical and operational knowledge base used to develop, plan, and execute this technology worldwide. Timothy has also held drilling operations and engineering positions, including Senior Drilling Engineer, Drilling Manager for North America, Senior Field Engineer/Directional Driller and Operations Coordinator for the Gulf Coast of Mexico.

With more than 25 years of oil and gas industry experience, he leads a team of world-class researchers in developing the next generation of drilling technology required by Saudi Aramco's Drilling and Workover stakeholders.

In 1996, Timothy received his B.S. degree in Petroleum Engineering from Marietta College, Marietta, OH.

Systems and Procedure for Obtaining Relative Permeability Ratio from Data Acquired during Drilling Operation

Babatope O. Kayode and Dr. Bander N. Al-Ghamdi

Abstract /

Relative permeability (k_r) is a concept introduced into Darcy's flow equation to account for multiphase flow. k_r is measured through steady-state or unsteady-state laboratory experiments, each with its peculiar advantages and disadvantages. This article discusses the basis for a new, faster, more reliable, and cost-effective methodology for acquiring relative permeability ratio (k_{rr}) data while drilling, and presents the modifications required to current flow equations to replace the use of k_r with the use of k_{rr}.

After drilling through a reservoir section, relevant logs like resistivity and porosity are acquired and interpreted for water saturation (s_w). Zones of constant average s_w are then tested using conventional drill stem test equipment, and the relative amounts of oil and water in the extracted liquid are determined at the surface using standard water cut determination procedures. Using equations derived and discussed in this article, these flow data are converted to a plot of k_{rr} as a function of average water saturation $k_{rr}(s_w)$ and saturation dependent total phase mobility $M_t(s_w)$. For the purpose of this article, an open source experimental k_r data and corresponding rock and fluid properties were used to simulate drill stem test fluid flow rates; the k_{rr} and M_t were then computed from these flow data at various averages of s_w.

Conventional steady-state and unsteady-state k_r experiments are carried out on restored cores having limited dimensions and whose initial s_w, wettability, and fluid viscosity ratio may need to be restored to representative in situ conditions using industry standard approaches. The new methodology presented acquires k_{rr} data at larger scale and at in situ conditions of initial s_w, wettability, and fluid viscosity ratio, thereby eliminating the need for core restoration.

A steady-state k_r experiment on a single core takes about 10 weeks, whereas k_{rr} acquisition on an entire pay interval can be carried out within hours. A steady-state k_r measurement does not permit the estimation of critical s_w, while the unsteady-state k_r experiment does not provide k_r data for all saturations less than the breakthrough saturation. The new methodology is designed to allow the estimation of critical s_w and residual oil saturation. These parameters are important inputs during numerical simulation tasks of history matching and field development predictions.

Introduction

Relative permeability (k_r) is the ratio of effective permeability of a phase to a reference such as its permeability when it fully saturates the porous medium. Experimental data over the years have noted multifaceted complexity associated with the direct laboratory measurement of k_r. Work by Leverett (1939)[1] and Leverette and Lewis (1941)[2] leads to the conclusion that k_r to a phase is only a function of the saturation of that phase. Later work by other researchers, e.g., Odeh (1959)[3] and Aboujafar (2014)[4], have shown that the k_r of the non-wetting phase is not only a function of saturation, but also a function of the fluid viscosity ratio when the sample's single-phase permeability is greater than 1 Darcy. Odeh (1959)[3] claims that theoretical explanations by Yuster (1951)[5] supports his conclusions, although several authors like Baker (1960)[6] have criticized Odeh's findings.

It has been shown that to obtain reliable k_r measurements in the laboratory, attention must be given to address problems such as capillary end effects, hysteresis, and scaling effects[7-9]. It has also been shown that in some situations of strong oil-water preferential wettability, useful k_r measurement data can be obtained at room temperature using dead or refined oil, however, such tests may provide misleading results for mixed wettability rocks[10, 11]. In addition, it has been shown that when transporting the core from the reservoir to the surface condition, this process removes the confining stresses and potentially results in changes in the core's pore structure.

For laboratory data to be useful in scaling up to the field level, measurements should be taken at conditions representative of those found in the reservoir. This entails aging[10] the core to restore the wettability state and performing the test with the appropriate combination of viscous, capillary, and gravity forces representative of reservoir conditions[8, 10], as well as restituting the reservoir's confined pressure and stress conditions.

Steady-State k_r Measurement

Oil and water are injected simultaneously into the core at a constant rate or constant pressure for a period required to reach equilibrium. Pressure gradient, flow rates, and saturations are measured — and with the aid of Darcy's law — used to obtain an effective permeability for each phase. The key advantage of this method is the ability to determine the k_r for a wider range of saturation levels; therefore, it is the method of choice by many. Its key demerit is its inherent time requirement and necessity for an independent measurement of fluid saturation in the core.

Unsteady-State k_r Measurement

This is the fastest approach for obtaining k_r in the laboratory. It consists of displacing fluid by a constant rate or the constant pressure injection of a driving fluid and measuring the flow rate of the displaced fluids at the core's exit face. The data is then analyzed using the Buckley-Leverette equation for linear displacement of immiscible and incompressible fluids by often neglecting capillary end effects.

The limitations of the unsteady-state approach is the occurrence of viscous fingering and channeling in heterogeneous cores, and the fact that no k_r data is measured prior to injected fluid breakthrough. In addition, the operational requirement for the use of viscous oil (as a means of reducing viscous fingering of injected water) and high injection rates masks the role of capillarity and wettability. The centrifuge technique is an unsteady-state measurement believed to overcome the viscous fingering problem of unsteady-state measurement and provides the most reliable estimate of residual non-wetting phase saturation than other techniques by better simulating the gravity drainage process[7, 12].

It is because of these limitations, difficulties, and uncertainties associated with the laboratory measurement of k_r, coupled with the fact that the most reliable tests are time-consuming — especially when it involves aging a core to its presumed original wettability (it can sometimes require about 5 weeks) — that several researchers[13-15] have been motivated to explore the possibility of obtaining k_r data in situ.

Some of these approaches are based on inverse solutions[14, 15] in which k_r is derived from history matching of field data, while Al-Rushaid et al. (2017)[13] has currently provided an approach to independently determine the k_r using downhole measured data.

Described next are some of the steps proposed[13] and the inherent limitations of assumptions.

1. Absolute permeability is calculated from pressure transient analysis (PTA) done at free water level. Conduct another PTA at the oil zone and divide the interpreted effective oil permeability by the absolute permeability obtained in the free water level. This step already assumes that the reservoir rock is homogeneous, and therefore, the differences in effective permeability thickness (kh) between the oil zone and free water level is due only to differences in the fluid viscosity of oil and water, respectively.

   This is a rarely adequate assumption. Moreover, in low permeability, reservoirs where the free water level may be significantly deeper than the dry-oil zone (large transition zone); drilling further down to free water level to conduct a baseline PTA measurement may represent a significant additional cost.

2. The k_r endpoints were determined from log interpretation. The minimum water saturation (s_w) on logs is used as the k_{rw} endpoint, while the lowest oil saturation is interpreted as the s_{or}. The limitation of this approach is that in reservoir rocks with sections containing significant bound water, if the lowest s_w in the reservoir interval is interpreted as the k_{rw} endpoint, this would lead to significant water production from the bound water region, whereas in reality, the bound water is immobile.

3. A PTA is conducted within the transition zone and interpreted for effective oil and water permeability using the relative flow rates of each phase. These effective oil and water permeabilities are then converted to k_r by normalizing with the absolute permeability obtained from the PTA conducted below the free water level. The limitations here are as explained earlier; the absolute permeability in the transition zone is not necessarily similar to that below the free water level. Therefore, the differences in effective permeability may not be only due to fluid viscosity differences.

In this current work, we propose an alternative multiphase flow parameter that can be determined from downhole data independent of history matching and propose modifications to multiphase flow equations that would permit the use of the proposed alternative multiphase flow parameter.

Mathematical Basis for New Methodology

The original Darcy's flow equation, Eqn. 1, was derived for flow of single-phase incompressible liquid; particularly the equation was derived for use in the field of hydrology to study the flow of water in the water table.

$$q = \frac{kA\Delta P}{\mu\beta\Delta x} \quad 1$$

In oil reservoir studies, single-phase flow is an idealistic assumption; this is because the drainage process through which oil accumulates in originally water-bearing sands does not completely eliminate the connate water. This connate water flows alongside the oil — in the transition zone — during production. In addition, most reservoirs either experience aquifer support or some sort of fluid injection (gas, water, surfactants) for pressure support or improvement of sweep.

Therefore, a correction term is needed to be incorporated into Eqn. 1 to account for the reduction in the flow of the main phase in the presence of other phases within the rock pore system. This correction term is referred to as k_r. Equation 1 can therefore be re-written as:

$$q = \frac{k\kappa_r A\Delta P}{\mu\beta\Delta x} \quad 2$$

In general, the equation for radial flow under semi-steady-state conditions is given by:

$$q = \frac{kh\kappa_r \Delta P}{141.2\mu\beta\left(ln\frac{r_e}{r_w}-0.75\right)} \quad 3$$

The k_r is measured in the laboratory using the steady-state approach or unsteady-state approach. Once the k_{ro} and k_{rw} data have been determined as a function of s_w, the flow of each phase can be independently calculated as:

$$q_o = \frac{kh\kappa_{r_o} \Delta P}{141.2\mu_o\beta_o\left(ln\frac{r_e}{r_w}-0.75\right)} \quad 4$$

$$q_w = \frac{kh\kappa_{r_w} \Delta P}{141.2\mu_w\beta_w\left(ln\frac{r_e}{r_w}-0.75\right)} \quad 5$$

An expression can be derived for the produced water-oil ratio at in situ conditions by dividing Eqn. 5 with Eqn. 4 as follows:

$$\frac{q_w}{q_o} = \frac{\kappa_{rw}/\mu_w\beta_w}{\kappa_{ro}/\mu_o\beta_o} \quad 6$$

An expression for k_{rr} can be obtained from Eqn. 6 as follows:

$$\kappa_{rr} = \frac{\kappa_{rw}}{\kappa_{ro}} = \frac{q_w\mu_w\beta_w}{q_o\mu_o\beta_o} \quad 7$$

In addition, an expression for the total liquid rate can be obtained by adding Eqn. 4 and Eqn. 5 as:

$$q_t = q_o + q_w = \frac{kh\Delta P}{141.2\left(ln\frac{r_e}{r_w}-0.75\right)}\left[\frac{\kappa_{ro}}{\mu_o\beta_o} + \frac{\kappa_{rw}}{\mu_w\beta_w}\right] \quad 8$$

We can re-write Eqn. 8 as:

$$q_t = \frac{kh\Delta P}{141.2\left(ln\frac{r_e}{r_w}-0.75\right)} M_t \quad 9$$

where $$M_t = \left[\frac{\kappa_{ro}}{\mu_o\beta_o} + \frac{\kappa_{rw}}{\mu_w\beta_w}\right] \quad 10$$

Note that over a moderate range of pressures, total phase mobility (M_t) can be sufficiently assumed as a sole function of s_w when reservoir fluids are of low compressibility and viscosity. These assumptions are adequate for the flow of oil above bubble point pressure.

If a flow test is performed on a known interval length of a reservoir at several ΔP, Eqn. 9 suggests that a plot of q_t vs. ΔP will yield a slope R from which M_t can be determined as:

$$M_t(S_w) = \frac{141.2\left(ln\frac{r_e}{r_w}-0.75\right)R}{kh} \quad 11$$

Where h is the flow interval and k is the average interval permeability, and r_e is the test's investigation radius. The product kh and r_e can be obtained from interpretation of the pressure transient data recorded during the mini drill stem test, Fig. 1.

From the principles of well testing[16], the sequence of pressure transient behavior during partial penetration is: (1) early radial flow representing only the contribution from the perforated interval, kh, (2) spherical flow from which k_v/k can be estimated, and (3) when the diffusion has reached the upper and lower boundaries, the flow regime becomes radial again, but this time corresponding to kh_t. Figure 2 shows the early radial flow kh.

From the foregoing, the phase flow rates at any saturation can be computed by rearranging Eqn. 9 and Eqn. 6 as follows:

$$q_t = q_o + q_w = \frac{kh\Delta P}{141.2\left(ln\frac{r_e}{r_w}-0.75\right)} M_t \quad 12$$

$$\frac{q_w}{q_o} = \frac{\mu_o\beta_o}{\mu_w\beta_w}\kappa_{rr} \quad 13$$

Equations 12 and 13 can be solved simultaneously for each phase flow rate to obtain:

$$q_o = \frac{kh\Delta P}{141.2\left(ln\frac{r_e}{r_w}-0.75\right)} * \frac{M_{t_{(sw)}}}{\left(1+\frac{\mu_o\beta_o\kappa_{rr}}{\mu_w\beta_w}\right)} \quad 14$$

$$q_w = \frac{q_o\mu_o\beta_o}{\mu_w\beta_w}\kappa_{rr} \quad 15$$

Procedure for Field Application

After a well has been logged, various sections with different s_w are identified, Fig. 3, and tested as described here.

- Impose a drawdown of 100 psi over a 1 ft interval and record the stabilized oil and water flow rate, then

Fig. 1 *A schematic of the flow regimes during a mini drill stem test.*

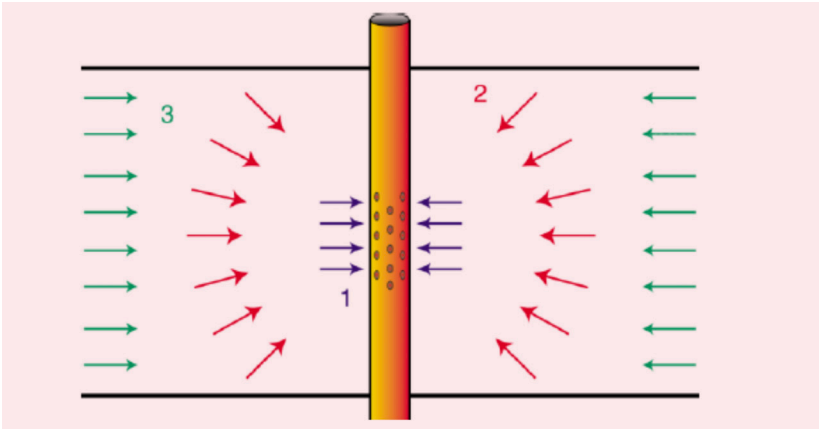

Fig. 2 *The sample Log-Log diagnostic plot showing stage-1 stabilization (permeability*perforation thickness).*

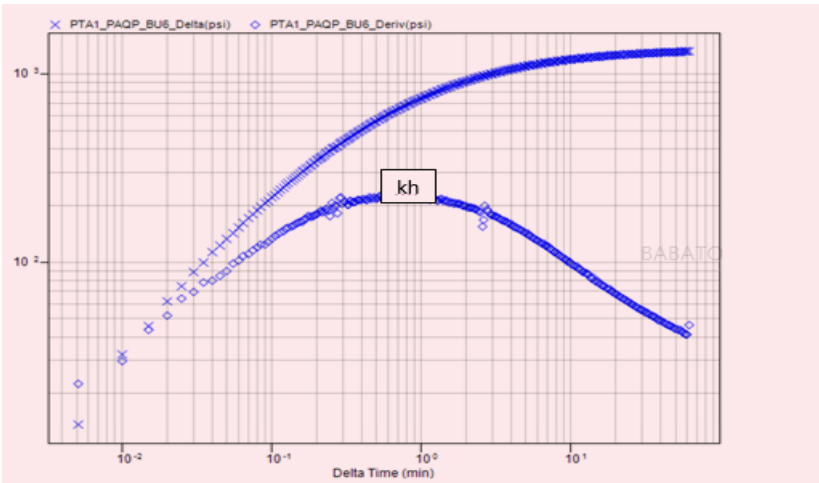

Fig. 3 *Example of S_w log.*

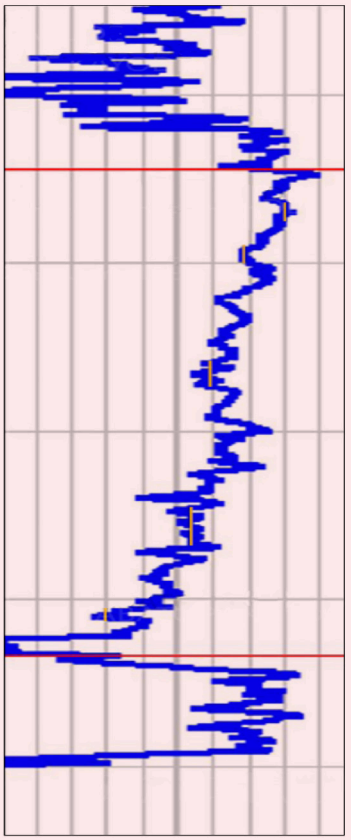

Table 1 *Open source relative permeability data.*

S_w	K_{rw}	K_{ro}
0.2	0	0.8
0.25	0.002	0.61
0.3	0.009	0.47
0.35	0.02	0.37
0.4	0.033	0.285
0.45	0.051	0.22
0.5	0.075	0.163
0.55	0.1	0.12
0.6	0.132	0.081
0.65	0.17	0.05
0.7	0.208	0.027
0.75	0.251	0.01
0.8	0.3	0

Table 2 *Calculation of k_{rr} from fluid phases' rate and rock and fluid properties.*

S_w	K_{rw}	K_{ro}	dP psi	Q_w bbl	Q_o bbl	K_{rr}
0.2	0	0.8	500	0	0.757654	0
0.25	0.002	0.61	500	0.024624	0.577711	0.003279
0.3	0.009	0.47	500	0.110807	0.445122	0.019149
0.35	0.02	0.37	500	0.246238	0.350415	0.054054
0.4	0.033	0.285	500	0.406292	0.269914	0.115789
0.45	0.051	0.22	500	0.627906	0.208355	0.231818
0.5	0.075	0.163	500	0.923391	0.154372	0.460123
0.55	0.1	0.12	500	1.231188	0.113648	0.833333
0.6	0.132	0.081	500	1.625169	0.076713	1.62963
0.65	0.17	0.05	500	2.09302	0.047353	3.4
0.7	0.208	0.027	500	2.560872	0.025571	7.703704
0.75	0.251	0.01	500	3.090283	0.009471	25.1
0.8	0.3	0	500	3.693565	0	—

increase the drawdown to 200 psi, 300 psi, and 500 psi, up to a maximum ΔP such that the $P_{wf} = P_b$, and measure the stabilized liquid flow rates in all cases.

- For each drawdown flow period, use Eqn. 7 to determine k_{rr}. This value should be approximately identical for all drawdown pressure values assuming that the fluids have low compressibility and low viscosity. This assumption is adequate for the flow of oil above P_b.
- From the recorded multirate pressure transients, kh and r_e can be estimated using principles of PTA, and then using Eqn. 11, the M_t is computed.
- Repeat these steps for various log saturation intervals and come up with a curve for k_{rr} vs. s_w and M_t vs. s_w.
- A plot of the interval kh vs. the interval average porosity (from density, sonic, or neutron log) from multiple wells is used for reservoir flow-type definition.
- Finally, Eqns. 14 and 15 can then be used to predict the phase flow rates at any saturation, and for any drawdown pressure.
- Any s_w interval where the maximum ΔP (Pi-P_b) produces single-phase oil is the operational critical water saturation, S_{wcr*} for the rock type and any s_w where the maximum ΔP produces single-phase water is the operational residual oil saturation, S_{or*}, for the rock type.

The S_{or*} determined from this new methodology is more operationally reliable than the S_{or} determined from laboratory experiments. This is because the S_{or*} is based on the maximum expected displacement pressure rather than the arbitrarily large displacement pressures used in determining the S_{or} in the laboratory. The S_{or*} provides a more reliable estimate of mobile oil recoverable by primary and secondary recovery mechanisms.

Also, the s_{wcr*} determined from this methodology reflects the presence of bound water. If a log section shows s_w that is higher than the lowest s_w in the reservoir interval, and if the application of maximum ΔP still does not result in water production, it simply implies such water represents bound water.

The k_r data shown in Table 1 is representative of the flow from a given reservoir Res-xyz.

Using Eqns. 4 and 5, individual phase flow rates were computed and the total flow rate calculated from the sum. A pressure drawdown of 500 psi was assumed, permeability of 10 md, flow interval of 1 ft, oil viscosity of 5 cP, water viscosity of 0.5 cP, oil formation volume factor of 1.3, and a water formation volume factor of 1.0.

Table 2 summarizes the computed flow rates, which are used to represent actual measured flow rate. Also shown is the calculated k_{rr}.

Figure 4 shows the plot of the k_{rr} vs. the s_w.

At each saturation, multirate flow tests are conducted and the results are shown in Table 3.

Figure 5 shows the plot of the total fluid rate vs. the drawdown pressure at each s_w.

The M_t is then determined from the slope of each data series using Eqn. 11.

Figure 6 shows the plot of M_t vs. s_w.

Finally, using Eqns. 14 and 15 together with the M_t and k_{rr} from the relevant plots, we can predict the phase flow rates. Table 4 shows that the predicted flow rates using the parameters k_{rr} and M_t derived in this article

Fig. 4 *The calculated* k_{rr} *vs.* s_w.

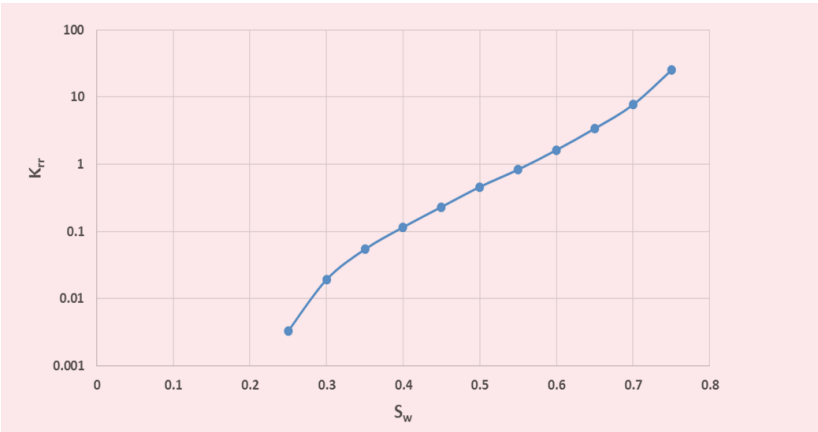

Table 3 *The fluid flow rate at various drawdown pressure for different average water saturations.*

S_w = 0.2		S_w = 0.3		S_w = 0.4		S_w = 0.5		S_w = 0.6		S_w = 0.7		S_w = 0.8	
ΔP	**qt**	**ΔP**	**qt**	**ΔP**	**qt**	**ΔP**	**qt**	**ΔP**	**qt**	**ΔP**	**qt**	**ΔP**	**qt**
100	0.151531	100	0.111186	100	0.135241	100	0.215553	100	0.340376	100	0.517289	100	0.738713
200	0.303062	200	0.222372	200	0.270483	200	0.431105	200	0.680752	200	1.034577	200	1.477426
300	0.454593	300	0.333557	300	0.405724	300	0.646658	300	1.021129	300	1.551866	300	2.216139
400	0.606124	400	0.444743	400	0.540965	400	0.862211	400	1.361505	400	2.069154	400	2.954852
500	0.757654	500	0.555929	500	0.676207	500	1.077763	500	1.701881	500	2.586443	500	3.693565

Fig. 5 *The total liquid rate vs. the drawdown pressure at different water saturations.*

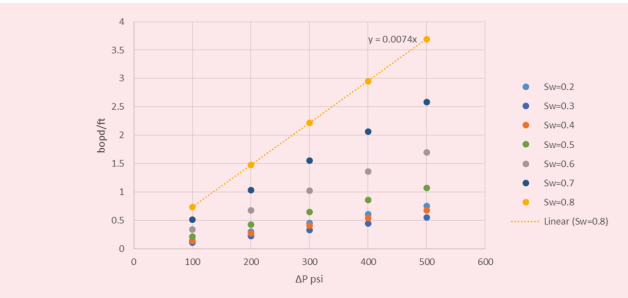

Fig. 6 *The plot of* M_t *vs.* s_w.

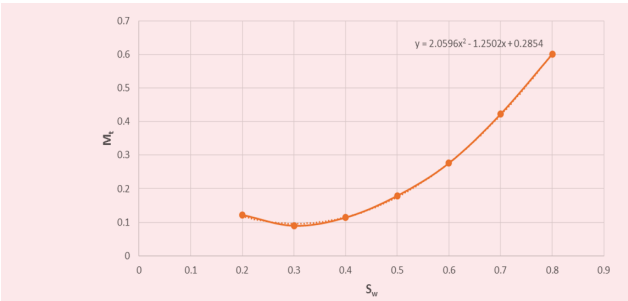

Fig. 7 *The comparison plot of the calculated rate vs. the measured rate.*

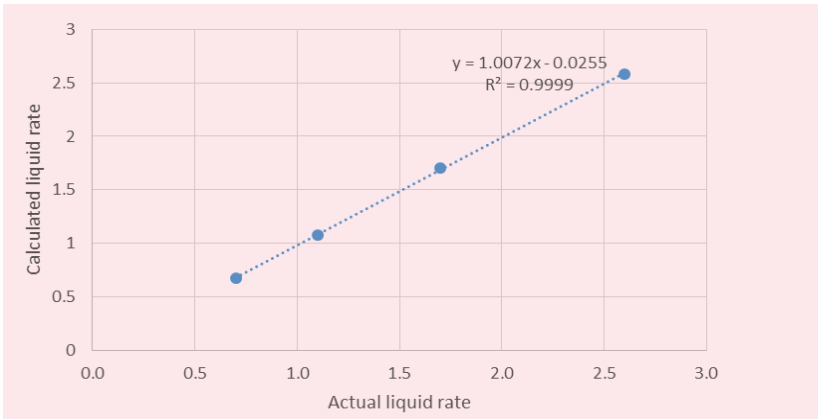

Table 4 *Using values of* k_{rr} *and* M_t *at various saturations to compute phase flow rates.*

S_w	K_{rr}	M_t	q_o	q_w	q_t	Measured
0.6	1.62963	0.276156	0.76628	1.623373	1.7000003	1.701881206
0.5	0.460123	0.178689	0.157557	0.942443	1.1000000	1.07776339
0.4	0.115789	0.113711	0.279412	0.420588	0.7000000	0.676206556
0.7	7.703704	0.422356	0.025705	2.574295	2.6000000	2.586442724

are very close to the actual data.

Figure 7 plots the correlation between the calculated rate and the measured rate, along with showing that the equations developed are able to effectively predict the measured rates.

Conclusions

In this article, we have developed equations and procedures for obtaining the k_{rr} from information obtained during drilling. The approach is faster than conventional steady-state and unsteady-state k_r experiments. It is more representative of in situ conditions of wettability and the viscosity ratio and provides data based on averaging larger rock volumes. Subsequently, due to the inherent assumptions, this approach cannot be used to obtain the gas-oil k_{rr} since the viscosity of gas is highly pressure dependent.

Acknowledgments

This article was prepared for presentation at the 14th Middle East Geosciences Conference and Exhibition, Manama, Kingdom of Bahrain, September 14-17, 2020.

Nomenclature

q_o, q_w, q_t = Flow rate (oil, water, total)

μ_o, μ_w = Viscosity (oil, water)

β_o, β_w = Formation volume factor (oil, water)

k_{ro}, k_{rw} = Relative permeability (oil, water)

r_w = Wellbore radius

r_e = Reservoir radius

R = slope of qt vs. ΔP plot

References

1. Leverett, M.C.: "Flow of Oil-Water Mixtures through Unconsolidated Sands," *Transactions of the AIME*, Vol. 132, Issue 1, December 1939, pp. 149-171.
2. Leverett, M.C. and Lewis, W.B.: "Steady Flow of Gas-Oil-Water Mixtures through Unconsolidated Sands," *Transactions of the AIME*, Vol. 142, Issue 1, December 1941, pp. 107-116.
3. Odeh, A.S.: "Effect of Viscosity Ratio on Relative Permeability," *Petroleum Transactions of the AIME*, Vol. 216, Issue 1, December 1959, pp. 346-353.
4. Aboujafar, S.M.: "Effect of Oil Viscosity and Brine Salinity/Viscosity on Water/Oil Relative Permeability and Residual Saturations," paper presented at the SPWLA 55th Annual Logging Symposium, Abu Dhabi, UAE, May 18-22, 2014.
5. Yuster, S.T.: "Theoretical Considerations of Multiphase Flow in Idealized Capillary Systems," paper WPC-4129, presented at the 3rd World Petroleum Congress, The Hague, the Netherlands, May 28-June 6, 1951.
6. Baker, P.E.: "Discussion of Effect of Viscosity Ratio on Relative Permeability," *Journal of Petroleum Technology*, Vol. 12, Issue 11, November 1960, pp. 65-66.
7. Heaviside, J.B., Black, C.J.J. and Berry, J.F.: "Fundamentals of Relative Permeability: Experimental and Theoretical Considerations," SPE paper 12173, presented at the SPE Annual Technical Conference and Exhibition, San Francisco, California, October 5-8, 1983.
8. Honarpour, M. and Mahmood, S.M.: "Relative Permeability Measurements: An Overview," *Journal of Petroleum Technology*, Vol. 40, Issue 8, August 1988, pp. 963-966.
9. Braun, E.M. and Blackwell, R.J.: "A Steady-State Technique for Measuring Oil-Water Relative Permeability Curves at Reservoir Conditions," SPE paper 10155, presented at the SPE Annual Technical Conference and Exhibition, San Antonio, Texas, October 4-7, 1981.
10. Jennings Jr., H.Y.: "Effect of Laboratory Core Cleaning on Water-Oil Relative Permeability," SPE paper 897-G, presented at the Fall Meeting of the Society of Petroleum Engineers of AIME, Dallas, Texas, October 6-9, 1957.
11. Hagoort, J.: "Oil Recovery by Gravity Drainage," *Society of Petroleum Engineers Journal*, Vol. 20, Issue 3, June 1980, pp. 139-150.
12. Osoba, J.S., Richardson, J.G., Kerver, J.K., Hafford, J.A., et al.: "Laboratory Measurements of Relative Permeability," *Journal of Petroleum Technology*, Vol. 3, Issue 2, February 1951, pp. 47-56.
13. Al-Rushaid, M., Al-Rashidi, H., Ahmad, M., Hadibeik, H., et al.: "Downhole Estimation of Relative Permeability with Integration of Formation Tester Measurements and Advanced Well Logs," paper presented at the SPWLA 58th Annual Logging Symposium, Oklahoma City, Oklahoma, June 17-21, 2017.
14. Liang, L., Zhu, J., Wang, F., Chen, J., et al.: "In Situ Estimation of Relative Permeability and Capillary Pressure from the Joint Inversion of Array Resistivity and Formation Test Data," SPE paper 187193, presented at the SPE Annual Technical Conference and Exhibition, San Antonio, Texas, October 9-11, 2017.
15. Zakirov, S.N., Indrupskiy, I.M., Zakirov, E.S., Anikeev, D.P., et al.: "Well Test for In Situ Determination of Oil and Water Relative Permeability," SPE paper 162011, presented at the SPE Russian Oil and Gas Exploration and Production Technical Conference and Exhibition, Moscow, Russia, October 16-18, 2012.
16. Houze, O., Viturat, D. and Fjaere, O.S.: *Dynamic Data Analysis, Chapter 6*, "Well Models," v4.12.03, KAPPA, 1988-2012.

About the Authors

Babatope O. Kayode

M.S. in Petroleum Engineering, Heriot-Watt University

Babatope O. Kayode is a Petroleum Engineer working with the Reservoir Simulation Division in Saudi Aramco's Reservoir Description & Simulation Department.

Babatope's previous work experience with SOWSCO Well Services Nigeria Ltd. involved the planning, supervision, and interpretation of pressure transient tests.

He also worked with Total Exploration and Production in Nigeria and in France, where he was involved in the construction and live updates of dynamic simulation models before joining Saudi Aramco in November 2014.

Babatope has 20 years of industry experience spanning Africa, Europe, and the Middle East with a research interest in the area of developing workflows for faster and better history matching. He is the author of nine technical papers and seven patents in this area.

Babatope received his B.S. degree in Petroleum Engineering from the University of Ibadan, Ibadan, Nigeria, and his M.S. degree in Petroleum Engineering from Heriot-Watt University, Edinburgh, Scotland, U.K.

Dr. Bander N. Al-Ghamdi

Ph.D. in Energy and Mineral Engineering, Pennsylvania State University

Dr. Bander N. Al-Ghamdi is the Division Head of the Reservoir Simulation Division of Saudi Aramco's Reservoir Description and Simulation Department. Bander's career has spanned major petroleum engineering disciplines, including drilling, production, and reservoir management. Much of his development have been focused on reservoir simulation, where he led major projects, currently in use as paramount in maximizing the potential of the company's hydrocarbon resources.

In 2019, Bander received Saudi Aramco's Excellence Award, for his leading role in the reserve certification project. During the same year, he graduated from the company's Technical Development Program with a specialty in Compositional Modeling.

Bander is an active member of the Society of Petroleum Engineers (SPE); he served as the Chairman of the SPE-Kingdom of Saudi Arabia Section during the 2018-2019 term, and is currently serving as a Board Director.

Bander received his Ph.D. degree in Energy and Mineral Engineering with a focus on Petroleum and Natural Gas Engineering from Pennsylvania State University, State College, PA.